CALCIUM CARBONATE DISPERSIONS

IN

NON-AQUEOUS MEDIA

by

I. Marković

A thesis submitted in partial fulfilment of the
requirements for the degree of Doctor of Philosophy
at the University of Bristol

Department of Physical Chemistry
University of Bristol

October 1984

MEMORANDUM

The work contained in this thesis is original except where due reference has been made. It has not been submitted for a degree at any other University.

I. MARKOVIC

To Miko and Tajko

ACKNOWLEDGEMENTS

I would like to thank Professor R.H. Ottewill, FRS, for his encouragement, guidance and help throughout this work.

I would also like to thank Dr. D.W. Thompson for his work in electron microscopy and Mr. M. Marshall for his help with the ultracentrifugation experiments.

I am indebted to Esso Chemical Co. Ltd. for financing this work, and in particular I would like to thank Dr. J. Marsh and Mr. I. Field for many stimulating discussions.

I am grateful to Dr. D.J. Cebula of Unilever, Colworth House, and Dr. J.B. Hayter of Oakridge Laboratory, Tennessee, for their assistance with the neutron scattering experiments.

I would also like to thank the technical staff of both Bristol University and Esso Chemical Co. Ltd. for their practical assistance, Dr. R.J. Newton for his help with the diagrams and Mrs. R. Williams for typing this thesis. Finally, many thanks to Mrs. J. Proctor and Miss F. Mills for keeping me sane.

ABSTRACT

Dispersions of calcium carbonate particles in a non-aqueous medium can be prepared by metathesis in the presence of surface active materials. The particles so formed have a small particle size, with diameters in the range 50 to 200 Å. Their principal industrial application is as additives in engine lubricating oils. Particles of this type which consist of an inorganic core particle with an adsorbed layer, and typically form dark brown dispersions, are difficult to characterize by conventional methods. Consequently, the technique of small angle neutron scattering has been adopted for the investigation of these systems and it has been shown to be experimentally successful.

In order to interpret the experimental data obtained, the theory of scattering has been developed for a spherical core particle surrounded by a concentric homogeneous shell. This appeared to model the form of the particle accurately and enabled both the radius of the particle and the thickness of the adsorbed layer to be determined in situ. The success of this model in defining the form factor for the particle made it possible to interpret the small angle neutron scattering from concentrated dispersions. The analysis indicated that the particles were sterically stabilized by the adsorbed layer and that the interaction potential was of the "hard-sphere" type. A comparison of the small angle neutron scattering data has been made with results obtained by ultracentrifugation on the same samples. A reasonable concordance in the values of the particle core radii was obtained between the two methods. However, the hydrodynamic thickness of the adsorbed layer determined by ultracentrifugation was found to be slightly greater than that obtained by neutron scattering. The decrease in the rate of sedimentation with the concentration of particles was attributed to a combination of viscosity effects and backward flow of solvent in the ultracentrifuge cell.

CONTENTS

CHAPTER ONE

CHAPTER 1

INTRODUCTION

Non-aqueous colloidal dispersions form a major part of the systems used in industrial processes, among which is the use of calcium carbonate dispersions as additives in lubricating oils[1]. Engine oils are nowadays a complex mixture of additives, each designed to counteract a specific problem. One of the serious problems encountered is that of corrosion caused by the oxidation products of the oil as well as the combustion products from the fuel. The marine engine is particularly susceptible to the latter hazard as it uses heavy residual fuel oil with a high sulphur content. During combustion sulphuric acid is formed which corrodes engine parts and consequently, an acid-neutralizing agent - in the form of colloidal calcium carbonate - is incorporated into the oil[2]. Hence, the study of calcium carbonate dispersions is not only of considerable commercial importance but it is also of great academic interest since this system is representative of dispersions of inorganic materials in non-aqueous media.

Owing to the importance of non-aqueous dispersions a lot of work has recently been devoted to their study. However, most of this work has been of a qualitative nature and it has not led to a fundamental understanding at the level available for aqueous dispersions. In part, this is because of a lack of suitable techniques for the study of non-aqueous dispersions since in many cases the methods employed for the investigation of aqueous systems are not applicable. This is primarily a consequence of the fact that electrostatic stabilization, usually common in aqueous dispersions, is not viable in non-aqueous dispersions.

Thus, in order to achieve colloidal stability the particles have to

be stabilized by an adsorbed layer of surface active agent or polymer. Moreover, this layer must be compatible with the medium of low dielectric constant to ensure steric stabilization. However, the existence of the adsorbed layer on the particles presents a number of problems for the examination of these systems. For example, in the case of aqueous dispersions, adsorption can be studied by adding the adsorbate to the system and measuring the amount taken up. This cannot be done with non-aqueous dispersions since removal of the adsorbed layer immediately causes destabilization.

Therefore, in order to progress the study of non-aqueous dispersions, techniques have to be found which enable the particles to be studied *in situ*. These techniques need to be able to provide information on:-

a) the size as well as the distribution of sizes of the native particles,

b) the thickness of the adsorbed layer,

c) the nature of the interactions between the particles,

d) the factors controlling the stability of the systems in both dilute and concentrated dispersions.

One technique which offers great promise for the investigation of these systems is that of small-angle neutron scattering. It enables an independent examination of the native particles and of the adsorbed layer to be carried out by applying the technique directly to the total system in situ. Moreover, it is particularly applicable to the study of small particles, i.e. with diameters in the size range 50 Å to 200 Å.

Calcium carbonate dispersions are an especially good system for such studies since the method of preparation ensures the formation of fairly monodisperse particles in the correct size range. In addition, the particles have adsorbed layers which occupy a substantial part of the volume

of the total particle which facilitates the theoretical modelling of systems of this type and results in relatively long term stability of the dispersions. Thus, it is also possible to study concentrated dispersions of these particles and moreover, the recent advances made in the theory of concentrated dispersions make it possible to interpret the experimental data obtained on such systems.

Finally, the information obtained by small-angle neutron scattering can be compared with that determined by more classical techniques, e.g. time-average light scattering and ultracentrifugation.

CHAPTER TWO

CHAPTER 2

BACKGROUND THEORY - NON-AQUEOUS DISPERSIONS

2.1 Colloid Stability in Non-Aqueous Media

Colloidal dispersions may be stabilized (i.e. prevented from flocculating or coagulating), either by incorporating charges into the particle surfaces, the counter-ions of which repel those near the surface of adjacent particles (electrostatic stabilization), or by protecting the particles with a layer of adsorbed polymer or surface active agent (steric stabilization). Electrostatic stabilization is of little value in many organic media because of the low density of ions in solution, and because the low dielectric constant of the medium (< 10) results in little attenuation of the coulombic repulsion between the particles as they come together. Therefore, the best method of protecting colloidal particles dispersed in non-aqueous media from the ever-present van der Waals force of attraction is by *steric stabilization.*

The phenomenon of steric stabilization has been exploited since ancient times in a variety of technological applications and products. These include nowadays paints, inks, glues, photography, various emulsions, polymer dispersions and, pertaining to this study, additives in lubricating oils. There are numerous practical advantages of this type of stabilization, one of which is its efficacy at both low and high volume fractions of the dispersed phase. Another characteristic feature of sterically stabilized dispersions is that they will redisperse spontaneously after drying and also upon changing the solvency of the medium.

The difference in the reversibility of flocculation between electrostatically and sterically stabilized dispersions probably stems from the fact that whereas sterically stabilized particles may be thermodynamically stable, dispersions that are electrostatically stabilized are usually only

kinetically stable. This is exemplified, in a very simplistic manner, by the difference between the potential energy diagrams for the two types of system. The essential features of the potential energy diagram of an electrostatically stabilized system comprise of an energy barrier to coagulation, called the primary maximum, and a deep primary minimum in which this irreversible coagulation occurs. A much shallower secondary minimum, where particle flocculation occurs, may also exist for electrostatically stabilized systems, whereas this is the only feature that may be present in the potential energy diagram of a sterically stabilized system (see Section 2.1.3).

2.1.1 Energy of interaction due to repulsion

Consider the approach of two spherical particles of radii a where each core particle is surrounded by an adsorbed layer of thickness δ, as depicted schematically in Figure 2.1. The thickness of the adsorbed layer equals the fully extended length of the surface active molecules stabilizing the particles. If the distance separating the cores of the particles is represented by H_o then one can delineate three possible regions of interaction between the particles[3]:-

i) $H_o \gg 2\delta$ - the particles are too far apart to experience any interaction;

ii) $\delta \lesssim H_o \lesssim 2\delta$ - if, upon contact of the adsorbed layers, the particles approach each other more closely then interpenetration of the two adsorbed layers will occur, with, possibly, concomitant desorption of some of the surface active molecules;

iii) $H_o < \delta$ - the two particle cores may approach to a distance less than the thickness of one adsorbed layer. In this

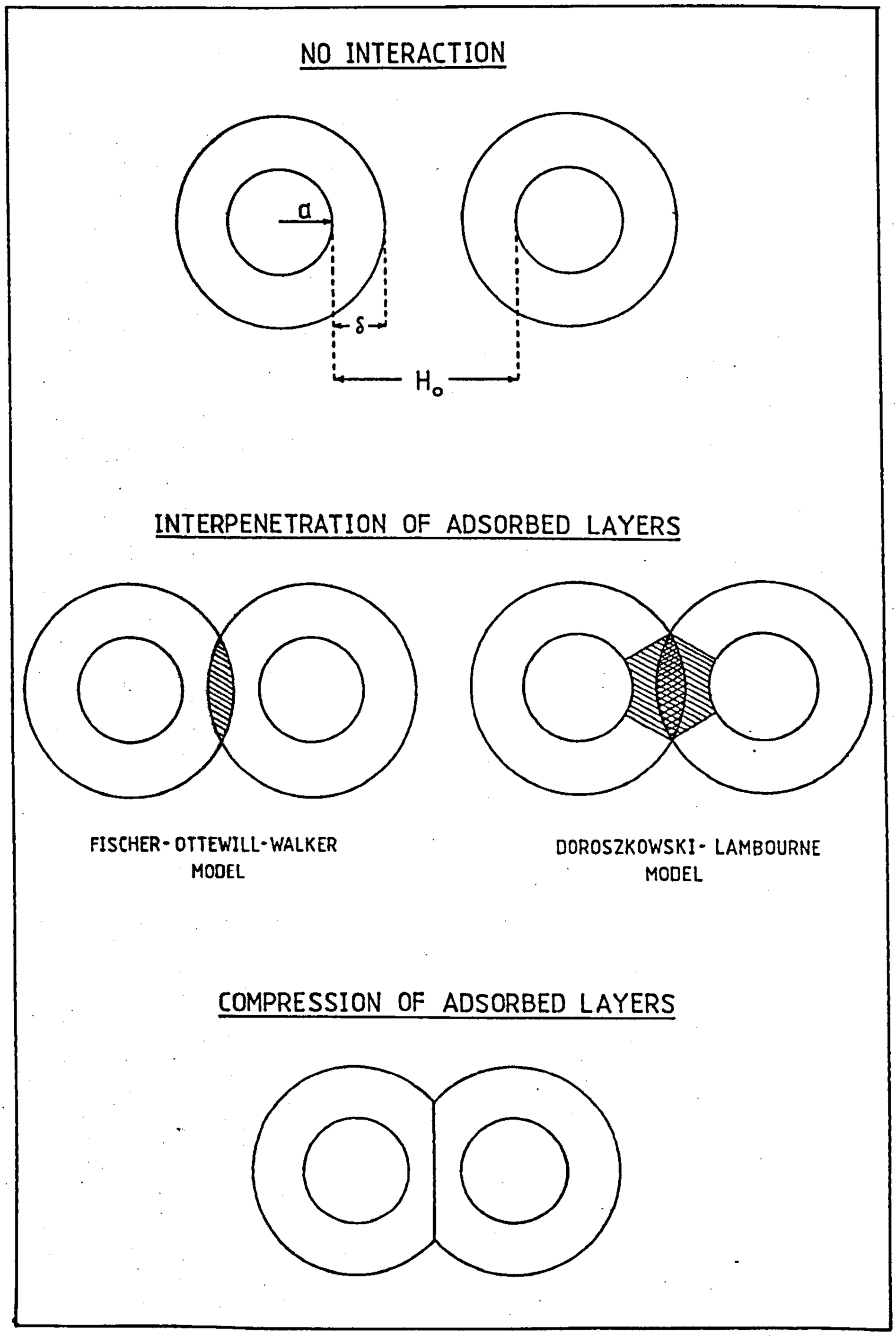

FIGURE 2.1 INTERACTIONS BETWEEN PARTICLES WITH ADSORBED LAYERS

case, the surface active molecules will experience a reduction in the volume available to them because of the presence of the core of the opposing particle. This is often called a "volume restriction" effect and leads to a compression of the adsorbed layers. This is very likely to result in desorption of the surface active agent in the compressed region of the layer.

The onset of steric interaction therefore occurs when the two adsorbed layers begin to overlap. The primary consequence of interpenetration is an increase in the concentration of stabilizing moieties in the overlap volume and the resulting decrease in concentration of molecules of the dispersion medium. Two effects arise from this. Firstly, the change in the concentration of molecules of the dispersion medium generates a difference in the chemical potential between the molecules of the medium in the region of interaction and those in the bulk medium since, by definition,

$$\mu_i = \left(\frac{\partial G}{\partial n_i} \right)_{T,P} \qquad \ldots \quad (2.1)$$

where μ_i is the chemical potential of component i

G is the Gibbs free energy of the system

n_i is the number of moles of component i.

This chemical potential difference can be related to an excess osmotic pressure in the following manner. If the chemical potential of the molecules of the bulk dispersion medium is μ_A and that of the molecules in the overlap volume is given by μ_B, then

$$\mu_A - \mu_B = \int_0^{\Pi_E} V \, dP \qquad \ldots \quad (2.2)$$

$$= V\Pi_E$$

where V is the volume of the region of interaction

and Π_E is the excess osmotic pressure.

The second effect arises due to the increase in the concentration of surface active molecules in the overlap volume, which reduces the lateral motion of these molecules. This leads to a loss of entropy of the stabilizer molecules attached to one particle owing to the physical presence of those attached on another particle. This effect is of much smaller magnitude than the previous one.

The inherent interaction between the surface active molecules and those of the dispersion medium will obviously be an important factor in both effects mentioned above. The overall interaction in the inter-penetrational domain can be described by the change in free energy which occurs as a result of the overlap of the adsorbed layers. This is usually called the *mixing free energy change*, ΔG_{mix}, a term originating from polymer solution theories.

In the third region of interaction, where greater interpenetration of the adsorbed layers results in compression of the layers, there will be, in addition to the effects mentioned above, a further loss of entropy. Namely, the surface active molecules will experience a loss in configurational entropy upon compression by the opposing particle core surfaces. This entropic effect, arising from a physical reduction in the volume available to the surface active molecules, is often called the "volume restriction" effect. The loss of entropic energy of the stabilizing moieties is balanced by a gain in elastic energy so that the magnitude of this effect can be described by an *elastic free energy change*, ΔG_{EL}.

Simplistically, one can represent the change in the operative free energy of steric interaction, ΔG_S, between two particles in a non-aqueous medium as

$$\Delta G_S = \Delta G_{MIX} + \Delta G_{EL} \qquad \ldots \quad (2.3)$$

The elastic contribution to the total energy generates an interaction that is always repulsive, i.e. ΔG_{EL} is positive. This is in contradistinction to the mixing term which may be a positive or negative quantity, depending on the interactions between the stabilizing surface active chains and the medium.

The early theories portrayed unrealistically the steric repulsive interaction as being dependent upon only one of the above mentioned terms. Also, some of these theories were originally formulated for particles stabilized by polymer chains. Surface active molecules are adsorbed at one end to the particle surface with the other end of the molecule extending into the dispersion medium in a direction approximately normal to the surface, whereas polymer chains can adopt various configurations on the surface of the particle. For example, certain segments of the chains, called trains, may be in contact with the surface while other segments may extend into the medium in the form of tails or loops (although it is possible to design polymers which adopt only one or two of these configurations). One of the basic differences between stabilization by surface active agents and polymeric stabilization can therefore be described by the density profile of the adsorbed layer. For the case of a fairly close-packed monolayer of surface active molecules, the density of the adsorbed layer may be assumed to be constant and to fall off abruptly to zero at the edge of the layer. On the other hand, the density profile of a layer composed of polymer chains in various configurations can fall off gradually with distance from the native particle.

A brief outline of the theories of steric interaction applicable to the systems in the present work, i.e. particles stabilized by a monolayer of surface active agent and dispersed in a non-aqueous medium, is given below.

Theories of steric interaction

Mackor[4] was perhaps the first to endeavour to calculate the free energy of repulsion between sterically stabilized particles. He adopted a model in which he assumed that rigid rods of length, L, were attached by ball joints to the particle surface represented by a flat plate. The repulsion was envisaged to arise solely from the loss of configurational entropy of the rods on close approach of the opposing surfaces. The interaction between the two plates, separated by a distance, H_o, was given by

$$\Delta G_{EL} = kT \ln (H_o/L) \qquad \ldots \quad (2.4)$$

The obvious criticisms of this model are the assumed inflexibility of the stabilizer, the complete neglect of the dispersion medium and its operation only at low coverage.

Jäckel[5] proposed that the protective layer around a colloidal particle can be considered to be similar to a cross-linked gel network, and that it is the mechanical properties of these gel layers which determine their protective action. He calculated the elastic energy of compression, V_{EL}, that would be typically generated in close-range interactions between the gel layers from an equation originally developed by Hertz,

$$V_{EL} = 0.75\ E\ (\delta - H_o/2)^{5/2}\ (a + \delta)^{\frac{1}{2}} \qquad \ldots \quad (2.5)$$

where E is the elastic modulus and the other terms are as defined previously.

The first theory to recognise the prime importance of the dispersion medium in steric stabilization was that published by Fischer[6]. The theory postulates the interaction between two similar spherical particles, each bearing a steric stabilizing layer. His model assumes that

a) the concentration of the stabilizer is uniform throughout the layer and falls off abruptly to zero at the outer edge,

b) the overlapping of the two steric layers produces a lens-like volume in which the stabilizer concentration is doubled.

Fischer calculated the steric interaction in terms of a "mutual exchange" energy (which for the sake of consistency is labelled ΔG_{MIX} here), which he related to an excess osmotic pressure in the overlap volume, viz.,

$$\Delta G_{MIX} = 2 \int_{o}^{V} \Pi_E \, dV \qquad \ldots \quad (2.6)$$

where V is the overlap volume. The excess osmotic pressure, Π_E, can be expressed in terms of the second virial coefficient by,

$$\Pi_E = RT \, B_2 c^2 + \ldots. \qquad \ldots \quad (2.7)$$

where c is the concentration of material in the adsorbed layer and B_2 is the second virial coefficient.

The free energy change of mixing was then expressed by Fischer in terms of B_2 as,

$$\Delta G_{MIX} = \frac{4}{3} \pi \, B_2 c^2 (\delta - H_o/2)^2 \, (3a + 2\delta + H_o/2) \qquad \ldots \quad (2.8)$$

Ottewill[7] pointed out that this approach relates the excess osmotic pressure, via the second virial coefficient, to the solvency of the medium. When the stabilizing species is in a good solvent B_2 is positive and repulsion ensues, whereas in a theta solvent $B_2 = 0$, and in a poor solvent B_2 is negative and attraction occurs leading to flocculation.

Moreover, Ottewill and Walker[8] also pointed out the applicability of the Flory-Huggins theory to calculate the second virial coefficient by using the relationship between the segment/solvent enthalpy interaction parameter, χ, and the entropy and enthalpy dilution parameters ψ and κ

respectively, i.e.,

$$B_2 = (\psi - \chi)/\overline{V}_1\rho^2 \qquad \ldots \quad (2.9)$$

where

$$(\psi - \chi) \equiv (\psi - \kappa) \qquad \ldots \quad (2.10)$$

In this case, $\overline{V}_1$ is the molar volume of the molecules of the dispersion medium and ρ is the density of the stabilizing species.

Assuming the entropy term ψ to be ideal, they obtained an alternative expression for the free energy of mixing, viz.,

$$\Delta G_{MIX} = (4\pi c^2/3V_1\rho^2)\, N_A kT\, (\tfrac{1}{2} - \chi)(\delta - H_o/2)^2(3a + 2\delta + H_o/2) \qquad \ldots \quad (2.11)$$

where N_A is Avogadro's number.

Thus, assuming that no desorption of the surface active agent occurs during interpenetration of the adsorbed layers, equation (2.11) could serve as an expression for the free energy of steric interaction (equation (2.3)).

One of the objections to the original Fischer model is the abrupt step from a uniform concentration in the adsorbed layer to double that concentration in the overlap volume, and consequently the fact that there is no perturbation of the rest of the layer. Doroszkowski and Lambourne[9] attempted to correct this by extending the "lens-like" overlap volume to a larger volume of interaction defined by the particle surfaces and the limiting radii beyond which the stabilizing layers are out of range for direct contact. Hence, their predicted energies of repulsion are significantly weaker than those calculated by the Fischer-Ottewill-Walker approach.

2.1.2 Energy of interaction due to attraction

The principal cause of association of neutral, chemically saturated molecules is the van der Waals force of attraction which originates from electron oscillations in the molecule. With the exception of highly polar materials, London dispersion forces[10], which result from interactions between rapidly oscillating induced dipoles, account for nearly all of the van der Waals attraction which is operative. The London attractive energy between two molecules is very short range, varying as the sixth power of the intermolecular distance, r, namely,

$$V_{LONDON} = -\frac{3}{4}\frac{h\nu_o\alpha_o^2}{r^6} \qquad \ldots \quad (2.12)$$

$$= -\frac{\lambda}{r^6}$$

where h = Planck's constant

ν_o = dispersion frequency

α_o = electronic polarizability

λ = London interaction constant

An important characteristic of London dispersion forces is that they are, to a first approximation, additive. Thus, the simultaneous interaction of many molecules can be easily built up as a superposition of simple forces between pairs. Using this assumption, Hamaker[11] showed that the attractive energy between two equal spheres, labelled 1 and 2, is given by

$$V_A = -\frac{\lambda}{r^6}\int_{V_1} q_1 dV_1 \int_{V_2} q_2 dV_2 \qquad \ldots \quad (2.13)$$

where q is the number of molecules per unit volume of the material

and V is the volume of the sphere.

For the case of two equal spheres of radii a in vacuum, the attractive energy is given by the following expression, providing that the distance of separation between them, H_o, is very small (i.e. $H_o/2a \ll 1$).

$$V_A = - \frac{Aa}{12H_o} \qquad \ldots \quad (2.14)$$

where A is known as the Hamaker constant and is given by

$$A = \pi^2 q^2 \lambda \qquad \ldots \quad (2.15)$$

For larger, more realistic separations between the spheres, Hamaker expanded equation (2.14) to obtain

$$V_A = - \frac{A}{12} \left\{ \frac{1}{x^2 + 2x} + \frac{1}{x^2 + 2x + 1} + 2 \ln \frac{x^2 + 2x}{x^2 + 2x + 1} \right\} \qquad \ldots \quad (2.16)$$

where $x = H_o/2a$.

When the two spheres are in a dispersion medium, the interaction between each sphere and the medium has to be taken into account and a composite Hamaker constant A_H is used.

$$A_H = A_{sp} + A_m - 2\left(A_{sp.m}\right) \qquad \ldots \quad (2.17)$$

where A_{sp} = Hamaker constant for the sphere

A_m = Hamaker constant for the medium.

Assuming via a geometric mean relationship that, $A_{sp.m} = (A_{sp} A_m)^{\frac{1}{2}}$ then,

$$A_H = \left(A_{sp}^{\frac{1}{2}} - A_m^{\frac{1}{2}} \right)^2 \qquad \ldots \quad (2.18)$$

and it follows that A_H must always be a positive quantity.

The oscillating electrical field which is responsible for the London attraction between molecules causes radiative transfer which propagates itself with the speed of light between the spheres. Thus, for large separations between molecules, (and consequently spheres), a time-lag or phase difference develops between vibrations at the two locations. This is known as the retardation effect and it decreases the magnitude of the London attractive energy (equation (2.12)), so that at long distances,

$$V_{LONDON}^{RET} = - \frac{\lambda}{r^7} \qquad \ldots \quad (2.19)$$

The crossover of the energy of attraction from an inverse sixth to an inverse seventh power law takes effect at separations in the range 10^2 to 10^3 Å, i.e. at separations which are comparable to the wavelength of the propagating radiation.

The Vold effect

Vold[12] extended the Hamaker treatment for the attraction between spherical particles to include the effect of homogeneous adsorbed layers on the particles. She derived the following expression for the attractive energy between two equal spheres, each surrounded by an adsorbed layer and dispersed in a medium:

$$V_A = - \frac{1}{12} \left\{ \left(A_m^{\frac{1}{2}} - A_s^{\frac{1}{2}} \right)^2 H_s + \left(A_s^{\frac{1}{2}} - A_p^{\frac{1}{2}} \right)^2 H_p + 2 \left(A_m^{\frac{1}{2}} - A_s^{\frac{1}{2}} \right) \left(A_s^{\frac{1}{2}} - A_p^{\frac{1}{2}} \right) H_{ps} \right\} \qquad \ldots \quad (2.20)$$

where A_p is the Hamaker constant for the core

A_s is the Hamaker constant for the layer

A_m is the Hamaker constant for the medium.

H_s, H_p and H_{ps} are geometrical functions for spheres of radii a and layer thickness δ, separated by a distance Δ between the surfaces of the adsorbed layers.

$$H(x,y) = \frac{y}{x^2 + xy + x} + \frac{y}{x^2 + xy + x + y} + 2\ln\left(\frac{x^2 + xy + x}{x^2 + xy + x + y}\right) \quad \ldots \quad (2.21)$$

For H_s, $x = \frac{\Delta}{2(a + \delta)}$ $\qquad y = 1$

For H_p, $x = \frac{\Delta + 2\delta}{2a}$ $\qquad y = 1$

For H_{ps}, $x = \frac{\Delta + \delta}{2a}$ $\qquad y = \frac{a + \delta}{a}$

Vold found that the presence of an adsorbed layer on the particle decreased the force of attraction, especially if the Hamaker constant of the layer was not the same as that of the medium. Hence, she derived an equation to calculate the value of A_s that produces the maximum decrease in attraction (A_s^*), and from this she deduced an optimum sequence of Hamaker constants. However, Osmond, Vincent and Waite[13] reported an algebraic error in the derivation, and showed the necessary sequence of Hamaker constants to be

$$A_s^* < A_m < A_p \quad \text{or} \quad A_s^* > A_m > A_p$$

where the optimum value for the Hamaker constant of the adsorbed layer is given by

$$A_s^* = \frac{A_m^{\frac{1}{2}}(H_s - H_{ps}) + A_p^{\frac{1}{2}}(H_p - H_{ps})}{H_p + H_s - 2H_{ps}} \quad \ldots \quad (2.22)$$

The Vold effect usually becomes more appreciable at longer distances of separation than a + δ. Nevertheless, it can often significantly decrease the force of attraction at short distances for particles with small radii and/or thick adsorbed layers.

The macroscopic approach

The use of the London-Hamaker theoretical treatment, known as the microscopic approach, is restricted by the following assumptions:-

i) of pairwise additivity of individual interatomic interactions in condensed media;

ii) the approximation that the contributions centred around a single dominant frequency of the electromagnetic spectrum are the only important ones; and

iii) that the insertion of a medium between two interacting bodies can be dealt with by the use of an arbitrary dielectric constant at a single frequency.

Lifshitz[14] approached the problem in a totally different manner by treating the interacting bodies as continuous macroscopic phases. He used quantum field theory and complex dielectric constants to derive an expression for the attraction which included inter alia, many-body interactions, contributions from all resonant electronic and molecular frequencies, and the effect of a medium between the interacting bodies.

The disadvantage of the Lifshitz treatment lies in the complexity of the calculations and the lack of basic data in many cases. Moreover, it has been shown[15,16] that for particles in non-aqueous media, the microscopic and the macroscopic approaches yield similar results.

2.1.3 The total energy of interaction

The total energy of interaction for the systems in this study can be represented by the sum of the two contributions mentioned above: the steric repulsive energy and van der Waals attractive energy. If the free energy of steric stabilization, ΔG_s, (equation (2.3)) is equated to a steric repulsive energy V_s, then the total interaction energy, V_T, can be written as

$$V_T = V_S + V_A \qquad \ldots \quad (2.23)$$

However, it is important to note that there is a fundamental problem which occurs when the two pair potentials are evaluated separately and then added, rather than a self-consistent model being used. The difficulty arises because the attractive energy (as given by the Vold equation) is calculated as a function of the distance separating the adsorbed layers, Δ, and as such does not allow interpenetration of the layers to occur. In contradistinction, the steric repulsive energy is calculated as a function of the distance of separation between the cores of the particles, H_o, which results in a discontinuity between the two terms V_s and V_A. There are a number of possible models which can be adopted in order to circumvent this problem, and they are outlined below.

Model A

The simplest approach is to use a hard-sphere model (see Section 2.2.3) for the steric repulsion if it is applicable to the system.

The Vold equation (2.20), in the limit as $\Delta \to 0$, approximates to

$$H(x,y)_{x \to o} = \frac{y}{x(1 + y)}$$

giving for the geometrical functions

$$H_s, \quad x = 0$$

H_p, $x = \delta/a$

and H_{ps}, $x = \delta/2a$

Thus, for the situation $\Delta = 0$ $V_A \to \infty$.

However, if the Hamaker constant of the adsorbed layer, A_s, is taken to be equal to that of the medium, A_m, a finite value of V_A is obtained when $\Delta = 0$. In this case, it is possible to add a hard-sphere repulsion, rising to infinity at $\Delta = 0$.

Model B

For the case when the Hamaker constants of the adsorbed layer and the medium cannot be assumed to be the same, one can postulate the existence of a solvation layer on the outer side of the adsorbed layer. If the thickness of the solvation layer is t_s, then the hard-sphere potential rises at the value $\Delta = 2t_s$. The difficulty with this model is in assigning a value for t_s. Ottewill and Walker[17] took $t_s = 3$ Å to represent a layer of water molecules surrounding a polystyrene latex particle stabilized by $C_{12}E_6$. In this model, unless a rigid solvent sheath is invoked, a discontinuity once again arises between V_s and V_A.

Model C

If interpenetration of the adsorbed layers is to be taken into account, i.e. in order to be able to use a steric repulsive energy as given by equation (2.11), then the following approach has to be taken. For the case of particles in non-aqueous media stabilized by a surface active agent the molecules usually adsorb with the head groups at the core particle surface and the hydrocarbon tails pointing outwards towards the medium. It is then plausible to assume that the Hamaker constant of the S.A.A. tails is equivalent to that of the medium so that the Hamaker constant of the head groups can be taken to represent A_s. If the length of the S.A.A.

chains is L, then it is possible to add either a hard-sphere potential or a steric repulsion potential to the attractive energy at the value $\Delta = 2L$.

This approach should give first approximation values for V_T for a system such as calcium carbonate particles stabilized by an alkyl aryl sulphonic acid in a hydrocarbon medium, e.g. dodecane. However, a much more refined approach would be to use a self-consistent treatment in which both V_S and V_A are considered together, e.g. the Weeks-Chandler-Andersen theory[18]. They divide the total potential into a reference system which represents the repulsive force and a perturbation to account for the attractive force between the particles.

For the systems in this study, the attractive energy is expected to be greatly reduced by the Vold effect. This is because the particles have small core radii and comparatively thick adsorbed layers as well as approximately the correct sequence for the Hamaker constants. Hence, the total energy of interaction can be assumed to be governed by the steric repulsive energy which, as a consequence of the adsorbed layer of surface active agent, can be assumed to have a very short range.

2.2 Concentrated Dispersions

2.2.1 Introduction

In the first part of this chapter, the interactions between the particles were described in terms of the existence of an attractive and a repulsive energy, and the resultant colloidal stability of the systems was attributed to a short-range repulsive energy. These interparticle forces which are present in dispersions of any number concentration will, however, be operational in dilute systems only when the translational diffusion of the particles (i.e. Brownian motion) leads to two-body collisions. In a concentrated system many-body interactions will occur leading to the formation of a structure dependent upon both spatial and temporal correlations between the particles.

This section describes very briefly how some basic concepts of liquid-state theory are extended to represent concentrated dispersions of colloidal particles[19]. The theories applicable to the experimental determination of the structure of such systems will be dealt with in Chapter 4.

2.2.2 The radial distribution function

Consider a container of volume V in which there are N_p particles; then the number density of the system ρ_o can be expressed as

$$\rho_o = N_p/V$$

Consider now the system microscopically, i.e. as seen by one representative particle within that system; this is illustrated in Figure 2.2. Proceeding radially from the central particle, it is clear that no neighbouring particles can be found until one reaches the first shell of thickness, dr. It can also be seen that each successive shell encloses a greater number of particles

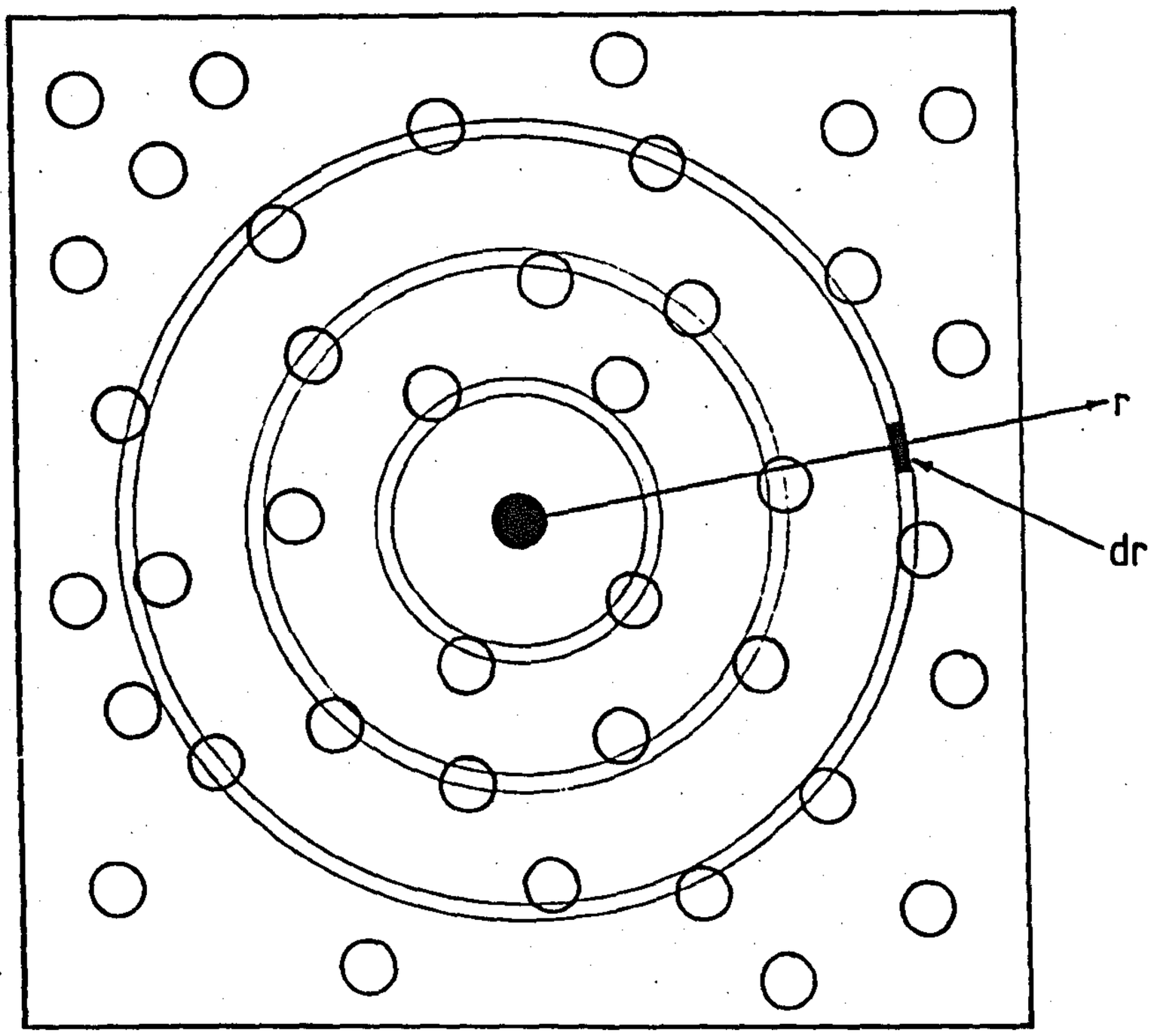

FIGURE 2.2

Schematic illustration of the radial distribution of particles around a central particle.

than the preceding one, and hence as $r \to \infty$ the density must approach ρ_o.

It is therefore possible to describe the distribution of particles within the system by a density distribution function $\rho(r)$, whose limiting values must be given by

$$\rho(r) \to \rho_o \quad \text{as} \quad r \to \infty$$

$$\rho(r) \to 0 \quad \text{as} \quad r \to 2R$$

where R is the radius of the central particle.

However, the arrangement of the particles in a colloidal dispersion is generally described by the *Radial Distribution Function* (RDF), which has its origin in statistical mechanical theories of fluids.

The radial distribution function is defined by

$$g(r) = \rho(r)/\rho_o \qquad \ldots \quad (2.24)$$

and has the properties that

$$g(r) \to 1 \quad \text{as} \quad r \to \infty$$

$$g(r) \to 0 \quad \text{as} \quad r \to 2R$$

The term RDF should strictly be used for the quantity $(4\pi r^2 \rho(r))$ but it is often used - as will be done here - to represent $g(r)$. It can be seen from Figure 2.3 that $g(r)$, for a concentrated "liquid-like" fluid, consists of a pronounced first peak followed by a number of subsidiary oscillations damping out to unity beyond four or five particle diameters. This indicates that the subsequent radial structure is uncorrelated to the presence of the particle at the origin and becomes "vapour-like". Another characteristic feature of the radial distribution function for liquids is that successive peaks become broader. The RDF for spherically symmetrical particles can thus be redefined as the relative probability of finding a second particle located a distance, r, from another particle simultaneously located at the origin.

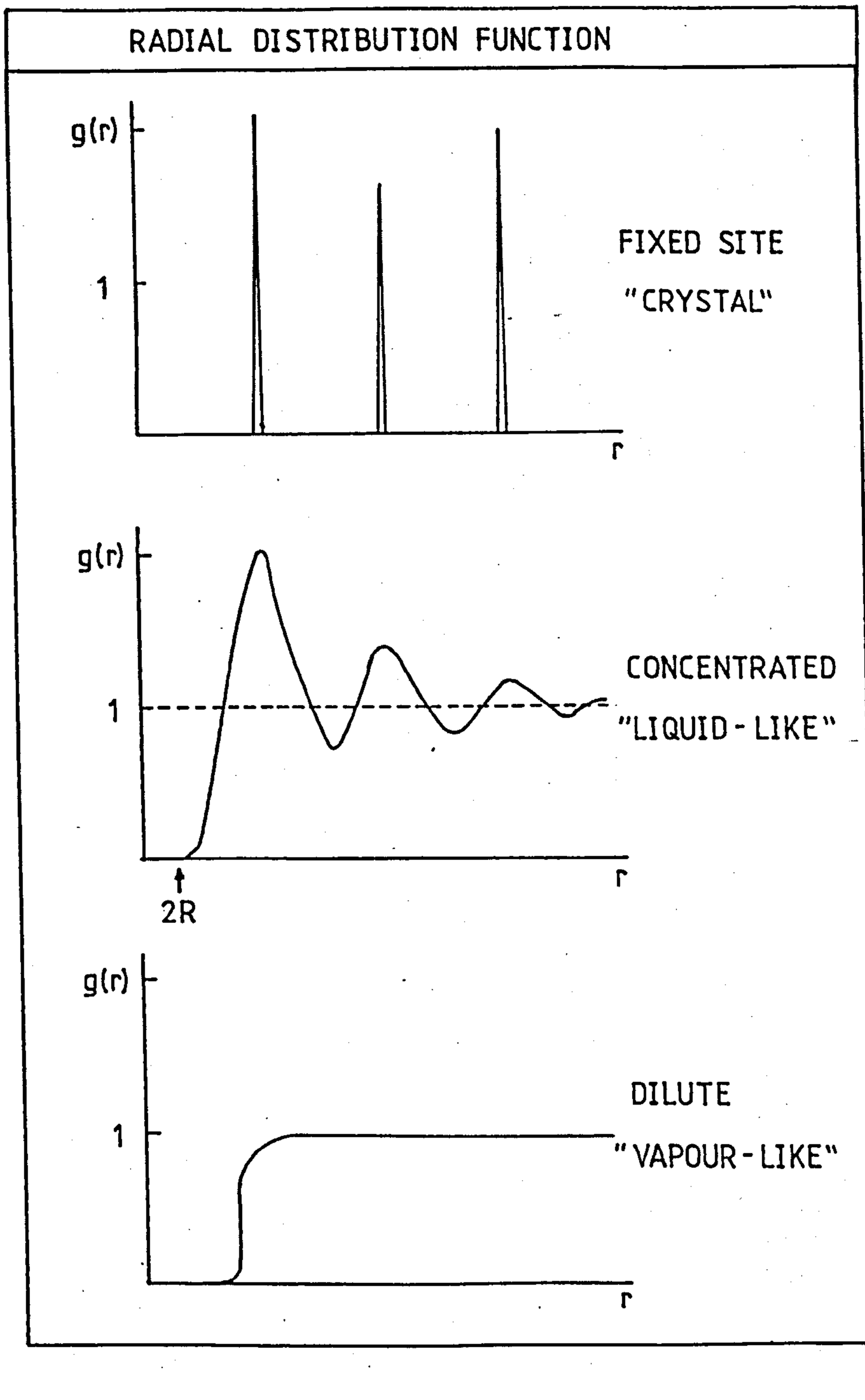

FIGURE 2.3

g(r) against r for various states

The shell of nearest neighbours which develops around the central particle is obviously excluded from the region of the short range repulsive core; therefore, the maximum probability of its location is at the potential minimum of the origin particle. In fact, it is found that the first peak is displaced slightly inwards, due to the collisional anisotropy of the particles[20]. It follows that the shell of second-nearest neighbours is located on (or close to) the potential minimum of the first shell and so on, which enables us to relate the radial distribution function to the potential of mean force between the particles, $\Phi(r)$,

$$g(r) = \exp\ (-\Phi(r)/kT) \qquad \ldots \quad (2.25)$$

where $\Phi(r) = V(r) + \psi(r)$ $\qquad \ldots \quad (2.26)$

$V(r)$ is the simple pair potential, whereas $\psi(r)$ is a perturbation potential which takes into account the effect of many body interactions.

The second Virial coefficient

One of the fundamental problems in the statistical description of liquids is that, unlike the gas and solid phases, the liquid state lacks an idealized model of reference. In the case of gases one starts with the equation of state for a perfect gas,

$$PV = NkT$$

and then corrections, which allow for intermolecular interactions, are introduced in the form of an expansion in powers of the density. This is called the Virial expansion and is given by

$$P = \rho kT + \rho^2 B_2 kT + \rho^3 B_3 kT + \ldots\ldots \qquad \ldots \quad (2.27)$$

where B_2, B_3 etc. are known as the second and third Virial coefficients respectively.

The Virial expansion does not converge for densities approaching those found in the liquid state, and, as such, does not provide the basis of a satisfactory theory of liquids. However, for densities of liquids, assuming pairwise additive interactions between spherical particles, the Virial equation of state is exact:

$$P = kT - \rho^2 \frac{2\pi}{3} \int_o^\infty r^3 \frac{\partial V(r)}{\partial r} g(r) \, dr \qquad \ldots \quad (2.28)$$

Substituting for g(r) (equation (2.25)) into the above equation, an expression for the second Virial coefficient can be obtained,

$$B_2 = - 2\pi \int_o^\infty r^2 \left[\exp \left(- \Phi(r)/kT \right) - 1 \right] dr \qquad \ldots \quad (2.29)$$

It was already noted in Section 2.1.1 that the free energy of mixing of a sterically stabilized system can be related to the second Virial coefficient (equation (2.8)). Hence, B_2, which describes an imperfect gas, can also be used as a measure of the interactions between colloidal particles, and its value can be determined experimentally by, for example, light scattering.

2.2.3 The hard-sphere model

Although there is no ideal liquid to form a basic model, assemblies of idealised particles interacting through some simple model interaction have an important theoretical status. For our systems, where the dominant force of interaction is a short-range repulsive force, (see Section 2.1.3), a likely model for the interaction is the "hard-sphere" potential, given by[21]

$$\Phi_{HS}(r) = \left\{ \begin{array}{l} \infty, \; r < \sigma \\ \\ 0, \; r \geqslant \sigma \end{array} \right\}$$

where σ is the effective hard-sphere diameter of the particles (i.e. $\sigma = 2R_{HS}$). We can then define a new volume fraction, the hard-sphere volume fraction, ϕ_{HS}, as

$$\phi_{HS} = \frac{N_p}{V} \frac{4\pi}{3} R_{HS}^3 \qquad \ldots \quad (2.30)$$

$$= \rho \frac{\pi}{6} \sigma^3$$

where N_p is the number of particles in the total volume of the dispersion V, and ρ is the fraction of the total density due to the particles.

The hard-sphere model, which is the prototype reference model for systems with harsh repulsion, can be described by the simple pressure equation,

$$P_{HS} = \rho kT + \rho^2 kT \frac{2\pi}{3} \sigma^3 g_{HS}(r) \qquad \ldots \quad (2.31)$$

where $g_{HS}(r)$ is the radial distribution function for hard spheres and is zero when $r < \sigma$. $g_{HS}(r)$ therefore rises steeply to the first probability maximum from a distance $r = \sigma$.

This model also allows fairly simple, semi-empirical expressions to be defined for macroscopic properties, such as the osmotic compressibility of the system. The two most frequently quoted expressions for the compressibility $(\partial P/\partial \rho)$, are the Percus-Yevick equation[22]

$$\frac{1}{kT}\left(\frac{\partial P}{\partial \rho}\right)_{P-Y} = \frac{(1 + 2\phi_{HS})^2}{(1 - \phi_{HS})^4} \qquad \ldots \quad (2.32)$$

and the Carnahan-Starling equation[23]

$$\frac{1}{kT}\left(\frac{\partial P}{\partial \rho}\right)_{C-S} = \frac{(1 + 4\phi_{HS} + 4\phi_{HS}^2 - 4\phi_{HS}^3 + \phi_{HS}^4)}{(1 - \phi_{HS})^4} \qquad \ldots \quad (2.33)$$

The assessment of the validity of this model for a particular system can only be obtained by an experimental determination of quantities such as the hard-sphere diameter, σ, and consequently of the potential operating in the system. A particularly suitable technique for this is small-angle neutron scattering (described in Chapter 4), and its use for the study of concentrated colloidal dispersions is discussed in Chapter 6.

CHAPTER THREE

CHAPTER 3

EXPERIMENTAL

3.1 Preparation of Calcium Carbonate Dispersions

Two types of dispersions of calcium carbonate particles stabilized by surface active agent were prepared. The difference between the two systems was the size of the calcium carbonate core particle; dispersions containing the smaller particles were designated as the V-series, whereas those containing the larger particles were designated the L-series. A third system was also used which was supplied by Esso Chemicals Limited, Abingdon, England. This system had been prepared by a similar procedure to that used for the preparation of the V-series but with a much smaller amount of surface active agent; this was termed the F-series.

3.1.1 Materials

Most of the materials used for the preparation of the calcium carbonate dispersions were supplied by the Paramins Division of Esso Chemicals Limited. These materials, as well as those used for the subsequent redispersion of the particles, are listed below.

The calcium oxide used was obtained as Setelime from Imperial Chemical Industries PLC.

Calcium hydroxide was obtained as Balshazard from France; its surface area was 11 $m^2 g^{-1}$.

The surface active agent was an alkyl aryl sulphonic acid. This was a dark brown, highly viscous liquid made by the sulphonation of an alkyl benzene. The distribution of molecular weights and isomers in the alkyl chain was assumed to consist of approximately eighty per cent branched chain

polypropylene hydrocarbon (C_{15} - C_{30}, peaking at C_{24}) and twenty per cent C_{18} straight chain hydrocarbon. It contained a proportion of impurities including mineral oil and water.

PIBSA, polyisobutene succinic anhydride, was supplied by Esso Chemical Company and was made by the treatment of polyisobutene (molecular weight ~1000) with maleic anhydride.

Stanco 150 was a commercial grade hydrocarbon solvent obtained as one of the heavier fractions of a vacuum distilled crude oil. It was a largely paraffinic, straw coloured liquid with a viscosity of 30 centistokes at 40°C and it contained a distribution of molecular weights and isomers.

"Special Speedflow" and "Speedplus" precoat were diatomaceous earth filter aids.

The methanol, acetone and heptane were all BDH laboratory grade solvents.

Toluene was obtained as BDH laboratory grade material with n^{20} = 1.4961 and ρ_4^{20} = 0.8669 g cm^{-3}.

The deuterated toluene used was obtained from the Aldrich Chemical Company Limited as 99% deuterated material. Its density was calculated from the ratio of molecular weights to be ρ_4^{20} = 0.9423 g cm^{-3}.

Dodecane was BDH laboratory grade material with n^{20} = 1.4216 and ρ_4^{20} = 0.7487 g cm^{-3}.

Deuterated dodecane was obtained from Prochem/BOC Limited as 99% deuterated material, and its density was calculated to be ρ_4^{20} = 0.8632 g cm^{-3}.

All the glassware used for the preparation of the dispersions was previously treated with nitric acid, rinsed firstly with distilled water, then acetone and finally dried in an oven.

3.1.2 Experimental procedure

The apparatus used for the preparation of the calcium carbonate dispersions is shown schematically in Figure 3.1. The entire apparatus was located in a fume-cupboard.

Preparation of the V-series

The quantities given below for the preparation of this system produced approximately one litre of a dispersion of particles in Stanco 150. This corresponded to about 28% w/w of the surface active agent.

A mixture of alkyl benzene sulphonic acid (217 g), toluene (219 g) and methanol (124 g) was placed in the reaction vessel and, while nitrogen was being bubbled through the vessel, it was homogenised by stirring. Calcium hydroxide (140 g) was added to the reactants and the temperature was adjusted to 25°C. The nitrogen supply was disconnected and replaced by carbon dioxide whose rate of delivery was controlled by the flow meter and was adjusted to 150 cm^3 min^{-1}.

The conversion of calcium hydroxide to calcium carbonate takes place according to the reaction:

$$Ca(OH)_2 + CO_2 \rightarrow CaCO_3 + H_2O$$

In the present work only about 90% of the stoichiometric amount of CO_2 required was used. Hence, while the temperature was being maintained at 25°C, 22.5 1 of carbon dioxide were passed through the reaction mixture. The temperature was then raised to 45°C over a period of thirty minutes, after which an additional 10.2 1 of carbon dioxide were passed through the vessel to allow for the efficiency of CO_2 absorption. At the end of the carbonation Stanco 150 (179 g) was added and the nitrogen supply was reconnected. The temperature was then allowed to rise in a regulated manner, and the condenser was set up for a distillation. When the temperature had

FIGURE 3.1 (overleaf)

FIGURE 3.1 LEGEND

A. A round-bottomed flask equipped with five inlets

B. A copper-constantan thermocouple immersed in a light oil

C. A stirring Teflon paddle connected to a motor

D. An aerator with a sintered glass end

E. An inlet for the introduction of reactants

F. A condenser

G. A Dreschel bottle containing a solution of NaOH

H. A flow meter to monitor the gas input rate

I. A heating mantle

J. A West-Gardian temperature control unit

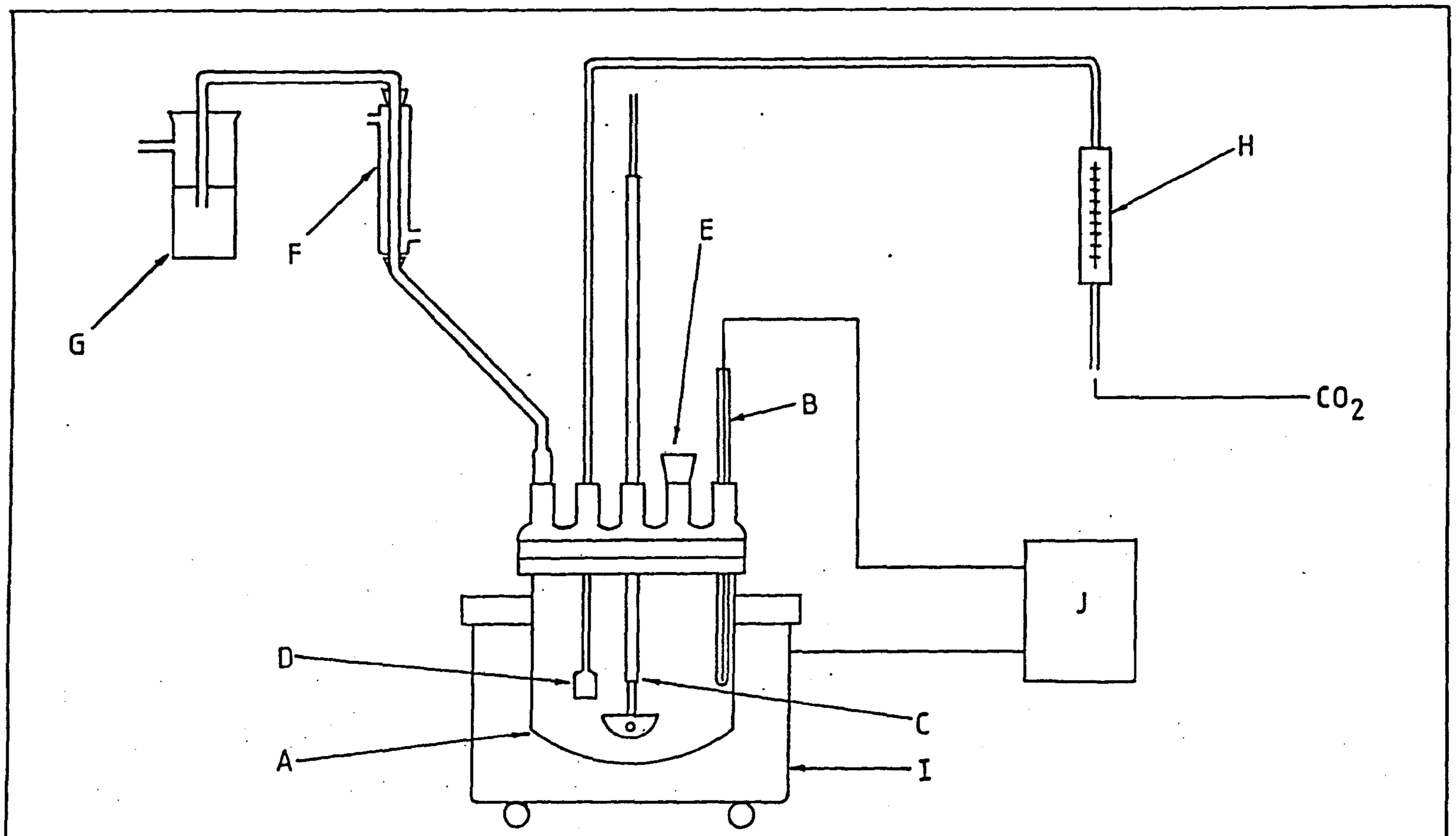

FIGURE 3.1 APPARATUS FOR THE PREPARATION OF DISPERSIONS

reached 80°C and all the methanol had been distilled, a further 2.2 l of carbon dioxide were added. The distillation process was continued under vacuum until the mixture had attained a temperature of 150°C and all the water and toluene had been driven off. The reaction was then stopped and a small sample was taken out for a sedimentation test.

Finally, "Special Speedflow" filter aid (10 g) was added to the hot mixture. This was filtered under a pressure of ~80 psi through a filter pad covered with "Speedplus" precoat (5 g). The light coloured filtrate was obtained at a rate of 96 kg m^{-2} hr^{-1}.

Preparation of the L-series

The method used for the preparation of the larger calcium carbonate particles differed from that described for the V-series in that CaO was used instead of $Ca(OH)_2$ and a low molecular weight polymer, PIBSA, was used in addition to the alkyl benzene sulphonic acid to stabilize the particles.

A mixture of alkyl benzene sulphonic acid (198.3 g), toluene (198 g), methanol (50 g), nonyl phenol (10.2 g), polyisobutene succinic anhydride (PIBSA) (27.4 g), Stanco 150 (167 g) and calcium chloride (3 g) was placed in the reaction vessel and homogenised. Calcium oxide (84.3 g) was added to the mixture which was then heated to ca. 55°C. The stoichiometric amount of carbon dioxide necessary to convert all the calcium oxide to calcium carbonate was then bubbled through the mixture at a rate of 150 cm^3 min^{-1}, after which the carbonation was continued for a further ten minutes. After the reaction had been completed, the dispersion formed was treated in a similar manner to that described for the V-series, in that the volatile solvents were distilled off at 150°C and the hot mixture was filtered under pressure.

Preparation of the F-series

The F-series was prepared in exactly the same manner as that described for the V-series, except that the amount of surface active agent was adjusted to be ca. 15% of the weight of the final product, whereas in the case of the V-series this was ca. 28% w/w. Thus, in this preparation, the amount of alkyl benzene sulphonic acid used was 116.3 g, whilst the weights of all the other reactants were the same as those given earlier for the preparation of the V-series.

Preparation of the large particles using only one stabilizer

The preparation of the L-series, as described above, involved the use of a surface active agent, namely alkyl benzene sulphonic acid, and a low molecular weight polymer, polyisobutene succinic anhydride (PIBSA). Various attempts were made to prepare large calcium carbonate particles using only one of the two above mentioned materials. The preparations were carried out using the process outlined for the L-series but varying the type and the proportion of the stabilizer used, i.e.

i) 28% w/w of alkyl benzene sulphonic acid

ii) 15% w/w of PIBSA

iii) 22.5% w/w of PIBSA

All three preparations failed to produce stable dispersions of calcium carbonate particles.

3.1.3 Concentration and redispersion of particles

The calcium carbonate particles prepared by the methods described above were dispersed in the hydrocarbon solvent, Stanco 150. In order that dispersions could be prepared in better characterized solvents and of known concentration of particles, it was necessary to precipitate the colloidal particles from the hydrocarbon oil. This was done by preparing a mixture

of the oil dispersion in heptane at an approximate weight ratio of 2:1 respectively, and then "titrating" this mixture against acetone until it became turbid and light yellow in colour. The amount of acetone needed was found to be approximately equal to the amount of the original oil dispersion used.

The turbid mixture was then centrifuged in a BTL bench centrifuge at ca. 3000 r.p.m. for 30 minutes. The supernatant oil phase was discarded while the viscous, colloidal phase was rotary evaporated to remove both the acetone and the heptane.

In the case of the V-series, the evaporation was quite sudden and sometimes violent. Hence, very careful heating, if any, of the samples was necessary. The residue was an orange to light brown, "solid-like" substance. The evaporation of the L-series required the heating of the sample for nearly two hours and the residue, which was light brown in colour, was less viscous than that obtained from the V-sample. The F-series proved to be extremely difficult to evaporate. This was because the turbid mixture did not separate into two well defined phases even after prolonged centrifugation, and hence the sample that was rotary evaporated contained some oil which prevented the evaporation of the solvents.

The concentration of calcium carbonate in the residual concentrated samples was determined from the "total base number", T.B.N. The latter is

"the quantity of perchloric acid, expressed in terms of the equivalent number of milligrams of potassium hydroxide, that is necessary to neutralise all basic constituents present in 1 g of sample".

The procedure for TBN analysis entails the addition of chlorobenzene and glacial acetic acid to a small amount of sample followed by a titration against 0.1 N perchloric acid using Ag/AgCl electrodes.

If it is assumed that the only basic constituent of the sample is

calcium carbonate, then the equivalent of two moles of KOH are necessary for each mole of $CaCO_3$. Hence, the weight of calcium carbonate in 1 g of sample can be calculated, i.e.

$$TBN \quad M_{CaCO_3} / \ 2M_{KOH} \equiv \text{mg } CaCO_3 / \text{ g of sample}$$

where M_{CaCO_3} is the molecular weight of calcium carbonate and M_{KOH} is the molecular weight of potassium hydroxide.

However, it was easier to represent the concentration of calcium carbonate as a weight/weight percentage, i.e.

$$\frac{TBN \times 100}{112 \times 10} \equiv \% \text{ wt/wt of } CaCO_3$$

Typical values of the TBN of the samples after rotary evaporation were ca. 450, which resulted in calcium carbonate concentrations of ca. 40% wt/wt. Also repeated TBN analysis of the same sample produced consistent results. Known amounts of the sample were subsequently re-dispersed in one of the two solvents chosen, namely toluene or dodecane.

In order that the volume fraction of the particles in these dispersions could be calculated, it was necessary to know the percentage of the other constituents in the concentrated sample; the major other constituent being the surface active agent. Since a TBN analysis was done on each of the original oil dispersions and the amount of surface active agent used in the preparation was known, it was possible to calculate the percentage of surface active agent in the concentrated sample in the following manner. Both the V- and the L-series were prepared using 28% wt/wt of alkyl benzene sulphonic acid and hence, assuming that the surface active agent concentration had increased proportionally to that of $CaCO_3$ (i.e. the TBN value),

$$\frac{TBN^c}{TBN^o} \times 28\% \equiv \% \text{ wt/wt of surface active agent in concentrated sample}$$

where TBN^o is the TBN value of the original oil dispersion and TBN^c is the value of the concentrated sample.

The remainder of the sample was assumed to consist of residual Stanco 150 oil which had not been removed by the acetone treatment.

3.2 Characterization of Calcium Carbonate Dispersions

A number of tests were carried out to obtain a rough indication of the general properties of the calcium carbonate particles, as well as an analysis to determine the accuracy of the TBN values.

3.2.1 Characterization of the particles

The first test that was carried out was an ultracentrifugal analysis of the original oil dispersions as an approximate guide to the size of the colloidal particles. Each dispersion was made up as a 10% v/v solution in hexane and a sedimentation run was carried out using a Beckman L5-50 preparative ultracentrifuge with a schlieren optical attachment. The data was analysed using a computer programme available at Esso Chemicals Limited, from which the following approximate values for the hydrodynamic radii of the particles were obtained:-

SYSTEM	HYDRODYNAMIC RADIUS/Å
V-series	47 ± 5
L-series	95 ± 10
F-series	61 ± 6

Once the dispersions had been rotary evaporated, infrared spectra were run on the concentrated V- and L-samples in order to try to determine the crystalline form of the calcium carbonate core. Calcium carbonate exists in three crystallographically distinct forms:

calcite, whose structure is rhombohedral,

aragonite, which is orthorhombic and

vaterite, which is thought to be hexagonal.

A spectrum of each of the samples, which was made into a Nujol mull, was run at Esso Chemicals Limited, Abingdon. Both spectra exhibited a fairly broad band at ca. 850 cm^{-1}, from which no conclusive evidence about

the crystalline form could be obtained. This is because, according to White in "The infrared spectra of minerals"[24]:-

"each vibrational spectrum will consist of a set of internal modes for each crystallographically distinct anion, with frequencies perturbed only slightly from the free ion values, and a set of low frequency lattice modes characteristic of the particular crystal structure. In general, the internal modes will be at higher frequencies and appear in the mid-infrared region while the lattice modes appear at lower frequencies. It is for this reason that the mid-infrared spectra of all carbonate minerals tend to look alike and that the IR spectrum is a useful identification tool for this anion."

Subsequently, further measurements were carried out using a Nicolet Fourier Transform infrared spectrophotometer with which a much greater resolution could be achieved. Moreover, it was possible to subtract the spectra of the hydrocarbon oil and the surface active agent from that of the sample. Although there was a small difference between the spectra of the V- and the L-samples, it was extremely difficult to assign the bands to a particular crystalline form as the values obtained did not coincide with those reported in the literature. This was possibly due to the very small size of the particles.

However, Partington[25] claims that on passing carbon dioxide through a cold solution of lime, calcite is deposited whereas if the lime solution is hot aragonite is formed. Since the carbonation of the systems was carried out at 25°C it seemed reasonable to assume, in the absence of additional information, that the crystalline form of calcium carbonate in the particles was calcite. The density of the $CaCO_3$ core particle was therefore taken to be $\rho^{18} = 2.71$ g cm^{-3}.

The density of the concentrated V-sample was then measured. This

was done by weighing a density bottle with 1 g of the sample, the volume of which had been previously calibrated with toluene. The density of the sample, which consisted of 41.3% w/w $CaCO_3$, 41.8% w/w of surface active agent and 16.9% w/w of oil, was found to be 1.25 g cm^{-3}.

The density of the surface active agent was estimated from the literature values[26] of the densities of sodium - C_{10}, C_{12}, C_{14} and C_{16} - alkyl benzene sulphonate given in Table 3.1.

TABLE 3.1 Densities of sodium alkyl benzene sulphonates

Surface Active Agent	Density
Na-decyl benzene sulphonate	1.102
Na-dodecyl benzene sulphonate	1.098
Na-tetradecyl benzene sulphonate	1.087
Na-hexadecyl benzene sulphonate	1.070

The values given above were extrapolated up to the value for Na - C_{24} - alkyl benzene sulphonate and then the average density of C_{18} and C_{24} - sodium alkyl benzene sulphonate was assumed to be the nearest to that of the surface active agent in our systems. This value was estimated as 1.05g cm^{-3}.

The density of the hydrocarbon oil, i.e. Stanco 150, was measured in a similar manner to that described for the concentrated V-sample, and was found to be 0.80 g cm^{-3}.

Since the density as well as the weight fraction of each constituent of the concentrated V-sample was known, it was possible to check whether they corresponded to the total density determined for the sample, viz.

$$\frac{F_{CaCO_3}}{\rho_{CaCO_3}} + \frac{F_{SAA}}{\rho_{SAA}} + \frac{F_{OIL}}{\rho_{OIL}} = \frac{1}{\rho_{SAMPLE}}$$

where F is the weight fraction of each constituent and ρ its density.

Using the values given earlier for F and ρ of each constituent, the density of the sample was calculated to be 1.31, whereas the experimentally determined value was 1.25. It was assumed that the prime source of error was an overestimation of the weight fraction of surface active agent. It has already been mentioned that the increase in concentration of the surface active agent upon rotary evaporation of the sample was assumed to be proportional to the increase in the TBN value. However, it is very likely that any "free" surface active agent (i.e. not adsorbed on the particles), present in the original oil dispersion, would have been removed with the oil by the acetone treatment. Hence, the surface active agent present in the concentrated sample would primarily consist of that adsorbed onto the particles. A speculative calculation to find the weight fractions of the constituents which correspond to a density of the sample of 1.25 resulted in the following values: 35% w/w of SAA, 24% w/w of oil, whereas the concentration of $CaCO_3$ was assumed to have been correct, i.e. 41% w/w.

The possibility of a lower weight fraction of surface active agent in the concentrated sample appears to be substantiated by the thermogravimetric analysis described below.

3.2.2 Thermogravimetric analysis and atomic absorption

A thermogravimetric analysis was carried out on the same concentrated V-sample described above in order to further assess the accuracy of the TBN values for the concentration of calcium carbonate.

1 g of the sample was placed in a thermogravimetric oven and the temperature was raised in a regulated manner up to 860°C over a period of 24 hours. The oven was connected to a chart recorder which monitored the oven temperature and the corresponding loss in weight of the sample. The

latter was recorded as a straight line, the gradient of which changed at the temperature at which a certain constituent of the sample was given off. It was therefore possible to estimate the nature of the constituent being evaporated from the oven temperature and the loss in weight of the sample, and this is given in Table 3.2.

TABLE 3.2 Results of Thermogravimetric Analysis

Temperature	Loss in Weight	Possible Cause
95°C - 115°C	0.010 g	Evaporation of water and toluene
115°C - 240°C	0.140 g	Evaporation of oil
240°C - 770°C	0.350 g	Decomposition of SAA and any residual $Ca(OH)_2$
770°C - 860°C	0.182 g	Decomposition of $CaCO_3$

The total loss in weight of the 1 g concentrated V-sample was 0.682 g. It is worth noting that although the weight percentage of oil in the sample appeared to be lower than expected, the loss in weight of the sample in the temperature range 240°C - 770°C was in very good agreement with the value for the weight percentage of SAA estimated from the density calculations, and this seems to signify that there was little unreacted $Ca(OH)_2$ present. Moreover, the decomposition of calcium carbonate, i.e.,

$$CaCO_3 \rightarrow CaO + CO_2$$

is known to go to completion at a temperature of 860°C. Hence, the loss in weight of 0.182 g can be assumed to be due to the loss of CO_2, and from the stoichiometric relationship (i.e. 0.182 x 100/44) this is equivalent to a weight percentage concentration of calcium carbonate of 41.3%. This result

was identical to that calculated from the TBN analysis of the concentrated V-sample. Although the excellent agreement of the two results could be fortuitous, it does however indicate the accuracy of the TBN values as a method of estimating the concentration of calcium carbonate.

The residue from the thermogravimetric analysis was 0.318 g of a white solid which was assumed to consist of mainly calcium oxide. An elemental analysis was carried out on this sample and the results are given in Table 3.3.

TABLE 3.3 Elemental Analysis of Residual Sample

Element	Weight Percentage
Carbon	0.5%
Hydrogen	0.76%
Sulphur	3.44%

Hence, 4.7% of the weight of the residual sample was due to the presence of other elements so that only 0.303 g of the white solid could be attributed to calcium oxide.

In order to test the validity of this assumption, an atomic absorption analysis was carried out to obtain the concentration of calcium in the sample. The principle of atomic absorption is the tendency of a population of unexcited atoms to absorb strongly the radiation emitted by excited atoms of the same element.

The instrument used was an IL 151 spectrophotometer. The source of radiation was a hollow cathode lamp, the cathode of which incorporated the element being determined, i.e. calcium. An atomizer-burner was used to aspirate a fine mist of the sample into an air/acetylene flame. The

pre-selected wavelength of the radiation (422.7 nm) was isolated with a grating monochromator. A photomultiplier tube tuned to the modulated signal from the hollow cathode tube was used as the detector.

The instrument was calibrated by noting the absorbance of standard solutions of calcium chloride of various concentration. Distilled water was aspirated in between each measurement until the absorbance reading was zero. The procedure was then repeated with a dilute solution of the sample. The result obtained indicated that 60% of the weight of the sample was calcium, i.e. 0.183 g, which corresponded to 0.458 g or 45.8% of calcium carbonate in the original concentrated V-sample. If the residual sample had consisted of only CaO, the weight percentage of calcium should have been 71.4% (i.e. 40/56). The discrepancy was probably due to errors in the elemental analysis. The final concentration of calcium carbonate was slightly higher than the value obtained by TBN analysis (~41% w/w) but the agreement was good enough to allow the subsequent use of the TBN analysis for the determination of the calcium carbonate concentration.

3.2.3 Electron microscopy

The V-particles and the L-particles were examined using a Jeol 100 CX electron microscope. The samples were prepared for direct examination by placing with a platinum loop a very small drop of a dilute dispersion (of concentration $\leqslant$ 0.5% w/w of $CaCO_3$) onto a carbon coated grid.

The determination of the particle size by the measurement of photographic prints of electronmicrographs of the particles was unsuccessful because the prints had to be enlarged to such an extent that the photographic resolution was poor. Attempts were also made to determine the particle size by measuring the photographic plate directly under a projectorscope. This, too, was unsuccessful since the particle images

a

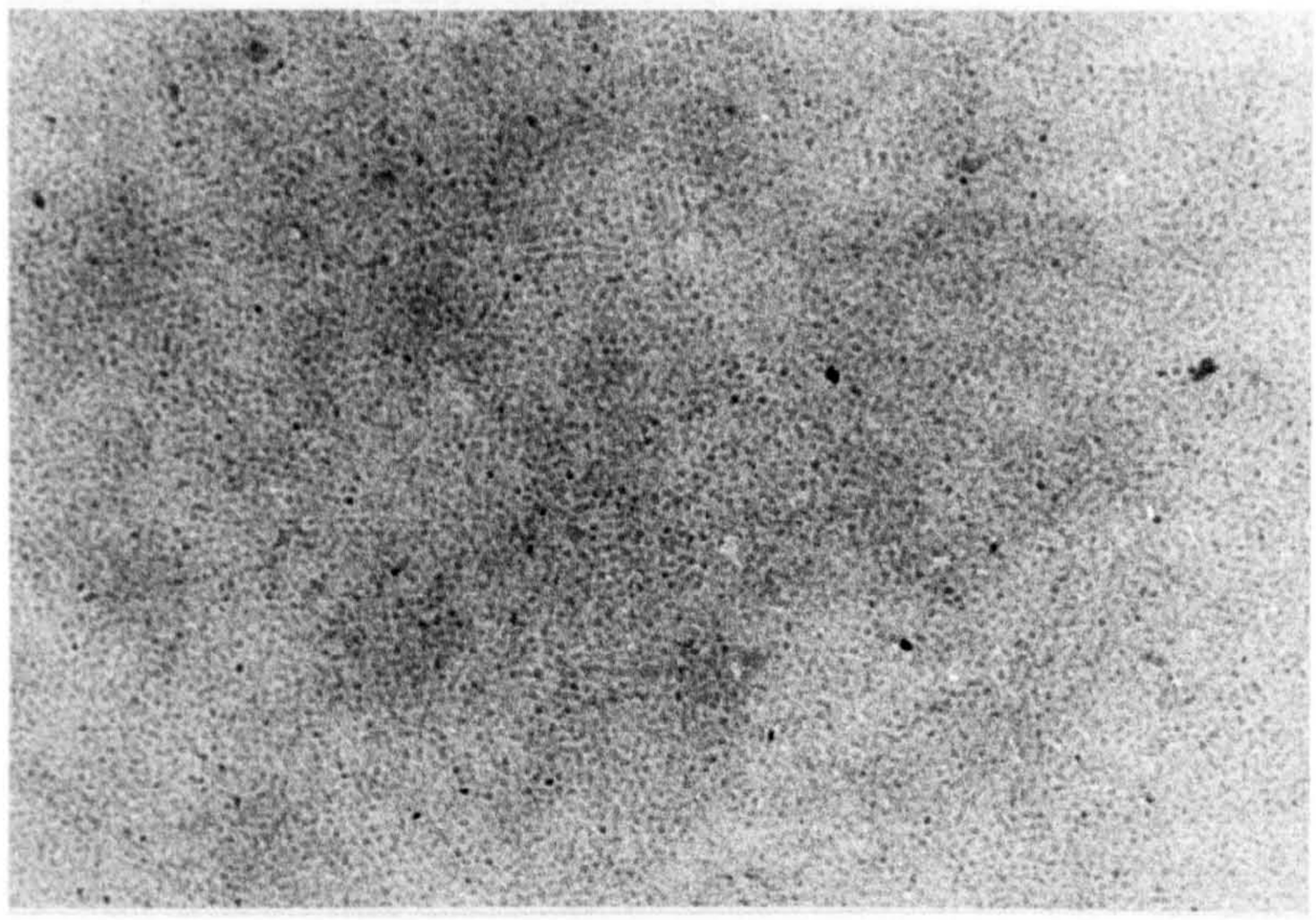

b

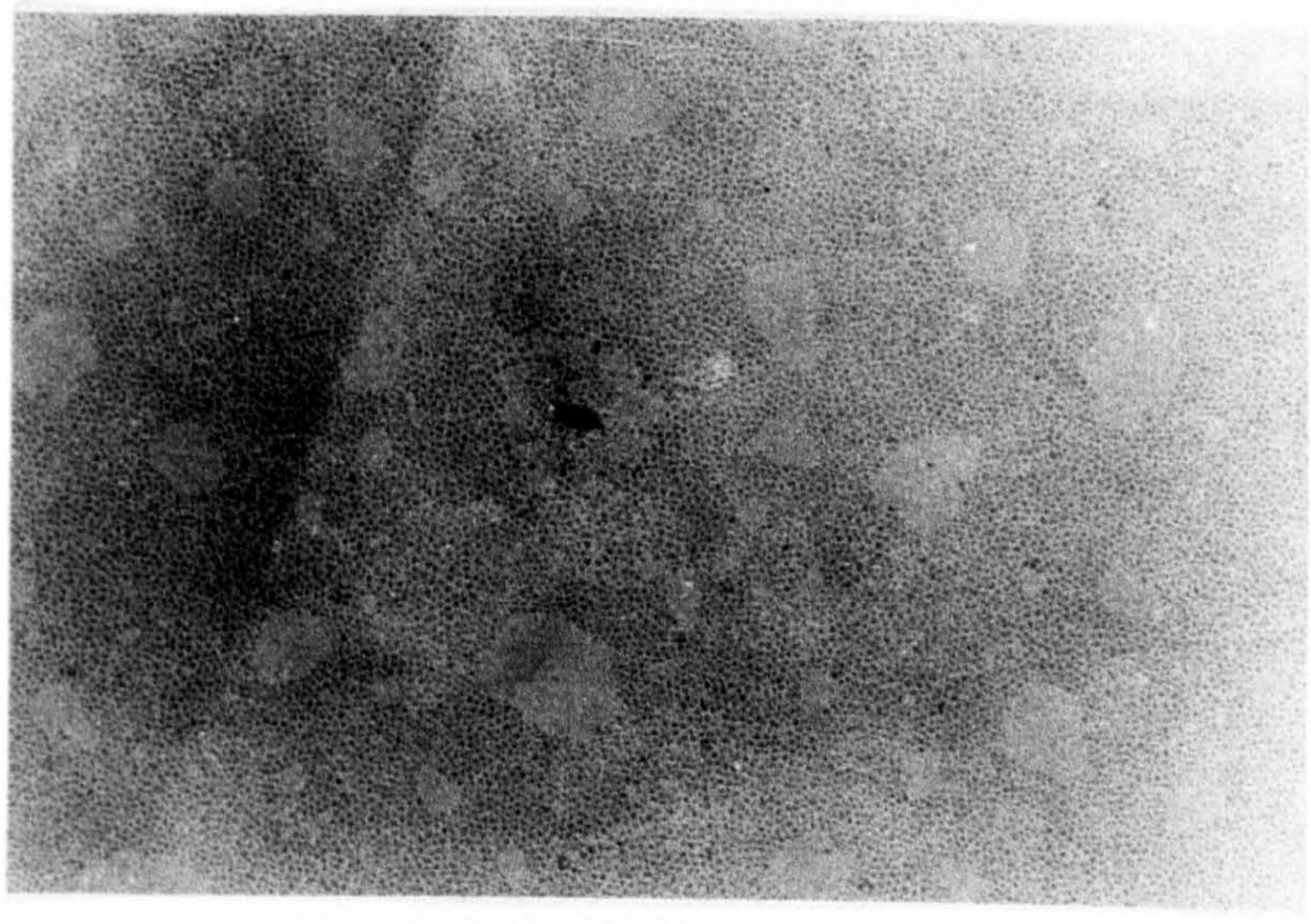

c

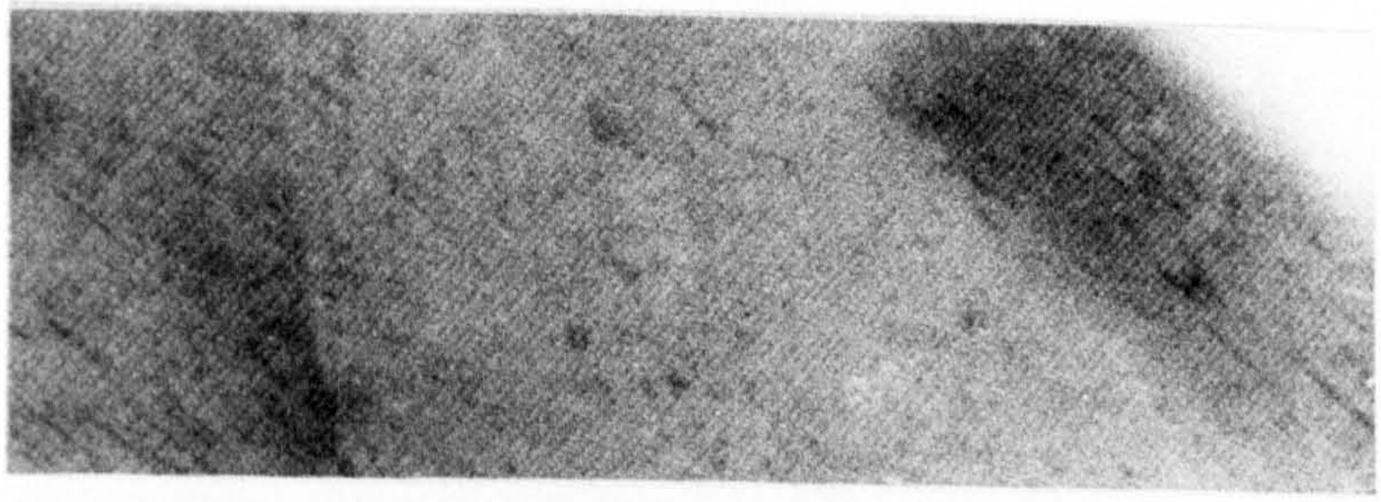

FIGURE 3.2 Electron micrographs of the samples

a) L-sample

b) V-sample

c) Beef liver catalase

were so small that it was difficult to gain a reasonable degree of accuracy. The best procedure was to measure the size of the particle images directly on an enlarged photographic print by comparison with a beef liver catalase graticule of known dimensions.

Figure 3.2 shows the electron micrographs obtained for a V-sample in dodecane and an L-sample in toluene. The beef liver catalase which was used as a reference graticule had spacings of 87.5 Å. The V-particles thus appeared to have a diameter of 58 Å ± 5 Å, whereas the diameter of the L-particles was 140 Å ± 5 Å. Since it was assumed that the electron micrographs revealed only the calcium carbonate core particles, these results appear to be consistent with those obtained by ultracentrifugation. Nevertheless, it is clear that a more accurate method for the determination of the size of the particles is needed.

CHAPTER FOUR

CHAPTER 4

SMALL ANGLE NEUTRON SCATTERING

4.1 General Theory

4.1.1 Introduction

The most widely used form of radiation for the examination of colloidal dispersions is that of visible light. However, the range of scattering vectors which can be obtained by light scattering restricts the distances which this technique can probe. A much wider range of scattering vectors is available if a shorter wavelength of radiation is used, and this is the case in small angle neutron scattering (SANS).

SANS refers to the scattering of a primary beam of cold neutrons of wavelengths up to 20Å, whose scattered intensity is measured at angles not exceeding 17^{o}. Thus, this technique measures the structure of matter over distances large with respect to interatomic separation. The information obtained is in reciprocal space and it is therefore the spatial Fourier transform which describes the average distribution of matter in the particles. An advantageous property of neutrons is that, being electrically neutral, their interaction with matter is weak and occurs at the level of the atomic nucleus. Consequently deeper penetration of matter with little attenuation of the radiation is possible, and multiple scattering is rarely a problem.

The basis of SANS

An outline of the general theory of small angle neutron scattering is given below. For more detailed accounts the reader is referred to standard texts on the subject[27-30].

When a neutron collides with an atom interaction can occur with:

a) the nucleus

b) the electrons with impaired spin

The latter is mainly important for magnetic materials although it also applies to the hydrogen atoms.

Consider the scattering from a single atom, which is represented schematically in Figure 4.1. The incident neutron beam is a planar wave represented by $\Psi(z) = \exp(i\underline{k}_o z)$ where $\underline{k}_o$ is the wavevector of magnitude $2\pi/\lambda$ and λ is the de Broglie wavelength defined by

$$\lambda = h/mv \qquad \ldots \quad (4.1)$$

where h is Planck's constant, and m and v are the mass and the velocity of the neutron respectively. It is obvious from the de Broglie relationship that the wavelength of the incident neutron beam will be controlled by the velocity of the neutrons. The atom scatters the beam in all directions in the form of a spherical wave, which can be represented by $\Psi(r) = (b_o/r)\exp(i\underline{k}\,\underline{r})$.

If an energy change occurs on scattering the magnitudes of $\underline{k}_o$ and $\underline{k}$ are different and the scattering is said to be inelastic. However, if the direction of the wavevector changes but not the magnitude no energy change occurs and the scattering is elastic. The momentum transfer or scattering vector, $\underline{Q}$, measures the difference between the scattered and incident wavevectors, i.e. $(\underline{k} - \underline{k}_o)$, and is shown in Figure 4.1. For the case of elastic scattering $\underline{Q}$ is defined by

$$|\underline{Q}| = Q = \frac{4\pi}{\lambda} \sin(\Theta/2) \qquad \ldots \quad (4.2)$$

where Θ is the scattering angle.

The scattered energy is distributed over the surface of a sphere of radius $4\pi r^2$, the minimum value of which is $4\pi b_o^2$. The quantity b_o is

FIGURE 4.1 THE SCATTERING FROM A SINGLE ATOM

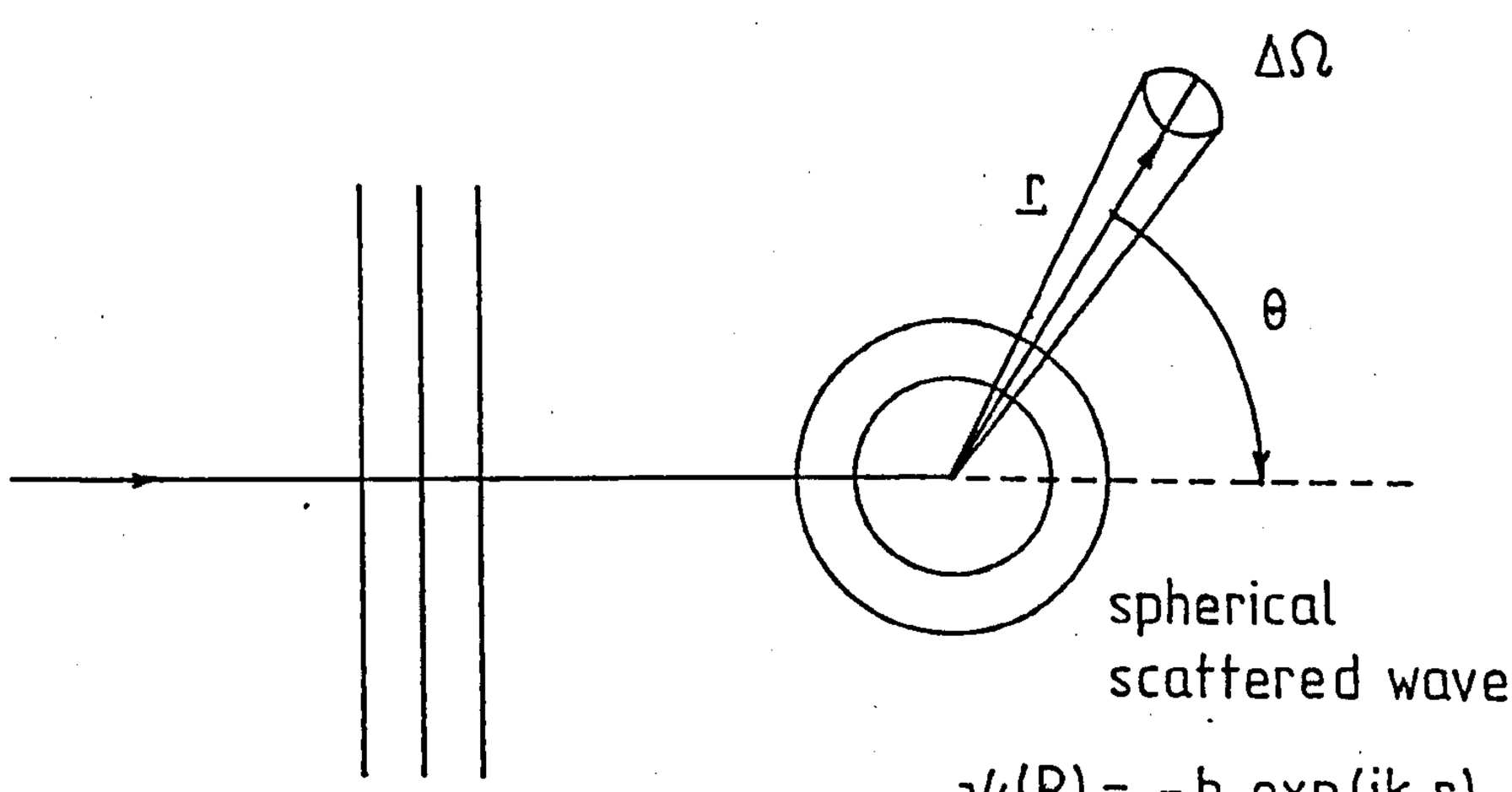

THE SCATTERING VECTOR

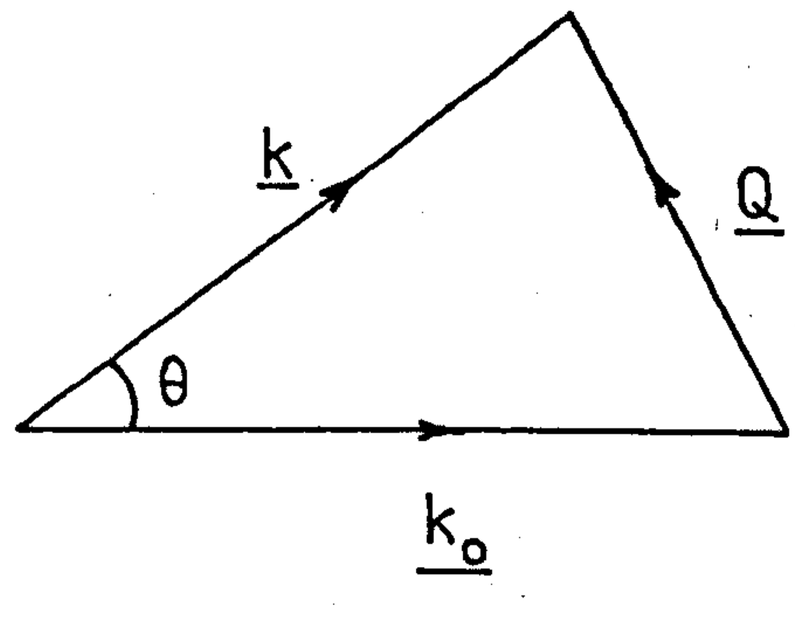

known as the neutron scattering length and its order of magnitude is 10^{-12} cm for all nuclei. The value of b can be positive, negative or complex and does not change with the scattering angle since the nucleus of an atom can be considered as a point scatterer. Usually b is a real number which means that there is no absorption or that it is negligible[30].

The scattering cross-section, σ_s, which is the ratio between the outgoing flux of scattered neutrons and the incident flux is given by

$$\sigma_s = 4\pi b_o^2 \qquad \ldots \quad (4.3)$$

If we now consider the scattering from a real sample which is made up of numerous atoms, two important features arise:

i) there will be interference between waves scattered by the nuclei of the sample;

ii) only part of the scattered waves will take part in that interference.

This means that the scattering cross-section, σ_s, must be split into two parts, called the coherent and incoherent cross-sections. The incoherent scattering includes contributions from "isotope incoherence" and "spin incoherence". The former is a consequence of the random distribution of isotopes throughout the sample, the neutron scattering lengths of which vary dramatically. Spin incoherence arises from the occupation of two spin states in a compound nucleus which is formed on collision of a nucleus with a spin I and a neutron with a spin $\frac{1}{2}$. Spin incoherence does not exist for zero-spin nuclei such as ^{12}C or ^{16}O.

4.1.2 Interference effects

It has been mentioned above that the scattering cross-section, σ_s, is made up of two parts, namely the coherent and incoherent scattering

cross-sections. We shall consider here to what extent each of these cross-sections contributes to the overall scattering of the sample and what effect each one has on the scattering profile.

The differential cross-section per atom per unit solid angle Ω is given by

$$\frac{d\sigma}{d\Omega} = \left| \Sigma_r b_r \exp\ (i\underline{Q}\cdot\underline{r}) \right|^2 \qquad \ldots \quad (4.4)$$

b_r = scattering length of nucleus at position r.

For an assembly of nuclei of the same element but with an assortment of different scattering lengths b_r, equation(4.4)can be expressed as a double sum over positions r and r' [31].

$$\frac{d\sigma}{d\Omega} = \Sigma_r b_r^{\,2} + \Sigma_{r,r'} b_r b_{r'} \exp\ (i\underline{Q}\cdot(\underline{r}-\underline{r}')) \qquad \ldots \quad (4.5)$$

If we now average over N nuclei which we denote by angular brackets $\langle\ \rangle$, and assume no spatial correlation between nuclei of different species (i.e. include both the terms r = r' and r ≠ r'), then

$$\frac{d\sigma}{d\Omega} = N\left\langle b_r^{\,2} \right\rangle + N\left\langle b_r \right\rangle^2 \Sigma_{r,r'} \exp\ (i\underline{Q}\cdot(\underline{r}-\underline{r}')) - N\left\langle b_r \right\rangle^2 \qquad \ldots \quad (4.6)$$

This can be rearranged to give:

$$\frac{d\sigma}{d\Omega} = N\left\langle b_r \right\rangle^2 \left| \Sigma_r \exp(i\underline{Q}\cdot r) \right|^2 + N\left[\left\langle b_r^{\,2} \right\rangle - \left\langle b_r \right\rangle^2 \right] \qquad \ldots \quad (4.7)$$

The first term in equation (4.7), depending on the mean scattering length b_r in the sample, gives rise to *coherent scattering*. The scattering is coherent because the phase factor exp ($i\underline{Q}\cdot r$), reflecting structure, assumes that all nuclei are the same, although individual nuclei

have a range of scattering lengths. Hence, the interference associated with coherent scattering has a spatial distribution which is a function of the atoms in the sample. The second term depends on the mean square deviation of each scattering length from the mean. It represents *incoherent scattering* because it contains no interference phase factor and gives no positional information. The incoherent scattering is thus isotropic; i.e. it is angular independent and moreover it is always present as background scattering.

The coherent scattering cross-section, σ_{coh}, can now be written as

$$\sigma_{coh} = 4\pi \langle b \rangle^2 \qquad \ldots \quad (4.8)$$

or $$\sigma_{coh} = 4\pi b_{coh}^2$$

whereas the incoherent cross-section is given by

$$\sigma_{incoh} = 4\pi \left(\langle b^2 \rangle - \langle b \rangle^2 \right) \qquad \ldots \quad (4.9)$$

or $$\sigma_{incoh} = 4\pi b_{incoh}^2$$

Lastly, the total cross-section, formed by the sum of the two is

$$\sigma_{tot} = 4\pi \langle b^2 \rangle \qquad \ldots \quad (4.10)$$

We have already noted that it is only the coherent scattering which gives rise to interference effects and, hence, to structural information about the sample. Therefore, we will consider subsequently only this type of scattering and the subscript coh will be omitted.

The coherent scattering lengths, b_{coh}, for a number of atoms relevant to this study, are given in Table 4.1.

TABLE 4.1 Coherent Scattering Lengths for Some Atoms

ATOM	$b_{coh}/10^{-12}$cm
Hydrogen, ^{1}H	- 0.374
Deuterium, ^{2}H	0.667
Carbon, ^{12}C	0.665
Oxygen, ^{16}O	0.580
Sulphur, ^{32}S	0.280
Calcium, ^{40}Ca	0.490

It is immediately obvious from Table 4.1 that the coherent scattering length does not scale with atomic number. Also the b_{coh} value for ^{1}H is negative which is a consequence of a phase shift of π between waves scattered by ^{1}H and ^{2}H. In fact, the scattering from H atoms is predominantly incoherent so that the value of b_{incoh} is large. The difference in scattering lengths between hydrogen and deuterium can be exploited experimentally to great advantage and this will be discussed later.

In a typical colloidal dispersion the scattering units are particles composed of an assembly of molecules rather than atoms. Since the resolution in SANS is greater than the interatomic distances condensed matter may be considered as being continuous and it suffices to calculate the average scattering length of one molecule. This is called "the scattering length density", ρ, and it can be defined as the integral over all the scattering lengths in the molecular volume, i.e.,

$$\rho(r) = \frac{1}{V}\int_{V} b_r \, dV \qquad \ldots \quad (4.11)$$

or, in terms of the summation previously used

$$\rho = \Sigma_{i=1}^{N} b_i/V \qquad \ldots \quad (4.12)$$

where b_i are the scattering lengths of the N atoms. The molecular volume, V, is calculated from

$$V = Mw/(N_A \cdot D) \qquad \ldots \quad (4.13)$$

where Mw is the molecular weight, N_A is Avogadro's number and D is the density.

Table 4.2 lists some of the scattering length densities used in this study. The value for calcium carbonate is based on a density value of 2.71 g cm^{-3} (refer to Chapter 3).

TABLE 4.2 Neutron scattering length densities of some molecules

SAMPLE	$\rho/10^{10}$ cm^{-2}
Calcium Carbonate	4.72
h_8-Toluene	0.94
d_8-Toluene	5.63
h_{26}-Dodecane	- 0.46
d_{26}-Dodecane	6.71

The differential coherent scattering cross-section (equation (4.4)) can now be written in terms of the variation of local scattering length, viz.

$$\frac{d\sigma}{d\Omega} = \frac{1}{N} \left| \int_{V_s} \rho(r) \exp(i\underline{Q}\cdot\underline{r})\, d^3r \right|^2 \qquad \ldots \quad (4.14)$$

where V_s is the total volume of the sample and N is the number of scattering nuclei. Since $\rho(r)$ is defined for all parts of the sample, differences of scattering length density are measured rather than absolute values. This is the basis of the important concept of "contrast-matching" which is described later.

4.1.3 Scattering from spherical colloidal particles

In a colloidal dispersion, interference effects will occur as a consequence of spatial correlations both within individual particles and between them.

For a single particle of homogeneous scattering length density ρ_p, surrounded by a medium described by a scattering length density ρ_m, the differential scattering cross-section is given by

$$\frac{d\sigma}{d\Omega} = \left(\rho_p - \rho_m\right)^2 \left| \int_{V_p} \exp\ (i\underline{Q}\cdot\underline{r})\ d^3r \right|^2 \qquad \ldots \quad (4.15)$$

where V_p is the volume of the particle, and the difference in scattering lengths $(\rho_p - \rho_m)$ is often called the contrast.

The interparticle structure factor, called the form factor, can now be defined as

$$F(Q) = \int_{V_p} \exp\ (i\underline{Q}\cdot\underline{r})\ d^3r \qquad \ldots \quad (4.16)$$

For the case of a monodisperse sphere of radius R, $|F(Q)|^2$ can be replaced by the scattering function[32],

$$P(Q) = \left[3\ (\sin QR - QR\cos QR)/Q^3R^3\right]^2 \qquad \ldots \quad (4.17)$$

The form of P(Q) for relatively large monodisperse spheres consists of a series of maxima and minima which diminish in intensity as Q increases.

With increase in particle size the first minimum moves to lower Q values and conversely for a very small sphere it will move to a value of Q which may be experimentally inaccessible.

For a more concentrated colloidal dispersion, in addition to the interference arising from individual particles, there will also be interference effects as a consequence of the spatial correlations between the particles[19]. The latter are described by the interparticle structure factor, S(Q), which can be written as

$$S(Q) = 1 + \rho_o \int_o^\infty \exp\ (i\underline{Q}\cdot\underline{r}) \Big[g(r) - 1 \Big] dr \qquad \ldots \quad (4.18)$$

or

$$S(Q) = 1 + \frac{4\pi\rho_o}{Q} \int_o^\infty r \sin Qr \Big[g(r) - 1 \Big] dr \qquad \ldots \quad (4.19)$$

where ρ_o is the number density (N_p/V) and g(r) is the radial distribution function discussed in Chapter 2. The structure factor, S(Q), yields information in reciprocal space about the total correlation of the dispersion and hence, a spatial Fourier transform of S(Q) leads directly to the radial distribution function g(r), (see Chapter 6).

The scattering cross-section for a concentrated dispersion can now be written to include both the interparticle and the intraparticle structure terms

$$N_p \frac{d\sigma}{d\Omega} \propto I(Q) \propto N_p \left\{ \left\langle |F(Q)|^2 \right\rangle - \left\langle |F(Q)| \right\rangle^2 + \left\langle |F(Q)| \right\rangle^2 S(Q) \right\} \qquad \ldots \quad (4.20)$$

where I(Q) is the observed scattered intensity as a function of Q and N_p is the number of particles in the sample volume.

As a consequence of the symmetry of spherical particles,

$$\left\langle |F(Q)| \right\rangle^2 = \left\langle |F(Q)|^2 \right\rangle = P(Q) \qquad \ldots \quad (4.21)$$

and equation (4.20) can be written as

$$I(Q) \propto N_p \; P(Q) \; S(Q)$$

or more accurately as

$$I(Q) = A \; N_p \; V_p^{\,2} \left[\rho_p - \rho_m\right]^2 P(Q) \; S(Q) \qquad \ldots \quad (4.22)$$

where A is an instrument constant.

For dilute systems where

i) the mean inter-particle distance is large with respect to the particle size, and

ii) the range of the steric repulsive interaction is small with respect to the particle size,

there will be no correlation between the particles, so that g(r) and hence S(Q) are both unity.

Scattering at zero angle

At zero scattering angle, i.e. Q = 0, the particle from factor P(Q) is unity and for a dilute system equation (4.22) can be written as

$$I(0) = A \; N_p \; V_p^{\,2} \left[\rho_p - \rho_m\right]^2 \qquad \ldots \quad (4.23)$$

Since the volume fraction of the particles, ϕ, is given by

$$\phi = N_p \; V_p$$

we can rewrite the above equation as

$$I(0) = A \; \phi \; V_p \left[\rho_p - \rho_m\right]^2 \qquad \ldots \quad (4.24)$$

An immediate use of this relationship is to determine the average scattering length of the particles.

The large difference in scattering lengths between hydrogen and denterium can be exploited to vary the scattering length density of the solvent with minimum disturbance to the chemical and physical equilibria of the system. This is known as *contrast variation* and involves the systematic change of ρ_m from the value for the hydrogenated solvent to that of the deuterated solvent by the use of various mixtures of the two. This technique can also be used to enhance or suppress ("contrast out") the scattering from different regions of a particle, and this is discussed for the case of particles with adsorbed layers in Chapter 5.

Rewriting equation (4.24) in the form

$$\pm \left[I(0)\right]^{\frac{1}{2}} = \left[\rho_p - \rho_m\right] \left[\phi A V_p\right]^{\frac{1}{2}} \qquad \ldots \quad (4.25)$$

it is immediately clear that for $\rho_p = \rho_m$ $\left[I(0)\right]^{\frac{1}{2}} = 0$. Hence a plot of $\pm \left[I(0)\right]^{\frac{1}{2}}$ versus ρ_m crosses the y-axis at the value of the scattering length density of the particles. It is worth noting that if all $\left[I(0)\right]^{\frac{1}{2}}$ data are plotted as positive values the plot will be a parabolic curve, the minimum of which extrapolates to $\rho_p = \rho_m$.

Zero angle intensity cannot be measured directly owing to the presence of the transmitted incident beam. I(0) values are therefore obtained by extrapolation of the observed I(Q) data, the most accurate values being those obtained using the Guinier approximation.

The Guinier Approximation

We have already seen that the scattered intensity for a dilute system of spherical particles is given by

$$I(Q) = A\phi V_p \left[\rho_p - \rho_m\right]^2 \left[3 \left[\frac{\sin QR - QR\cos QR}{Q^3R^3}\right]\right]^2$$

For small values of QR the terms in P(Q) can be expanded to give

$$I(Q) = A\phi V_p\left(\rho_p - \rho_m\right)^2 \left\{1 - \frac{Q^2R^2}{10} + \ldots\right\}^2 \qquad \ldots \quad (4.26)$$

Using the expression for I(0) (equation(4.24)), the above equation can be rewritten as

$$I(Q) = I(0) \left\{1 - \frac{Q^2R^2}{10} + \ldots\right\}^2 \qquad \ldots \quad (4.27)$$

For a sphere, the radius R can be expressed in terms of the radius of gyration, R_g, where

$$R_g^2 = \frac{3}{5} R^2 \qquad \ldots \quad (4.28)$$

giving

$$I(Q) = I(0) \left\{1 - \frac{Q^2R_g^2}{2.3} + \ldots\right\}^2 \qquad \ldots \quad (4.29)$$

Expansion of this equation using the binomial theorem gives

$$I(Q) = I(0) \left[1 - \frac{Q^2R_g^2}{3} + \frac{1}{2^2}\left\{\frac{Q^2R_g^2}{3}\right\}^2\right] \qquad \ldots \quad (4.30)$$

which, to a first approximation, becomes

$$I(Q) = I(0) \exp\left\{-\frac{Q^2R_g^2}{3}\right\} \qquad \ldots \quad (4.31)$$

This equation is often called the Guinier equation[27] and is only valid for values of $QR \ll 1$. When applied under these conditions it leads to linear plots of ln I(Q) versus Q^2, the slope of which yields a value for R_g and hence R[28]. The application of the Guinier approximation for the case of concentric spheres is discussed in Chapter 5.

4.2 Experimental

All the small angle neutron scattering data presented in this thesis was obtained at the Institut Lane-Langevin (I.L.L.), Grenoble, France[33].

4.2.1 SANS instrumentation

Two small angle diffractometers were used at the I.L.L., namely D17 and D11. A brief description of the reactor and of the instrumental features common to both D17 and D11 is given below, and a schematic representation of each instrument is given in Figures 4.2 and 4.3 respectively.

The Source

The high flux reactor at the I.L.L. consists of a single fuel element and operates at a thermal power of 57 MW. The fuel element contains approximately 8.5 kg of 93% enriched uranium, and its dimensions are very small (40 x 140 cm). The fission process providing the neutrons is thus concentrated into a small volume and the neutron flux produced is correspondingly intense. The neutrons are slowed down to thermal energies by a surrounding heavy water moderator. For SANS experiments "cold neutrons" are used which have been further slowed down with the aid of a cold source containing 25 litres of liquid D_2 at 25K. The cold neutron beam is then channelled along curved guide tubes to the instruments using the phenomenon of total reflection. The curvature of the guide tubes eliminates most of the undesirable fast neutrons and the background γ-radiation.

The Monochromator

The incident "white beam" of dimensions 3 cm x 5 cm is monochromatized using a velocity selector. This consists of a drum with helical passages rotating with its axis parallel to the axis of the beam. The only neutrons

FIGURE 4.2 SCHEMATIC VIEW OF THE LOW Q-HIGH RESOLUTION SPECTROMETER D17.

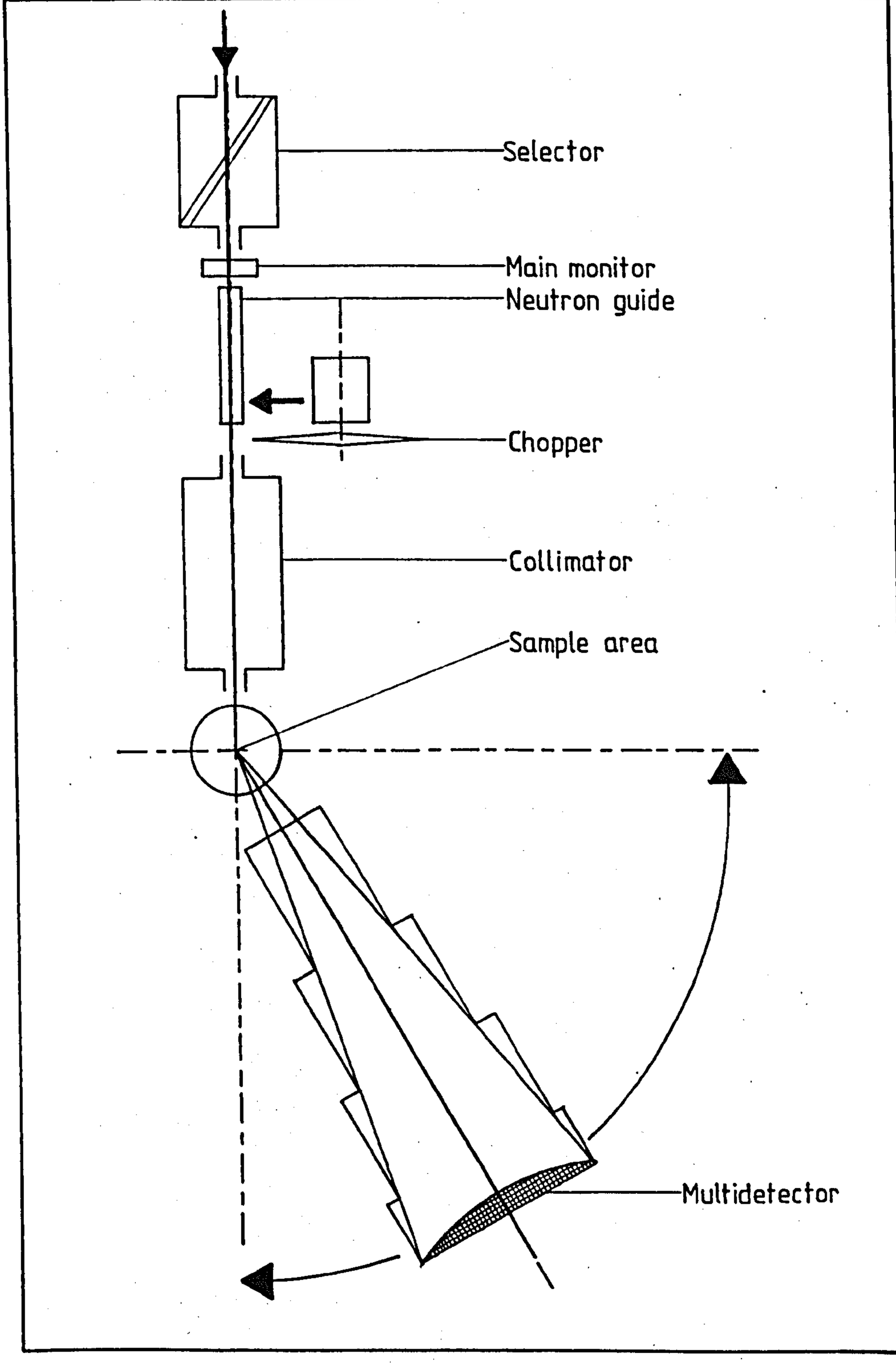

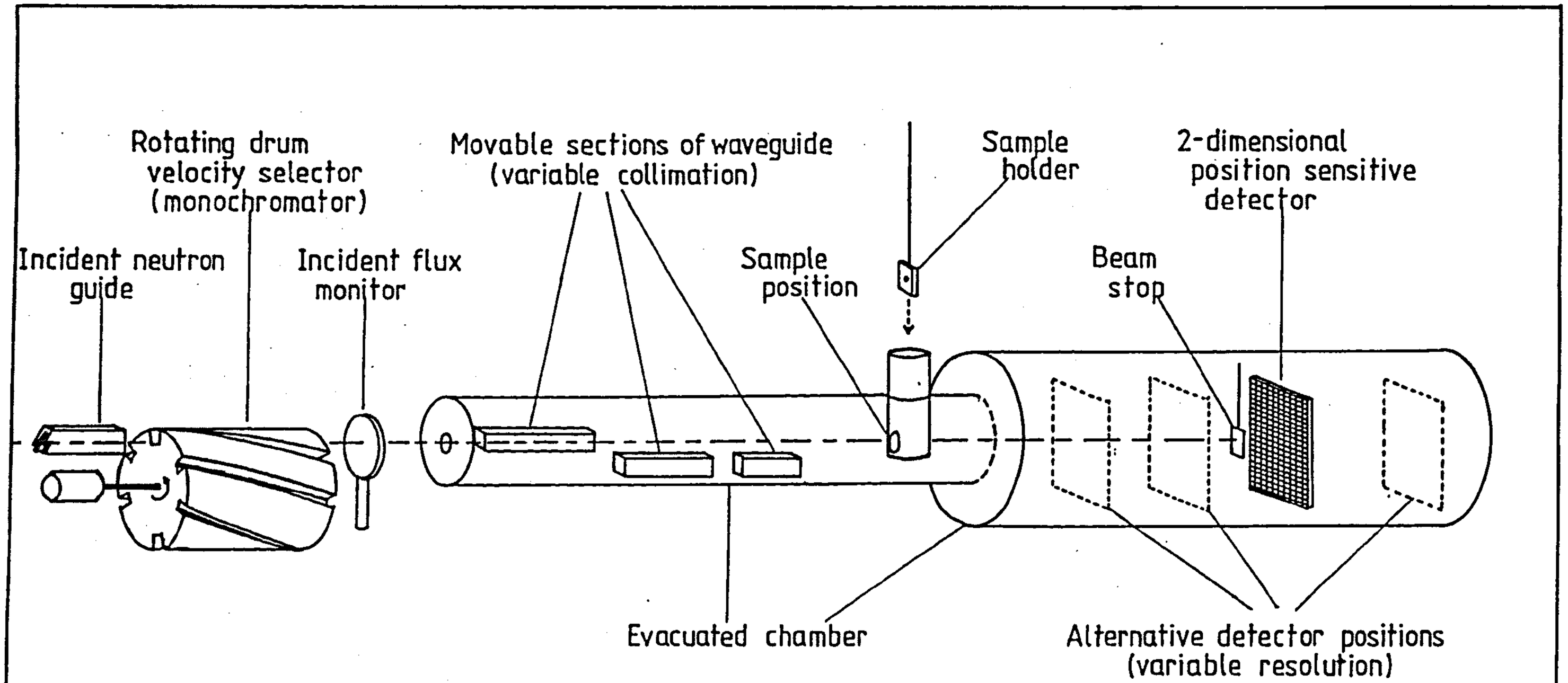

FIGURE 4.3 SCHEMATIC VIEW OF THE D11A S.A.N.S. INSTRUMENT AT THE INSTITUT LAUE-LANGEVIN.

that are transmitted are those whose velocities match the rotation of the drum. Thus, by altering the rotational speed of the drum neutron wavelengths in the range 4Å to 20Å can be selected. The wavelength distribution of the monochromatized beam is roughly triangular with a full width at half height, $\delta\lambda/\lambda$, of ~9% for D11 and ~11% for D17.

The Camera

After the velocity selector the neutron beam passes down an evacuated guide tube, the effective source of the neutrons being taken as the end of the guide. The distance between the sample and the effective source, known as the collimation distance, determines the divergence of the incident beam. For the case of D11 this distance can be varied by movable sections of the guide and is usually adjusted to equal the sample to detector distance.

The beam then passes through a chopper which allows easy wavelength calibration and then a cadmium diaphragm of dimensions 8 mm x 10 mm positioned directly in front of the sample. The dispersions are contained in optically polished quartz cells of 1 mm path length (Helma type 110 QS). Both instruments are equipped with automatic sample changers which are normally at room temperature and pressure, although when necessary it is possible to control the temperature.

The scattered neutrons are detected on to a 64 x 64 element BF_3 multi-detector. Each element, which is defined by the intersection of electrodes, has the dimensions 1 cm x 1 cm and is arranged in a plane perpendicular to the beam. The D11 detector is always centred on the axis of the beam, whereas it is possible to swing the D17 detector to an offset position, i.e. at an angle to the beam, to increase the accessible Q range. Each neutron is captured by a boron atom and the resultant secondary radiation produces a current between the electrodes nearest to the event.

It is necessary to mask the centre of the detector by a cadmium beam stop as the high flux unscattered neutrons can saturate the counting rates of the central elements.

The resolution in scattering angle, i.e. the Q range, is not only defined by the wavelength but also by the distance of the detector from the sample. Distances of approximately 1.4 m and 2.8 m are available on the D17 diffractometer whereas five positions are possible for the D11 detector, namely 2.5 m, 5 m, 10 m, 20 m and 40 m. The resolution is proportional to the maximum scattering angle observed, which in turn is indirectly proportional to the sample-detector distance. Thus, the very long distances available on D11 allow data to be obtained in the low Q region.

Finally, one can summarise the three factors affecting the total resolution of the two SANS instruments as:

i) the incident beam wavelength distribution

ii) the angular divergence of the incident beam

iii) the finite size of the detector element

4.2.2 Data acquisition

Both the D17 and D11 instruments were equipped with a PDP 11/40 computer for controlling the experiment and storing the data. Counts recorded for each element were stored in the electronics unit which incorporated a visual display for continuous supervision of the experiment. The data were collected for a length of time proportional to the accumulation of a set number of counts on the incident flux monitor. The monitor counts were varied according to the scattering intensity expected for a sample so that very dilute samples, background solvent and quartz had to be measured for longer periods of time in order to obtain adequate counting statistics.

Conversely, the transmission run for each sample, which was measured from the intensity of the transmitted primary beam (with the beam stop removed), needed low monitor counts. At the end of each run the data set was stored on a disc with a unique run number for subsequent transfer to the main I.L.L. DEC 10 computer.

Multiple scattering

A possible experimental problem that may be encountered is that of multiple scattering. It is assumed to be approximately isotropic and its general effect is to decrease peak heights in the spectrum and to fill in the minima (cf. with particle size polydispersity).

Schmatz and Shelten[34] have shown that the effect may be evaluated for SANS in terms of a total scattering probability, P, given by

$$P = \frac{3}{2} \lambda^2 \rho^2 R \, \phi \, t \qquad \ldots \quad (4.32)$$

where ρ is the contrast of the particles

R is the particle radius

ϕ is the particle volume fraction

t is the sample thickness

Harris[35] suggests that the total scattering probability should be less than ~0.1 if significant multiple scattering is to be avoided. P was calculated to be well below that value for even the most concentrated systems in this study.

4.2.3 Data treatment

Scattering is radial about the transmitted beam and the data are reduced from a matrix of counts per detector element to a radial distribution of mean counts per element about the beam centre on the detector. The radial

interval on the detector over which the element counts are averaged is generally taken as 1 cm, giving scattering curves defined by ~35 data points at equally spaced values of momentum transfer Q.

Regrouping into radial intensity distributions was done using the I.L.L. standard programme SNILS described by Ghosh[36]. Prior to this it is advisable to inspect raw data matrices visually (as printed out by the I.L.L. programme DETEC) to check for faulty counting, particularly of whole rows and columns. In practice, the side edges of the detector, i.e. columns and rows 0, 1, 2, 62 and 63 and the beam stop area were omitted from the analysis using the I.L.L. standard programme RMASK.

Once the data is in the form of a radial distribution function I(Q) two principal corrections have to be carried out, viz.

i) the subtraction of the background incoherent scattering from the sample scattering

ii) the normalization of the sample scattering by the scattering from water in order to account for the spatial variation of the detector response.

For dilute samples, the I.L.L. programme SPOLLY performs these corrections adequately, and is outlined below. However, for the case of concentrated dispersions a different procedure has to be adopted and this will be described in Chapter 6.

The SPOLLY programme corrects the sample spectrum by combining individual spectra or sets of similar spectra which have all been normalised for unit incident flux by dividing by the monitor counts, and then performing the following calculations for each value of Q.

Let Z represent the number of counts at a fixed detector setting, then

Z(S + Q) = counts from sample + quartz cell

$Z(SB + Q)$ = counts from sample background + quartz cell.

The corrected intensity of the sample is then given by

$$Z(S) = Z(S + Q) - \frac{T_S}{T_{SB}} Z(SB + Q) \quad \ldots \quad (4.33)$$

where $\frac{T_S}{T_{SB}} = \frac{\text{transmission of sample}}{\text{transmission of sample background}}$

and is a factor which corrects for the attenuation of the beam due to refraction at the quartz windows and sample absorption.

As incoherent scattering is isotropic it can be used to correct for the variation of the detector response. The most frequently used incoherent scatterer for this purpose is water. The scattering from the water sample also has to be treated in the manner described above, except that the sample background is now the quartz cell.

If $Z(H + Q)$ = counts from water + quartz cell

$Z(Q)$ = counts from empty quartz cell

then $$Z(H) = Z(H + Q) - \frac{T_H}{T_Q} Z(Q) \quad \ldots \quad (4.34)$$

where $\frac{T_H}{T_Q} = \frac{\text{transmission of water}}{\text{transmission of quartz cell}}$

Finally, the programme normalises the corrected sample scattering to the corrected water scattering at each Q value, i.e.

$$I(Q) = \frac{Z(S)}{Z(H)} \cdot \frac{T_H}{T_S} \quad \ldots \quad (4.35)$$

where the transmission ratio $\frac{T_H}{T_S}$ is known as the "total sample cross-section" and corrects for sample self-absorption. The data in the form of I(Q) are then stored in a DISDAT.SAS file from which a printed outprint can be obtained.

CHAPTER FIVE

CHAPTER 5

SANS OF DILUTE DISPERSIONS

The basic theory of small angle neutron scattering, as applicable to simple spherical particles, has already been derived in the preceding chapter. However, the systems in this study were assumed, in the absence of more detailed information, to consist of particles composed of a spherical inorganic core surrounded by a stabilizing layer of organic material. This adsorbed layer is essential to provide the colloidal stability of the particles by the mechanism of steric stabilization, so that any attempt to remove it causes immediate destabilization. Consequently, this type of system must be investigated in situ and the methods employed with aqueous dispersions of starting with the native particle and adding the adsorbate are not applicable[37].

Small angle neutron scattering is a particularly useful technique for the investigation of systems where the particle and layer cannot be separated[38], and it was consequently used in this study. The characterization of such a system must primarily involve the determination of the size of the core and the thickness of the adsorbed layer. In order to interpret the SANS results obtained for this purpose, a model had to be adopted to represent the particles.

The model used was that of a concentric sphere and it is shown in Figure 5.1. The basis of the model is a spherical homogeneous core particle of radius R_1 and neutron coherent scattering length density ρ_P, surrounded by a spherical shell of adsorbed material, taken as a homogeneous adsorbed layer of coherent scattering length density ρ_A. The radius of the total spherical unit was taken as R_2, giving the thickness of the adsorbed layer as $(R_2 - R_1)$.

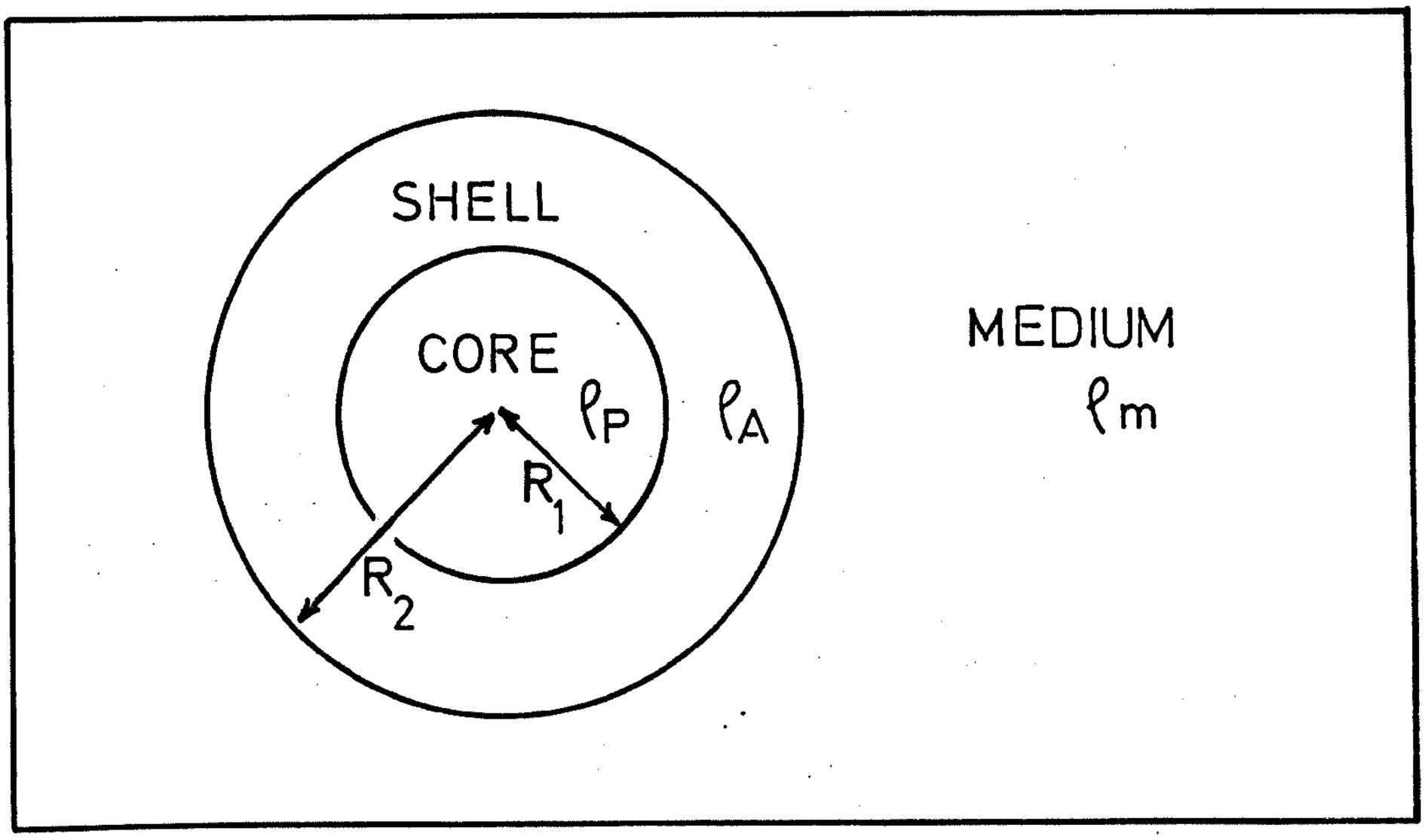

FIGURE 5.1 Concentric Sphere Model

The ability of the neutron beam to distinguish between hydrogen and deuterium atoms has already been discussed in Chapter 4, as well as the use of this feature in the technique known as contrast matching. This method of analysis is most relevant in our case, since it is possible to use mixtures of hydrogenated and deuterated solvents to obtain a scattering length density of the dispersion medium, ρ_m, which matches that of either the core or the adsorbed layer. Hence, the scattering from a particular region of the particle can be enhanced, or conversely suppressed, facilitating the analysis of the results. The determination of the dimensions of the particle is further simplified if dilute dispersions are used for the experiments. In this case, the particle number concentration is low so that there is no interparticle interference, and it is only the intraparticle interference, i.e. the particle form factor, which contributes to the scattering intensity.

The extension of SANS theory for the case of dilute dispersions of

concentric spheres is presented in this chapter and, for convenience, it has been subdivided into two parts, namely the Guinier approach and the curve fitting approach.

5.1 The Guinier Approach

Experimental

Dilute dispersions of all three systems were used for this investigation, namely the V-series, the L-series and the F-series. The materials used, as well as the method of preparation of these dispersions, were described in Chapter 3.

The SANS measurements were carried out on the D17 neutron diffractometer at the I.L.L. For these experiments, the samples were contained in optical quality quartz cells having a path length of 1 mm. The measurements were carried out using a sample-to-detector distance of 2.87 m and an incident neutron beam wavelength of 10 $\mathring{A}$ so that the Q-range was 0.01 - 0.1 $\mathring{A}^{-1}$. Standard I.L.L. computer programmes were used to process the basic data to give the intensity of scattering as a function of Q, I(Q), relative to water. The appropriate background was subtracted from the scattering patterns of each of the samples and corrections were made for the attenuation of the beam due to absorption. A detailed account of the acquisition and the treatment of SANS data was given in Chapter 4.

5.1.1 Theory

The differential coherent scattering cross-section for a homogeneous spherical particle of scattering length density ρ_p dispersed in a medium of scattering length density ρ_m was derived in Section 4.1.3 of the preceding chapter, as equation (4.15), and is repeated here for convenience.

$$\frac{d\sigma}{d\Omega} = (\rho_p - \rho_m)^2 \left| \int_{V_p} \exp\,(i\underline{Q}\cdot\underline{r})\, d^3r \right|^2 \qquad \ldots \quad (4.15)$$

where V_p is the volume of the particle and N_p is the number concentration of particles per cm^3. The particle form factor was defined as

$$\left| F(Q) \right|^2 = \left| \int_{V_p} \exp\,(i\underline{Q}\cdot\underline{r})\, d^3r \right|^2 \qquad \ldots \quad (4.16)$$

However, for the case of a concentric sphere, as illustrated in Figure (5.1), the intraparticle structure factor has to be expanded to include a phase factor resulting from the interference of the neutron beam due to the presence of the adsorbed layer. Also, the extent of the scattering of the neutron beam by each of the two regions of the particle (i.e. the difference in the phase factors associated with each region) will depend on the relative coherent scattering lengths of the particle with respect to the medium.

Hence, the differential coherent scattering cross-section for a concentric sphere is given by,

$$\left\{\frac{d\sigma}{d\Omega}\right\}_{c.s.} = \left[(\rho_A - \rho_m)\left\{\left|\int_{V_T} \exp(iQ\cdot R_2)\, d^3R_2\right| - \left|\int_{V_p} \exp(iQ\cdot R_1)\, d^3R_1\right|\right\} + (\rho_p - \rho_m)\left|\int_{V_p} \exp(iQ\cdot R_1) d^3R_1\right|\right]^2$$

$$\ldots \quad (5.1)$$

where V_p is now the volume of the core and V_T is the volume of the whole particle. As we have already seen, for spheres of radius R, the form factor $|F(Q)|^2$ can be replaced by the function,

$$P(Q) = \left[3\,(\sin QR - QR\cos QR)/(QR)^3\right]^2 \qquad \ldots \quad (4.17)$$

Whereas, for a concentric sphere we need to define the following form factors:-

$$f(QR_2) = 3R_2^3 \ (\sin QR_2 - QR_2 \cos QR_2)/(QR_2)^3$$

$$f(QR_1) = 3R_1^3 \ (\sin QR_1 - QR_1 \cos QR_1)/(QR_1)^3$$

Substituting these functions into equation (5.1),

$$\left(\frac{d\sigma}{d\Omega}\right)_{c.s.} = \left(\frac{4\pi}{3}\right)^2 \left[(\rho_A - \rho_m)\left[f(QR_2) - f(QR_1)\right] + (\rho_p - \rho_m)\ f(QR_1)\right]^2 \quad \ldots \quad (5.2)$$

or in terms of the full expressions for the form factors,

$$\left(\frac{d\sigma}{d\Omega}\right)_{c.s.} = \left(\frac{4\pi}{3}\right)^2 \left[(\rho_A - \rho_m)\left\{3R_2^3 \left(\frac{\sin QR_2 - QR_2 \cos QR_2}{Q^3R_2^3}\right)\right.\right.$$

$$\left.\left. - 3R_1^3 \left(\frac{\sin QR_1 - QR_1 \cos QR_1}{Q^3R_1^3}\right)\right\} + (\rho_p - \rho_m) \left(\frac{\sin QR_1 - QR_1 \cos QR_1}{Q^3R_1^3}\right)\right]^2 \quad \ldots \quad (5.3)$$

The differential scattering cross-section can be replaced by the scattering intensity, I(Q), as a function of Q, since

$$\left(\frac{d\sigma}{d\Omega}\right)_{c.s.} A\ N_p = I(Q)$$

where A is a calibration constant and I(Q) for a dilute system was defined in Chapter 4 as,

$$I(Q) = A\ N_p\ V_p^2\ (\rho_p - \rho_m)^2 P(Q) \quad \ldots \quad (4.22)$$

For concentric spheres the volume fraction, ϕ, is given by

$$\phi = N_p V_p$$

$$\phi = N_p \frac{4\pi}{3} R_1^3 \qquad \ldots \quad (5.4)$$

Since the radii of the particle are included in the expressions for the form factors, the scattering intensity for a dilute system of this type is given by[37,39]

$$I(Q) = \frac{AN_p 16\pi^2}{9} \left[(\rho_A - \rho_m) \left[f(QR_2) - f(QR_1) \right] + (\rho_p - \rho_m) f(QR_1) \right]^2 \qquad \ldots \quad (5.5)$$

Multiplying out the terms in the square brackets,

$$I(Q) = \frac{AN_p 16\pi^2}{9} \left[(\rho_A - \rho_m) f(QR_2) + (\rho_p - \rho_A) f(QR_1) \right]^2 \qquad \ldots \quad (5.5a)$$

or

$$I(Q) = \frac{AN_p 16\pi^2}{9} \left[(\rho_A - \rho_m)^2 f(QR_2)^2 + (\rho_p - \rho_A)^2 f(QR_1)^2 \right.$$

$$\left. + 2(\rho_A - \rho_m)(\rho_p - \rho_A) f(QR_2) f(QR_1) \right] \qquad \ldots \quad (5.6)$$

If measurements are restricted to the range $QR_2 \ll 1$ then it is possible to apply the Guinier approximation[27] (see equation (4.31) in Chapter 4), and introduce a number of simplifications. For small values of QR_2 by expanding $f(QR_2)$ and $f(QR_1)$ we obtain

$$f(QR_2) = R_2^3 \ (1 - Q^2R_2^2/10 \ \ldots)$$

$$f(QR_1) = R_1^3 \ (1 - Q^2R_1^2/10 \ \ldots)$$

Substituting into equation (5.5),

$$I(Q) = \frac{AN_p 16\pi^2}{9} \left[(\rho_A - \rho_m) \left\{ R_2^3 \ (1 - Q^2R_2^2/10 \ \ldots) - R_1^2 \ (1 - Q^2R_1^2/10 \ \ldots) \right\} + (\rho_p - \rho_m) \ R_1^3 \ (1 - Q^2R_1^2/10 \ \ldots) \right]^2 \quad \ldots \quad (5.7)$$

This gives

$$I(Q) = AN_p \left[(\rho_A - \rho_m) \ V_T - (\rho_A - \rho_m) \ V_p + (\rho_p - \rho_m) \ V_p - \frac{Q^2}{10} \left(R_2^2 \ (\rho_A - \rho_m) \ V_T - R_1^2 \ (\rho_A - \rho_m) \ V_p + R_1^2 \ (\rho_p - \rho_m) \ V_p \right) \right]^2 \quad \ldots \quad (5.8)$$

The volume of the whole particle, V_T, is defined as

$$V_T = V_p + V_A$$

where V_p is the volume of the core particle as given by $4\pi R_1^3/3$, and V_A is the volume of the adsorbed layer and is given by $4\pi(R_2^3 - R_1^3)/3$.

Equation (5.8) can now be written as,

$$I(Q) = AN_p \left[(\rho_A - \rho_m) \ V_A + (\rho_p - \rho_m) \ V_p - \frac{Q^2}{10} \left((\rho_A - \rho_m)(V_T R_2^2 - V_p R_1^2) + (\rho_p - \rho_m) \ V_p R_1^2 \right) \right]^2 \quad \ldots \quad (5.9)$$

The term, $(\rho_A - \rho_m) \ V_A + (\rho_p - \rho_m) \ V_p$

$$= V_A\rho_A + V_p\rho_p - (V_A + V_p) \ \rho_m$$

$$= V_T \left[\frac{V_A\rho_A + V_p\rho_p}{V_T} - \rho_m \right] \quad \ldots \quad (5.10)$$

Since ρ_A and ρ_p are volume properties, the average coherent scattering length density of a concentric sphere is defined as,

$$\bar{\rho} = \frac{V_A\rho_A + V_p\rho_p}{V_T} \quad \ldots \quad (5.11)$$

Hence, the term given in equation (5.10) becomes,

$$V_T\ (\bar{\rho} - \rho_m)$$

It is immediately clear from equation (5.9) that at $Q = 0$, when $\rho_m = \bar{\rho}$, that $I(0) = 0$. Hence, the quantity $\bar{\rho}$ can be determined by measuring $I(0)$ as a function of ρ_m.

A new quantity can now be defined to represent the deviation from the coherent scattering length density of the medium, as

$$\rho = \bar{\rho} - \rho_m \quad \ldots \quad (5.12)$$

Hence, using equations (5.10) and (5.12), we obtain from equation (5.9)

$$I(Q) = AN_p \left[V_T \rho - \frac{Q^2}{10} \left\{ (\rho_A - \rho_m)(R_2^2 V_T - R_1^2 V_p) + (\rho_p - \rho_m) R_1^2 V_p \right\} \right]^2 \quad \ldots \quad (5.13)$$

At $Q = 0$ this gives,

$$I(0) = AN_p V_T^2 \rho^2 \quad \ldots \quad (5.14)$$

Substituting for $I(0)$, equation (5.13) becomes,

$$I(Q) = I(0) \left[1 - \frac{Q^2}{10V_T\rho} \left\{ (\rho_A - \rho_m)(R_2^2 V_T - R_1^2 V_p) + (\rho_p - \rho_m) R_1^2 V_p \right\} \right]^2 \quad \ldots \quad (5.15)$$

By multiplying out equation (5.15) and taking only the leading terms, i.e.

the condition for small QR_2, we obtain,

$$I(Q) = I(0)\left[1 - \frac{Q^2}{5V_T\rho}\left\{(\rho_A - \rho_m)(R_2^2\ V_T - R_1^2\ V_p) + (\rho_p - \rho_m)\ R_1^2\ V_p\right\}\ldots\right]$$

... (5.16)

The term within the curly brackets has the dimension of a radius squared so that we can define a new quantity $\bar{R}^2$ as,

$$\bar{R}^2 = \frac{1}{\rho V_T}\left\{(\rho_A - \rho_m)(R_2^2\ V_T - R_1^2\ V_p) + (\rho_p - \rho_m)\ R_1^2\ V_p\right\}$$

... (5.17)

$$\bar{R}^2 = \frac{1}{\rho V_T}\left\{(\rho_A - \rho_m)\ R_2^2\ V_T - (\rho_A - \rho_m)\ R_1^2\ V_p + (\rho_p - \rho_m)\ R_1^2\ V_p\right\}$$

or $$\bar{R}^2 \rho\ V_T = (\rho_p - \rho_A)\ R_1^2\ V_p + (\rho_A - \rho_m)\ R_2^2\ V_T \quad \ldots \quad (5.18)$$

It is also convenient to assign to the adsorbed layer a geometric radius R_A so that we can write

$$R_2^2\ V_T = R_1^2\ V_p + R_A^2\ V_A \quad \ldots \quad (5.19)$$

Combination of equations (5.18) and (5.19) gives,

$$\bar{R}_2\ \rho\ V_T = (\rho_p - \rho_m)\ R_1^2\ V_p + (\rho_A - \rho_m)\ R_A^2\ V_A$$

and since,

$$\rho_m = \bar{\rho} - \rho$$

$$\bar{R}_2\ \rho\ V_T = (\rho_p - \bar{\rho} + \rho)\ R_1^2\ V_p + (\rho_A - \bar{\rho} + \rho)\ R_A^2\ V_A$$

$$= \rho\ R_2^2\ V_T + (\rho_p - \bar{\rho})\ R_1^2\ V_p + (\rho_A - \bar{\rho})\ R_A^2\ V_A$$

... (5.20)

and $$\bar{R}^2 = R_2^2 + \frac{1}{V_T \rho} \left\{ (\rho_p - \bar{\rho})\, R_1^2\, V_p + (\rho_A - \bar{\rho})\, R_A^2\, V_A \right\} \quad \ldots \quad (5.21)$$

It is necessary at this point to define a radius of gyration for the adsorbed layer. Referring to Figure 5.1 , consider a concentrically spherical element of the adsorbed layer of thickness, dr, and a distance, r, away from the centre of the particle. The volume of the element is $4\pi r^2 \cdot dr$ and its mass is $4\pi r^2 dr \rho_o$, where ρ_o is the density. The radius of gyration of the whole adsorbed layer is then given by

$$Rg_A^2 = \frac{\int_{R_1}^{R_2} 4\pi r^2 \rho_o \cdot r^2 \, dr}{\int_{R_1}^{R_2} 4\pi r^2 \rho_o \, dr} = \frac{\int_{R_1}^{R_2} r^4 \, dr}{\int_{R_1}^{R_2} r^2 \, dr}$$

$$Rg_A^2 = \frac{\left[r^5/5 \right]_{R_1}^{R_2}}{\left[r^3/3 \right]_{R_1}^{R_2}}$$

$$Rg_A^2 = \frac{3}{5} \frac{\left[R_2^5 - R_1^5 \right]}{\left[R_2^3 - R_1^3 \right]} \quad \ldots \quad (5.22)$$

It follows that the previously mentioned geometric radius of the adsorbed layer can now be defined as

$$R_A^2 = \frac{R_2^5 - R_1^5}{R_2^3 - R_1^3} \quad \ldots \quad (5.23)$$

Returning to equation (5.21), we can now express it in terms of radii of gyration in the form,

$$\bar{R}g^2 = \frac{3}{5}\bar{R}^2 = Rg_2^2 + \frac{1}{V_T\rho}\left\{(\rho_p - \bar{\rho})\, Rg_1^2\, V_p + (\rho_A - \bar{\rho})\, Rg_A^2\, V_A\right\} \quad \ldots \quad (5.24)$$

where $\bar{R}g^2$ is a mean square radius of gyration of the whole particle.

By analogy to simple spheres, we can use the Guinier equation for $QR \ll 1$, i.e.,

$$I(Q) = I(0)\, \exp\left(\frac{-Q^2\, \bar{R}g^2}{3}\right) \quad \ldots \quad (5.25)$$

Thus, $\bar{R}g^2$ and hence $\bar{R}^2$ can be obtained at various values of ρ_m and therefore of ρ, and a plot of $\bar{R}g^2$ against $1/\rho$ constructed.

Figure 5.2 shows simulated plots of $\bar{R}g^2$ against $1/\rho$ for systems with a constant core radius and variable adsorbed layer thicknesses (Figure 5.2a), and systems with a constant adsorbed layer thickness and different core radii (Figure 5.2b). These plots show how the intercepts on the abscissa and the ordinate change with particle dimensions. They also demonstrate the value of ρ beyond which $\bar{R}g^2$ becomes negative - useful information to have when designing experiments.

An examination of equation (5.21) shows several properties of interest related to a plot of $\bar{R}^2$ against $1/\rho$. For example, when

$$1/\rho = 0 \quad \text{then} \quad \bar{R}^2 = R_2^2 \quad \ldots \quad (5.26)$$

giving an estimate of the overall size of the particle. When $\bar{R}^2 = 0$, then the intercept on the x-axis is given as,

$$\frac{1}{\rho_o} = \frac{-V_T\, R_2^2}{(\rho_p - \bar{\rho})\, R_1^2\, V_p + (\rho_A - \bar{\rho})\, R_A^2\, V_A} \quad \ldots \quad (5.27)$$

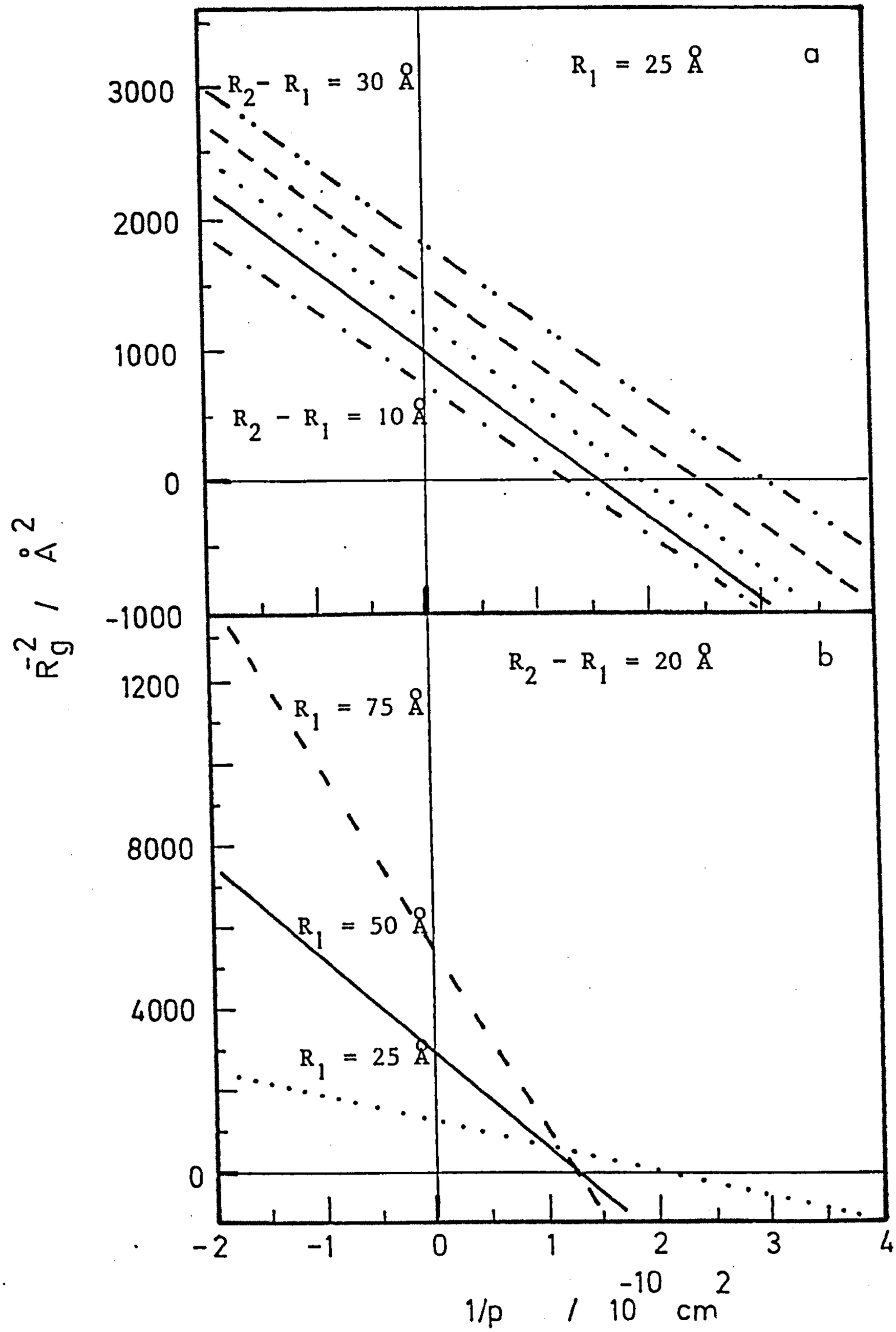

FIGURE 5.2 Calculated curves of $\bar{R}g^2$ against $1/\rho$

a) R_1 = 25 Å; $(R_2 - R_1)$: -•-, 10 Å; ——, 15 Å; ...., 20 Å; ---, 25 Å; -••-, 30 Å

b) $(R_2 - R_1)$ = 20 Å; R_1 : ...., 25 Å; ——, 50 Å; ---, 75 Å

$$\text{or} \qquad -\rho_o V_T R_2^2 = (\rho_p - \bar{\rho}) R_1^2 V_p + (\rho_A - \bar{\rho}) R_A^2 V_A$$

which on substitution for $R_A^2 V_A$ (equation (5.19)) gives,

$$-\rho_o V_T R_2^2 = (\rho_p - \bar{\rho}) R_1^2 V_p + (\rho_A - \bar{\rho}) R_2^2 V_T - (\rho_A - \bar{\rho}) R_1^2 V_p$$

$$R_1^5 = \frac{\left[\bar{\rho} - (\rho_o + \rho_A)\right] R_2^5}{(\rho_p - \rho_A)} \qquad \ldots \quad (5.28)$$

and hence an estimate of R_1 can be obtained from the data.

Moreover, we also note that the gradient is given by,

$$\frac{\partial(\bar{R}^2)}{\partial(1/\rho)} = \frac{1}{V_T}\left\{(\rho_p - \bar{\rho}) R_1^2 V_p + (\rho_A - \bar{\rho}) R_A^2 V_A\right\}$$

and hence the product,

$$\text{(Gradient)} \times \text{(Intercept on x-axis)} = -R_2^2$$

gives a check on the consistency of the data.

It should be noted both from Figure 5.2 and from equation (5.24) that under certain conditions, particularly when the volume of the adsorbed layer is greater than that of the particle, then the value of $\bar{R}g^2$ can be negative. A further consideration of this effect is given in Section 5.2.

5.1.2 Results

The basic materials used for this work were calcium carbonate, the surface active agent - an alkyl aryl sulphonic acid, and the dispersion media which were the hydrogenated and the deuterated forms of both toluene and dodecane. In addition, the samples contained a small amount of hydrocarbon oil and this was taken into account when the scattering length density of the medium, ρ_m, was calculated. The scattering length densities of the materials used are given in Table 5.1.

TABLE 5.1 Coherent Neutron Scattering Length Densities

Material	$\rho/10^{10}cm^{-2}$
Calcium carbonate	4.72
Surface active agent	0.35
Hydrocarbon oil	- 0.53
h_8 - Toluene	0.94
d_8 - Toluene	5.63
h_{26}- Dodecane	- 0.46
d_{26}- Dodecane	6.71

The V-series, the L-series and the F-series of dispersions of calcium carbonate were examined at concentrations of 1% and 2% w/w in h_8 - toluene and in mixtures of h_8 - toluene and d_8 - toluene. In addition, each of the series was examined at one of these two concentrations in h_{26} - dodecane and in mixtures of h_{26} - dodecane and d_{26} - dodecane. The weight/weight concentrations of 1% and 2% of calcium carbonate correspond to the following volume fractions of the core and of the whole particle, the latter having been calculated using the volume fractions of the constituents of the original sample (see Chapter 3).

TABLE 5.2 Volume Fractions for the Systems

System	Concentration	ϕ_p	ϕ_T
V-series	1% w/w	3.69×10^{-3}	1.26×10^{-2}
	2% w/w	7.38×10^{-3}	2.52×10^{-2}
L-series	1% w/w	3.69×10^{-3}	1.25×10^{-2}
	2% w/w	7.38×10^{-3}	2.50×10^{-2}
F-series	1% w/w	3.69×10^{-3}	8.1×10^{-3}
	2% w/w	7.38×10^{-3}	1.62×10^{-2}

These volume fractions were thought to be low enough, even the values for the total volume fraction (ϕ_T), i.e. particle + shell, to avoid significant interparticle interference effects at low Q values, and at the same time to be high enough to give scattering intensities from the particles well above those of the background solvent.

Figure 5.3 shows typical examples of experimental curves of I(Q) against Q that were obtained for the V-series, the L-series and the F-series at a concentration of 1% w/w of calcium carbonate dispersed in a medium composed of 10% h_8 - toluene and 90% d_8 - toluene by weight. As can be seen, the data were of good quality, even for the fairly polydisperse F-sample, and allowed curve fitting to be undertaken in order to extrapolate the data to Q = 0 and thus obtain I(0).

Scattering results were obtained for the three series in dispersion media containing 0%, 10%, 60%, 70%, 80% and 90% of d_8 - toluene by weight. In addition, the V-series at a concentration of 2% w/w of calcium carbonate, and the L-series and the F-series both at a concentration of 1% w/w, were

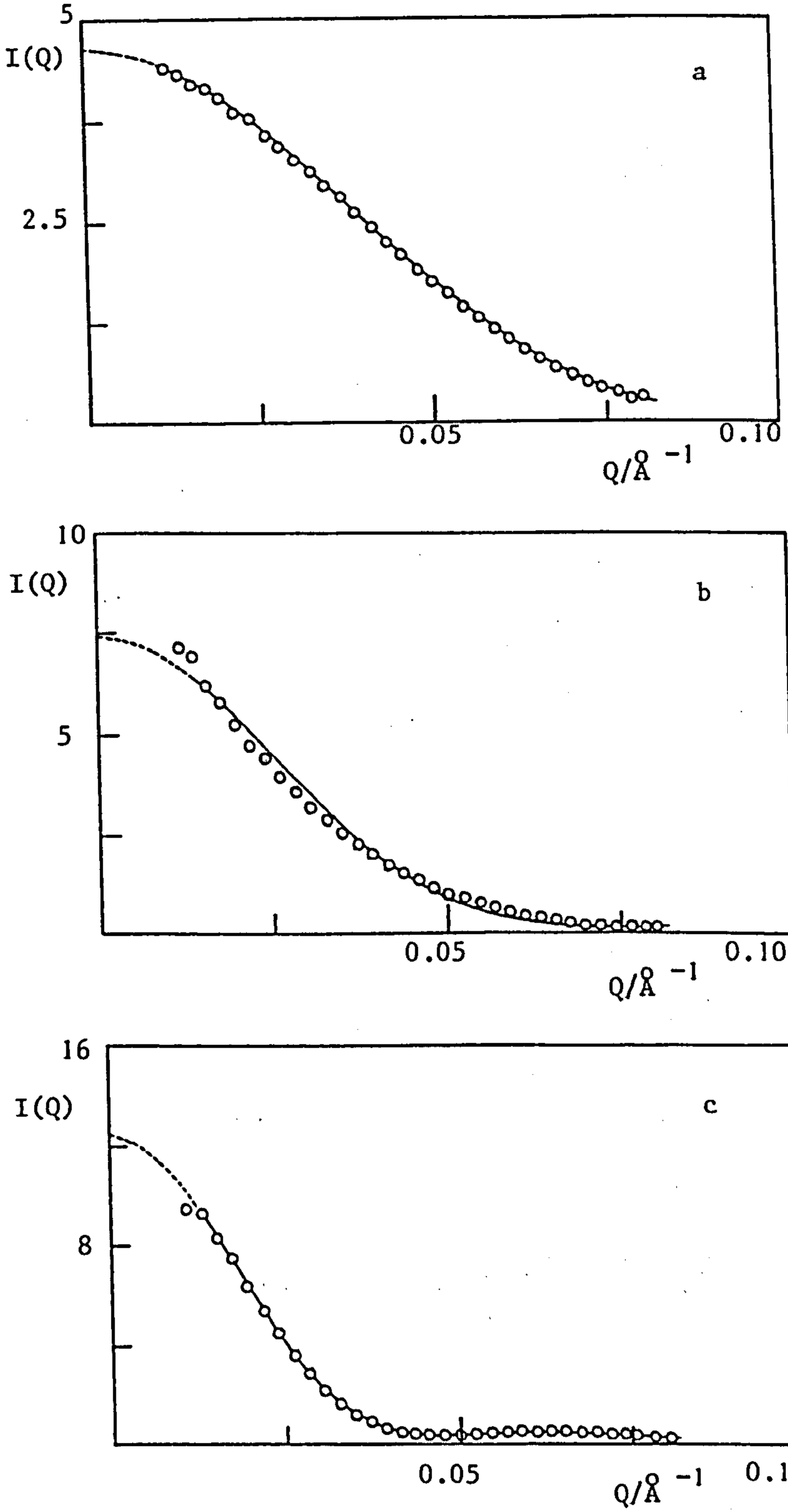

FIGURE 5.3 I(Q) against Q for the three series of particles, 1% w/w $CaCO_3$ in 90% d_8 - toluene

a) 1 V/90 TOL

b) 1 F/90 TOL

c) 1 L/90 TOL

examined in dispersion media containing 0%, 10%, 60%, 80% and 90% d_{26} - dodecane. The experimental scattering curves for the samples dispersed in dodecane were similar to those presented in Figure 5.3. All the results obtained were plotted in the form of (ln I(Q)) against Q^2, following equation (5.25). As can be seen from Figure 5.4, which shows some results for the V-series, good linear plots were obtained over the Q^2 range from 0 to 5×10^{-3} Å^{-2}. Values of $\bar{R}g^2$, and hence $\bar{R}^2$, were obtained from the slopes of these lines.

Figure 5.5 shows the experimental data obtained for the L-series of calcium carbonate dispersions in 60%, 70%, 80% and 90% d_8 - toluene; whereas Figure 5.6 shows the results for the F-series dispersed in 60%, 70%, 80% and 90% d_8 - toluene. Similar linear plots were obtained for the series dispersed in mixtures of h_{26} - dodecane and d_{26} - dodecane. The results obtained in h_8 - toluene for all three samples are shown in Figure 5.7. It can be seen that not only does the slope of the line decrease with overall particle size, but also as was predicted in the last section, the result for the V-sample shows that under some conditions negative values of $\bar{R}g^2$ can be obtained. The values of $\bar{R}g^2$ and $\bar{R}^2$ obtained for the three series in the various dispersion media examined are tabulated in Tables 5.3, 5.4 and 5.5.

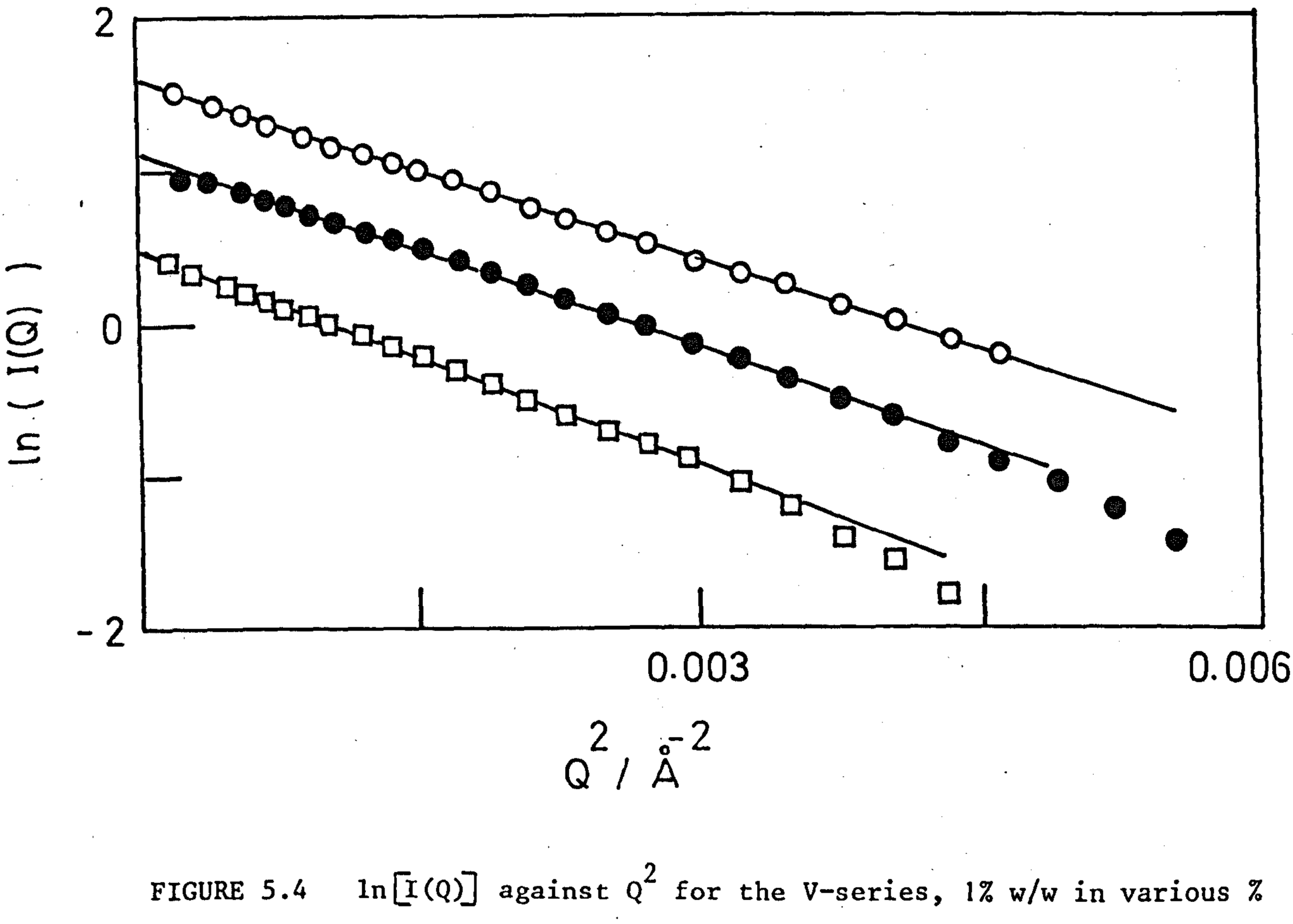

FIGURE 5.4 $\ln[I(Q)]$ against Q^2 for the V-series, 1% w/w in various % d_8 - toluene mixtures:

—○— , 90%; —●— , 80%; —□— , 60%.

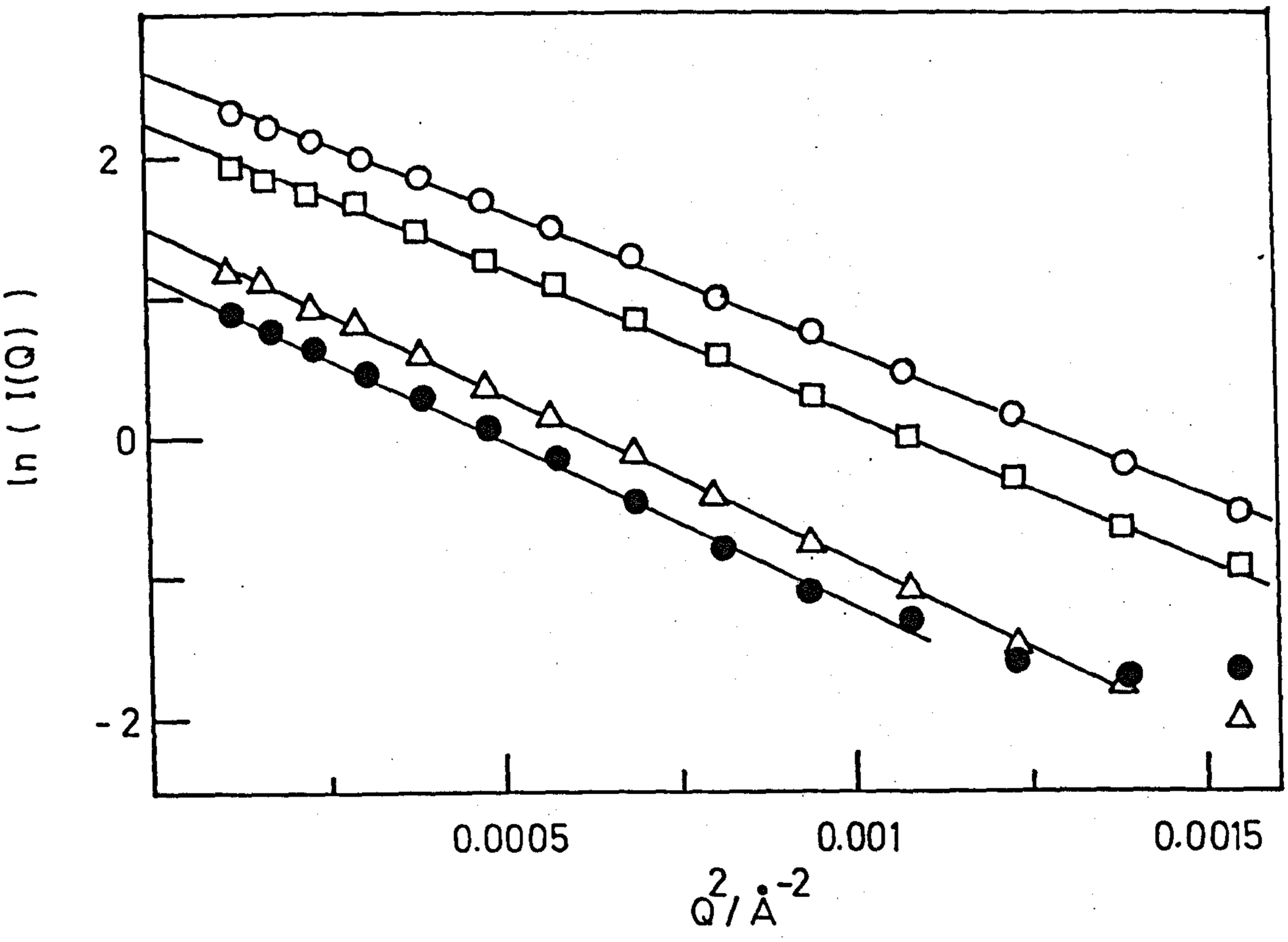

FIGURE 5.5 $\ln[I(Q)]$ against Q^2 for the L-series, 1% w/w in various % d_8 - toluene mixtures:

—○—, 90%; —□—, 80%, —△—, 70%; —●—, 60%.

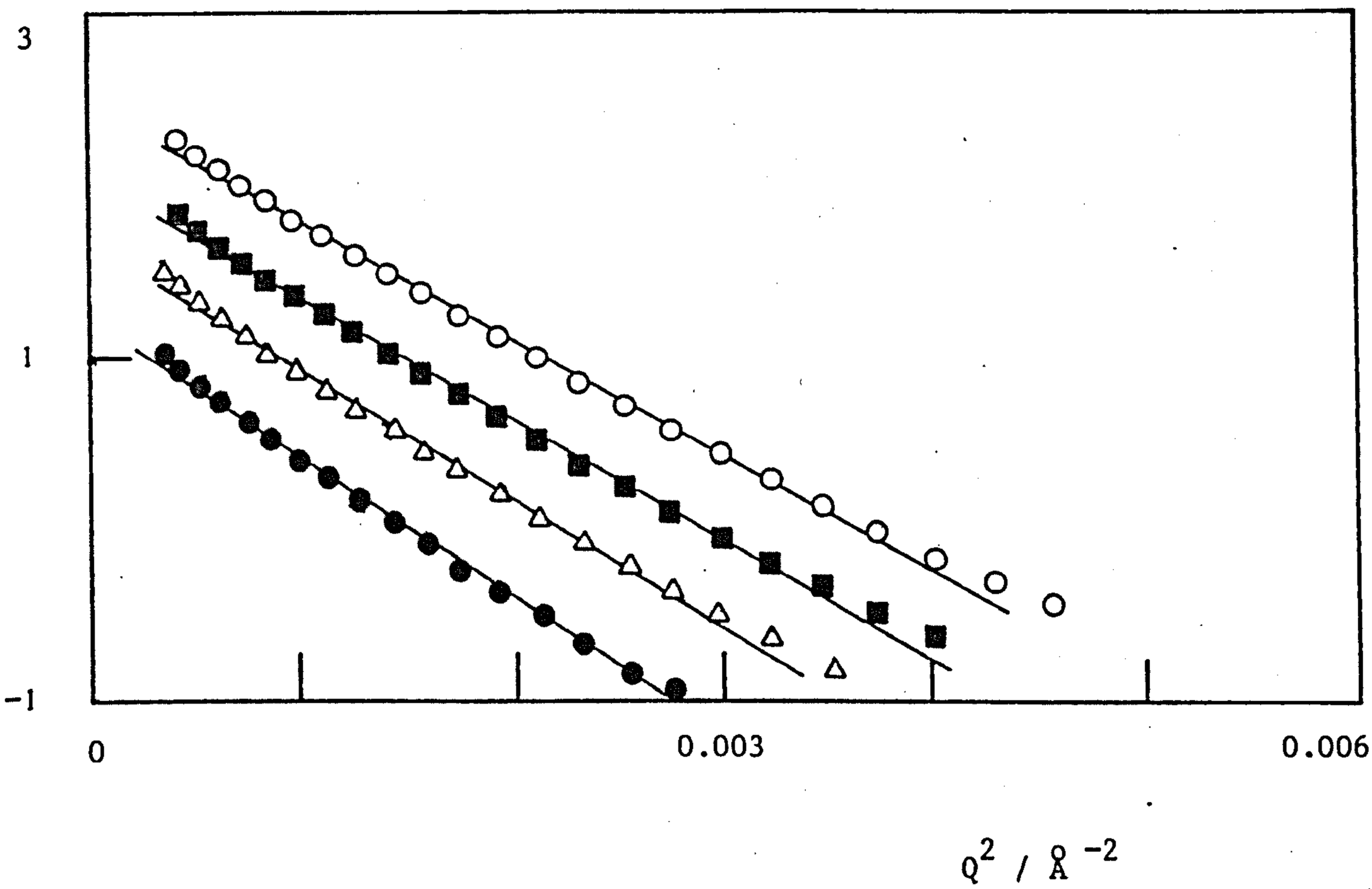

FIGURE 5.6 ln [I(Q)] against Q^2 for the F-series, 2% w/w in various % d_8 - toluene:

—○—, 90%; —■— , 80%; —△— , 70%; —●— 60%

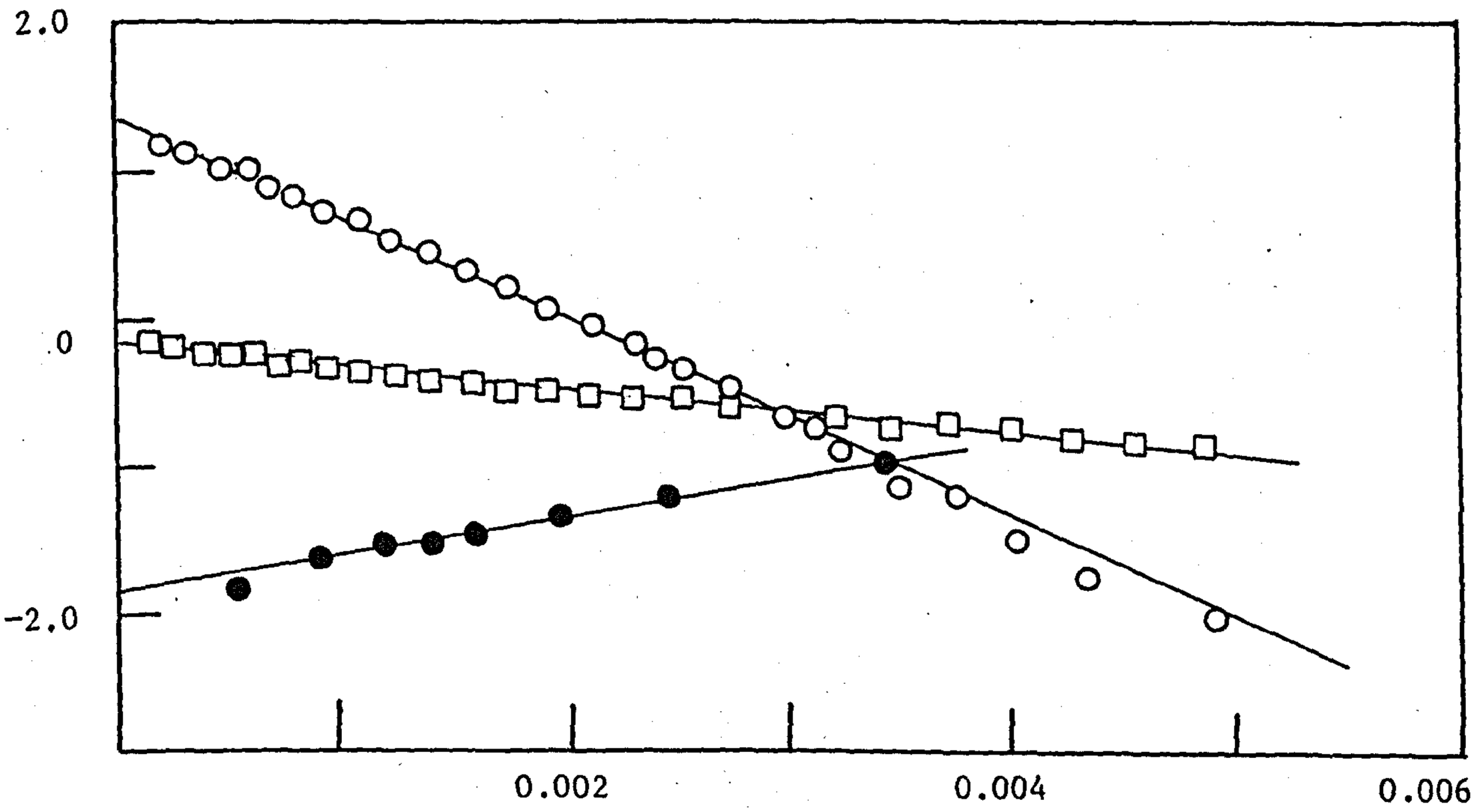

FIGURE 5.7 ln [I(Q)] against Q^2 for particles in h_8 - toluene:

—○—, L-series; —□—, F-series; —●—, V-series

TABLE 5.3 Results for V-series (1% w/w)

Dispersion Medium	$\bar{R}g^2/Å^2$	$\bar{R}^2/Å^2$	$\rho/10^{10}cm^{-2}$
60% d_8 - toluene	1436	2393	- 2.25
70% d_8 - toluene	1310	2183	- 2.74
80% d_8 - toluene	1253	2088	- 3.23
90% d_8 - toluene	1197	1995	- 3.73
h_8 - toluene	- 750	- 1250	0.51

TABLE 5.4 Results for L-series (1% w/w)

Dispersion Medium	$\bar{R}g^2/Å^2$	$\bar{R}^2/Å^2$	$\rho/10^{10}cm^{-2}$
60% d_8 - toluene	7788	12980	- 1.19
70% d_8 - toluene	7049	11748	- 1.67
80% d_8 - toluene	6164	10273	- 2.16
90% d_8 - toluene	6032	10053	- 2.66
h_8 - toluene	2039	3398	1.52

TABLE 5.5 Results for F-series (2% w/w)

Dispersion Medium	$\bar{R}g^2/Å^2$	$\bar{R}^2/Å^2$	$\rho/10^{10}cm^{-2}$
60% d_8 - toluene	2450	4083	- 1.23
70% d_8 - toluene	2200	3667	- 2.22
80% d_8 - toluene	2079	3466	- 2.70
90% d_8 - toluene	2016	3360	- 3.13
h_8 - toluene	484	807	0.87

The values of I(0) were estimated from curve fitting of the I(Q) against Q results and from the Guinier plots of ln I(Q) against Q^2. The values were usually in good agreement. From these data curves were constructed of $[I(0)]^{\frac{1}{2}}$ against ρ_m and these are shown for the V-series and the L-series in toluene at 1% w/w concentration of calcium carbonate in Figure 5.8. The results for the F-series in toluene at both 1% w/w and 2% w/w concentration are given in Figure 5.9. From these two figures the values of ρ_m for I(0) = 0 were obtained, and they are as follows:-

V-series $\quad \bar{\rho} = 1.45 \times 10^{10}$ cm^{-2}

L-series $\quad \bar{\rho} = 2.45 \times 10^{10}$ cm^{-2}

F-series $\quad \bar{\rho} = 1.70 \times 10^{10}$ cm^{-2}

Similarly to the F-series, the values of $\bar{\rho}$ obtained for the V- and the L-series at 2% w/w concentration were identical to those quoted above for 1% w/w concentration of calcium carbonate. From the curves in Figure 5.8 it can immediately be seen, using the arguments of the previous section, that the particles of the L-series were larger than the V-series and that the latter, via equation (5.9) had a greater volume of material per particle in the adsorbed layer. Moreover, a comparison with Figure 5.9 shows that the particles of the F-series were intermediate between those of the L-series and the V-series.

Similar curves of $[I(0)]^{\frac{1}{2}}$ against ρ_m were obtained for the three series using h_{26} - dodecane and mixtures of hydrogenated and deuterated dodecane as the dispersion medium. Each series was examined at only one concentration and the values obtained for the "match-point", i.e. $\bar{\rho}$, are given below:-

V-series (2% w/w) $\quad \bar{\rho} = 1.30 \times 10^{10}$ cm^{-2}

L-series (1% w/w) $\quad \bar{\rho} = 2.25 \times 10^{10}$ cm^{-2}

F-series (1% w/w) $\quad \bar{\rho} = 1.65 \times 10^{10}$ cm^{-2}

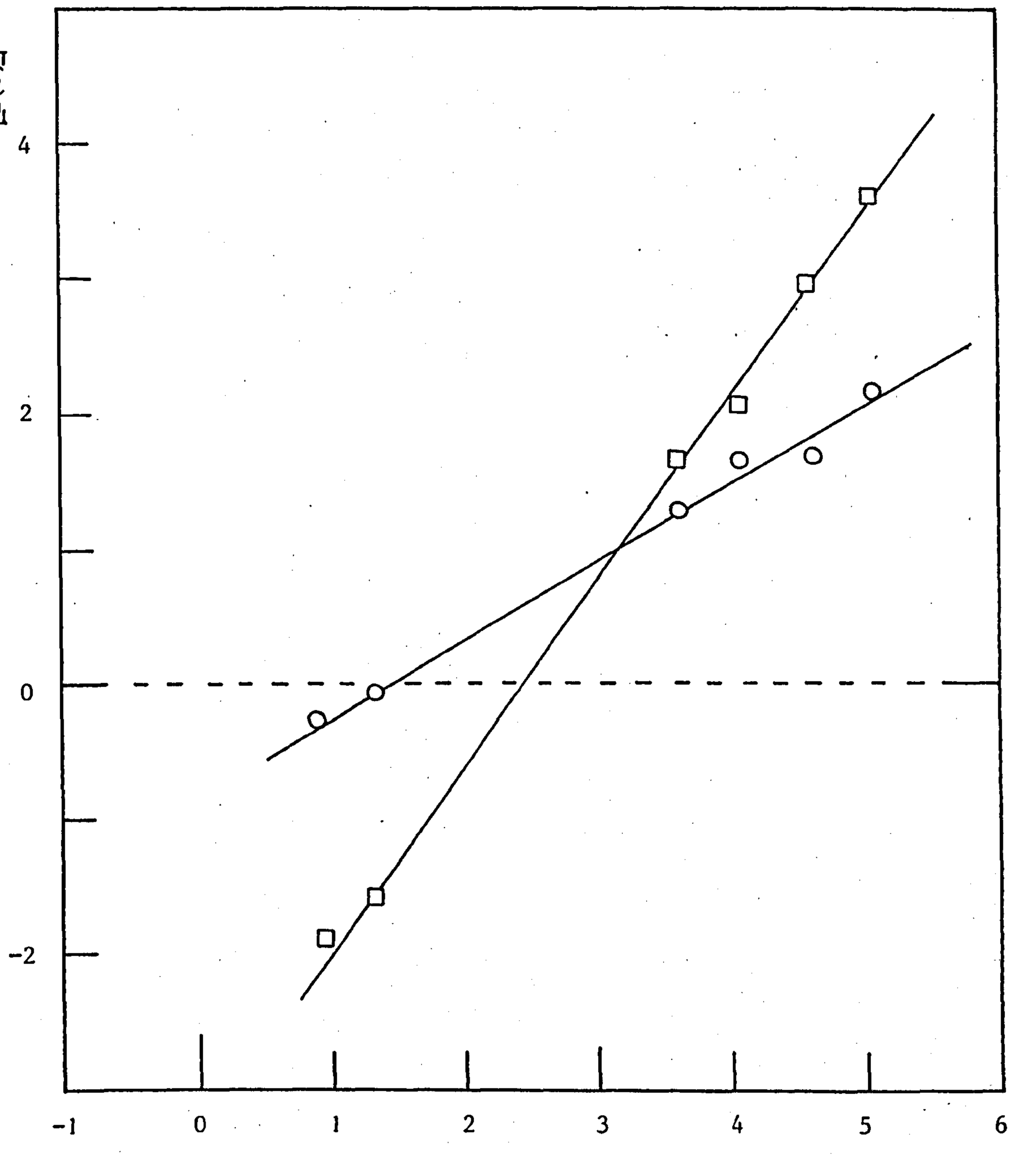

FIGURE 5.8 $[I(0)]^{\frac{1}{2}}$ against ρ_m for 1% w/w dispersions of particles:

—○— , V-series; —□— , L-series

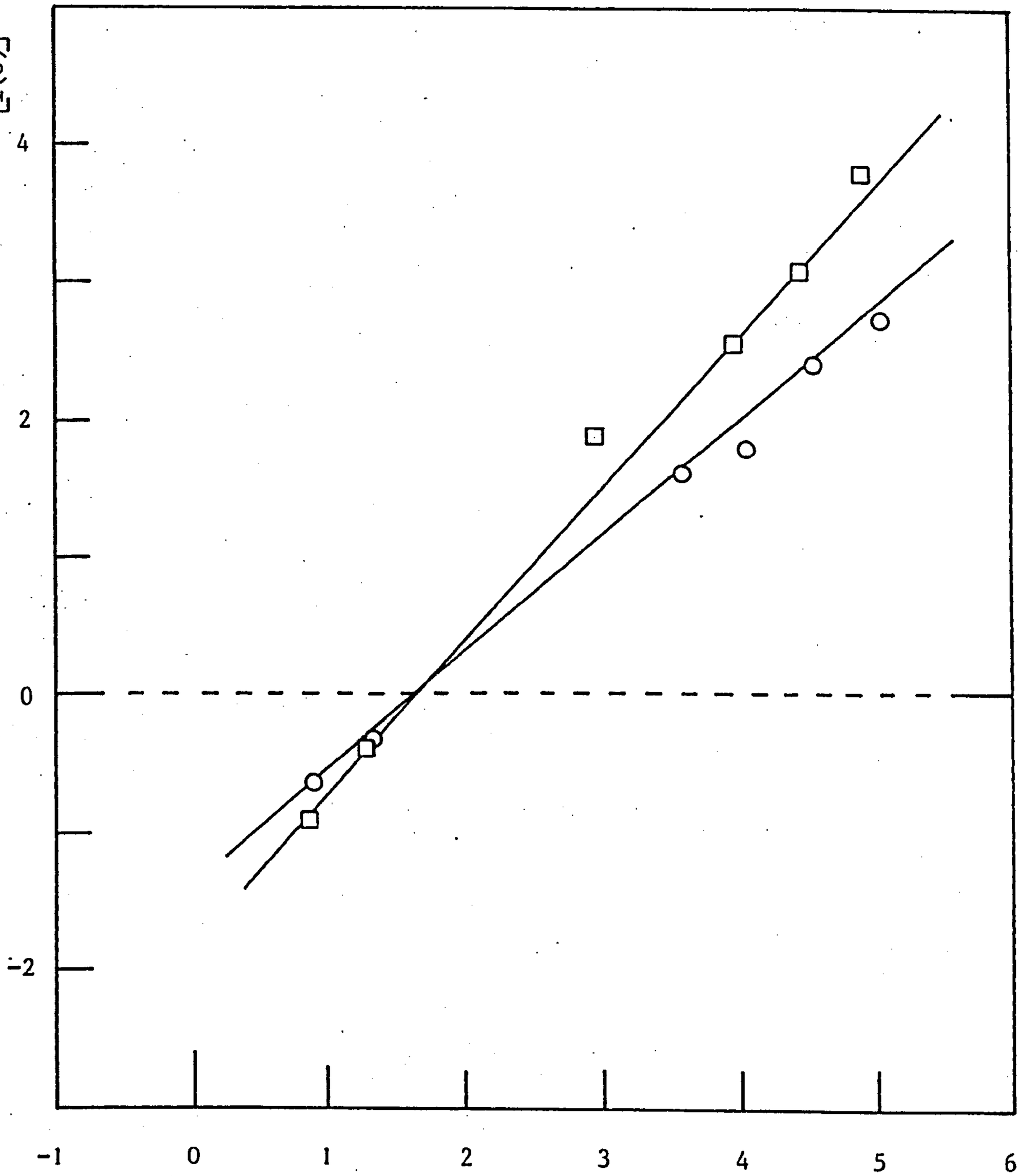

FIGURE 5.9 $[I(0)]^{\frac{1}{2}}$ against ρ_m for the F-series of particles:

—○— , 1% w/w; —□— , 2% w/w

It can be seen that the values of $\bar{\rho}$ obtained for the three series in dodecane are consistently lower than those obtained for the samples in toluene. This appears to signify from equation (5.9) that the volume of the adsorbed layer had increased, provided that the volume of the core of the particles remained constant in the two dispersion media.

Once the values of ρ had been obtained for the three materials, giving $\rho = \bar{\rho} - \rho_m$, then plots of $\bar{R}g^2$ against $1/\rho$ were constructed. These are given in Figure 5.10 for the V-series and the L-series in toluene each at a concentration of 1% w/w, and in Figure 5.11 for the F-series in toluene at a concentration of 2% w/w of calcium carbonate. The Guinier plots for the F-series at a concentration of 1% w/w were slightly curved and it was therefore difficult to obtain accurate values for $\bar{R}g^2$. However, as anticipated from the theory, equation (5.24), good linear plots were obtained for all the other samples in toluene. These confirm that the predictions shown in Figure 5.2 are in good accord with experiment. Figure 5.12 shows the results obtained for the V-series at a concentration of 2% w/w of calcium carbonate, and for the L-series and the F-series each at a concentration of 1% w/w when dodecane was used as the dispersion medium. It can be seen that these plots were not as accurate as those obtained for the samples in toluene and this is represented by using bigger symbols for the experimental points than those in Figure 5.10. The values of $\bar{R}g^2$ obtained for the three series in dodecane are given in Tables 5.6, 5.7 and 5.8.

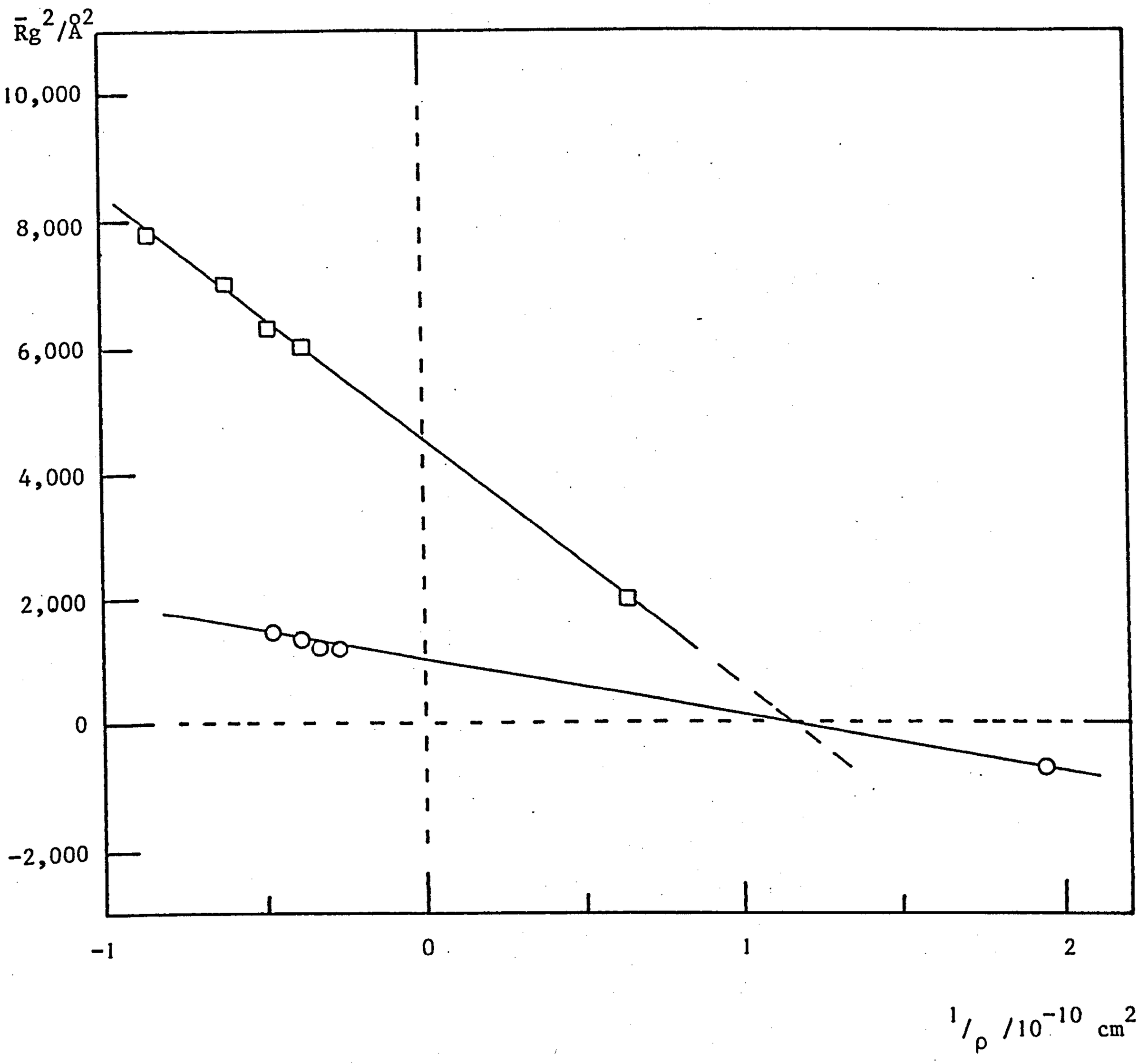

FIGURE 5.10 $\bar{R}g^2$ against $^1/_\rho$ for 1% w/w dispersions of particles:

—○— , V-series; —□— , L-series

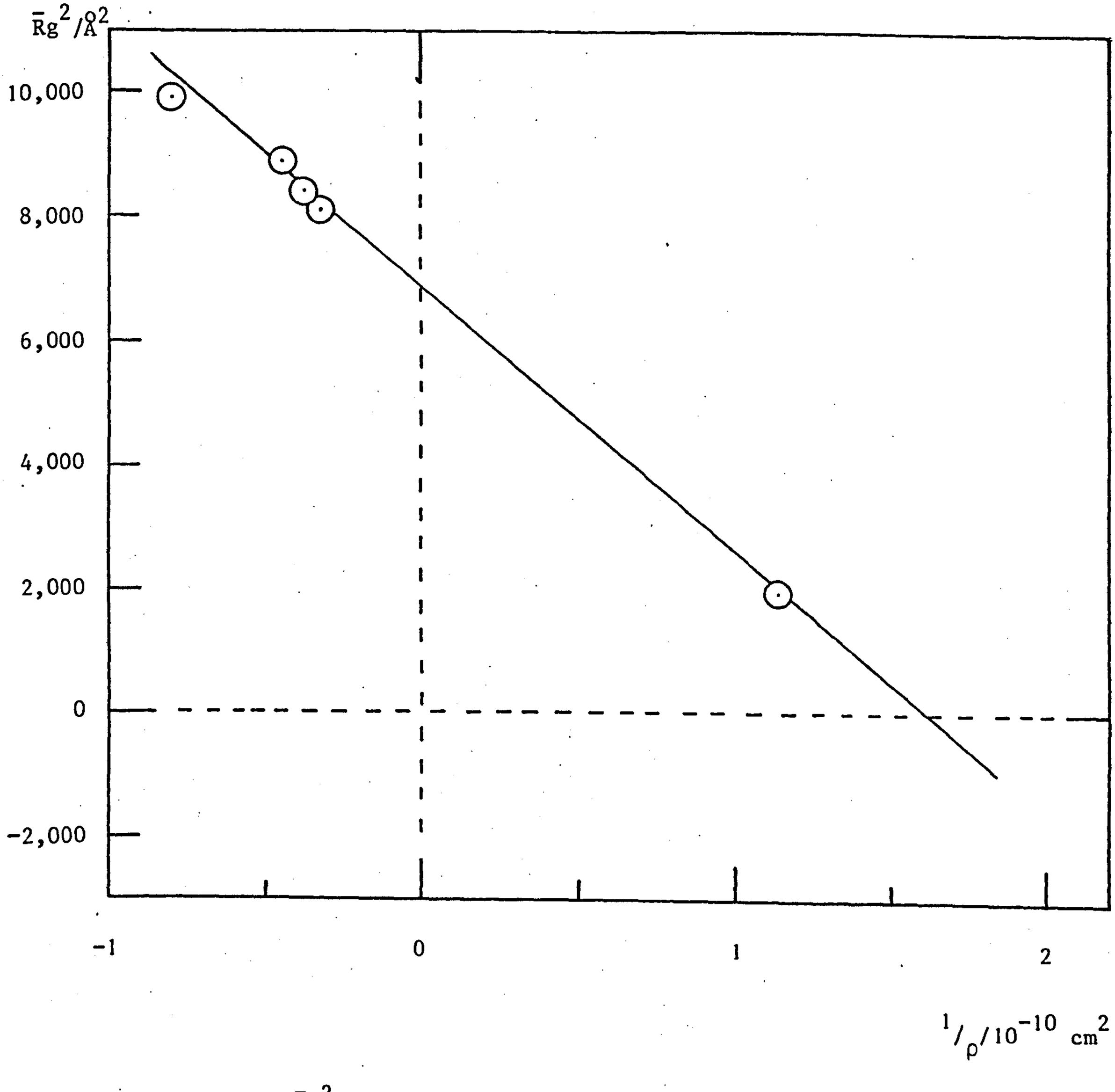

FIGURE 5.11 $\bar{R}g^2$ against $^1/_\rho$ for the F-series at a concentration of 2% w/w of $CaCO_3$

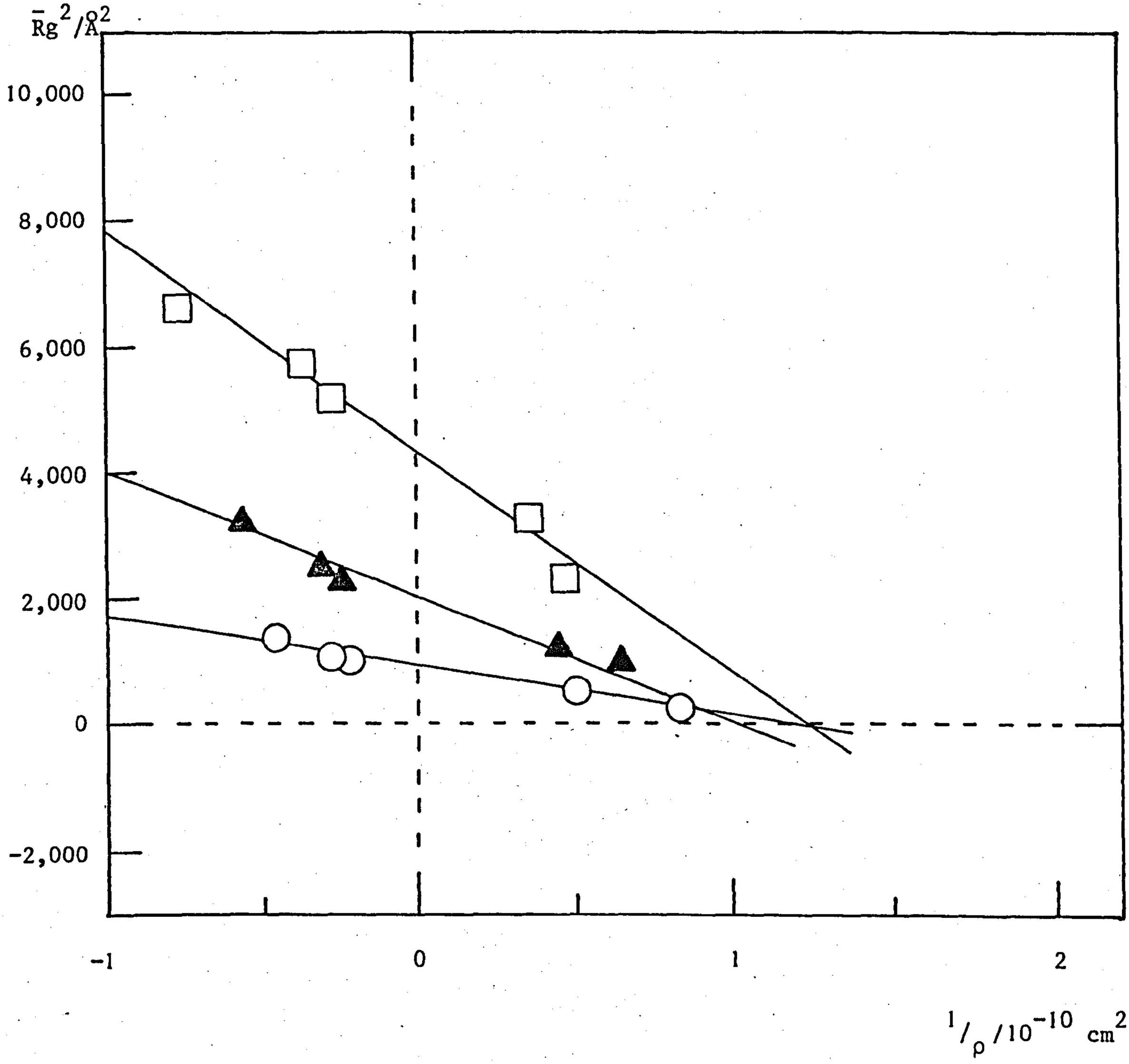

FIGURE 5.12 $\bar{R}g^2$ against $^1/_\rho$ for particles in dodecane:

—○— , V-series, 2% w/w; —▲— , F-series, 1% w/w;

—□— , L-series, 2% w/w.

TABLE 5.6 Results for the V-series (2% w/w)

Dispersion Medium	$\bar{R}g^2/Å^2$	$\bar{R}^2/Å^2$	$\rho/10^{10}cm^{-2}$
60% d_{26} - dodecane	1370	2283	- 2.22
80% d_{26} - dodecane	1070	1783	- 3.70
90% d_{26} - dodecane	1017	1695	- 4.55
h_{26} - dodecane	515	858	1.82
10% d_{26} - dodecane	253	422	1.19

TABLE 5.7 Results for L-series (1% w/w)

Dispersion Medium	$\bar{R}g^2/Å^2$	$\bar{R}^2/Å^2$	$\rho/10^{10}cm^{-2}$
60% d_{26} - dodecane	6500	10833	- 1.32
80% d_{26} - dodecane	5620	9367	- 2.78
90% d_{26} - dodecane	5082	8470	- 3.70
h_{26} - dodecane	3200	5333	2.70
10% d_{26} - dodecane	2270	3783	2.08

TABLE 5.8 Results for the F-series (1% w/w)

Dispersion Medium	$\bar{R}g^2/Å^2$	$\bar{R}^2/Å^2$	$\rho/10^{10}cm^{-2}$
60% d_{26} - dodecane	3106	5177	- 1.79
80% d_{26} - dodecane	2460	4100	- 3.33
90% d_{26} - dodecane	2180	3633	- 4.08
h_{26} - dodecane	1180	1967	2.17
10% d_{26} - dodecane	950	1583	1.54

5.1.3 Discussion

The method described in the theoretical section depends upon the use of the Guinier approximation and the determination of the square of the mean radius of gyration $\bar{R}g^2$, or $\bar{R}^2$, for the particles in dispersion media of varying D-content. Application of the method in this way avoids the need for absolute intensity data provided that all data are brought to the same basis by the use of water as a standard material. Thus, the values of I(0) either obtained from the Guinier plots or from curve fitting can be used for equation (5.16), see Figures 5.8 and 5.9, in order to obtain values of ρ_o and hence $\bar{\rho}$. This procedure gave the plots of $\bar{R}g^2$ against $1/\rho$ shown in Figures 5.10, 5.11 and 5.12 and, when toluene was the dispersion medium, confirmed the expectation of the theory (equation (5.24)) that good linear plots should be obtained. It also confirmed that under some conditions negative values of $\bar{R}g^2$ can be obtained, in this case for the V-particles in h_8 - toluene (see Section 5.2).

From the data in these plots, using equations (5.26), (5.27) and (5.28), values of R_2 and R_1 were obtained for the three series of particles. The results are given in Tables 5.9 and 5.10.

TABLE 5.9 Summary of Particle Size Values Dispersion Medium - Toluene

	R_2/Å	R_1/Å	$(R_2 - R_1)$/Å
V-series	40	22	18
L-series	86	67	19
F-series	53	37	16

TABLE 5.10 Summary of Particle Size Values Dispersion Medium - Dodecane

	R_2/Å	R_1/Å	$(R_2 - R_1)$/Å
V-series	39	20	19
L-series	83	63	20
F-series	56	33	23

The results for the three series in toluene show clearly that the calcium carbonate core particles of the V-series were substantially smaller than those of the L-series, whereas the average value obtained for the very polydisperse F-series was intermediate between the two. However, the dimensions of the adsorbed layer, as represented by $(R_2 - R_1)$, are the same within experimental error (± 2.0%) for the V-series and the L-series. The slightly lower value obtained for the thickness of the adsorbed layer of the F-particles was not surprising since this system was prepared with a much smaller amount of surface active agent than was used for the other two series (see later). The effects of the particle size values are reflected in the contrast match points. For the V-particles in toluene, $\bar{\rho} = 1.45 \times 10^{10}$ cm^{-2}, V_A is ca. 5.2 times V_p and hence, as expected from equation (5.11), the match point is closer to the value of ρ_A than it is for the L-series with $V_A = 1.13\ V_p$ and a higher volume of calcium carbonate. Once again, the match point for the F-series is, as expected, intermediate between the other two values.

The alkyl aryl sulphonic acid used in this work was a mixture of materials with the aryl component substituted along the alkyl chain. From computer simulated molecular models[40], represented in Figure 5.13, the

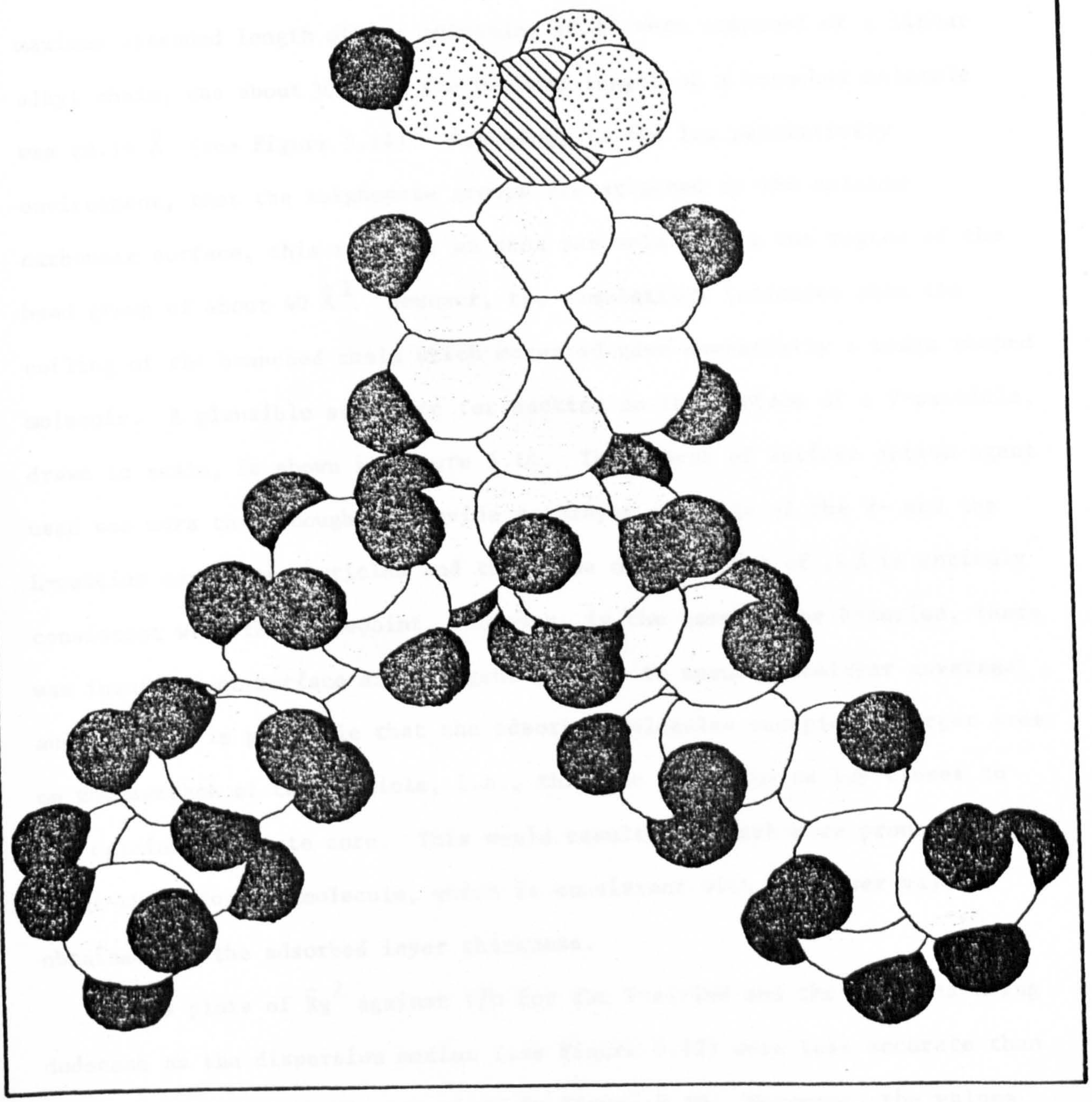

FIGURE 5.13 Computer simulated molecular model of alkyl aryl sulphonic acid

○ , C-atom; ● , H-atom; ▨ , S-atom, ⊙ , O-atom

maximum extended length of the molecule, if it were composed of a linear alkyl chain, was about 30 Å and the minimum length of a branched molecule was ca.16 Å (see Figure 5.14). Assuming, in the low permittivity environment, that the sulphonate groups are attached to the calcium carbonate surface, this suggests an area per molecule in the region of the head group of about 40 $Å^2$. However, the simulations indicated that the coiling of the branched chain which occurred gave essentially a wedge shaped molecule. A plausible structure for packing on the surface of a V-particle, drawn to scale, is shown in Figure 5.14. The amount of surface active agent used was more than enough to provide monolayer coverage of the V- and the L-calcium carbonate particles and the value of $(R_2 - R_1)$ of 19 Å is entirely consistent with this viewpoint. However, in the case of the F-series, there was insufficient surface active agent present to ensure monolayer coverage and hence it is plausible that the adsorbed molecules occupied a larger area on the surface of the particle, i.e., that the alkyl chains lay closer to the calcium carbonate core. This would result in a much more pronounced wedge shape for the molecule, which is consistent with the lower value obtained for the adsorbed layer thickness.

The plots of $\bar{R}g^2$ against $1/\rho$ for the V-series and the L-series using dodecane as the dispersion medium (see Figure 5.12) were less accurate than those obtained using toluene, given in Figure 5.10. Moreover, the values obtained from these plots of R_2 for the V-series and the L-series were 2.5% and 3.5% respectively lower than those quoted in Table 5.8. However, if for each series the value of R_2 is assumed to be the average between the values given in Tables 5.8 and 5.9, then the experimental errors amount to ± 1.3% for the V-series and ± 1.8% for the L-series. The greatest source of error in this type of procedure is the determination of R_2 from a plot of $\bar{R}g^2$ against $1/\rho$. The value of the radius of the core particle, R_1,

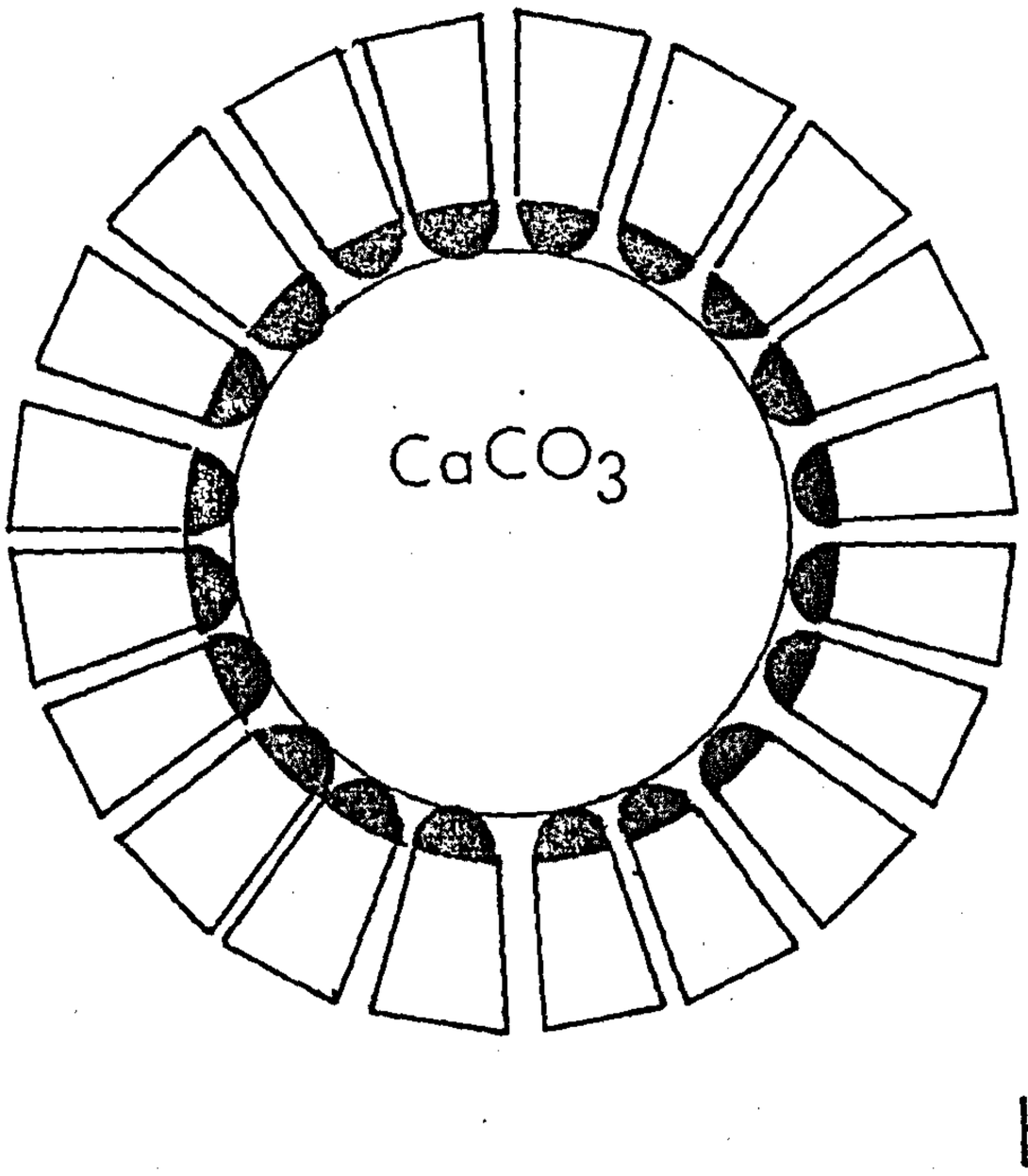

FIGURE 5.14 Schematic illustration of a V-particle, drawn to scale, showing packing of surface active agent molecules on the surface

(and hence the value of $(R_2 - R_1)$), is calculated from equation (5.28), and is consequently dependent upon the accuracy of the value obtained for R_2. Thus, the values of R_1 for the V-series and the L-series in dodecane were also lower than those given in Table 5.8. Errors in the determination of the match point for the particles, $\bar{\rho}$, will affect the values calculated for $1/\rho$; this was considered to be the cause of the discrepancy in the values obtained in toluene and in dodecane for the F-series. However, as mentioned in the theoretical section, these can be checked by multiplying the slope of $\bar{R}g^2$ against $1/\rho$ by ρ_o, which should yield the same value for $\bar{R}g^2$ as obtained from the intercept at $1/\rho = 0$. This was carried out for all the plots and the values of $\bar{R}g^2$ obtained from both procedures were found to be consistent. Generally, the results tend to indicate that the dimensional errors involved in the procedures suggested are small and that the method provides immediate access to information on non-aqueous dispersions which is otherwise difficult, or almost impossible, to obtain.

In the concentric sphere model adopted for the theory, we have assumed that the adsorbed layer was homogeneous and had a constant dimension. In order to utilise equations (5.27) and (5.28), we have also assumed that the value for ρ_A was that of the surface active agent. Consequently, no allowance was made for penetration of the dispersion medium into the adsorbed layer. However, for a surface active agent monolayer of the type shown in Figure 5.14, applicable to both the V-series and the L-series, these assumptions appear to be a good first order approximation. Although the values obtained for the match points of the particles dispersed in dodecane appeared to signify a larger adsorbed layer volume than that for the systems in toluene, the concordance obtained for the $(R_2 - R_1)$ values in Tables 5.8 and 5.9 did not support this.

A basic quantity, which would be useful to obtain, is the product

$\rho_A V_A$, but this is not easily accessible unless the core particle is independently measured, as was the case for aqueous dispersions of polystyrene latex examined by Harris[35].

In terms of obtaining a quick estimate of the overall size of the particle, R_2, it becomes clear from equations (5.24) and (5.26) that if a single measurement is to be made it should be under conditions as close as possible to $1/\rho = 0$. For the present system, a close approach to this condition was obtained by carrying out measurements in a fully deuterated solvent - a situation which also gave good intensity for the measurements. An estimated value of R_2 for the dispersions in d_8 - toluene gave values of R_2 as 45 Å for the V-series and 98 Å for the L-series. This would amount to errors of 11% and 13% respectively, which could be acceptable if a rapid determination were required.

5.2 The Curve Fitting Approach

In the preceding section the use of the Guinier approximation has been outlined for the characterization of the dimensions of a concentric sphere. It was also noted in the discussion that the determination of the radius of the core particle, R_1, as well as the thickness of the adsorbed layer, were both dependent upon the value obtained for the radius of the whole particle, R_2. This section describes an approach by which values for R_1 and $(R_2 - R_1)$ can be obtained independently, thus leading to a value for R_2. This method is based upon the determination of the experimental particle form factor, P(Q), which is then "fitted" to a theoretical form factor for a concentric sphere. In addition, the sensitivity of the form factor for concentric spheres to the scattering length density of the dispersion medium is demonstrated, and the conditions under which negative values can be obtained for the radius of gyration of the whole particle are described.

The curve fitting approach was adopted for the dispersions of the three series described in Section 5.1, as well as for some additional samples, which differed from the previous ones only in the composition of the dispersion medium. These additional dispersions were also measured at the I.L.L., Grenoble – the samples for which the dispersion medium was 6.4%, 11% and 72% deuterated dodecane and a V-sample at a concentration of 2% w/w of calcium carbonate dispersed in h_8 - toluene, were measured on the D17 diffractometer using a neutron beam wavelength of 10.0 Å at sample-to-detector distances of 1.41 m and 2.83 m. All the other additional samples were measured on the D11 diffractometer using a neutron beam wavelength of 8.0 Å and three sample-to-detector distances, namely, 2.66 m, 5.66 m and 10.66 m.

5.2.1 Theory

The form factor for a concentric sphere

From the previous section (equation (5.3)), the differential scattering cross-section for a single concentric sphere can be written in the form,

$$\left(\frac{d\sigma}{d\Omega}\right)_{c.s.} = \left[(\rho_A - \rho_m)\left\{3V_T\left(\frac{\sin QR_2 - QR_2 \cos QR_2}{Q^3R_2^3}\right)\right.\right.$$

$$\left.\left. - 3V_p\left(\frac{\sin QR_1 - QR_1 \cos QR_1}{Q^3R_1^3}\right)\right\} + (\rho_p - \rho_m)\, 3V_p \left(\frac{\sin QR_1 - QR_1 \cos QR_1}{Q^3R_1^3}\right)\right]^2 \quad \ldots \quad (5.29)$$

Putting

$$A(QR) = 3\left(\frac{\sin QR - QR \cos QR}{Q^3R^3}\right)$$

$$\equiv f\,(QR) \,/\, R^3 \text{ used in Section 5.1.1 we can write,}$$

$$\left(\frac{d\sigma}{d\Omega}\right)_{c.s.} = \left[(\rho_A - \rho_m)\left\{V_T\, A(QR_2) - V_p\, A(QR_1)\right\} + (\rho_p - \rho_m)\, V_p\, A(QR_1)\right]^2 \quad \ldots \quad (5.30)$$

which can be expressed as,

$$\left(\frac{d\sigma}{d\Omega}\right)_{c.s.} = \left[(\rho_A - \rho_m)^2\, V_T^{\,2}\, A(QR_2)^2\right] + \left[(\rho_p - \rho_A)^2\, V_p^{\,2}\, A(QR_1)^2\right]$$

$$+ \left[2(\rho_A - \rho_m)(\rho_p - \rho_A)\, V_T\, A(QR_2)\, V_p\, A(QR_1)\right] \quad \ldots \quad (5.31)$$

A study of each of the three terms in equation (5.31) reveals a number of very interesting points, viz.,

i) the first term is always positive but it varies in magnitude

with the value of the scattering length density of the medium, ρ_m;

ii) the second term is also positive but is of a constant magnitude for a particular concentric sphere;

iii) the third term can be either positive or negative according to whether constructive or destructive interference occurs either between the scattering from the two regions of the concentric sphere or between the scattering from the adsorbed layer and the medium. In other words, this term is negative when either $\rho_m > \rho_A$ or $\rho_A > \rho_p$. The term can also be negative when any of the three scattering lengths has a negative value and it varies in magnitude with the value of ρ_m. For our systems where $\rho_A < \rho_p$, only the first condition for a negative value applies.

The variation of each of these three terms with the scattering vector, Q, is complicated and it is illustrated in Figure 5.15 for two values of the coherent scattering length density of the medium.

It should be noted from equation (5.31) that,

$$A(QR_2)^2 = P(QR_2)$$

and $$A(QR_1)^2 = P(QR_1)$$

i.e., the form factors for spheres of radii R_2 and R_1.

At Q = 0, equation (5.31) becomes,

$$\left\{\frac{d\sigma}{d\Omega}\right\}_{c.s.}(0) = (\rho_A - \rho_m)^2 V_T^2 + (\rho_p - \rho_A)^2 V_p^2 + 2(\rho_A - \rho_m)(\rho_p - \rho_A) V_T V_p \quad \ldots \quad (5.32)$$

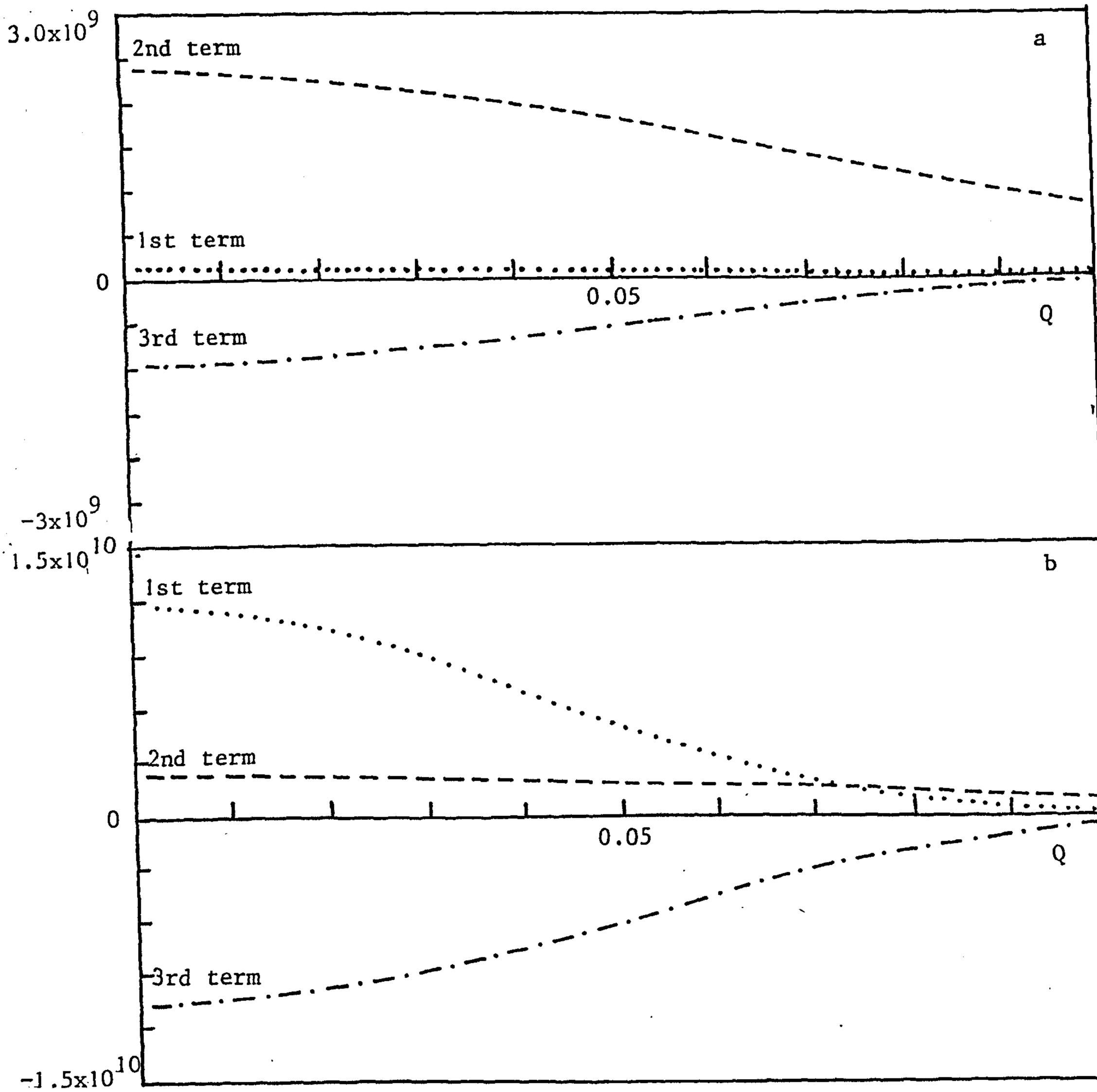

FIGURE 5.15 The variation of the three terms in equation (5.31) with Q calculated for $R_1 = 22$ Å; $(R_2 - R_1) = 18$ Å; $\rho_p = 4.72 \times 10^{10}$ cm^{-2}; $\rho_A = 0.35 \times 10^{10}$ cm^{-2} and

a) $\rho_m = 0.5 \times 10^{10}$ cm^{-2}

b) $\rho_m = 2.0 \times 10^{10}$ cm^{-2}

Hence, the form factor for a concentric sphere is given by,

$$\left[P(Q)\right]_{c.s.} = \frac{(d\sigma/d\Omega)_{c.s.}\ (Q)}{(d\sigma/d\Omega)_{c.s.}\ (0)} \qquad \ldots \quad (5.33)$$

It is immediately clear that the terms in equation (5.32) exhibit the same behaviour as that discussed for the terms in equation (5.31) and thus $\left[P(Q)\right]_{c.s.}$ is expected to be very sensitive to the scattering length density of the dispersion medium (see later).

There are a number of special cases of equation (5.31) which are of importance from the experimental point of view. In neutron scattering, it is possible to vary the coherent scattering length density of the dispersion medium with the use of mixtures of hydrogenated and deuterated solvents to obtain a value which matches, for example, that of either the adsorbed layer or the core particle (see Figure 5.16).

I <u>Matching Medium and Adsorbed Layer</u>

When the coherent scattering length density of the medium is made equal to that of the adsorbed layer, then

$$\rho_m = \rho_A$$

and equation (5.31) reduces to

$$\left(\frac{d\sigma}{d\Omega}\right)_p = (\rho_p - \rho_m)^2\ V_p^{\,2}\ P(QR_1) \qquad \ldots \quad (5.34)$$

the equation for scattering from a single sphere of scattering length density ρ_p and radius R_1.

II <u>Matching Medium and Core</u>

If the coherent scattering length densities of the medium and the core

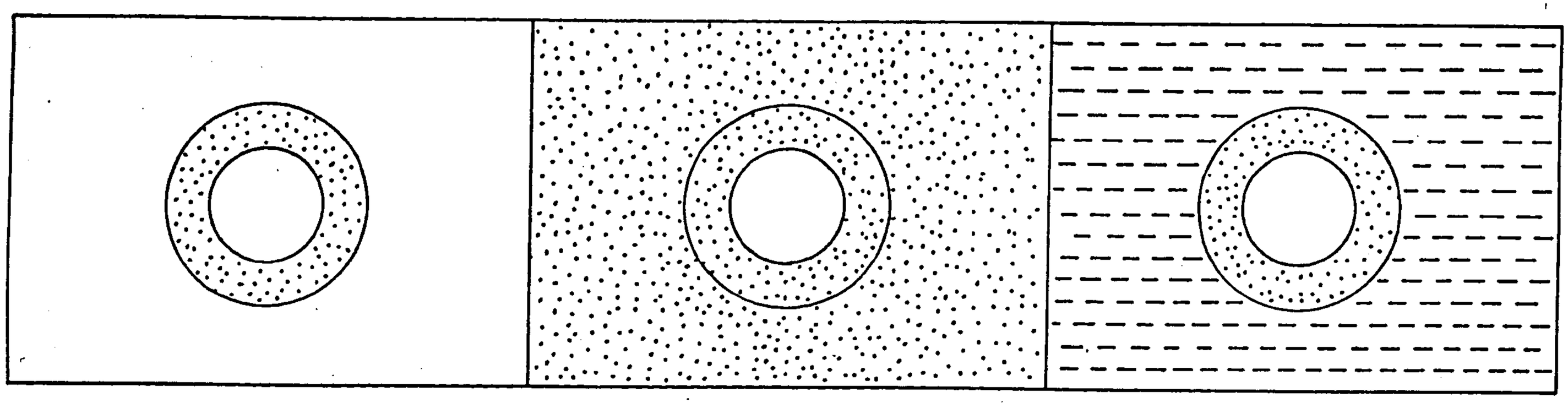

$\rho_m = \rho_p$ $\rho_m = \rho_A$ $\rho_m = 0$

FIGURE 5.16 Schematic representation of the contrast matching technique

particle are matched, i.e.,

$$\rho_m = \rho_p$$

no straightforward simplification of equation (5.31) is possible, except in the Guinier approximation which was discussed in the first part of this chapter and will be repeated in this section later.

III Solvent Scattering is Zero

In neutron scattering, it is possible to use an admixture of certain hydrogenated and deuterated solvents, in the present case h_{26} - dodecane and d_{26} - dodecane, such that $\rho_m = 0$. Equation (5.31) then reduces to,

$$\left(\frac{d\sigma}{d\Omega}\right)_{c.s.} = \left[\rho_A^2 V_T^2 A(QR_2)^2 + (\rho_p - \rho_A)^2 V_p^2 A(QR_1)^2 + 2 \rho_A (\rho_p - \rho_A) V_T A(QR_2) V_p A(QR_1)\right] \quad \ldots \quad (5.35)$$

The radius of gyration for a concentric sphere

If data analysis is restricted to conditions such that $QR_2 << 1.0$, then it is possible to apply the Guinier approximation (see Section 5.1.1) and to introduce a simplification of the equations, since for small values of QR_1 we can write,

$$A(QR_2) = 1 - (Q^2R_2^2/10) \ldots\ldots\ldots$$

$$A(QR_1) = 1 - (Q^2R_1^2/10) \ldots\ldots\ldots$$

and hence equation (5.30) becomes,

$$\left(\frac{d\sigma}{d\Omega}\right)_{c.s.} = \left[(\rho_A - \rho_m)\left\{V_T\left(1 - \frac{Q^2R_2^2}{10}\right) - V_p\left(1 - \frac{Q^2R_1^2}{10}\right)\right\} + (\rho_p - \rho_m) V_p \left(1 - \frac{Q^2R_1^2}{10}\right)\right]^2 \quad \ldots \quad (5.36)$$

It is now immediately clear that for the case $\rho_m = \rho_p$, mentioned above, the differential scattering cross-section for small values of QR is given by,

$$\left\{\frac{d\sigma}{d\Omega}\right\}_{c.s.} = \left[(\rho_A - \rho_m)\left\{V_T\left(1 - \frac{Q^2R_2^2}{10}\right) - V_p\left(1 - \frac{Q^2R_1^2}{10}\right)\right\}\right]^2 \quad \ldots \quad (5.37)$$

Multiplying out the terms in equation (5.36), we find,

$$\left\{\frac{d\sigma}{d\Omega}\right\}_{c.s.} = \left[(\rho_A - \rho_m)\, V_T + (\rho_p - \rho_A)\, V_p - \frac{Q^2}{10}\left(R_2^2\, V_T\, (\rho_A - \rho_m) + R_1^2\, V_p\, (\rho_p - \rho_A)\right)\right]^2 \quad \ldots \quad (5.38)$$

and at Q = 0,

$$\left\{\frac{d\sigma}{d\Omega}\right\}_{c.s.}(0) = \left[(\rho_A - \rho_m)\, V_T + (\rho_p - \rho_A)\, V_p\right]^2 \quad \ldots \quad (5.39)$$

giving,

$$\frac{(d\sigma/d\Omega)_{c.s.}}{(d\sigma/d\Omega)_{c.s.}(0)} = 1 - \frac{Q^2}{5}\left\{\frac{(\rho_A - \rho_m)\, R_2^5 - (\rho_p - \rho_A)\, R_1^5}{(\rho_A - \rho_m)\, R_2^3 - (\rho_p - \rho_A)\, R_1^3}\right\} \quad \ldots \quad (5.40)$$

or introducing the radius of gyration,

$$\frac{(d\sigma/d\Omega)_{c.s.}}{(d\sigma/d\Omega)_{c.s.}(0)} = \left[P(Q)\right]_{c.s.} = 1 - \frac{Q^2 Rg^2_{c.s.}}{3} \quad \ldots \quad (5.41)$$

whence the neutron scattering radius of gyration for a concentric sphere, $Rg_{c.s.}$, is given by,

$$Rg^2_{c.s.} = \frac{3}{5}\left\{\frac{(\rho_A - \rho_m)\, R_2^5 - (\rho_p - \rho_A)\, R_1^5}{(\rho_A - \rho_m)\, R_2^3 - (\rho_p - \rho_A)\, R_1^3}\right\} \quad \ldots \quad (5.42)$$

An important point arising from equation (5.42) is that, as mentioned in Section 5.1, under certain conditions the value of $Rg^2_{c.s.}$ can be negative. This will apply just below the condition for contrast match of the coherent scattering length of the medium and the coherent scattering length of the overall particle, $\bar{\rho}$. Figure 5.17 shows a simulated plot of $Rg^2_{c.s.}$ as a function of ρ_m for a typical V-sample and it can be seen that just below the value of $\rho_m = \bar{\rho} = 1.45 \times 10^{10}$ cm^{-2} the values of $Rg^2_{c.s.}$ are negative and then become discontinuous.

Once again, for the condition that $\rho_A = \rho_m$ we find,

$$Rg^2_{c.s.} = \frac{3}{5} R_1^2 \qquad \ldots \quad (5.43)$$

the radius of gyration of the core particle.

It should be noted that for the purpose of the analysis we have assumed a model in which the adsorbed layer is taken to be homogeneous. Hence, the analysis is based on the assumption that no solvent penetration of the layer occurs.

Solvent penetration could be allowed for in the model by writing the coherent scattering length density of the penetrated adsorbed layer as ρ_A' in equation (5.42), where ρ_A' is defined as

$$\rho_A' = (1 - \alpha)\, \rho_A + \alpha\rho_m \qquad \ldots \quad (5.44)$$

and α is the fraction of the layer occupied by the solvent molecules. However, this approach does introduce an additional adjustable parameter, and thus it was not considered further for the present and hence α was assumed to be zero. This is probably a reasonable assumption for a close-packed monolayer of surface active agent but it may lead to a small error in the estimate of the adsorbed layer thickness. In addition, for the surface active agent used in this work, there was a distribution of isomers, and hence there was probably a small error in the estimation of ρ_A.

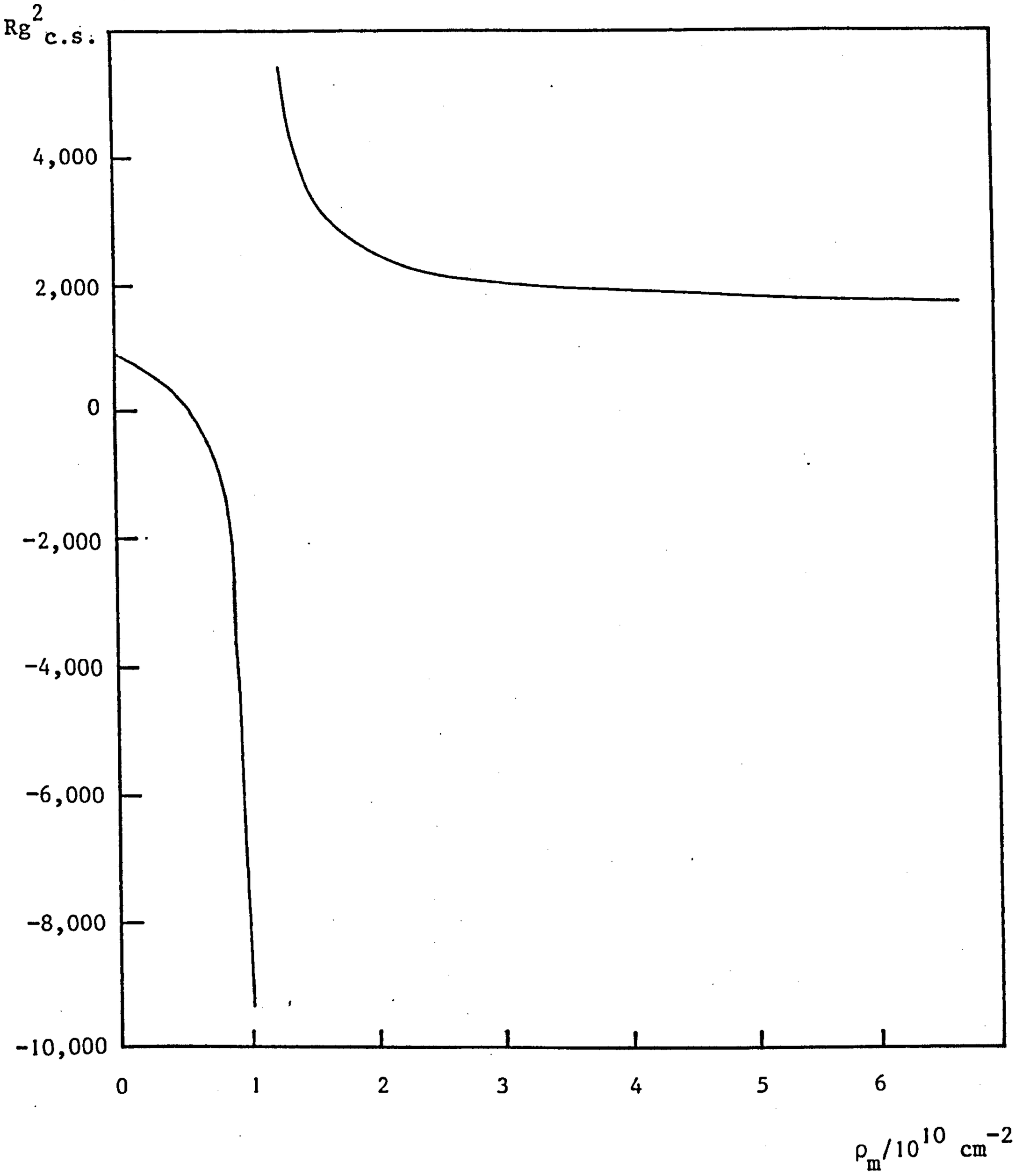

FIGURE 5.17 Calculated curve of $Rg^2_{c.s.}$ against ρ_m for R_1 = 22 Å; $(R_2 - R_1)$ = 18 Å; $\rho_p = 4.72 \times 10^{10}$ cm^{-2}; $\rho_A = 0.35 \times 10^{10}$ cm^{-2}

Polydispersity of the core particles

The equations given so far in this Section have been for a single particle. However, if the dispersion contains N_p identical particles per cm^3, the total scattering per unit solid angle will be given by

$$N_p \left\{ \frac{d\sigma}{d\Omega} \right\}_{c.s.} (Q) = N_p \left[(\rho_A - \rho_m) \left[V_T A(QR_2) - V_p A(QR_1) \right] + (\rho_p - \rho_m) V_p A(QR_1) \right]^2 \quad \ldots \quad (5.45)$$

In practical dispersions it is unlikely that all the particles will be identical, and consequently some allowance must be made for the distribution of particle sizes present in the system. In the present work, it seemed probable that the thickness of the adsorbed layer was essentially constant. It was therefore assumed that the major source of polydispersity in particle size was likely to be in the core particles and that the distribution of particle core radii followed a zeroth order log normal distribution as given by,

$$p(R) = \frac{\exp \left[- (\ln R - \ln R_m)^2 / 2\sigma_o^2 \right]}{(2\pi)^{\frac{1}{2}} \sigma_o R_m \exp (\sigma_o^2 / 2)} \quad \ldots \quad (5.46)$$

where $p(R)$ = the proportion of particles of radius R,

R_m = the mean modal radius of the particles,

σ_o = a parameter describing the width and skewness of the distribution.

The mean value of R, taken as $\bar{R}$, is given by,

$$\ln \bar{R} = \ln R_m + 1.5 \sigma_o^2 \quad \ldots \quad (5.47)$$

and the standard deviation, σ, by

$$\sigma = R_m \left[\exp (4\sigma_o^2) - \exp (3\sigma_o^2) \right]^{\frac{1}{2}} \quad \ldots \quad (5.48)$$

For small values of σ_o the equation for standard deviation takes the simple form,

$$\sigma = R_m \sigma_o$$

For computational purposes in order to obtain a value of R_1 to insert into the scattering equations, it was taken as,

$$R_1 = R = \bar{R} \pm \frac{n\sigma}{2} \quad \ldots \quad (5.49)$$

where n was taken from 1 to 13 in order to determine the distribution.

A typical particle size distribution curve is shown in Figure 5.18. Taking R_m = 28 Å and σ_o = 0.1, we find $\bar{R}$ = 28.4 Å and σ = 2.8 Å.

Simulations of the particle form factor

Using equation (5.31), values of $(d\sigma/d\Omega)_{c.s.}$ as a function of Q were calculated with allowance for polydispersity of the core particle radii. The volume of the core particle, V_p, was calculated using the mean radius $\bar{R}$ (equation (5.47)), and the volume of the whole particle V_T by taking $\bar{R}$ plus a constant value for the thickness of the adsorbed layer. The values of $A(QR_2)$ and $A(QR_1)$ were, however, averaged over the whole particle size distribution range, i.e., they were calculated for each of the 13 values of R and then averaged using equation (5.46). Once again, for the case of $A(QR_2)$, R_2 was obtained by adding the thickness of the adsorbed layer to each value of R taken.

The particle form factor $\left[P(Q)\right]_{c.s.}$ was then calculated using equation (5.33) as a function of Q. Figure 5.19 shows simulated curves of $\left[P(Q)\right]_{c.s.}$ as a function of Q for a typical V-sample of core radius R_1 = 28 Å and total

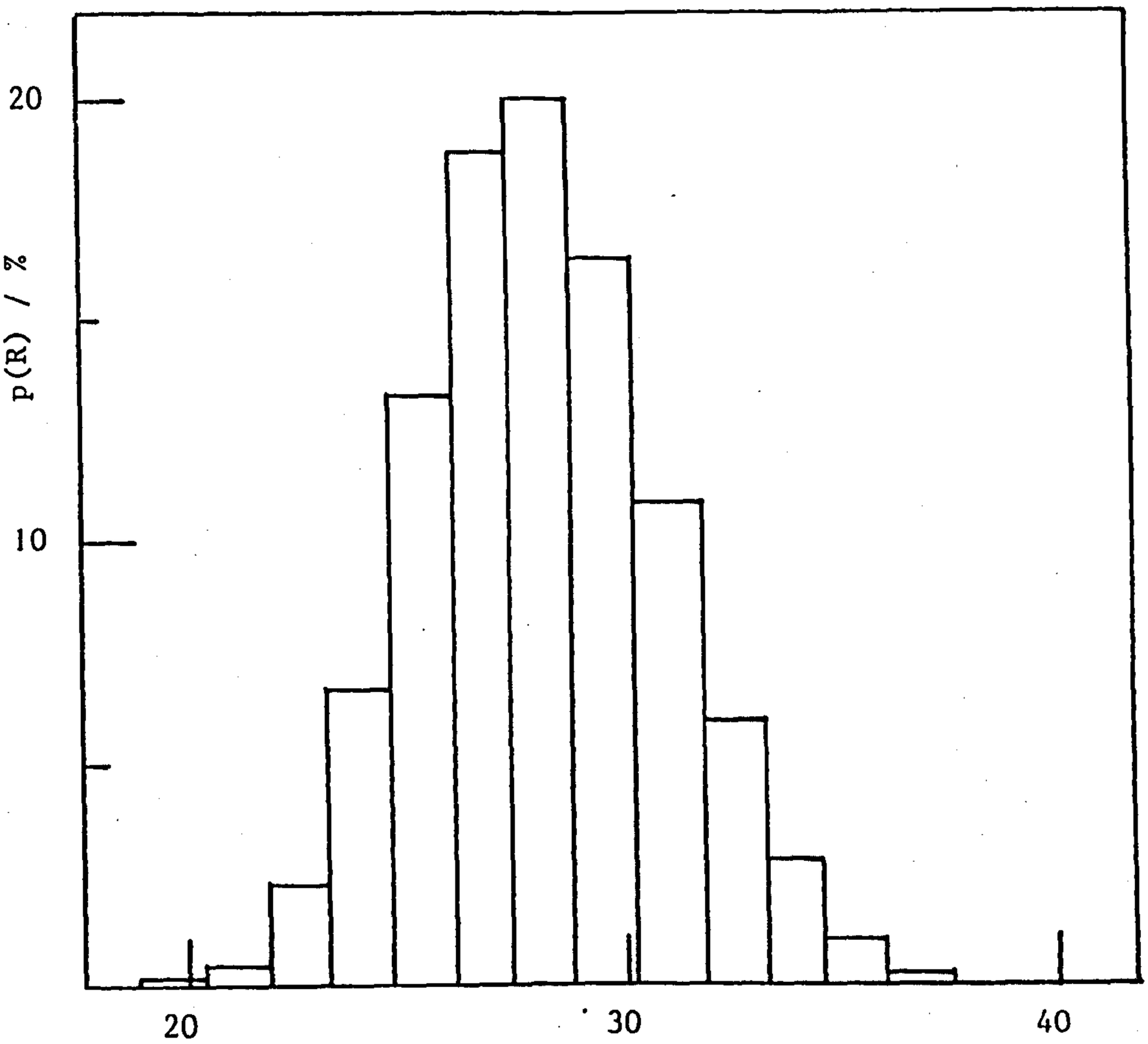

FIGURE 5.18 Zeroth order log normal particle size distribution for R_m = 28 Å and σ_o = 0.1

radius R_2 = 46 Å and σ_o = 0.1. The curves are plotted for various values of the scattering length density of the medium, ρ_m, and it can be seen that as ρ_m approaches the expected value for the contrast match point of the particle, $\bar{\rho} \simeq 1.45 \times 10^{10}$ cm^{-2}, $[P(Q)]_{c.s.}$ exhibits a progressively more pronounced peak above the value of P(Q) = 1. This behaviour results in the predicted negative values for the radius of gyration of the particle just below the contrast match point. Where there is a large difference between the value of the scattering length density of the medium and that of $\bar{\rho}$, as in the cases $\rho_m = 0.5 \times 10^{10}$ cm^{-2} and $\rho_m = 4.72 \times 10^{10}$ cm^{-2}, the curve of $[P(Q)]_{c.s.}$ adopts the shape for an isotropic sphere.

Figure 5.20 shows the simulated $[P(Q)]_{c.s.}$ curves for a typical L-sample taking R_1 = 62 Å, R_2 = 80 Å and σ_o = 0.1. Once again, as the value of ρ_m approaches the expected value for the contrast match point of the particle, i.e. $\bar{\rho} \simeq 2.45 \times 10^{10}$ cm^{-2}, $[P(Q)]_{c.s.}$ increases from 1 to a pronounced first peak followed by a series of peaks of much smaller magnitude which decay with Q. However, when $\rho_m > \bar{\rho}$, as in the case $\rho_m = 2.6 \times 10^{10}$ cm^{-2}, $[P(Q)]_{c.s.}$ decreases to zero at low Q and then exhibits the oscillations described above. A comparison of Figure 5.20 with Figure 5.19 shows that, owing to the larger size of the L-particle, a greater number of oscillations of $[P(Q)]_{c.s.}$ is seen in the same Q-range, and the magnitude of the values of $[P(Q)]_{c.s.}$ is also greater.

However, in the case of both the V-sample and the L-sample, the detection in the scattering curves of the effects described above for $[P(Q)]_{c.s.}$, especially the pronounced peaks near the contrast match point of the particle, will depend upon the magnitude of the absolute intensity of the coherent scattering of the sample and the possibility of making measurements. This is discussed in the next section.

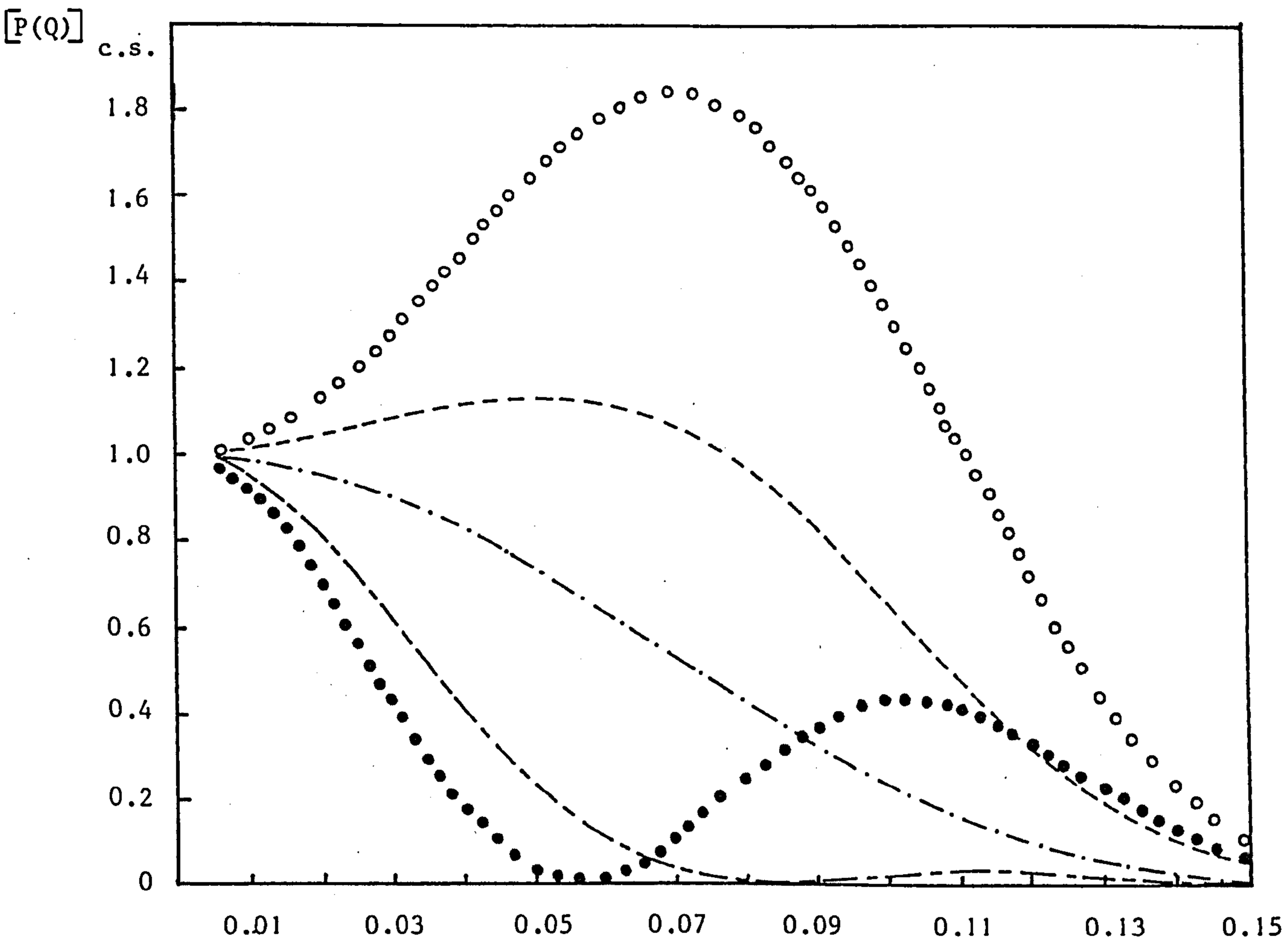

FIGURE 5.19 Calculated curves of $[P(Q)]_{c.s.}$ against Q for R_1 = 28 Å; R_2 = 46 Å; $\rho_p = 4.72 \times 10^{10}$ cm^{-2}; $\rho_A = 0.35 \times 10^{10}$ cm^{-2} and for various values of ρ_m:

·—·—·—·, 0.5×10^{10} cm^{-2}; ————, 0.85×10^{10} cm^{-2};

oooo , 1.0×10^{10} cm^{-2}; ●●●● , 2.0×10^{10} cm^{-2};

————, 4.72×10^{10} cm^{-2}.

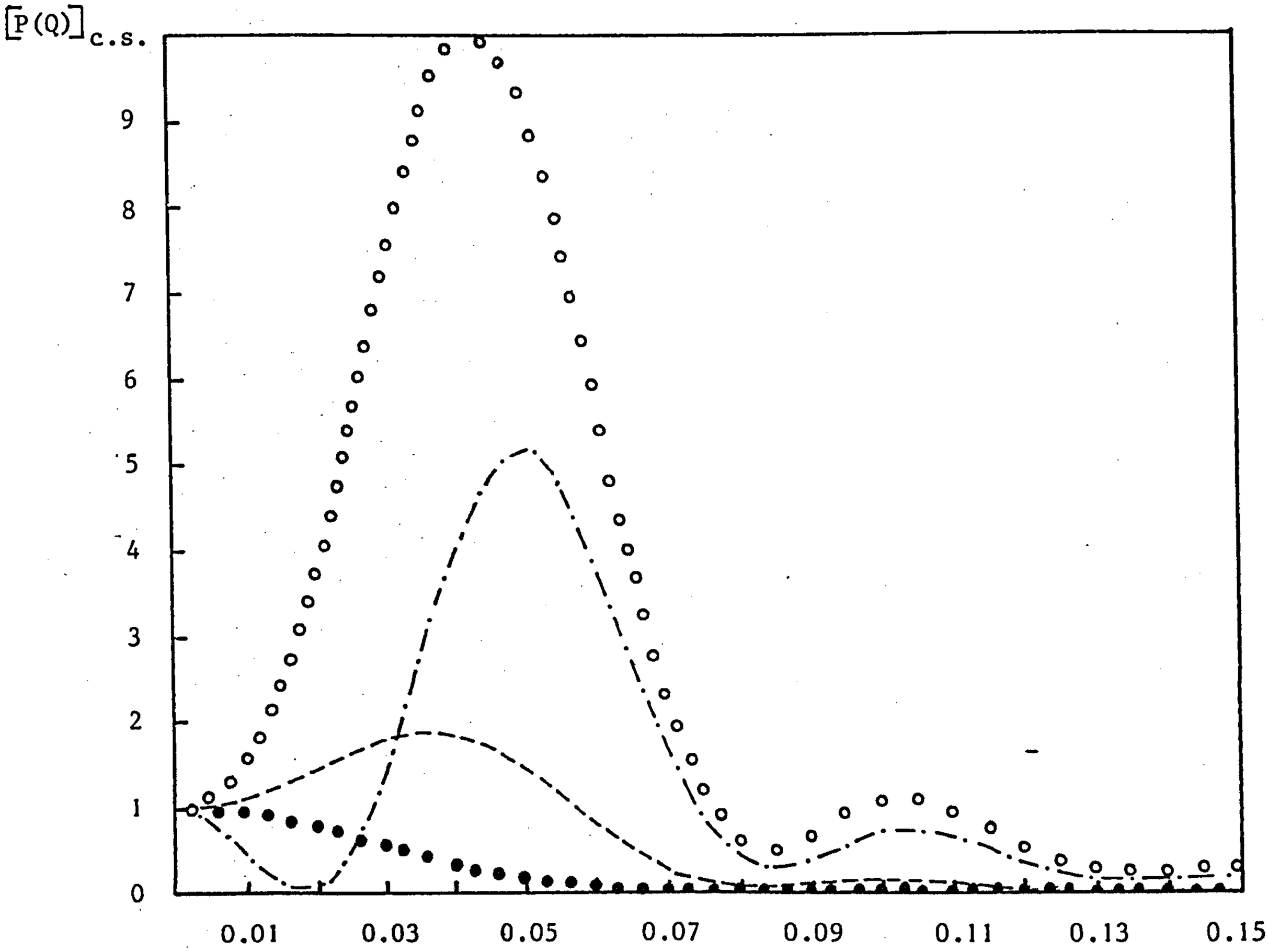

FIGURE 5.20 Calculated curves of $[\overline{P(Q)}]_{c.s.}$ against Q for R_1 = 62 Å; R_2 = 80 Å; $\rho_p = 4.72 \times 10^{10}$ cm^{-2}; $\rho_A = 0.35 \times 10^{10}$ cm^{-2} and for various values of ρ_m:

●●●● , 0.94×10^{10} cm^{-2}; ———— , 2.0×10^{10} cm^{-2};

—·—·—·— , 2.6×10^{10} cm^{-2}; oooo , 2.25×10^{10} cm^{-2}.

Conversion to absolute intensities

It was already mentioned at the end of Chapter 4 that for dilute dispersions the small angle scattering results from the samples are corrected for the presence of the dispersion medium and the presence of the quartz cell. The results so obtained, as a function of Q, are then divided by the small angle scattering from water which has been similarly treated. The scattering from water can be written in the form,

$$N_{H_2O} \left\{ \frac{d\sigma}{d\Omega} \right\}_{H_2O} (Q) \qquad \ldots \quad (5.50)$$

where N_{H_2O} is the number of water molecules per cm^3.

If the experimentally determined intensity from the particulate sample is denoted by I_S and that from the water by I_W, assuming that both results have been corrected for the presence of the background and normalised to the same monitor count and path length, then

$$\frac{I_S}{I_W} = \frac{N_p \, (d\sigma/d\Omega)_{c.s.} \, (Q)}{N_{H_2O} (d\sigma/d\Omega)_{H_2O} \, (Q)} \quad \frac{T_{S+SB}}{T_{W+Q}} \qquad \ldots \quad (5.51)$$

where T_{S+SB} is the transmission of the dispersion (i.e. the sample plus the sample background) and T_{W+Q} is the transmission of water in the quartz cell.

Hence,

$$N_p \left\{ \frac{d\sigma}{d\Omega} \right\}_{c.s.} (Q) = \frac{I_S}{I_W} \cdot \frac{T_{W+Q}}{T_{S+SB}} \quad \frac{N_{H_2O} \, \sigma_{H_2O}}{4\pi} \qquad \ldots \quad (5.52)$$

since $(d\sigma/d\Omega)_{H_2O} = \sigma_{H_2O}/4\pi$, where σ_{H_2O} is the scattering cross-section of water, expressed in cm^2 (10^{-24} $cm^2 \equiv$ 1 barn) giving the dimensions of $N_p \, (d\sigma/d\Omega)_{c.s.}(Q)$ as cm^{-1}. The value of σ_{H_2O} is wavelength dependent, and if expressed in barnes, with λ in $\mathring{A}$ is given by the expression,

$$\ln \sigma_{H_2O} = 4.45 + 0.46 \ln \lambda \qquad \ldots \quad (5.53)$$

A typical value is σ_{H_2O} = 247 barnes ≡ 2.47 x 10^{-22} cm^2 at λ = 10 Å. At a temperature of 25°C N_{H_2O} = 3.341 x 10^{22} molecules cm^{-3}.

Rewriting equation (5.52) in the form,

$$I(Q) \equiv \left(\frac{I_S}{I_W} \right) = \left(\frac{d\sigma}{d\Omega} \right)_{c.s.}(Q) \quad \frac{T_{S+SB}\ N_p\ 4\pi}{T_{W+Q}\ N_{H_2O}\ \sigma_{H_2O}} \qquad \ldots \quad (5.54)$$

it is possible to calculate the theoretical absolute intensity of scattering as a function of Q for a particular system if one estimates the value of (T_{S+SB}/T_{W+Q}). However, for a dilute dispersion of particles the transmission of the dispersion should be similar to the transmission of the sample background, i.e., the dispersion medium. Thus, for an aqueous system $(T_{S+SB}/T_{W+Q}) \simeq 1$, whereas when the medium is an organic phase then $(T_{S+SB}/T_{W+Q}) \simeq (T_{SB}/T_{W+Q})$.

Using equation (5.54), I(Q) was calculated for both the V-series and the L-series allowing for the polydispersity of particle core radii in a manner similar to that described for $\left[P(Q)\right]_{c.s.}$. The number of particles per cm^3, N_p, was obtained from,

$$N_p = \phi / V_p$$

where ϕ is the volume fraction of the core particles and V_p was calculated using the mean value for the particle core radius, $\bar{R}$ (equation (5.47)). This was considered an adequate procedure for the systems in this study where polydispersity was low. However, for a system where the standard deviation of particle size is large, the number concentration of particles should be averaged over the whole particle size distribution range, i.e.,

$$p_i\ N_i = \frac{\phi}{(4/3)\ \pi\ (R_i^3)} \qquad \ldots \quad (5.55)$$

where $N_p = \Sigma\ p_i\ N_i$

Figure 5.21 shows the calculated absolute intensity as a function of Q for a typical dispersion of V-particles of volume fraction $\phi = 3.7 \times 10^{-3}$, taking $R_1 = 28$ Å, $R_2 = 46$ Å and $\sigma_o = 0.1$, The ratio of the transmissions was estimated from the experimentally determined values of T_{SB} and T_{W+Q}. It can be seen that the magnitude of the value of I(Q) is extremely low, especially when the scattering length density of the medium is close to the value of the contrast match point of the particle, i.e. $\rho_m = 0.85 \times 10^{10}$ cm^2. Thus, the pronounced peak seen in the $\left[P(Q) \right]_{c.s.}$ curve for that value of ρ_m (Figure 5.19) is not as apparent in the I(Q) curve.

Figure 5.22 shows the calculated I(Q) scattering curves for a typical dispersion of L-particles of volume fraction $\phi = 3.7 \times 10^{-3}$, taking $R_1 = 62$ Å, $R_2 = 80$ Å, $\sigma_o = 0.1$ and $(T_{S+SB}/T_{W+Q}) = 1.2$. Although the magnitude of the absolute intensity values is slightly higher than for the case of the V-sample, it nevertheless decreases substantially when the value of ρ_m is close to the value of $\bar{\rho}$. Hence, the very pronounced peaks seen in the $\left[P(Q) \right]_{c.s.}$ curves (Figure 5.20) when $\rho_m = 2.25 \times 10^{10}$ cm^2 and $\rho_m = 2.6 \times 10^{10}$ cm^2 are now barely apparent. The magnitude of the I(Q) values increases noticeably when $\rho_m = 1.5 \times 10^{10}$ cm^2, i.e. when the scattering length density of the medium deviates sufficiently from the contrast match point of the particle.

When the experimentally determined small angle neutron scattering intensity data is in absolute units, it is possible to extract additional information about the particles using the Guinier approximation.

Reverting to equation (5.39), we find that for the situation Q = 0,

$$N_p \left(\frac{d\sigma}{d\Omega} \right)_{c.s.} (0) = N_p \left[(\rho_A - \rho_m) V_T + (\rho_p - \rho_A) V_p \right]^2$$

$$= \left[\frac{I_S}{I_W} (0) \frac{T_{W+Q}}{T_{S+SB}} \right] \frac{N_{H_2O} \sigma_{H_2O}}{4\pi} \quad \ldots \quad (5.56)$$

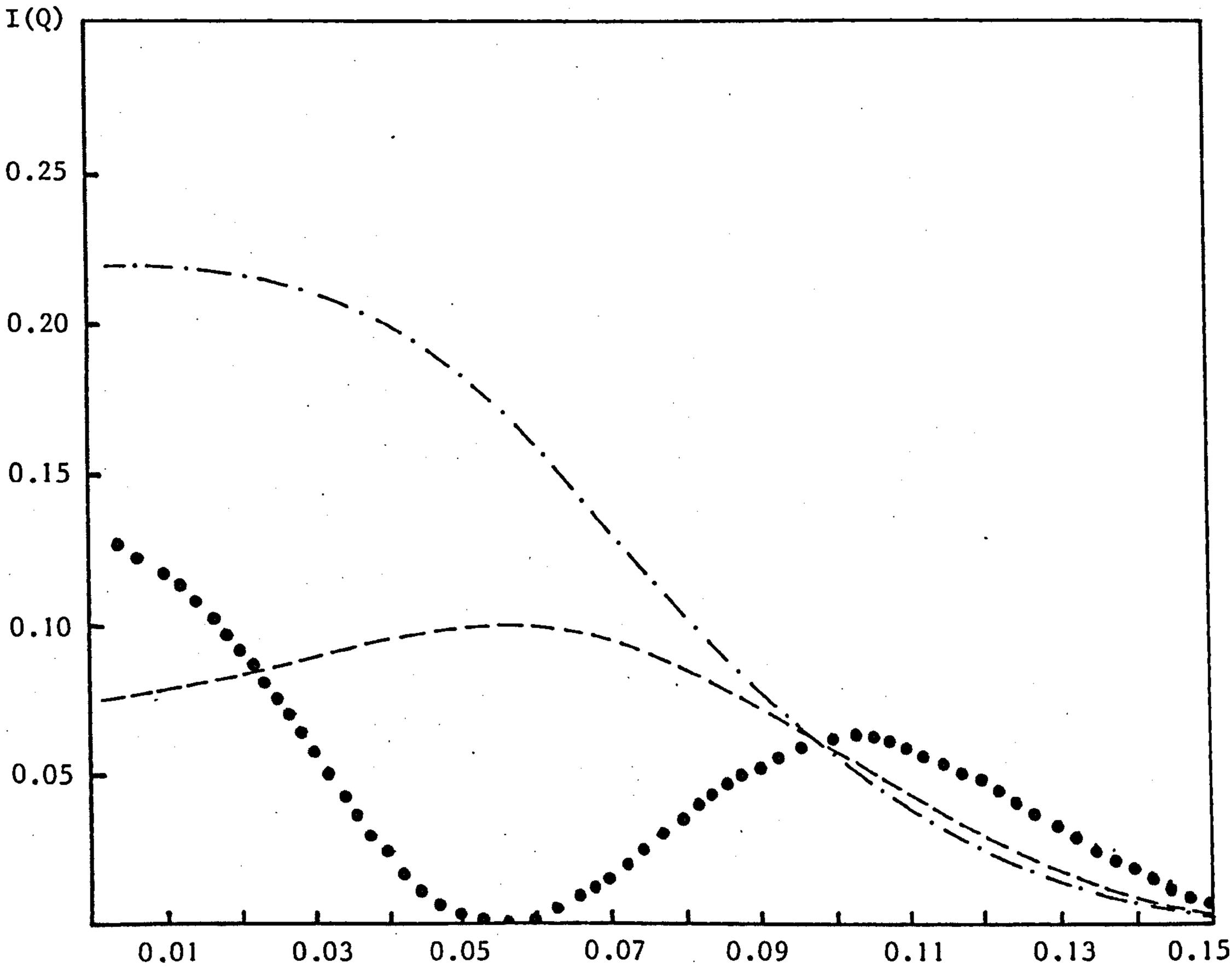

FIGURE 5.21 Calculated curves of the absolute intensity, I(Q), against Q for R_1 = 28 Å; R_2 = 46 Å; $\rho_p = 4.72 \times 10^{10}$ cm^{-2}; $\rho_A = 0.35 \times 10^{10}$ cm^{-2} and ρ_m:

—·—·—, 0.5×10^{10} cm^{-2}; ————, 0.85×10^{10} cm^{-2};

●●●●, 2.0×10^{10} cm^{-2}.

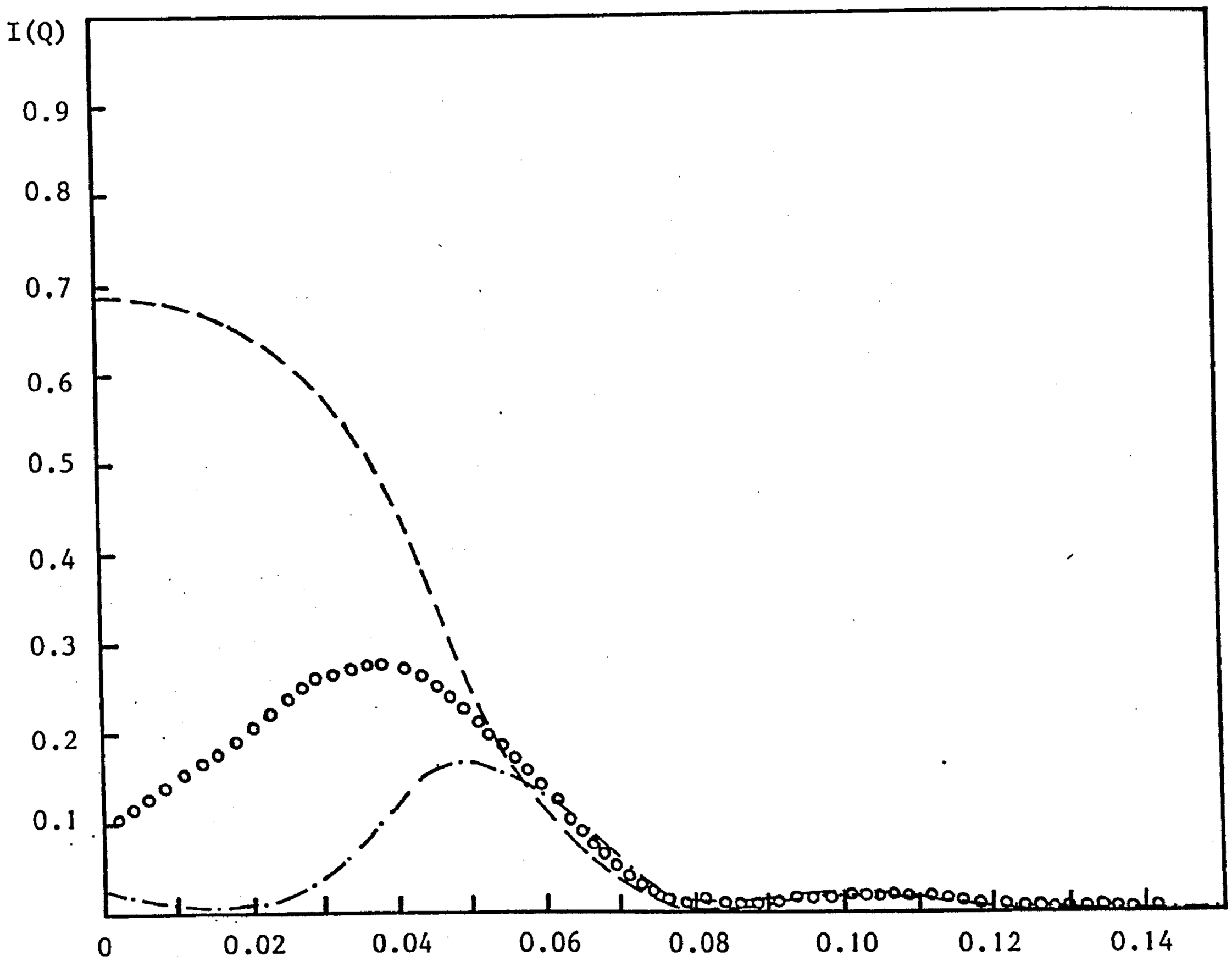

FIGURE 5.22 Absolute intensity, I(Q), against Q for R_1 = 62 Å; R_2 = 80 Å; $\rho_p = 4.72 \times 10^{10}$ cm^{-2}; $\rho_A = 0.35 \times 10^{10}$ cm^{-2} and for various values of ρ_m:

———, 1.5×10^{10} cm^{-2}; oooo , 2.0×10^{10} cm^{-2};

.—.—.—., 2.6×10^{10} cm^{-2}.

However, we have already shown in Section 5.1.1 of this chapter, equation (5.10), that the term,

$$(\rho_A - \rho_m)\ V_T + (\rho_p - \rho_m)\ V_p$$

$$= \rho_A\ (V_T - V_p) + \rho_p\ V_p \doteq \rho_m\ V_T$$

$$= V_T \left[\frac{\rho_A\ V_A + \rho_p\ V_p}{V_T} - \rho_m \right] \qquad \ldots \quad (5.10)$$

$$= V_T\ (\bar{\rho} - \rho_m)$$

$$= V_T\ \rho$$

Thus,

$$N_p \left(\frac{d\sigma}{d\Omega} \right)_{c.s.} (0) = N_p\ V_T^{\,2}\ \rho^2 \qquad \ldots \quad (5.57)$$

which was also derived in Section 5.1.1, equation (5.14);

or,

$$\frac{I_S}{I_W}\ (0) = \left[\frac{T_{S+SB}\ 4\pi}{T_{W+Q}\ N_{H_2O}\ \sigma_{H_2O}} \right] N_p\ V_T^{\,2}\ \rho^2 \qquad \ldots \quad (5.58)$$

All the terms in the square brackets are known, but in order to calculate N_p one must know the volume of the core particle, V_p, since $N_p = \phi/V_p$. However, since we have assumed a homogeneous adsorbed layer around the core particle, it must follow that,

$$V_T = x\ V_p \qquad \ldots \quad (5.59)$$

and hence we can write

$$N_p = x\phi/V_T$$

Substituting this into equation (5.58) we find that a plot of $(I_S/I_W)(0)$ against ρ^2 yields a value for x V_T.

Using the relationship in equation (5.59) and substituting it into equation (5.56) we can also write,

$$N_p \left[(\rho_A - \rho_m)\, V_T + (\rho_p - \rho_A)\, V_p\right]^2$$

$$= N_p\, V_p^{\,2} \left[x\,(\rho_A - \rho_m) + (\rho_p - \rho_A)\right]^2$$

This gives,

$$V_p = \frac{\left[\frac{I_S}{I_W}(0)\,\frac{T_{W+Q}}{T_{S+SB}}\right]\,\frac{N_{H_2O}\,\sigma_{H_2O}}{4\pi}}{\phi\left[x(\rho_A - \rho_m) + (\rho_p - \rho_A)\right]^2} \qquad \ldots \quad (5.60)$$

Hence, using equations (5.58) and (5.60), it is possible to solve for x and thus obtain values for both V_T and V_p.

For the condition that $\rho_A = \rho_m$, a value for V_p can be obtained directly since equation (5.60) simplifies to,

$$V_p = \frac{\left[\frac{I_S}{I_W}\,(0)\,\frac{T_{W+Q}}{T_{S+SB}}\right]\,\frac{N_{H_2O}\,\sigma_{H_2O}}{4\pi}}{\phi\,(\rho_p - \rho_m)^2} \qquad \ldots \quad (5.61)$$

5.2.2 Results

We have already shown that,

$$N_p \left\{\frac{d\sigma}{d\Omega}\right\}_{c.s.}(Q) = \frac{I_S}{I_W}\,(Q)\,\frac{T_{W+Q}}{T_{S+SB}}\,\frac{N_{H_2O}\,\sigma_{H_2O}}{4\pi} \qquad \ldots \quad (5.52)$$

and that

$$N_p \left(\frac{d\sigma}{d\Omega} \right)_{c.s.} (0) = \frac{I_S}{I_W} (0) \frac{T_{W+Q}}{T_{S+SB}} \frac{N_{H_2O} \sigma_{H_2O}}{4\pi} \quad \ldots \quad (5.56)$$

and hence,

$$\frac{(d\sigma/d\Omega)_{c.s.} (Q)}{(d\sigma/d\Omega)_{c.s.} (0)} = \left[P(Q)\right]_{c.s.} = \frac{I_S}{I_W} (Q) \Big/ \frac{I_S}{I_W} (0) \quad \ldots \quad (5.62)$$

Thus, if the experimentally determined scattering intensity from a particulate sample, I(Q), is divided by the value of I(Q = 0) the particle form factor, $\left[P(Q)\right]_{c.s.}$, is obtained since all the other terms are constant. Equation (5.56) can therefore be used as a scaling factor in order to obtain a match between the theoretical and the experimental particle form factors.

This was done for the three systems used in this study, namely the V-series, the L-series and the F-series, and in each case for a number of dispersions of varying scattering length density of the medium. In addition, particles from a second preparation of the L-series were examined and these samples were labelled L'-. The values for the intensity at Q = 0 were obtained using the Guinier approximation, i.e. by extrapolation of the plot of ln I(Q) against Q^2.

All the samples used in this work were labelled in such a manner that DOD and TOL corresponded to the dispersion medium being dodecane or toluene respectively, whereas the number preceding the abbreviation corresponded to the percentage of deuterated material in the medium. The number preceding the name of the series corresponded to the concentration of particles expressed in terms of a w/w percentage of calcium carbonate. Thus, for example, IV/6.4 DOD is equivalent to the V-series at a concentration of 1% w/w calcium carbonate dispersed in 6.4% deuterated dodecane.

Figure 5.23 shows $[\bar{P(Q)}]_{c.s.}$ for the V-series at a concentration of 1% w/w calcium carbonate in three different dispersion media. 1V/6.4 DOD corresponds to the scattering length density of the medium being zero; 1V/11 DOD corresponds to the scattering length density of the medium being equal to that of the adsorbed layer, whereas in the case of 1V/72 DOD the scattering length density of the medium matches that of the core particle. It can be seen that in each case a good fit to the theoretical $[\bar{P(Q)}]_{c.s.}$ was obtained using $R_1 = 22$ Å and $R_2 - R_1 = 18$ Å.

These three samples, as well as all the examples subsequently given for the three series, were fitted using 4.72×10^{10} cm^{-2} for the scattering length density of the calcium carbonate core particle, ρ_p, and 0.35×10^{10} cm^{-2} for the scattering length density of the adsorbed layer, ρ_A. In addition, for the V-series and the L-series a good match was obtained to the experimental $[\bar{P(Q)}]_{c.s.}$ if the theoretical form factor was calculated using $\sigma_o = 0.1$ for the polydispersity. Therefore, the values for these three parameters, namely ρ_p, ρ_A and σ_o will not be subsequently repeated.

Figure 5.24 shows $[\bar{P(Q)}]_{c.s.}$ for the V-series at a concentration of 2% w/w calcium carbonate when the scattering length of the medium is close to the value of the contrast match point of the particle ($\bar{\rho} \simeq 1.45 \times 10^{10}$ cm^{-2}). It can be seen that $[\bar{P(Q)}]_{c.s.}$ displays the oscillations discussed in Section 5.2.1 and that in the case of 2V/0 TOL, for which the value of ρ_m is just below that of $\bar{\rho}$, $[\bar{P(Q)}]_{c.s.}$ displays a pronounced peak. 2V/23 TOL was fitted using $R_1 = 28$ Å and $R_2 - R_1 = 18$ Å, whereas 2V/0 TOL was fitted using $R_1 = 22$ Å and $R_2 - R_1 = 18$ Å. The different values obtained for the core particle radius are discussed later.

Figure 5.25 shows the particle form factor for the V-series when the scattering length density of the medium is substantially different from the contrast match point of the particle. It can be seen that the profile of

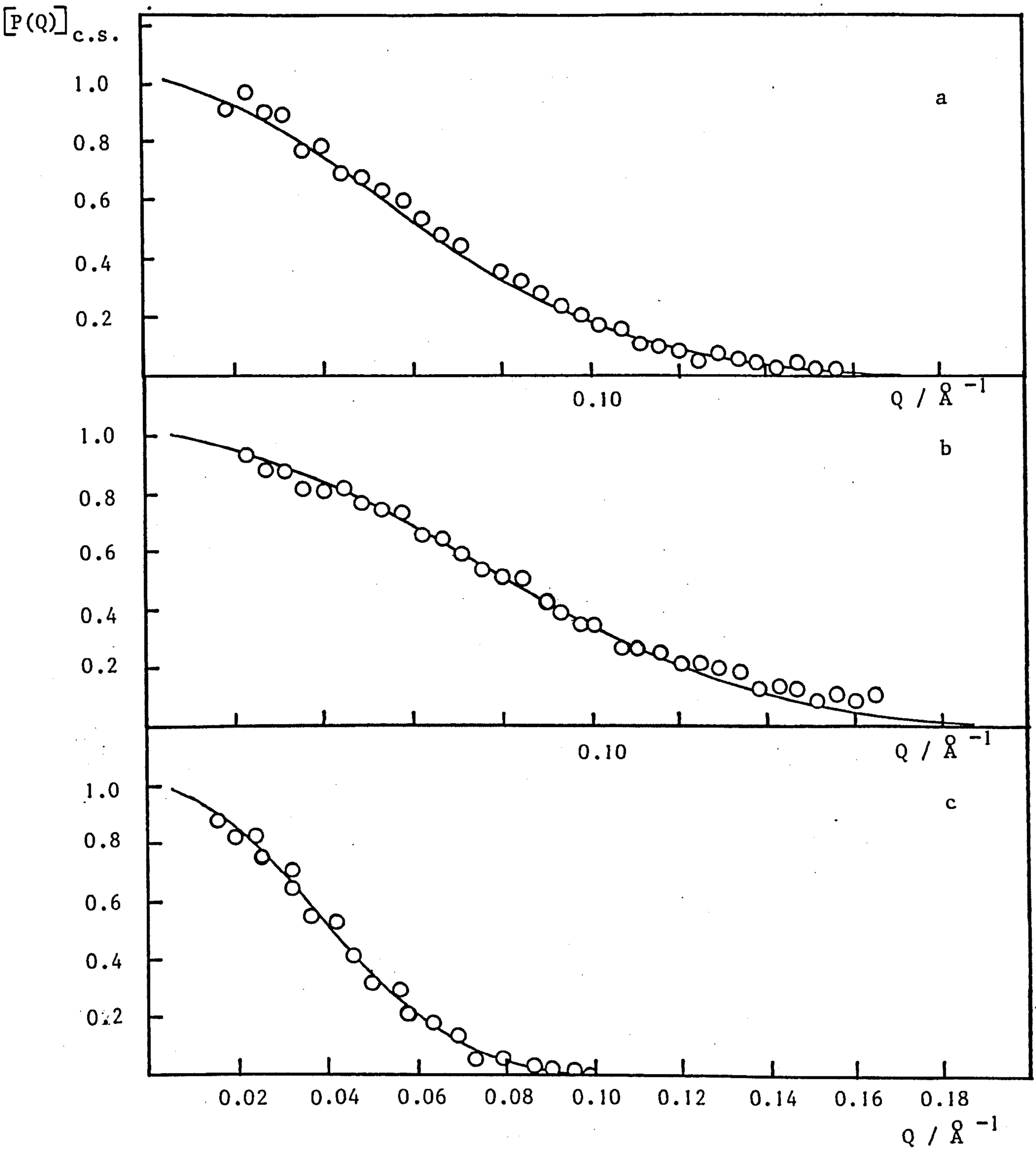

FIGURE 5.23 $[P(Q)]_{c.s.}$ against Q

O , experimental data; ——— , calculated curves using R_1 = 22 Å; R_2-R_1 = 18 Å; $\rho_p = 4.72 \times 10^{10}$ cm^{-2}; $\rho_A = 0.35 \times 10^{10}$ cm^{-2}

a) 1V/6.4 DOD; $\rho_m = 0$

b) 1V/11 DOD; $\rho_m = 0.35 \times 10^{10}$ cm^{-2}

c) 1V/72 DOD; $\rho_m = 4.72 \times 10^{10}$ cm^{-2}

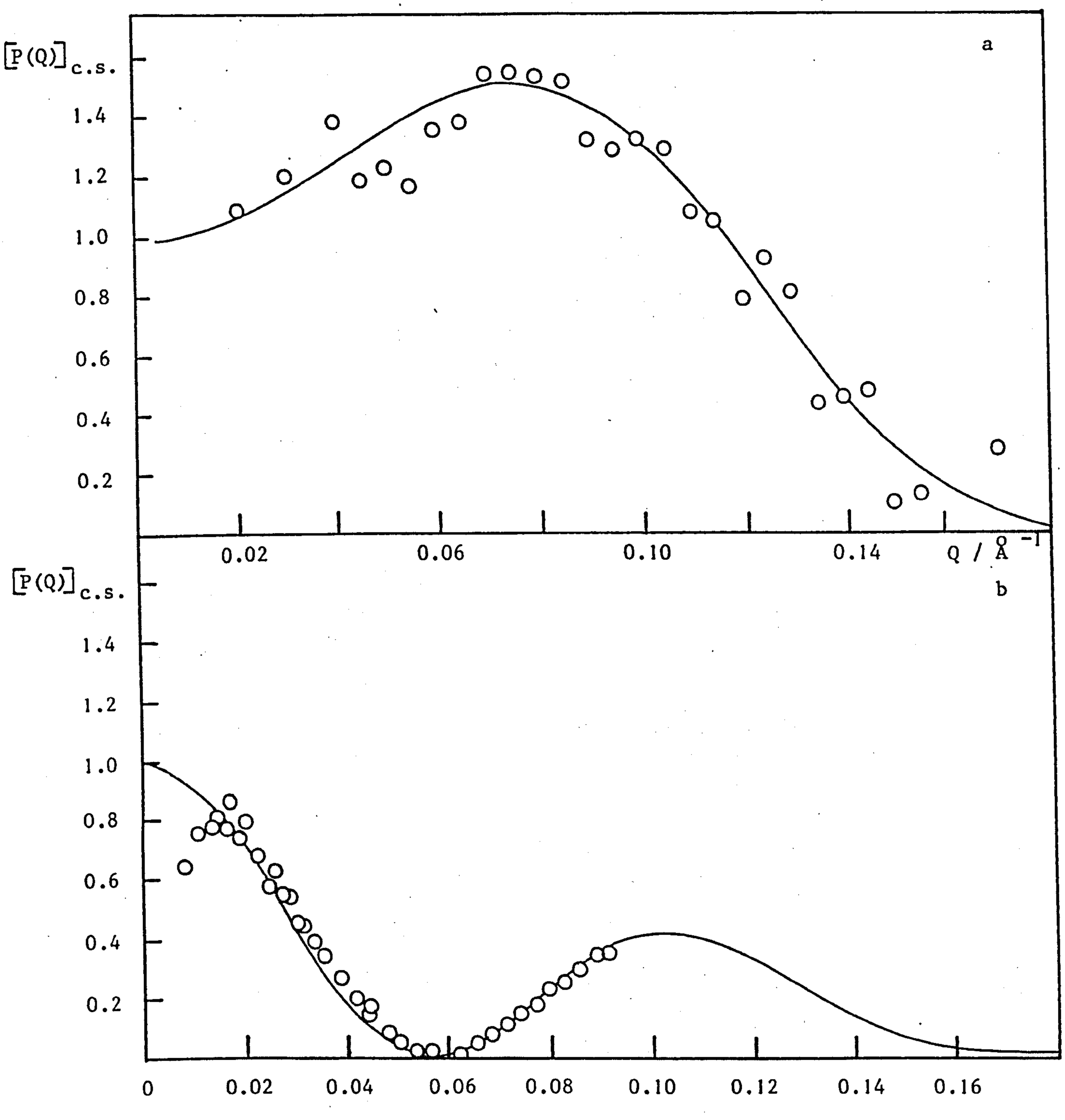

FIGURE 5.24 $[P(Q)]_{c.s.}$ against Q.

O , experimental data; ——— , calculated curve for

a) 2 V/0 TOL using R_1 = 22 Å; $R_2 - R_1$ = 18 Å;

$\rho_m = 0.94 \times 10^{10}$ cm^{-2}

b) 2 V/23 TOL using R_1 = 28 Å; $R_2 - R_1$ = 18 Å;

$\rho_m = 2.0 \times 10^{10}$ cm^{-2}

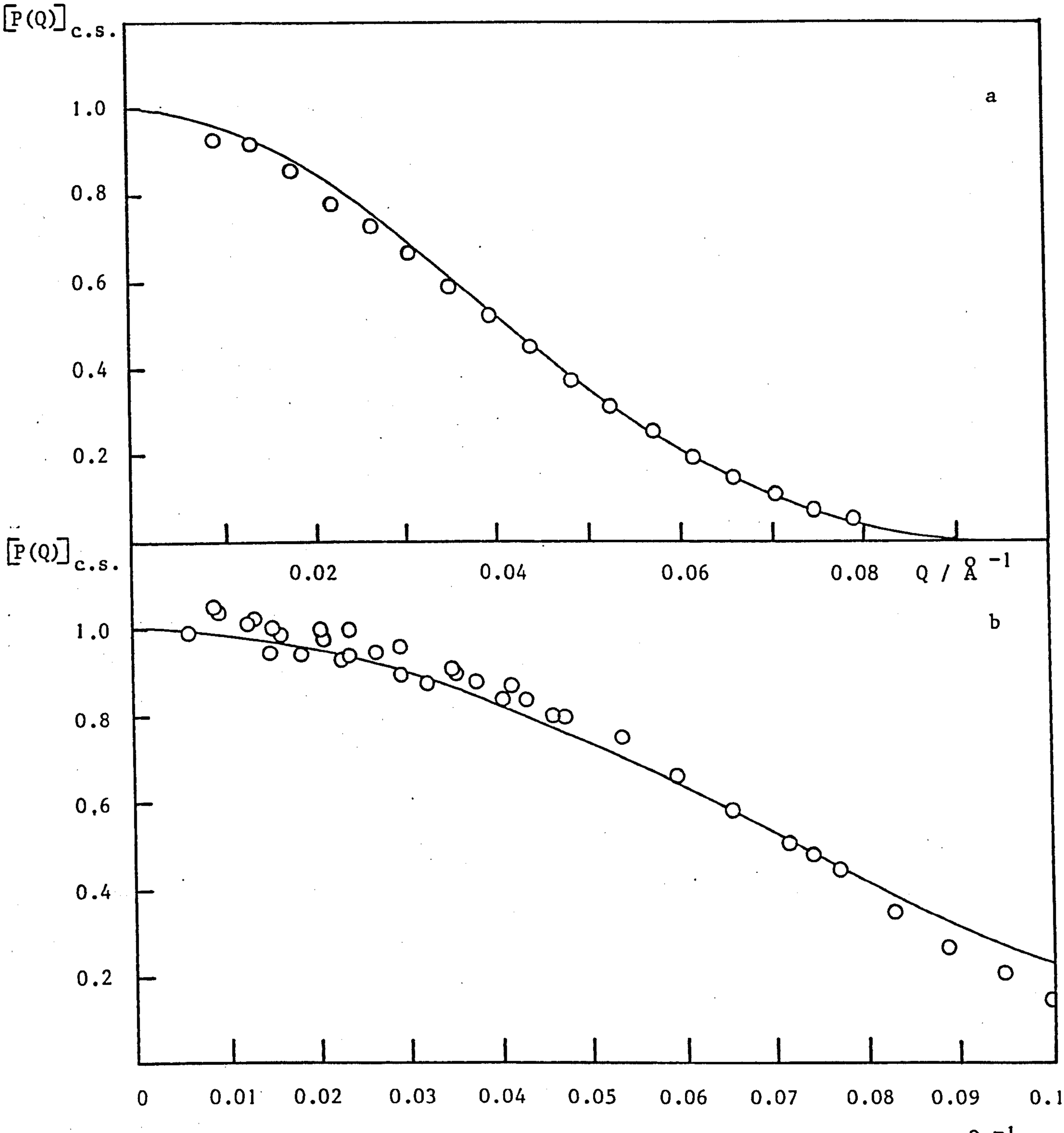

FIGURE 5.25 $[P(Q)]_{c.s.}$ against Q

O , experimental data; ———, calculated curve for

a) 1 V/80 TOL using R_1 = 22 Å; $R_2 - R_1$ = 18 Å;

$\rho_m = 4.61 \times 10^{10}$ cm^{-2}

b) 1 V/DOD TOL using R_1 = 28 Å; $R_2 - R_1$ = 18 Å;

$\rho_m = 0.5 \times 10^{10}$ cm^{-2}

the $[P(Q)]_{c.s.}$ curve is now that of a single, isotropic sphere. 1V/DOD TOL corresponds to the dispersion medium being a mixture of h_8 - toluene and h_{26} - dodecane such that $\rho_m = 0.5 \times 10^{10}$ cm^{-2}, and this was fitted to the theoretical $[P(Q)]_{c.s.}$ using $R_1 = 28$ Å and $R_2 - R_1 = 18$ Å. 1V/80 TOL was fitted using $R_1 = 22$ Å and $R_2 - R_1 = 18$ Å.

Figure 5.26 shows $[P(Q)]_{c.s.}$ for two dispersions of the V-series in 100% deuterated toluene. The sample $^{2}/_{3}$ V/100 TOL was obtained by diluting 2V/100 TOL by a factor of 3 with deuterated toluene. It is clear that dilution of the sample does not alter the particle form factor as very good fits were obtained in both cases using $R_1 = 22$ Å and $R_2 - R_1 = 18$ Å. It also shows the absence of any particle-particle interactions.

Figure 5.27 shows $[P(Q)]_{c.s.}$ for four samples of the L-series dispersed in various mixtures of hydrogenated and deuterated dodecane. 1L/6.4 DOD corresponds to the scattering length density of the medium being zero, 1L/11 DOD corresponds to the situation $\rho_m = \rho_A$, in the case of 1L/0 DOD $\rho_m = 0.46 \times 10^{10}$ cm^{-2}, whereas 1L/72 DOD corresponds to the case $\rho_m = \rho_p$. A comparison of 1L/11 DOD and 1L/72 DOD shows that in the former case only the scattering from the core particle is seen, $[P(Q)]_{c.s.}$ decays to zero at a higher value of Q since the particle now behaves like a sphere of radius R_1. Conversely, in the case of 1L/72 DOD, for which $\rho_m = \rho_p$ the scattering from the whole particle is seen and $[P(Q)]_{c.s.}$ decays at a lower value of Q. All four samples were fitted using $R_1 = 62$ Å and $R_2 - R_1 = 18$ Å.

Figure 5.28 shows the $[P(Q)]_{c.s.}$ curves obtained for the L-series when the dispersion medium consisted of mixtures of hydrogenated and deuterated toluene. It can be seen that in the case of 1L'/23 TOL, where the scattering length density of the medium is just below the contrast match point of the particle ($\bar{\rho} \simeq 2.45 \times 10^{10}$ cm^{-2}), $[P(Q)]_{c.s.}$ displays

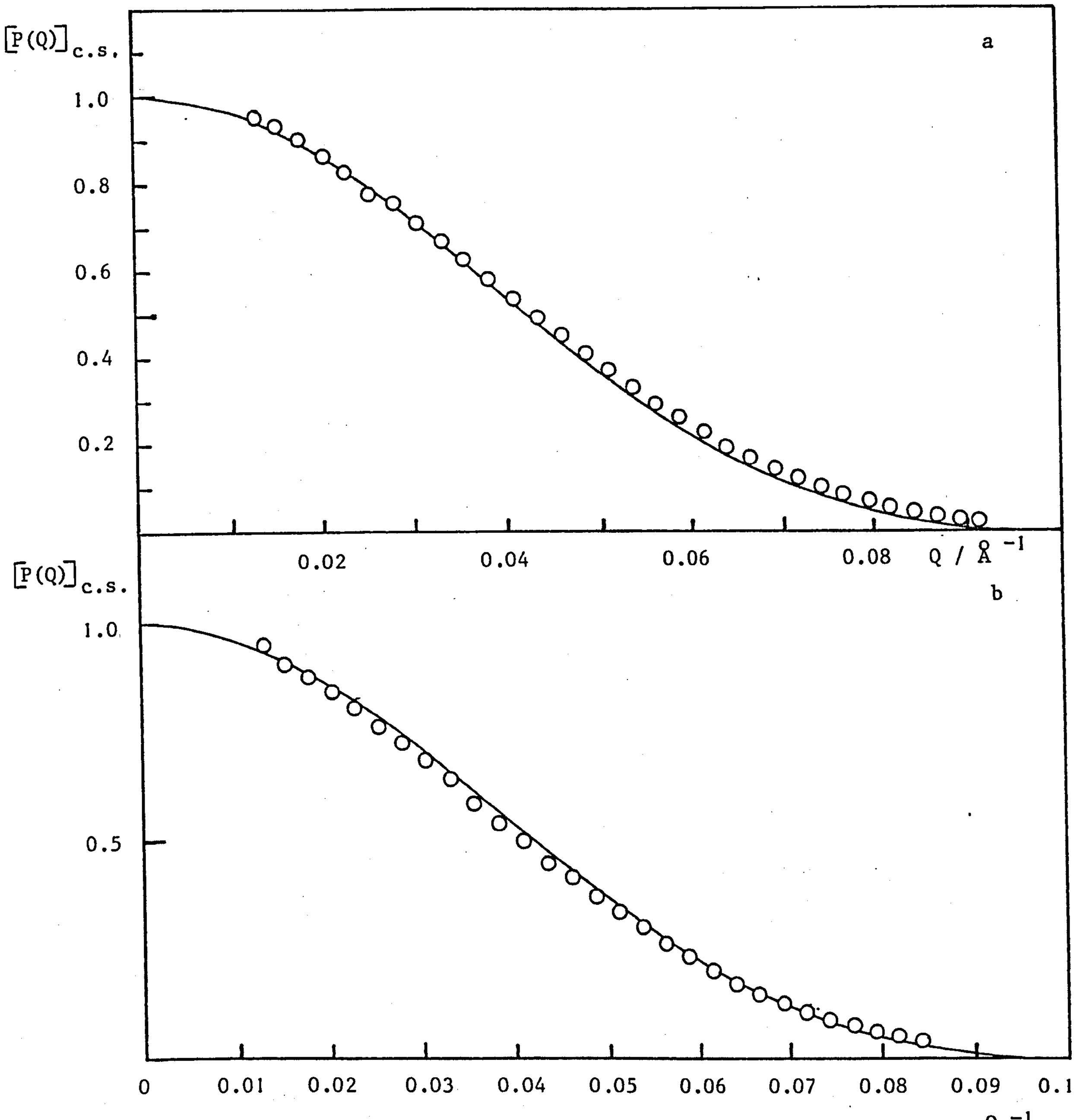

FIGURE 5.26 $[P(Q)]_{c.s.}$ against Q

○ , experimental data; ——— , calculated curves for a) 2 V/100 TOL and b) $^2/_3$ V/100 TOL using $R_1 = 22$ Å; $R_2 - R_1 = 18$ Å; $\rho_m = 5.63 \times 10^{10}$ cm^{-2}.

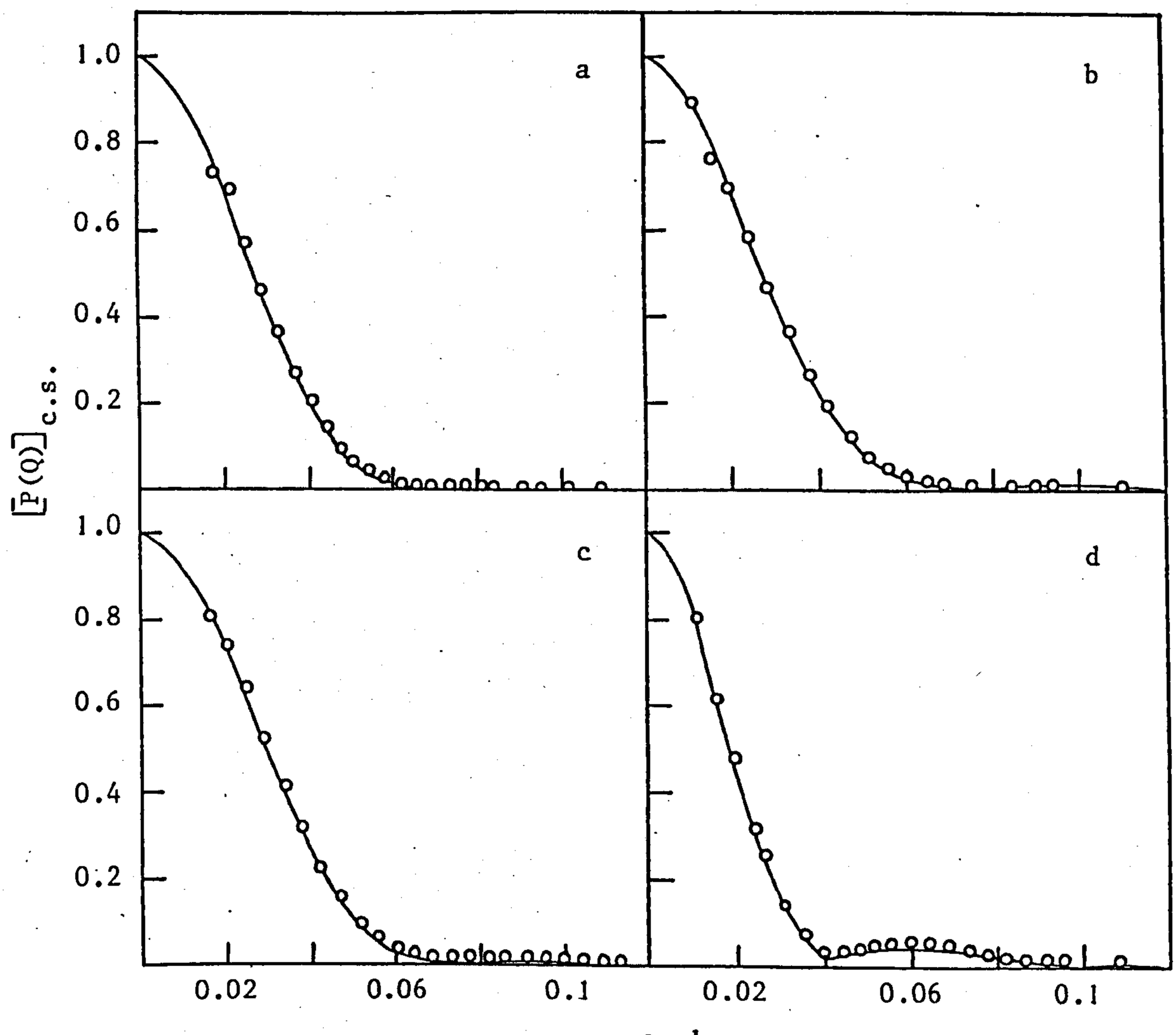

FIGURE 5.27 $[P(Q)]_{c.s.}$ against Q

ooo, experimental data; ——, calculated curves using $R_1 = 62$ Å, $R_2 - R_1 = 18$ Å for

a) 1 L/0 DOD; $\rho_m = -0.46 \times 10^{10}$ cm^{-2}

b) 1 L/6.4 DOD; $\rho_m = 0$

c) 1 L/11 DOD; $\rho_m = 0.35 \times 10^{10}$ cm^{-2}

d) 1 L/72 DOD; $\rho_m = 4.72 \times 10^{10}$ cm^{-2}

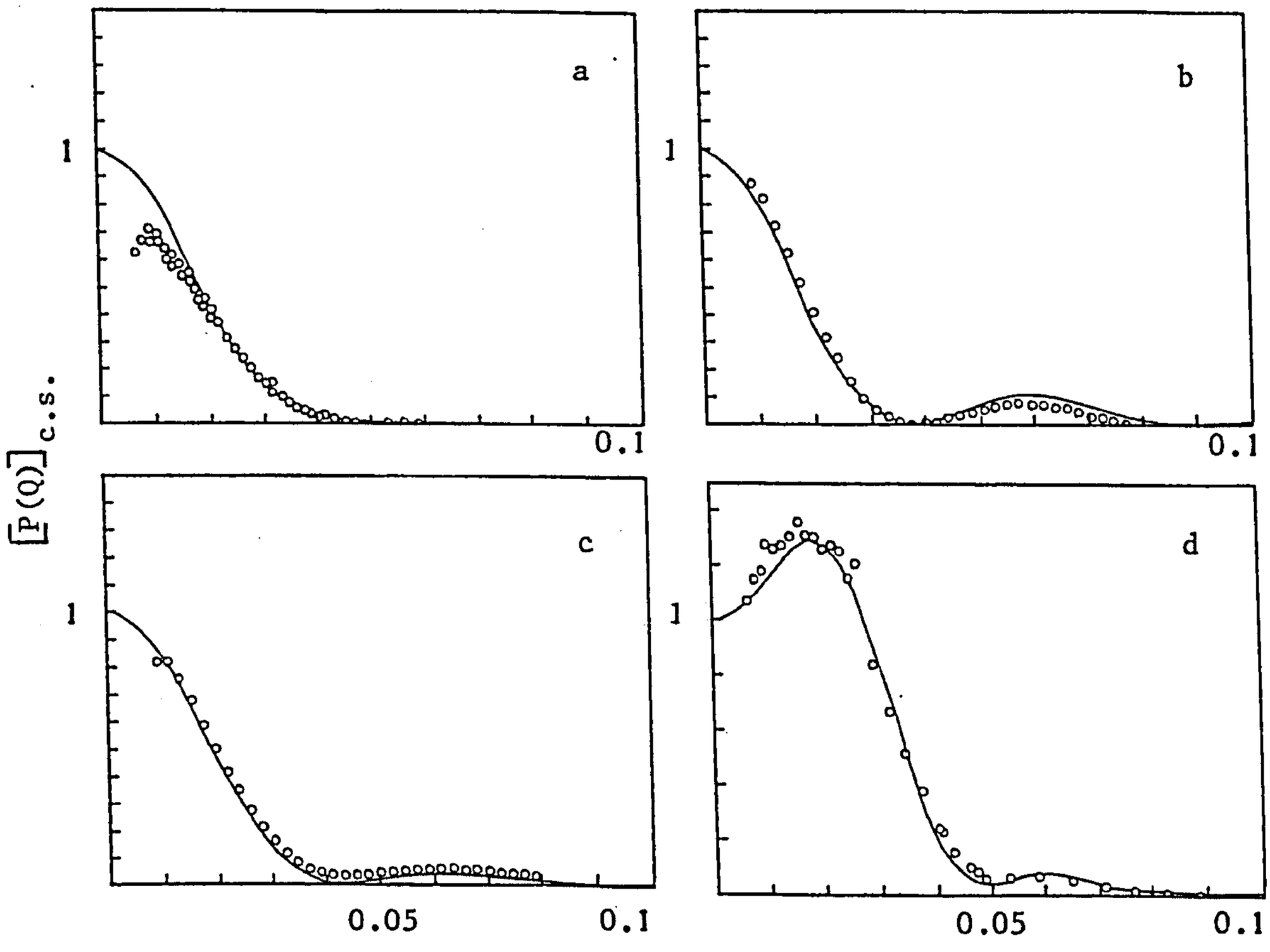

FIGURE 5.28 $[P(Q)]_{c.s.}$ against Q

ooo , experimental data; ——,calculated curves for

a) 1L'/0 TOL; R_1 = 105 Å; R_2-R_1 = 26 Å; $\rho_m = 0.94 \times 10^{10}$ cm^{-2}

b) 1L/60 TOL; R_1 = 62 Å; R_2-R_1 = 18 Å; $\rho_m = 3.64 \times 10^{10}$ cm^{-2}

c) 1L/80 TOL; R_1 = 62 Å; R_2-R_1 = 17 Å; $\rho_m = 4.61 \times 10^{10}$ cm^{-2}

d) 1L'/23 TOL; R_1 = 105 Å; R_2-R_1 = 26 Å; $\rho_m = 2.00 \times 10^{10}$ cm^{-2}

a pronounced peak above the value of $[P(Q)]_{c.s.} = 1$. 1L'/0 TOL and 1L'/23 TOL were both fitted using $R_1 = 105$ Å and $R_2 - R_1 = 26$ Å, 1L/60 TOL was fitted using $R_1 = 62$ Å and $R_2 - R_1 = 18$ Å, whereas in the case of 1L/80 TOL $R_2 - R_1 = 17$ Å.

Figure 5.29 shows the $[P(Q)]_{c.s.}$ fits obtained for the F-series. 1F/6.4 DOD corresponds to $\rho_m = 0$, 1F/11 DOD corresponds to the case $\rho_m = \rho_A$ and 1F/72 DOD corresponds to the case $\rho_m = \rho_p$. It is immediately noticeable that the fits of the experimental and theoretical particle form factors for this series are not as good as those obtained previously for the V-series and the L-series. Moreover, a much higher polydispersity, i.e. $\sigma_o = 0.2 - 0.25$, had to be incorporated into the theoretical $[P(Q)]_{c.s.}$ in order to obtain a fit. The core particle polydispersity is, as expected, most apparent in the case of 1F/11 DOD when $\rho_m = \rho_A$. This sample appears to have a bimodal distribution of core particle radii and the smaller particles were fitted using $R_1 = 36$ Å, $R_2 - R_1 = 16$ Å and $\sigma_o = 0.25$, whereas the larger particles were fitted using $R_1 = 52$ Å, $R_2 - R_1 = 17$ Å and $\sigma_o = 0.2$. 1F/6.4 DOD was fitted using $R_1 = 35$ Å, $R_2 - R_1 = 19$ Å and $\sigma_o = 0.2$. A reasonable fit was obtained for 1F/72 DOD using $R_1 = 35$ Å, $R_2 - R_1 = 16$ Å and $\sigma_o = 0.2$.

Figure 5.30 shows two samples of the F-series at a concentration of 2% w/w calcium carbonate dispersed in 60% deuterated and 80% deuterated toluene. The best fit for 2F/60 TOL was obtained using $R_1 = 33$ Å, $R_2 - R_1 = 16$ Å and $\sigma_o = 0.2$, whereas 2F/80 TOL was fitted using $R_1 = 35$ Å, $R_2 - R_1 = 15$ Å and $\sigma_o = 0.25$. In both cases it was very difficult to fit the middle Q-range.

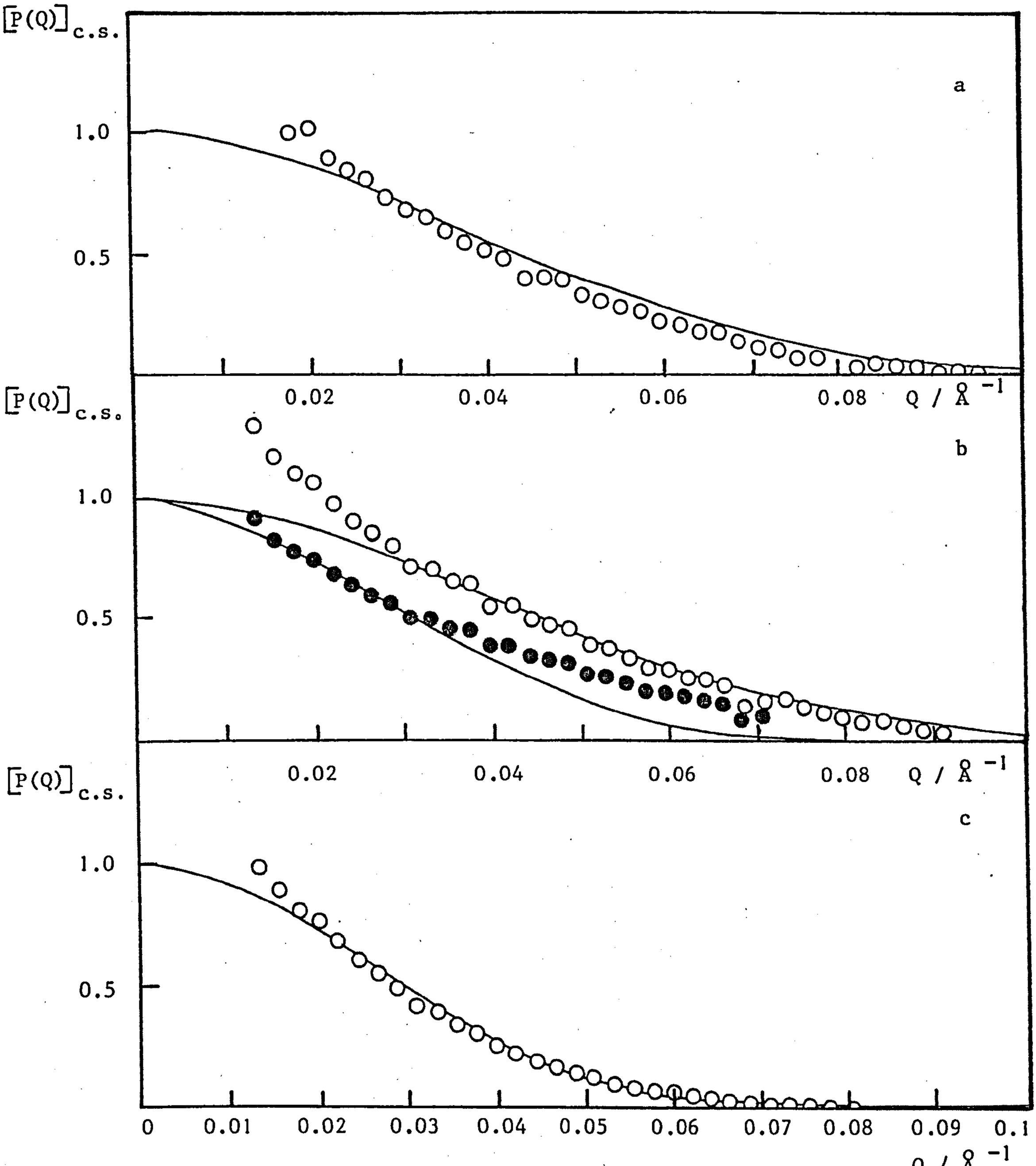

FIGURE 5.29 $[P(Q)]_{c.s.}$ against Q

○ , experimental data; ——— , calculated curve for

a) 1F/6.4 DOD using R_1 = 35 Å; R_2-R_1 = 19 Å; ρ_m = 0

b) 1F/11 DOD using R_1 = 36 Å; R_2-R_1 = 16 Å; $\rho_m = 0.35 \times 10^{10}$ cm^{-2}

c) 1F/72 DOD using R_1 = 35 Å; R_2-R_1 = 16 Å; $\rho_m = 4.72 \times 10^{10}$ cm^{-2}

● , experimental data; ——— , calculated curve for

b) 1F/11 DOD using R_1 = 52 Å; R_2-R_1 = 17 Å; $\rho_m = 0.35 \times 10^{10}$ cm^{-2}

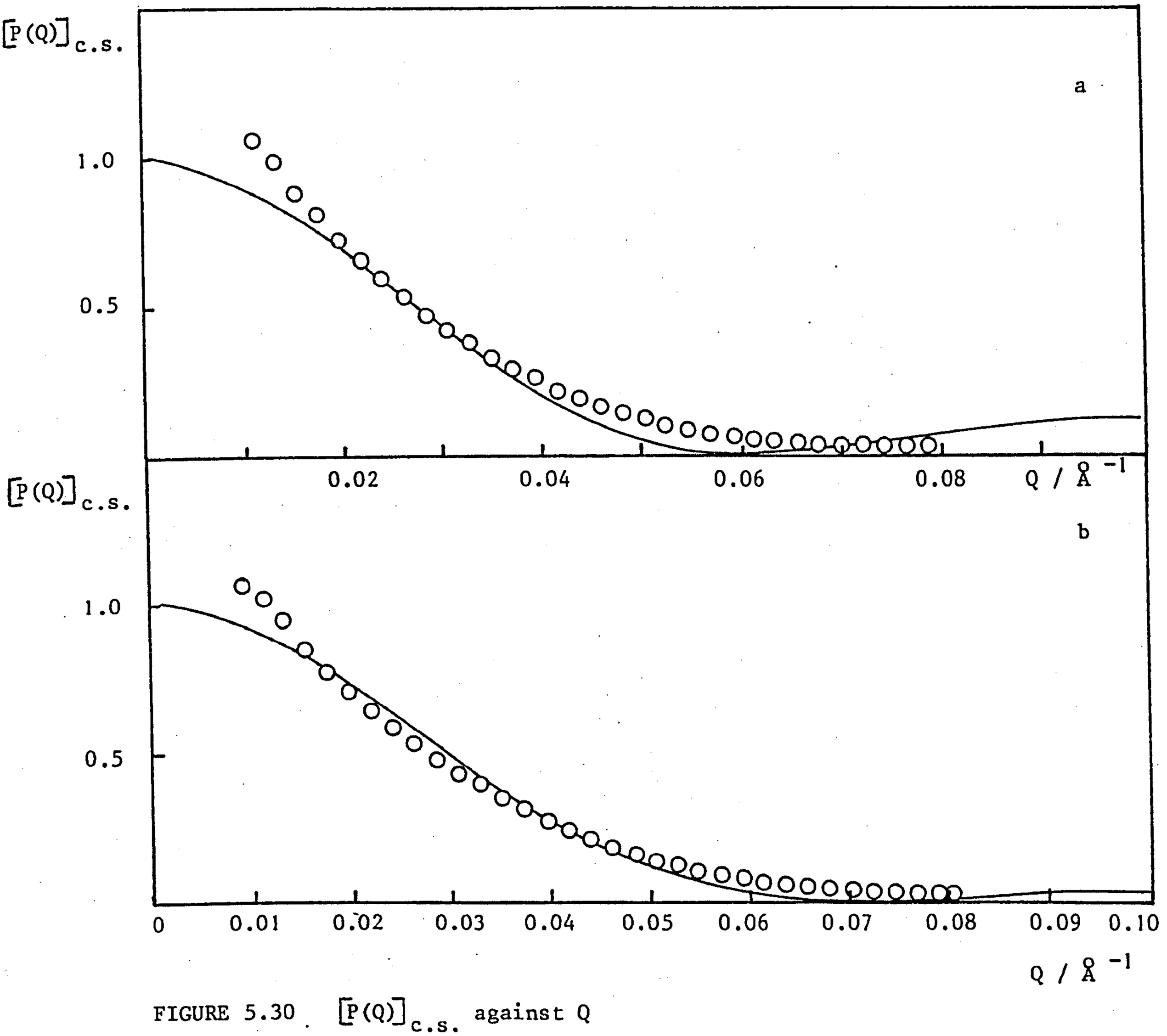

FIGURE 5.30 $[P(Q)]_{c.s.}$ against Q

○ , experimental data; ——— , calculated curve for

a) 2F/60 TOL using R_1 = 33 Å; $R_2 - R_1$ = 16 Å;
$\rho_m = 2.98 \times 10^{10}$ cm^{-2}

b) 2F/80 TOL using R_1 = 35 Å; $R_2 - R_1$ = 15 Å;
$\rho_m = 4.45 \times 10^{10}$ cm^{-2}

5.2.3 Discussion

The curve fitting approach outlined above depends upon obtaining a match between the experimental particle form factor and the theoretical $[P(Q)]_{c.s.}$, calculated using equation (5.33), by varying a number of parameters, such as R_1, $R_2 - R_1$ and σ_o. In Section 5.2.1, $[P(Q)]_{c.s.}$ was predicted to be very sensitive to the scattering length density of the medium, especially just below the contrast match point of the particle, and this was substantiated by the experimentally determined particle form factors shown in Section 5.2.2. Moreover, the pronounced peak displayed by $[P(Q)]_{c.s.}$ just below the contrast match point of the particle was shown to be still present, although less apparent, in the scattering intensity curves (Figures 5.21 and 5.22) and hence, as predicted, a negative value for the radius of gyration of the particle is obtained under those conditions.

For the case of both the V-series and the L-series, Figures 5.23 to 5.28 show that a very good match was obtained between the experimental and the theoretical particle form factors. The values determined for the particle core radius, R_1, and the adsorbed layer thickness, $R_2 - R_1$, for the V-series and the L-series are given in Tables 5.11 and 5.12 respectively.

TABLE 5.11 Results for the V-series using the curve fitting approach

SAMPLE	R_1/Å	R_2-R_1/Å	$\rho_m/10^{10}cm^{-2}$
1V/6.4 DOD	22	18	0
1V/11 DOD	22	18	0.35
1V/DOD TOL*	28	18	0.50
2V/0 TOL	22	18	0.94
2V/23 TOL*	28	18	2.00
1V/80 TOL	22	18	4.61
1V/72 DOD	22	18	4.72
2V/100 TOL	22	18	5.63
[2]/3V/100 TOL	22	18	5.63

*measured in October 1983

Table 5.11 shows that a consistent value of 18 Å was obtained for the thickness of the adsorbed layer and that for the majority of the samples the particle core radius was 22 Å. In the case of the two samples, for which a core radius of 28 Å was obtained, the measurements were carried out in October 1983, whereas the measurements on all the other samples were carried out over a period of time from January 1981 until September 1982. Hence, the particle core radius appears to have abruptly increased in size between September 1982 and October 1983. This could be due to a case of Ostwald ripening although, for the present, no satisfactory explanation is available. All the samples were fitted using $\sigma_o = 0.1$ for the polydispersity which, in the case of $R_1 = 22$ Å, corresponds to a standard deviation of 2.2 Å and in

the case of R_1 = 28 Å corresponds to a standard deviation of 2.8 Å. The V-series thus appears to be fairly monodisperse .

TABLE 5.12 Results for the L-series using the curve fitting approach

SAMPLE	R_1/Å	R_2-R_1/Å	$\rho_m/10^{10}cm^{-2}$
1L/6.4 DOD	62	18	0
1L/11 DOD	62	18	0.35
1L/0 DOD	62	18	0.46
1L'/0 TOL	105	26	0.94
1L'/23 TOL	105	26	2.00
1L/60 TOL	62	18	3.64
1L/80 TOL	62	17	4.61
1L/72 DOD	62	18	4.72

Table 5.12 shows the results obtained for the L-series. Two samples, namely 1L'/0 TOL and 1L'/23 TOL, were fitted using a particle core radius of 105 Å and an adsorbed layer thickness of 26 Å, and they corresponded to a second preparation of the L-series. This new sample of the L-series was obtained from Esso Chemical Limited and should have been prepared in the manner outlined in Chapter 3 for the original L-series. However, it appears that particles of a larger core radius were formed. A possible explanation for the increase in the adsorbed layer thickness is that a greater proportion of polyisobutene succinic anhydride (PIBSA) was present in the adsorbed layer, whose extended chain length is longer than that of calcium alkyl benzene

sulphonate. The consistency obtained for the value of the adsorbed layer thickness for the V-series and the original L-series indicates that although in the latter some PIBSA was present, it was not sufficient to contribute to the average adsorbed layer thickness as determined by small angle neutron scattering. The original L-samples were all fitted using a value for the particle core radius of 62 Å. Once again, good fits were obtained using σ_o = 0.1 for the polydispersity, and this corresponds to a standard deviation of 6.3 Å when R_1 = 62 Å and 10.7 Å when R_1 = 105 Å.

The results obtained for the F-series using the curve fitting approach are given below in Table 5.13. It was much more difficult to obtain a good match between the experimental and the theoretical particle form factors for this series, and this was attributed to the greater degree of polydispersity of core particle radii. It was found necessary to use values as high as 0.25 for σ_o and this corresponds to a standard deviation of 9.8 Å when R_1 = 35 Å. Moreover, in the case of 1F/11 DOD ($\rho_m = \rho_A$), for which the fit should be most sensitive to the core particle polydispersity, a bimodal distribution of particle core radii seemed to be present.

TABLE 5.13 Results for the F-series using the curve fitting approach

SAMPLE	R_1/Å	R_2-R_1/Å	$\rho_m/10^{10}$ cm^{-2}
1F/6.4 DOD	35	19	0
1F/11 DOD	36 (52)	16 (17)	0.35
2F/60 TOL	33	16	2.98
2F/80 TOL	35	15	4.45
1F/72 DOD	35	16	4.72

The results obtained for all three series of particles were in very good agreement with those obtained using the Guinier approach. The curve fitting approach is a very accurate method of characterising a particular system, since not only can values for R_1 and $R_2 - R_1$ be determined independently of one another, but also an indication of the accuracy of the values used for ρ_p and ρ_A is obtained.

The curve fitting procedure is rather sensitive to the value of I(0) used as a scaling factor for the determination of the experimental particle form factor. However, it is possible to check the accuracy of the value used by calculating the absolute intensity expected at Q = 0, using equation (5.56). This can be done if values obtained from the fit are used for the various parameters, such as R_1, $R_2 - R_1$, ρ_p, ρ_A and ρ_m. This was carried out for a number of samples and two typical results are given here. For the case of 1V/11 DOD, the experimentally determined value for I(Q = 0) was 0.39, whereas the calculated value was 0.40. The experimentally determined value for I(Q = 0) for 1L/11 DOD was 6.70 and the theoretical value was 7.05. In addition, these two values for I(Q = 0) for the V-sample and the L-sample were used in equation (5.61) to calculate the volume of the core particle, and hence R_1. The value of the particle core radius thus obtained for 1V/11 DOD was 21.3 Å, and that for 1L/11 DOD was 60.95 Å. These values are in very good agreement with those obtained using the curve fitting approach.

It is probably important, from the experimental point of view, if approximate values are available for the various parameters which characterize a system in order to simulate the absolute values for the scattering intensity. It was shown in Figure 5.21 that the absolute intensity values for the V-series were extremely low for a volume fraction of 0.0037, and especially when the scattering length density of the medium was close to

the contrast match point of the particle. Thus, simulations of the expected absolute intensity can give an indication of, say, the volume fraction required to give reasonable intensities and the scattering length density of the medium necessary to give measurable scattering above background.

CHAPTER SIX

CHAPTER 6

SANS OF CONCENTRATED DISPERSIONS

6.1 Theory

In dispersions of low number concentration, such as those discussed in the preceding chapter, the particles can undergo Brownian motion in the unoccupied volume of the dispersion medium. However, as the particle number concentration of the dispersion increases, the volume of space occupied by the particles increases, and thus a proportion of the space is excluded in terms of its possible occupancy by any single particle. It is in this situation that the nature of the forces acting between the particles plays an important role in determining the overall properties of the dispersion[41]. In a system in which the dominant force of interaction between the particles is a repulsive force, many-body interactions lead to the formation of a dispersion with a high degree of ordering, i.e. structure which is dependent upon both spatial and temporal correlations between the particles[42]. It was already mentioned in Chapter 4 that the spatial correlation between the particles gives rise to an interference contribution to the small angle neutron scattering intensity. This contribution to the total scattering of the dispersion is known as *the interparticle structure factor*, S(Q), and it is given by,

$$S(Q) = 1 + \frac{4\pi\rho_o}{Q} \int_o^\infty r \left[g(r) - 1\right] \sin Qr \, dr \qquad \ldots \quad (6.1)$$

where ρ_o is the number density of the dispersion and g(r) is the radial distribution function (described in Chapter 2). The form of S(Q) consists of a series of oscillations about the value S(Q) = 1 which diminish in magnitude with increasing Q. Since for a perfect gas S(Q) = g(r) = 1,

deviations of S(Q) from this value represent structure in the system.

Using the expression derived in Chapter 5 for the differential scattering cross-section of a single concentric sphere (equation (5.30)), one can write for an assembly of interacting particles of the same type,

$$\left[\frac{d\sigma}{d\Omega}\right]_{c.s.}^{conc} N_p = \left[(\rho_A - \rho_m)\left\{V_T\, A(QR_2) - V_p\, A(QR_1)\right\} + (\rho_p - \rho_m)\, V_P\, A(QR_1)\right]^2 . N_p . S(Q) \quad \ldots \quad (6.2)$$

where $$A(QR) = 3\left(\frac{\sin QR - QR\cos QR}{Q^3R^3}\right)$$

and the other symbols are as defined in the preceding chapter; the superscript conc refers to concentrated.

Thus the interparticle structure factor, S(Q), can be obtained experimentally from neutron scattering measurements on interacting systems. This is particularly useful since Fourier transformation of S(Q) (equation (6.1)) leads directly to,

$$g(r) = 1 + \frac{1}{2\pi^2 r\rho_o}\int_o^\infty \left[S(Q) - 1\right] Q \sin Qr\, dr \quad \ldots \quad (6.3)$$

Moreover, it has already been shown in Chapter 2 that the radial distribution function g(r) is directly related to the potential of mean force, $\Phi(r)$, between the particles, viz.,

$$g(r) = \exp(-\Phi(r)/kT)$$

$$= \exp(-\left[V(r) + \Psi(r)\right]/kT) \quad \ldots \quad (6.4)$$

where V(r) is the pair potential and $\Psi(r)$ is a perturbation occurring as a consequence of many-body interations. In the limit $g(r) \to 0$, i.e. $r \to 2R$,

where R is the radius of the central particle, then $\Phi(r) \rightarrow V(r)$.

In addition to the microscopic information that the determination of S(Q) yields, a particularly useful macroscopic quantity which can be obtained is the osmotic compressibility. This is related to the structure factor at Q = 0, i.e. S(0) by,

$$\left[\frac{\partial \Pi}{\partial \rho_o}\right]_T = \frac{kT}{S(0)} \qquad \ldots \quad (6.5)$$

S(0) can be determined from scattering experiments by extrapolation of the data to zero Q. Π is the excess osmotic pressure in the system owing to the presence of the particles and their interactions.

In order to simulate the form of the experimentally determined structure factor, various models can be used to calculate S(Q) as a function of Q. One of the simplest of these to use is the hard-sphere model as proposed by Percus and Yevick[22] (see Chapter 2). It was shown by Ashcroft and Lekner[43] that this model leads directly to the interparticle structure factor in the form,

$$S(Q) = \frac{1}{\left[1 - N_p \cdot C(2QR_{HS})\right]} \qquad \ldots \quad (6.6)$$

with

$$C(2QR_{HS}) = -32\pi R_{HS}^3 \int_o^1 \frac{\sin 2s\, QR_{HS}}{2sQR_{HS}} \left(\alpha + \beta s + \gamma s^3\right) s^2\, ds \qquad \ldots \quad (6.7)$$

The coefficients α, β and γ are defined by,

$$\alpha = (1 + 2\phi_{HS})^2 \,/\, (1 - \phi_{HS})^4 \qquad \ldots \quad (6.8)$$

$$\beta = -6\phi_{HS} (1 + 0.5\phi_{HS})^2 \,/\, (1 - \phi_{HS})^4 \qquad \ldots \quad (6.9)$$

$$\gamma = 0.5\phi_{HS} (1 + 2\phi_{HS})^2 \,/\, (1 - \phi_{HS})^4 \qquad \ldots \quad (6.10)$$

where ϕ_{HS} is the hard-sphere volume fraction as defined in Chapter 2 (equation (2.30)).

The hard-sphere model also provides a simple expression for S(0), namely,

$$S(0) = \frac{(1 - \phi_{HS})^4}{(1 + 2\phi_{HS})^2} \quad \ldots \quad (6.11)$$

which enables an estimate to be made of the excess osmotic pressure of the system.

6.1.1 Treatment of data

The basic procedure for the treatment of data from a SANS experiment, as carried out by the programme SPOLLY at I.L.L., Grenoble, was described in Chapter 4. However, in the case of more concentrated dispersions additional corrections have to be made to the scattering of the sample background, i.e. the dispersion medium, and hence a different procedure should be used for the treatment of the data.

In the case of dilute dispersions, the number of counts measured for the pure solvent, Z(SB), is equal to the number of counts that would be obtained from the dispersion, so that the corrected sample scattering is given by equation (4.33) in Chapter 4, i.e.,

$$Z(S) = Z(S + Q) - \frac{T_S}{T_{SB}} Z(SB + Q) \quad \ldots \quad (4.33)$$

where $Z(S + Q)$ = number of counts from sample + quartz cell

and $\frac{T_S}{T_{SB}} = \frac{\text{transmission of sample}}{\text{transmission of sample background}}$

However, in a sample which contains a higher number concentration of particles a volume fraction ϕ of the dispersion medium will be replaced by the particles.

Hence, a correction has to be made to the scattering of the pure solvent in order to relate it to the actual dispersion medium. The necessary correction will depend on the sample and there are thus several possible cases:-

1) The particle scattering is totally coherent, then

$$\left[Z(SB)\right]_{cor} = (1 - \phi)\ Z(SB) \qquad \ldots \quad (6.12)$$

2) The sample contains H atoms which scatter incoherently, then

$$\left[Z(SB)\right]_{cor} = (1 - \phi)\ Z(SB) + \phi \frac{N_H^S}{N_H^{SB}}\ Z(SB) \qquad \ldots \quad (6.13)$$

where N_H^S = the number of H atoms per unit volume in the sample (i.e. particle).

N_H^{SB} = the number of H atoms per unit volume in the dispersion medium.

3) The system contains two components occupying volume fractions ϕ_1 and ϕ_2, then

$$\left[Z(SB)\right]_{cor} = (1 - \phi_1 - \phi_2)\ Z(SB) + \phi_1 \frac{N_H^1}{N_H^{SB}}\ Z(SB) + \phi_2 \frac{N_H^2}{N_H^{SB}}\ Z(SB)$$

$$\ldots \quad (6.14)$$

4) If in case 3) component 1 is totally coherent, then

$$\left[Z(SB)\right]_{cor} = (1 - \phi_1 - \phi_2)\ Z(SB) + \phi_2 \frac{N_H^2}{N_H^{SB}}\ Z(SB) \qquad \ldots \quad (6.15)$$

The above mentioned corrections to the scattering from the pure solvent simulate the scattering from the dispersion medium. Alternatively, one can assume that the background scattering from the medium is all due to incoherent scattering and in this case it should be possible to measure it directly at high values of Q.

In order to correct the scattering from the pure solvent, the following procedure should be adopted for the treatment of the data:-

1) The intensity of the sample, corrected for the presence of the quartz cell and normalised by the corrected water scattering, is given by:

$$Z(S + SB) = \frac{Z(S + Q) - (T_S/T_Q)\ Z(Q)}{Z(H + Q) - (T_H/T_Q)\ Z(Q)} \qquad \ldots \quad (6.16)$$

where $$\frac{T_S}{T_Q} = \frac{\text{transmission of sample}}{\text{transmission of quartz cell}}$$

$$\frac{T_H}{T_Q} = \frac{\text{transmission of water}}{\text{transmission of quartz cell}}$$

and the other symbols are as defined in Chapter 4.

2) The intensity of the sample background, corrected for the presence of the quartz cell and normalised by the scattering from water, is given by,

$$Z(SB) = \frac{Z(SB + Q) - (T_{SB}/T_Q)\ Z(Q)}{Z(H + Q) - (T_H/T_Q)\ Z(Q)} \qquad \ldots \quad (6.17)$$

The intensity of the sample background (i.e. solvent) scattering can then be corrected for the presence of various components in the actual dispersion medium in the manner described above by equations (6.12) to (6.15).

In a typical concentrated dispersion in this study, the dispersion medium contained two components, viz.,

a) the calcium carbonate core particles, and

b) the surface active agent

and some residual mineral oil (see Chapter 3). Hence, the solvent

scattering was corrected using equation (6.15), i.e.,

$$\left[Z(SB)\right]_{cor} = (1 - \phi_{CaCO_3} - \phi_{SAA+oil})\, Z(SB) + \phi_{SAA+oil} \frac{N_H^{S+O}}{N_H^{SB}} Z(SB) \quad \ldots \quad (6.18)$$

for which the values of the two volume fractions were calculated in the manner described in Section 3.1.3 of Chapter 3. For example, in the case of a 20% w/w dispersion of $CaCO_3$ particles, the calculated value of $\left[Z(SB)\right]_{cor}$ was approximately 7% greater than the experimentally determined value of Z(SB).

3) The absolute scattering intensity of the particles in the sample, expressed in the form of I(Q), is finally given by,

$$I(Q) = \left[Z(S + SB) - \left[Z(SB)\right]_{cor}\right] \frac{T_S}{T_H} \quad \ldots \quad (6.19)$$

where $$\frac{T_S}{T_H} = \frac{\text{transmission of sample}}{\text{transmission of water}}$$

6.1.2 Theoretical simulations of absolute intensities

The theoretical simulation of the absolute intensity of scattering for the case of dilute dispersions has already been described in Section 5.2 of Chapter 5. It was shown in equations (5.51) and (5.52) that if the differential scattering cross-section of the particles is divided by that of water, it is then possible to calculate the absolute scattering intensity, I(Q), namely,

$$I(Q) = \frac{N_p (d\sigma/d\Omega)_{c.s.}(Q)}{N_{H_2O} (d\sigma/d\Omega)_{H_2O}(Q)} \frac{T_{S+SB}}{T_{W+Q}} \quad \ldots \quad (5.51)$$

Similarly, for a concentrated dispersion of particles, the above equation can be written in the form,

$$I(Q) = \left(\frac{d\sigma}{d\Omega} \right)_{c.s.}^{conc} (Q) \frac{N_p \, 4\pi}{N_{H_2O} \, \sigma_{H_2O}} \frac{T_{S+SB}}{T_{W+Q}} \quad \ldots \quad (6.20)$$

where $\sigma_{H_2O}/4\pi = (d\sigma/d\Omega)_{H_2O}$

The differential scattering cross-section of a concentrated system was shown in equation (6.2) to be equivalent to:

$$\left(\frac{d\sigma}{d\Omega} \right)_{c.s.}^{conc} (Q) \, N_p{}^{conc} = \left(\frac{d\sigma}{d\Omega} \right)_{c.s.} (Q) \, N_p \, . \, S(Q) \quad \ldots \quad (6.21)$$

Thus, in order to calculate $(d\sigma/d\Omega)_{c.s.}^{conc}$ a model has to be adopted to simulate the interparticle structure factor, S(Q). For the systems in this study, where the dominant force of interaction is a short-range repulsive force, the most likely model for the interaction, and hence S(Q), is the hard-sphere model.

The Ashcroft and Lekner solution of the hard-sphere structure factor, given in equation (6.6), was therefore incorporated into the programme for the calculation of $(d\sigma/d\Omega)_{c.s.}$ which was described in Section 5.2 of Chapter 5. It is important to note that equation (6.6) uses the hard-sphere radius of the particle for the calculation of S(Q) which is not necessarily equivalent to R_2, the radius of the whole particle. Hence, a "hard-sphere thickness of the adsorbed layer", t_{HS}, was included in the programme, so that,

$$R_{HS} = R_1 + t_{HS} \quad \ldots \quad (6.22)$$

where R_1 is the radius of the core particle.

The polydispersity of the particle core radii was assumed in Chapter 5 to follow a zeroth order log normal distribution, and it was taken into account in the calculation of the intraparticle form factor. However, for the calculation of S(Q) a single value of R_1 was used in equation (6.22), namely the calculated mean value of the core radius, $\bar{R}$ (see equation 5.47)). This was considered to be an adequate procedure for the systems in this study which exhibited low polydispersity.

Finally, using equation (6.20) theoretical scattering curves were calculated as a function of Q and fitted to the experimentally determined data, as given by equation (6.19) of the preceding section.

6.1.3 Determination of S(Q)

In order to determine the type of interaction operating in a concentrated system, the interparticle scattering contribution to the overall scattering intensity has to be determined.

Two methods for the determination of S(Q) were used in this study and they are outlined below.

1) It is clear from equation (6.21) that the scattering intensity of a concentrated system is the product of the scattering intensity of a dilute system and S(Q), normalised by the respective number concentrations of the particles. Since N_p is proportional to the volume fraction of core particles ϕ_p, we can write,

$$S(Q) = \frac{I(Q)^{conc}}{I(Q)^{dil}} \times \frac{\phi_p{}^{dil}}{\phi_p{}^{conc}} \quad \ldots \quad (6.23)$$

where the superscripts conc and dil refer to concentrated and dilute respectively. Thus, S(Q) can be obtained by dividing the experimental data for the concentrated sample by the data for the dilute sample and

correcting for the difference in volume fractions, assuming that all the instrumental factors are the same for the two samples.

2) The second method of extracting S(Q) from the scattering intensity involves the fitting procedure outlined in the preceding section. It was shown that, using equation (6.20), a theoretical scattering intensity curve can be calculated which is then fitted to the experimental I(Q) curve. If the two scattering curves are in good agreement, it is then reasonable to assume that the theoretical structure factor used in the fitting procedure is analogous to the experimental S(Q).

6.2 Results

Concentrated dispersions of the V-particles and the L'-particles were investigated by SANS at various volume fractions and in solvents of different scattering length density. In the case of the V-series, the measurements were usually carried out on the D17 neutron diffractometer, whereas the larger particles of the L'-series were investigated using the D11 diffractometer which provided the necessary low Q-range. The basic raw data was first treated by the standard I.L.L. computer programmes RMASK and SNILS, and subsequently corrected for the presence of the background and normalised to water in the manner described in Section 6.1.1.

The labelling of the samples was similar to that described for dilute dispersions in Chapter 5; i.e., the number preceding the name of the series corresponded to the concentration of the particles expressed in terms of a w/w percentage of $CaCO_3$. Thus, for example, 10 V/70 TOL was equivalent to a dispersion containing 10% w/w of $CaCO_3$ core particles of the V-series in 70% deuterated toluene. Since the weight percentages of the surface active agent as well as the mineral oil were also known (see Chapter 3), it was possible to calculate the respective volume fractions of all the constituents of the dispersion. This was a prerequisite for two important corrections, viz.,

a) the scattering intensity of the sample background could be corrected for the presence of the surface active agent and the residual mineral oil according to equation (6.18);

b) the scattering length density of the actual dispersion medium, ρ_m, could be calculated. This was done by assuming that the medium consisted of pure solvent and a certain amount of mineral oil which was proportional to the concentration of the particles (see Table 5.1 for the

neutron scattering length densities of the materials).

The corrected experimental data could then be fitted to the theoretically calculated absolute intensity scattering curves. It is clear from equation (6.2) that the calculation of $(d\sigma/d\Omega)^{conc}_{c.s.}$ involves the assignment of values to a number of parameters. If all these parameters were allowed to "float" (i.e. vary) the fitting procedure would become nonsensical. Hence, the values for a number of parameters should be established unambiguously so that the variation of a maximum of 2 or 3 parameters produces a fit.

In the case of the concentrated samples in this study, it was possible to calculate $(d\sigma/d\Omega)^{conc}_{c.s.}$ using a number of values determined by the theoretical fitting of $[\bar{P}(Q)]_{c.s.}$ for the dilute data. Thus, all the samples were fitted using 4.72×10^{10} cm^{-2} for the scattering length density of the core particle, 0.35×10^{10} cm^{-2} for the scattering length density of the adsorbed layer and $\sigma_o = 0.1$ for the polydispersity. The number of particles per cm^3, N_p, was calculated from the volume fraction of the core particles, i.e.,

$$N_p = \phi_p / V_p \qquad \ldots \quad (6.24)$$

where $V_p = (4\pi R_1^3/3)$

Consequently, the total volume fraction of the particles in the dispersion (i.e. core + shell) could be determined since,

$$\phi_T = N_p V_T \qquad \ldots \quad (6.25)$$

where $V_T = (4\pi R_2^3/3)$

The hard-sphere volume fraction used in the calculation of S(Q) was

obtained from,

$$\phi_{HS} = N_p (4\pi R_{HS}^3 / 3) \quad \ldots (6.26)$$

where R_{HS} was defined by equation (6.22).

Good fits were ultimately obtained between the experimental data and the theoretical scattering curves by varying one or two of the following three parameters:-

1. the hard-sphere thickness, t_{HS};
2. the adsorbed layer thickness, $(R_2 - R_1)$;
3. the particle core radius, R_1.

The V-series

Figure 6.1 shows the fits obtained between the experimental data and the theoretically calculated scattering curves for a series of V-particles in 100% deuterated toleune. The SANS measurements were carried out on the D17 diffractometer using a sample-to-detector distance of 2.83 m and an incident neutron beam wavelength of 8.66 Å. The series, which consisted of 2%, 5%, 10%, 20% and 25% w/w of $CaCO_3$ particles, was fitted using 22 Å for the core particle radius, R_1. The values used for the adsorbed layer thickness, $(R_2 - R_1)$ and the hard-sphere thickness in the fitting procedure are listed in Table 6.1.

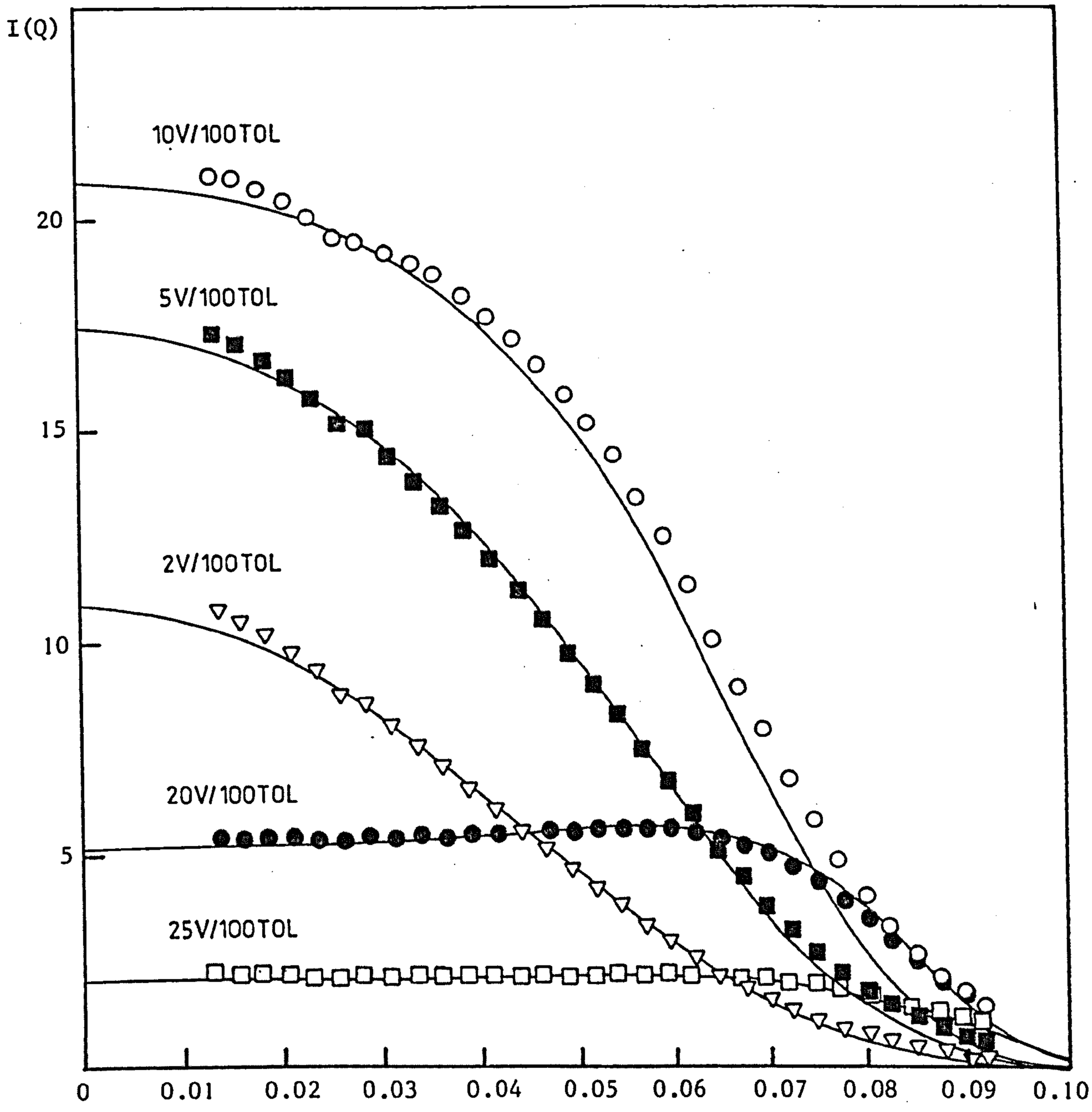

FIGURE 6.1 Absolute intensity, I(Q), against Q for a series of increasing concentration of V-particles in d_8 - toluene.

○ , ■ , ▽ , ● , □ , experimental data;

—— , calculated curves (refer to Tables 6.1 and 6.2)

TABLE 6.1 Results for the V/100 TOL series using the curve fitting approach

SAMPLE	(R_2-R_1)/Å	t_{HS}/Å
2V/100 TOL	18.0	11.0
5V/100 TOL	18.0	13.0
10V/100 TOL	18.4	12.5
20V/100 TOL	15.2	12.1
25V/100 TOL	11.6	9.2

The values of the volume fraction of the particles and the corresponding hard-sphere volume fractions, as well as the calculated values for the scattering length density of the dispersion medium are given for each sample in Table 6.2.

TABLE 6.2 Parameters used in the fitting of the V/100 TOL series

SAMPLE	ϕ_p	ϕ_{HS}	$\rho_m/10^{10}cm^{-2}$
2V/100 TOL	7.4×10^{-3}	2.46×10^{-2}	5.61
5V/100 TOL	1.8×10^{-2}	7.13×10^{-2}	5.50
10V/100 TOL	3.7×10^{-2}	1.40×10^{-1}	5.30
20V/100 TOL	8.0×10^{-2}	2.93×10^{-1}	4.70
25V/100 TOL	1.05×10^{-1}	2.96×10^{-1}	4.22

It is clear from Table 6.2 that owing to the comparatively large hard-sphere layer there is a considerable difference between the volume fraction of the core particles and the hard-sphere volume fraction. Furthermore, as the concentration of the particles increases there is more mineral oil present in the dispersion medium and the scattering length density of the dispersion medium decreases substantially.

Figure 6.2 shows the experimental results and the theoretical fits obtained for a series of V-particles in 70% deuterated toluene. The SANS measurements were carried out on the D17 diffractometer using a sample-to-detector distance of 2.83 m with the detector set at an angle beam of $2\theta = 6^{o}$ to the incident neutron beam of wavelength $\lambda = 10$ Å. This enabled the accessible Q-range to be increased to 0.15 $Å^{-1}$ and hence the peak in the intensity curves in the region $Q > 0.10$ $Å^{-1}$ can now be seen. A good match was obtained between the experimental and the theoretically calculated results using $R_1 = 22$ Å in the case of 2V/70 TOL and 5V/70 TOL (not shown), whereas 10V/70 TOL, 15V/70 TOL and 20V/70 TOL were fitted using $R_1 = 24$ Å. This discrepancy in the value of the core radius was attributed to a possible error in the intensity of the sample background which would be significant in this case where the absolute intensity values were low. A comparison with Figure 6.1 shows that a change in the dispersion medium from 100% d_8 - toluene to 70% d_8 - toluene decreases the absolute intensity by a factor of 2. This is exemplified by the fact that it was extremely difficult to fit 25V/70 TOL since in this case the intensity was practically zero. The values of the adsorbed layer thickness and the hard-sphere thickness used in the fitting procedure are listed in Table 6.3.

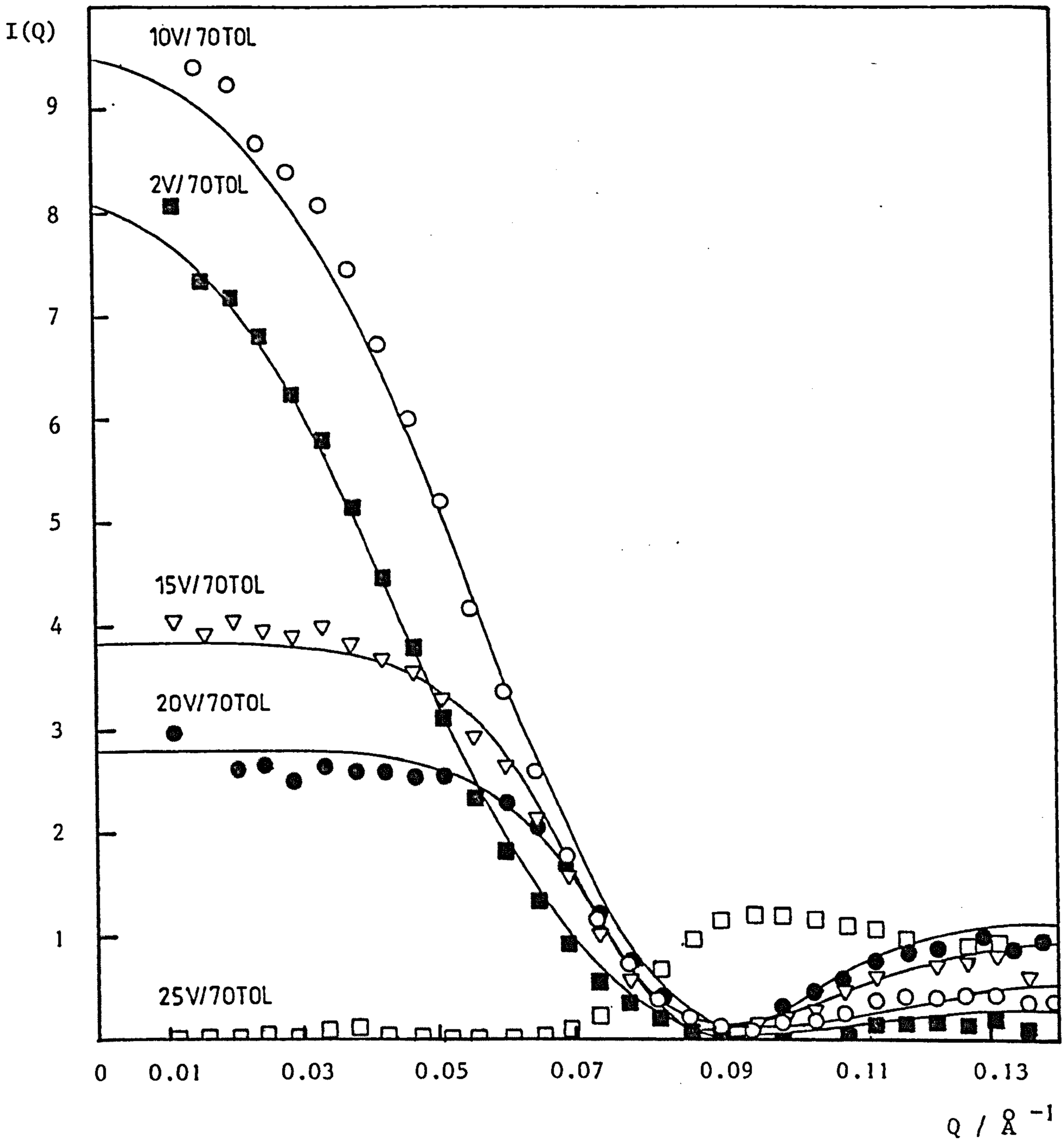

FIGURE 6.2 Absolute intensity, I(Q), against Q for a series of increasing concentration of V-particles in 70% d_8 - toluene.

○ , ■ , ▽ , ● , □ , experimental data;

—— , calculated curves (refer to Tables 6.3 and 6.4)

TABLE 6.3 Results for the V/70 TOL series using the curve fitting approach

SAMPLE	(R_2-R_1)/Å	t_{HS}/Å
2V/70 TOL	18.0	12.0
5V/70 TOL	16.5	12.7
10V/70 TOL	15.8	12.5
15V/70 TOL	13.8	12.5
20V/70 TOL	14.0	12.0

The values of the volume fraction of the particles, the hard-sphere volume fraction and the scattering length density of the medium used in the fitting of each sample are given in Table 6.4.

TABLE 6.4 Parameters used in the fitting of the V/70 TOL series

SAMPLE	ϕ_p	ϕ_{HS}	$\rho_m/10^{10}cm^{-2}$
2V/70 TOL	7.4×10^{-3}	2.46×10^{-2}	4.2
5V/70 TOL	1.8×10^{-2}	6.98×10^{-2}	4.1
10V/70 TOL	3.8×10^{-2}	1.29×10^{-1}	3.9
15V/70 TOL	6.0×10^{-2}	2.04×10^{-1}	3.7
20V/70 TOL	8.0×10^{-2}	2.61×10^{-1}	3.5

Figure 6.3 shows the results obtained for a series of V-particles dispersed in a mixture containing 30% h_{26} - dodecane and 70% d_8 - toluene so that the scattering length density of dispersion medium was ca. 0.5×10^{10} cm^{-2}. This solvent was chosen because the form of $[\bar{P}(Q)]_{c.s.}$ was particularly flat for this value of ρ_m (see Section 5.2). The SANS measurements were carried out on the D11 neutron diffractometer using a sample-to-detector distance of 2.66 m and an incident neutron beam wavelength of 8.0 Å. It is immediately obvious that the profile of the scattering curves is quite different from those of the preceding two series (Figures 6.1 and 6.2) in that they display pronounced peaks in the same Q-range (discussed further in Section 6.3). The values of the core radius, adsorbed layer thickness and hard-sphere thickness used in the fitting procedure are given in Table 6.5.

TABLE 6.5 Results for the V/DOD TOL series using the curve fitting procedure

	R_1/Å	(R_2-R_1)/Å	t_{HS}/Å
5V/DOD TOL	28.0	18	15.0
10V/DOD TOL	26.8	14.2	15.6
15V/DOD TOL	25.8	10	14.3

The value for the core radius used to fit the 5V/DOD TOL sample was identical to that obtained from the fitting of the dilute 1V/DOD TOL sample in Chapter 5. However, in order to fit the position of the peak in the intensity curves of the 10V/DOD TOL and the 15V/DOD TOL samples the value

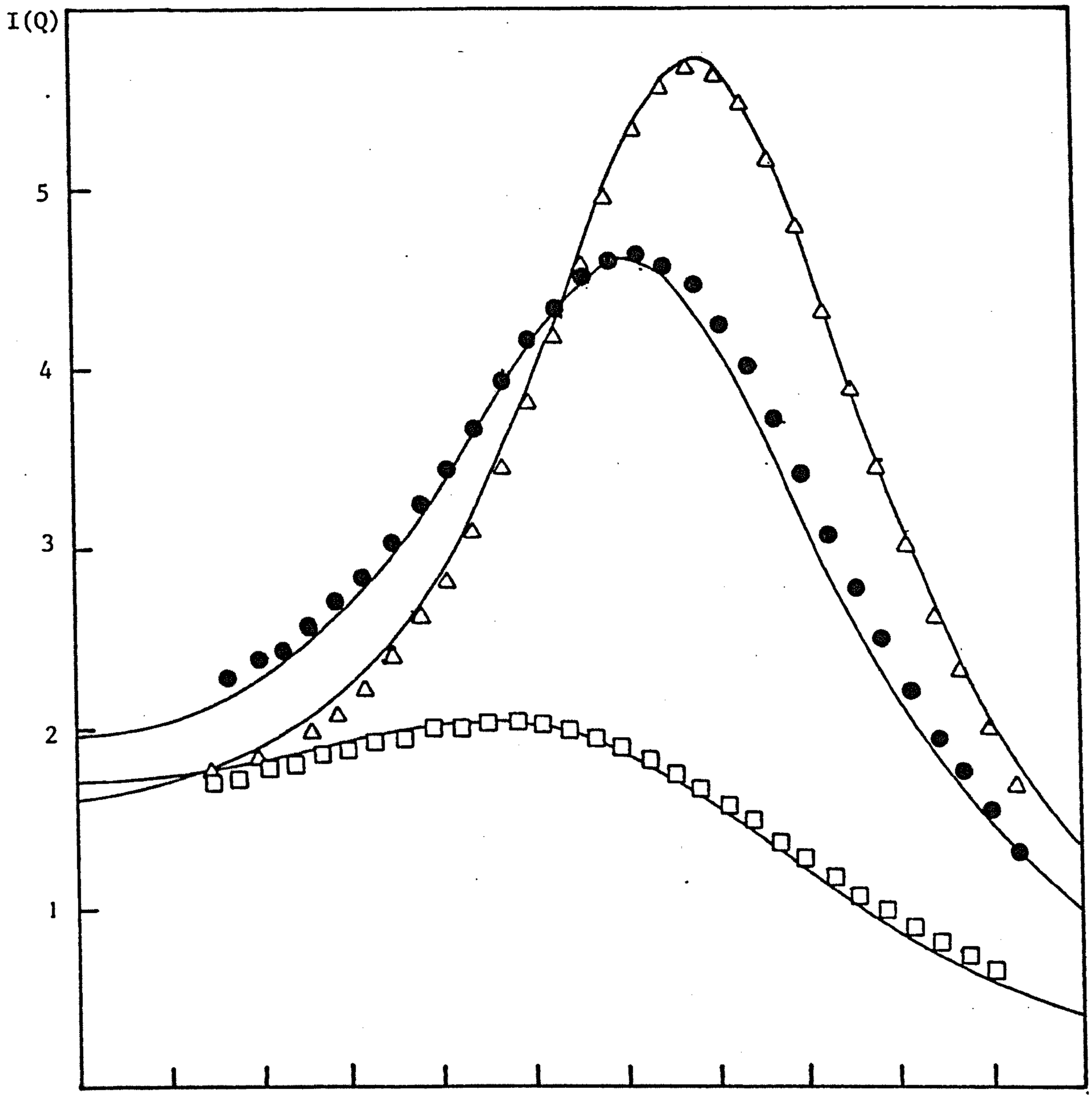

FIGURE 6.3 Absolute intensity, I(Q), against Q for the V/DOD TOL series of particles; ——— , calculated curves for:

□ , 5 V/DOD TOL; ● , 10 V/DOD TOL; △ , 15 V/DOD TOL

(refer to Tables 6.5 and 6.6)

of R_1 had to be decreased. The various parameters used in the fitting procedure are listed in Table 6.6.

TABLE 6.6 Parameters used in the fitting of the V/DOD TOL series

SAMPLE	ϕ_p	ϕ_{HS}	$\rho_m/10^{10}cm^{-2}$
5V/DOD TOL	1.9×10^{-2}	6.77×10^{-2}	0.46
10V/DOD TOL	4.2×10^{-2}	1.65×10^{-1}	0.42
15V/DOD TOL	6.0×10^{-2}	2.21×10^{-1}	0.40

The experimental results obtained for a series of V-particles dispersed in h_8 - toluene are shown in Figures 6.4 and 6.5. The SANS measurements were carried out on the D17 diffractometer using a sample-to-detector distance of 1.40 m and an incident nuetron beam wavelength of 9 Å. Although these samples displayed pronounced peaks in the intensity curves similar to those of the V/DOD TOL series, a comparison of 10V/0 TOL (Figure 6.4) and 10V/DOD TOL (figure 6.3) shows that in the case of the former the absolute intensity had decreased by a factor of ~2.1. Moreover, it was shown in Section 5.2 of Chapter 5 that $[\overline{P(Q)}]_{c.s.}$ for a V-sample dispersed in toluene also displayed a sharp peak. Consequently, it was impossible to obtain a reasonable match between the experimental data for this series and the theoretically calculated curve (this is further discussed in Section 6.3).

Figure 6.6 shows the experimental data for 10V/0 TOL and 20V/0 TOL determined at a later date. On this occasion the D17 diffractometer was used with a sample-to-detector distance of 1.41 m and an incident neutron beam wavelength of 10.0 Å. The measurements were first carried out with

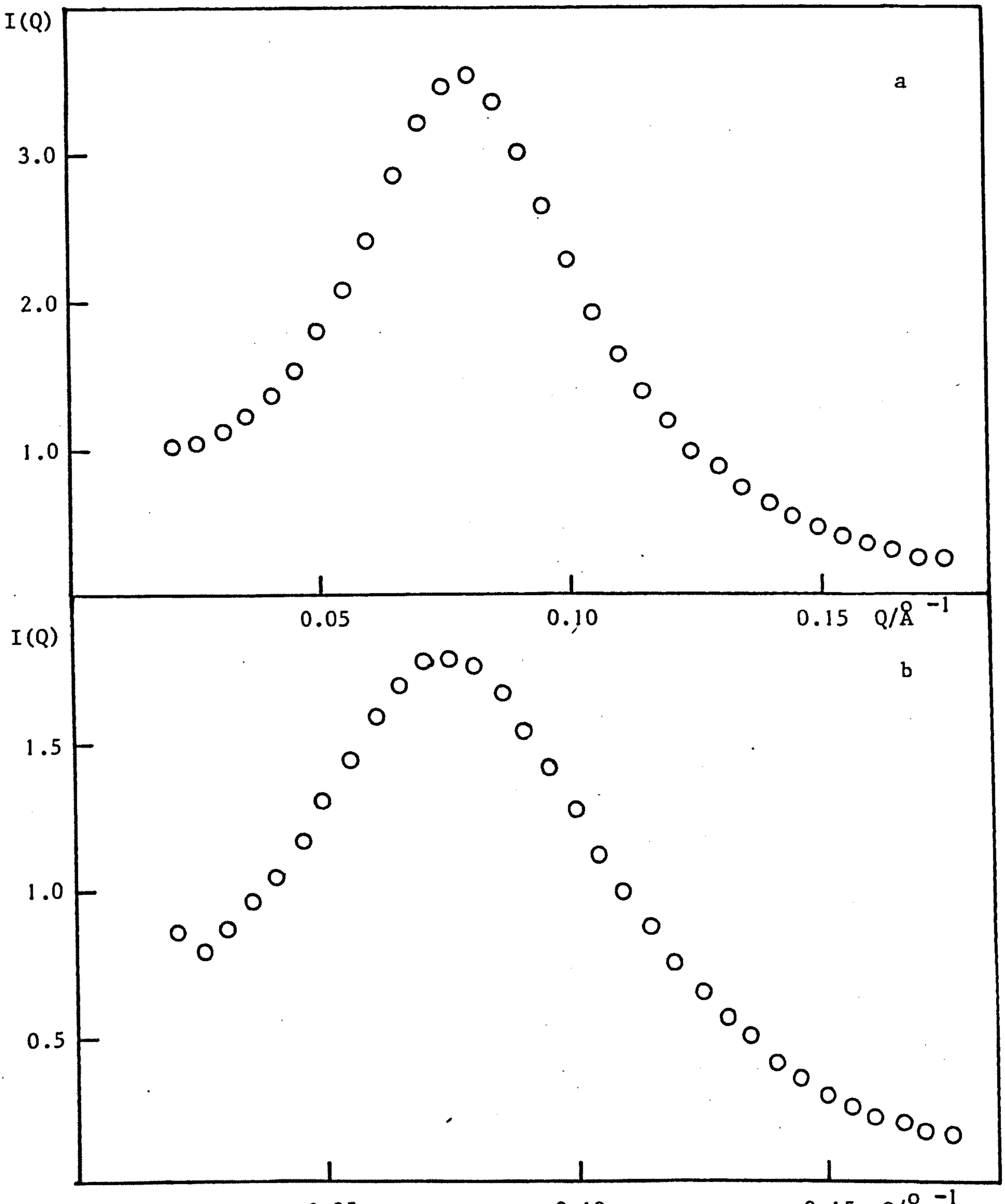

FIGURE 6.4 Experimental I(Q) against Q for V-particles in h_8 - toluene.

O , experimental data for

a) 20 V/O TOL and

b) 10 V/O TOL

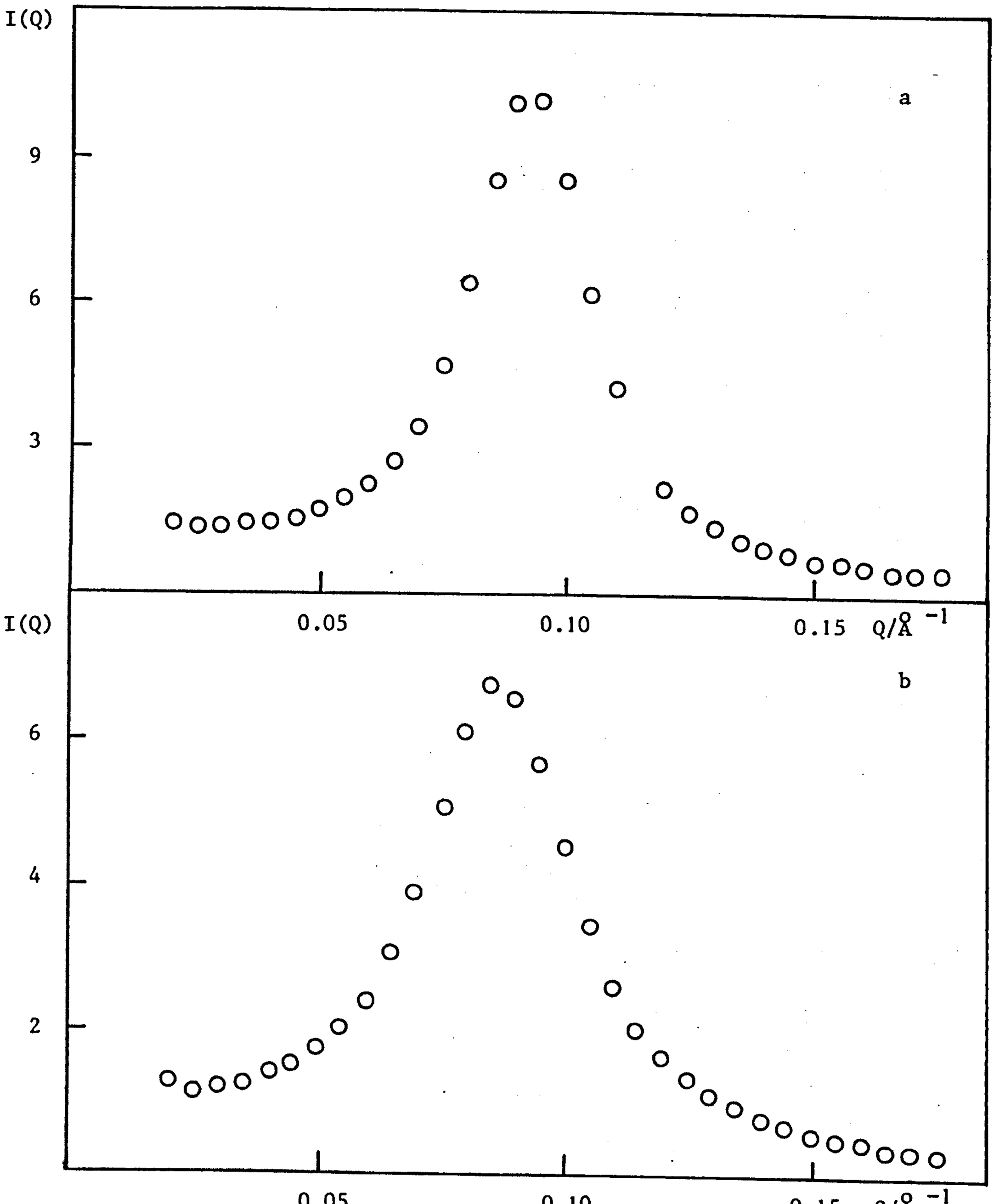

FIGURE 6.5 Experimental I(Q) against Q for V-particles in h_8 - toluene.

O , experimental data for

a) 30 V/O TOL and

b) 25 V/O TOL

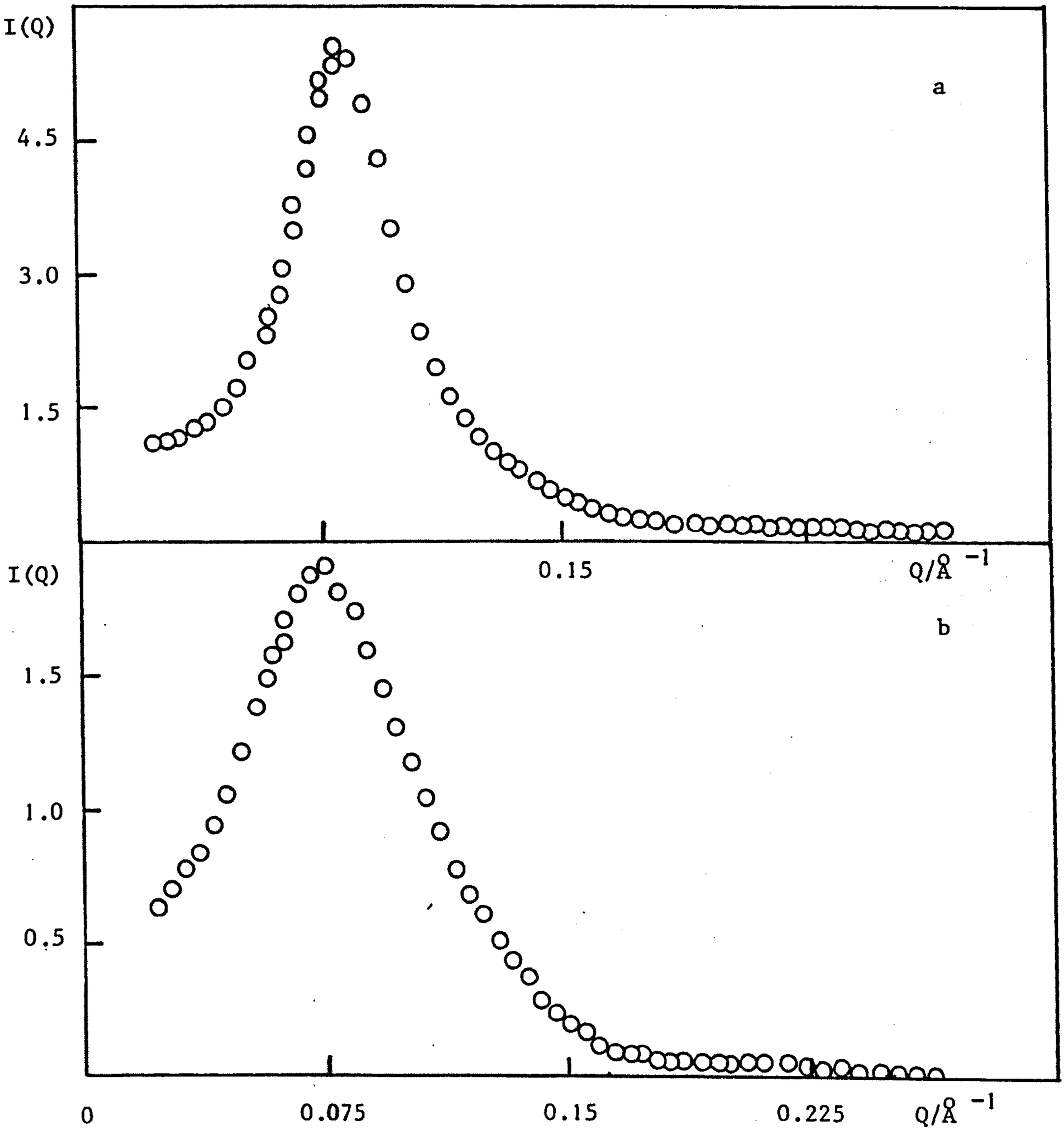

FIGURE 6.6 Experimental I(Q) against Q for V-particles in h_8 - toluene.

O , experimental data for

a) 20 V/O TOL and

b) 10 V/O TOL

the detector set at an angle of $2\theta = 2^{o}$ and then, in order to increase the accessible Q-range, at an angle of $2\theta = 12^{o}$. The two sets of data which overlapped in the middle Q-region were found to coincide. A comparison with Figure 6.4 shows that, within experimental error, identical values for the absolute intensities were obtained on the two occasions; once again, it was impossible to fit the experimental data to a theoretically calculated intensity curve.

The L'-series

The experimental results obtained for a series of seven samples of varying concentration of L'-particles, dispersed in h_8 - toluene, are shown in Figure 6.7. These measurements were carried out using the D11 neutron diffractometer with a sample-to-detector distance of 5.66 m and an incident neutron beam wavelength of 8.0 Å. This resulted in a Q-range of 0 to 0.05 $Å^{-1}$. It is clear from Figure 6.7 that, as the concentration of the particles increased, the height of the intensity peak also increased and, furthermore, the position of the peak moved to higher values of Q. Each of the samples of this series was fitted to a theoretically calculated curve and this is illustrated in Figures 6.8 to 6.12. The various parameters used in the fitting procedure of this series are given in Table 6.7.

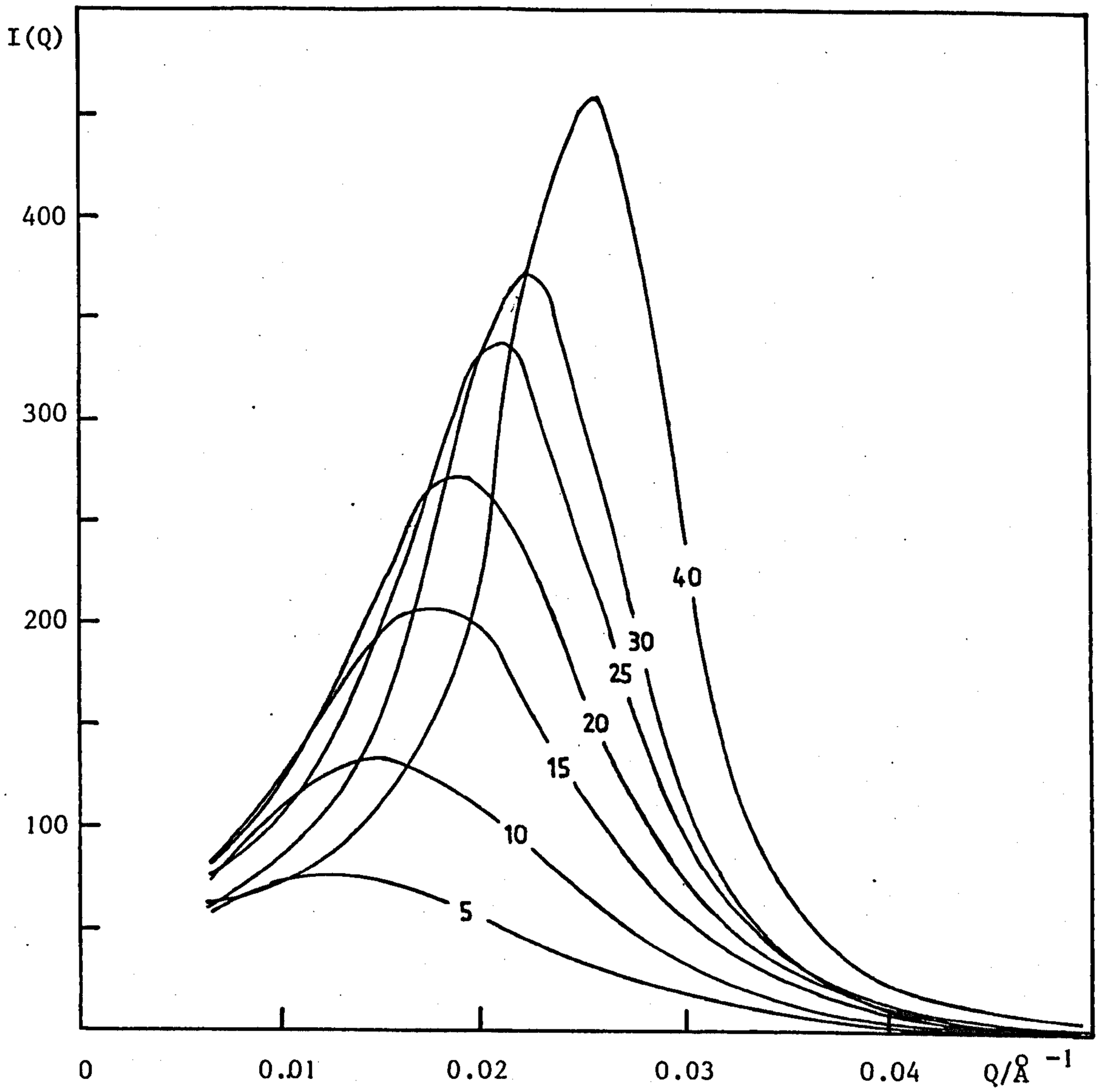

FIGURE 6.7 Experimental I(Q) against Q for a series of increasing concentration of L'-particles from 5% w/w $CaCO_3$ up to 40% w/w $CaCO_3$

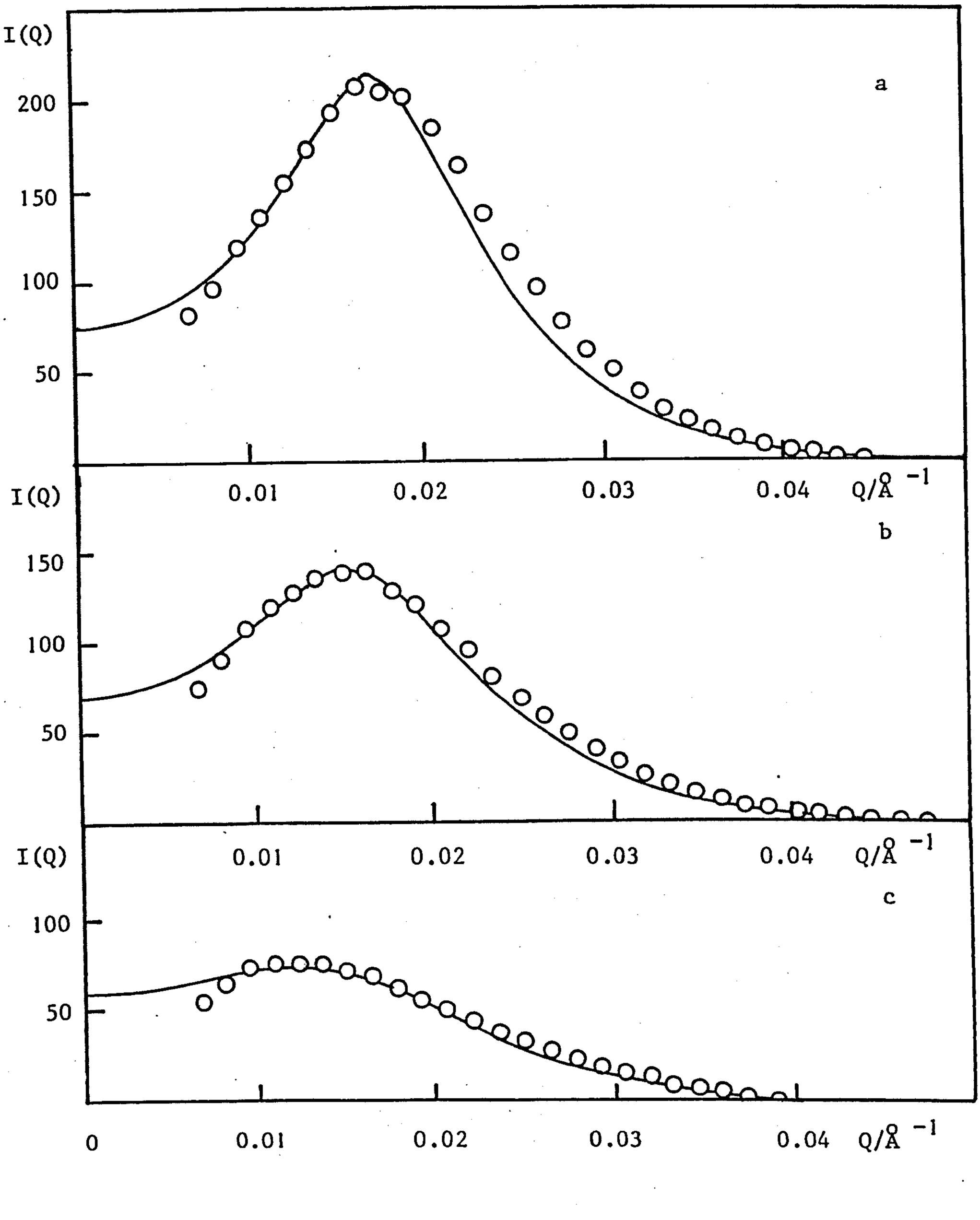

FIGURE 6.8 Absolute intensity, I(Q), against Q

O , experimental data; —— , calculated curves for

a) 15 L'/O TOL

b) 10 L'/O TOL

c) 5 L'/O TOL

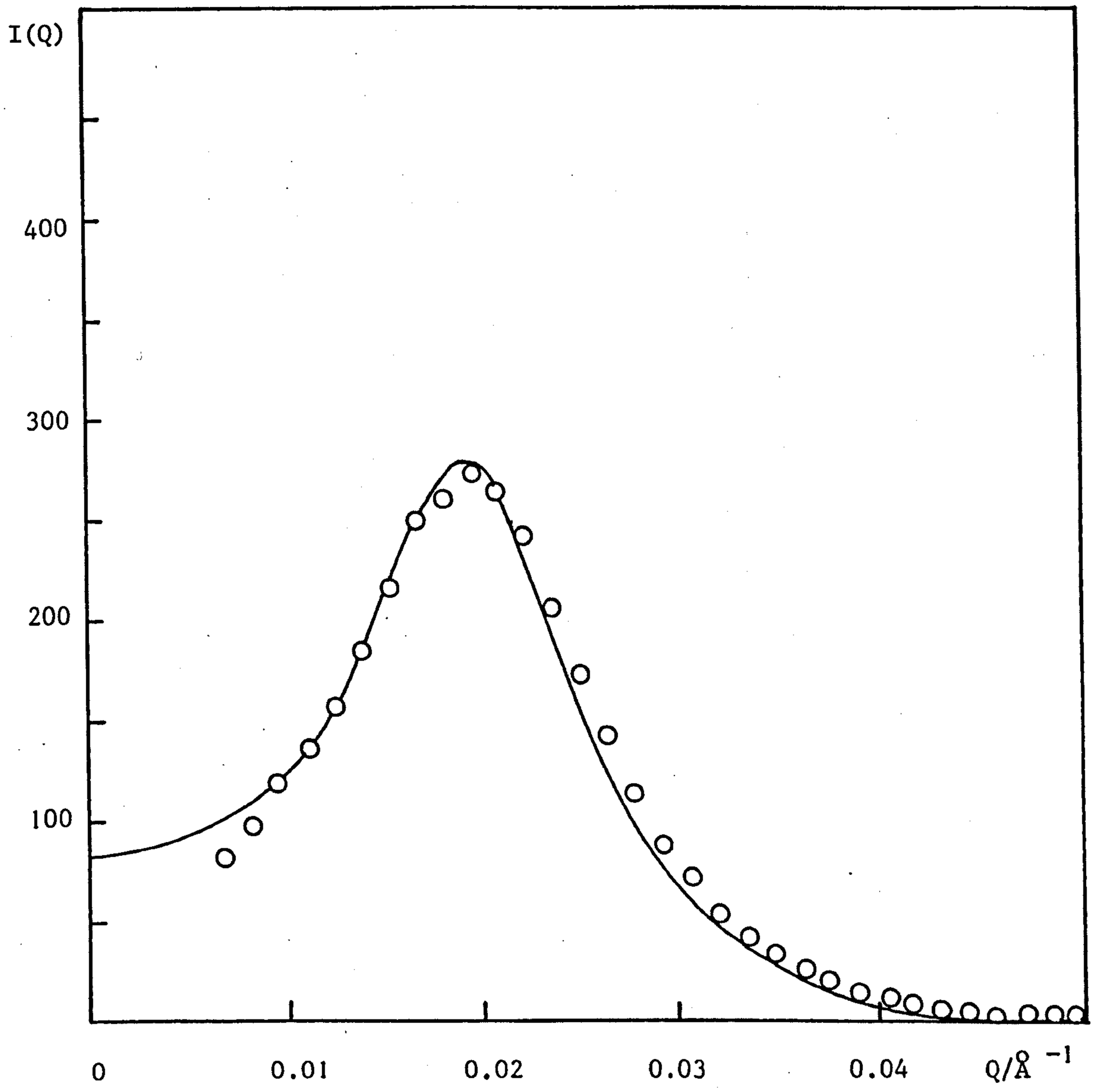

FIGURE 6.9 Absolute intensity, I(Q), against Q for 20 L'/0 TOL

O , experimental data;

—— , calculated intensity curve

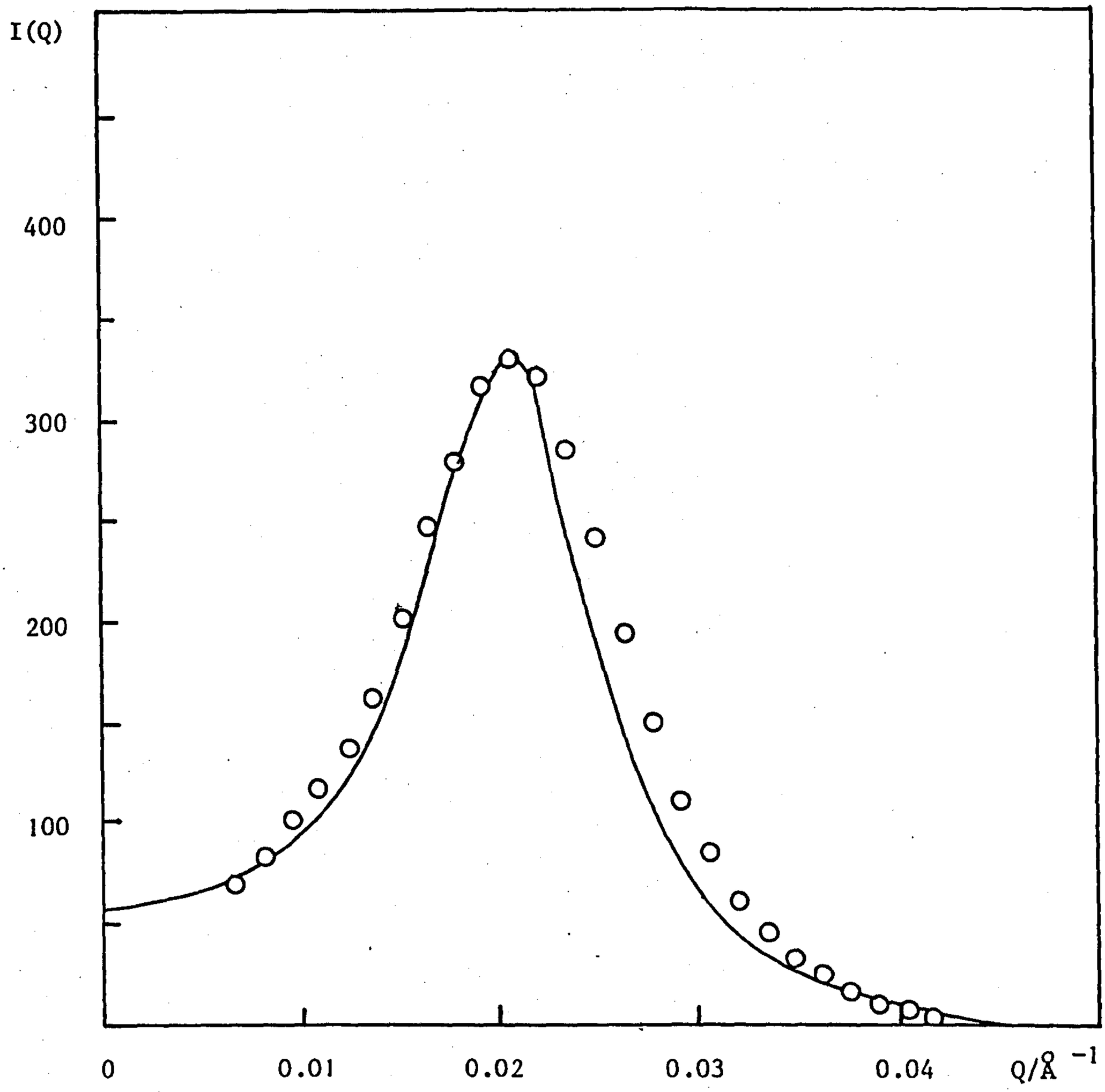

FIGURE 6.10 Absolute intensity, I(Q), against Q for 25 L'/0 TOL

O , experimental data; ——— , calculated curve

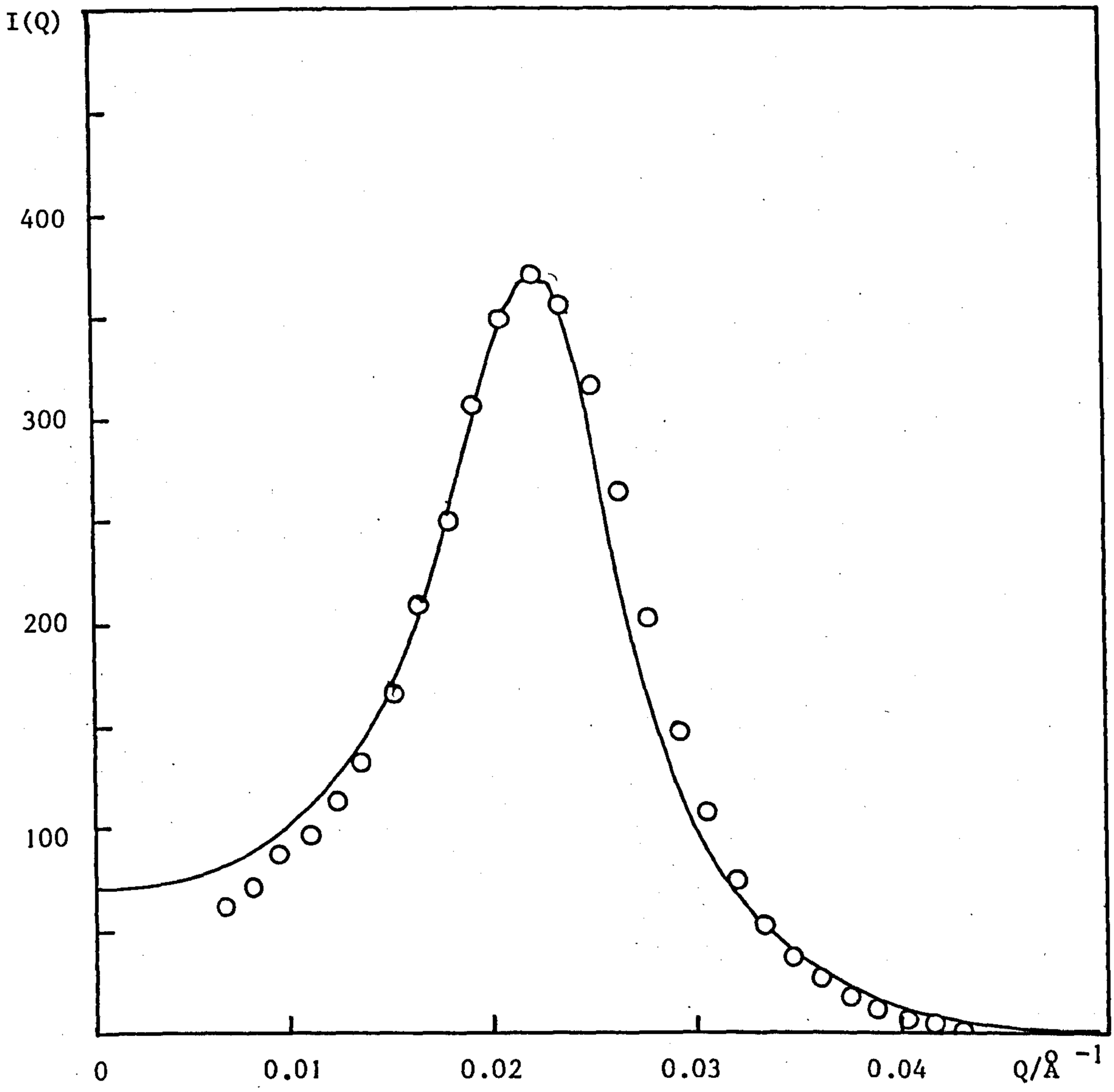

FIGURE 6.11 Absolute intensity, I(Q), against Q for 30 L'/0 TOL

O , experimental data; —— , calculated curve

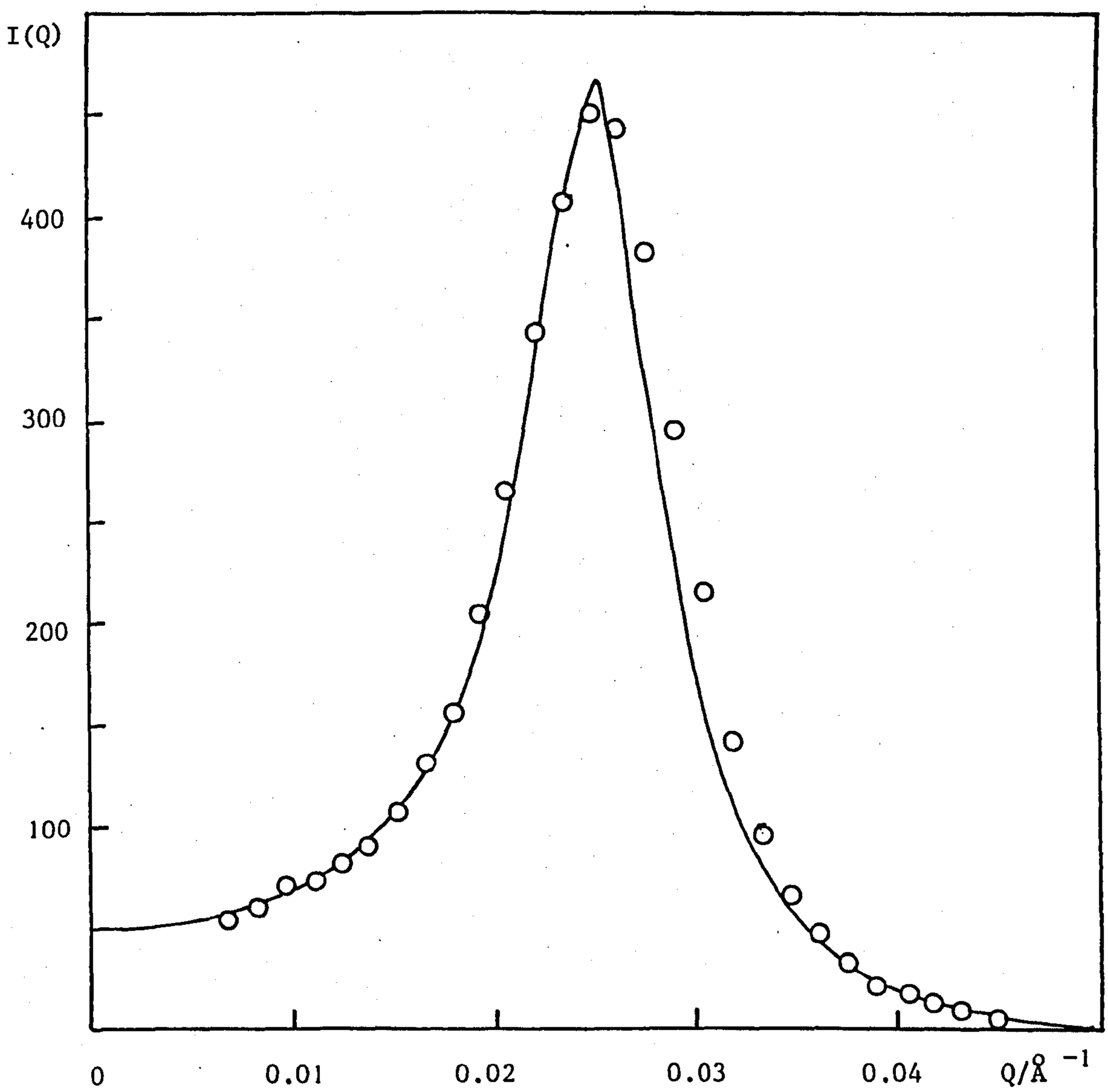

FIGURE 6.12 Absolute intensity, I(Q) against Q for 40 L'/0 TOL

O , experimental data; ——— , calculated curve

TABLE 6.7 Results for the L'-series using the curve fitting approach

SAMPLE	FIGURE NO.	R_1/Å	(R_2-R_1)/Å	t_{HS}/Å	ϕ_P	ϕ_{HS}	$\rho_m/10^{10}cm^{-2}$
5L'/0 TOL	6.8	105	26	60	2.0×10^{-2}	7.64×10^{-2}	0.85
10L'/0 TOL	6.8	103	26	56	4.0×10^{-2}	1.45×10^{-1}	0.80
15L'/0 TOL	6.8	103	26	50	6.0×10^{-2}	1.94×10^{-1}	0.69
20L'/0 TOL	6.9	100	26	42	8.0×10^{-2}	2.26×10^{-1}	0.65
25L'/0 TOL	6.10	100	26	41	1.02×10^{-1}	2.82×10^{-1}	0.60
30L'/0 TOL	6.11	98	26	33	1.25×10^{-1}	2.95×10^{-1}	0.51
40L'/0 TOL	6.12	95	26	28	1.70×10^{-1}	3.65×10^{-1}	0.40

6.3 Discussion

The results presented above consisted of obtaining a match between the experimental and the theoretically calculated absolute scattering intensities. The quintessence of this approach is in not only theoretically matching the shape, peak position, etc., of the experimental curve but the exact values of *the absolute intensity*. Moreover, this curve fitting procedure is very sensitive to the values chosen for the various parameters in the calculation of $(d\sigma/d\Omega)^{conc}_{c.s.}$ This is exemplified in Figure 6.13 which shows the effect on the fit of altering the particle core radius and the shell thicknesses for two samples, namely 15L'/0 TOL and 15V/DOD TOL. In both cases the solid line represents the best theoretical fit, as depicted in Figures 6.3 and 6.8; the dashed line represents the effect of increasing the particle core radius by 1 Å, and the dash-dotted line represents the effect of simultaneously decreasing the adsorbed layer thickness by 1 Å and increasing the hard-sphere thickness by 1 Å. It is clear from Figure 6.13 that the fits are most sensitive to the value chosen for the particle core radius, R_1; this is amplified in the case of 15V/DOD TOL because the values of the absolute intensity are very much smaller than those for 15L'/0 TOL. The main consequence of changing the two shell thicknesses is an alteration in the height of the I(Q) peak. Furthermore, it was found that the fitting procedure was sensitive to the value chosen for the scattering length density of the dispersion medium, especially when the value of ρ_m was close to that of the contrast match point of the particles (see later). In practice, it was found that the theoretically calculated absolute intensity was least affected by the value used for the polydispersity parameter σ_o. This was probably due to the low values of σ_o (σ_o (ca. 0.1) for the systems in this study. Moreover, van Beurten and Vrij[44] have shown that there is no appreciable influence of polydispersity

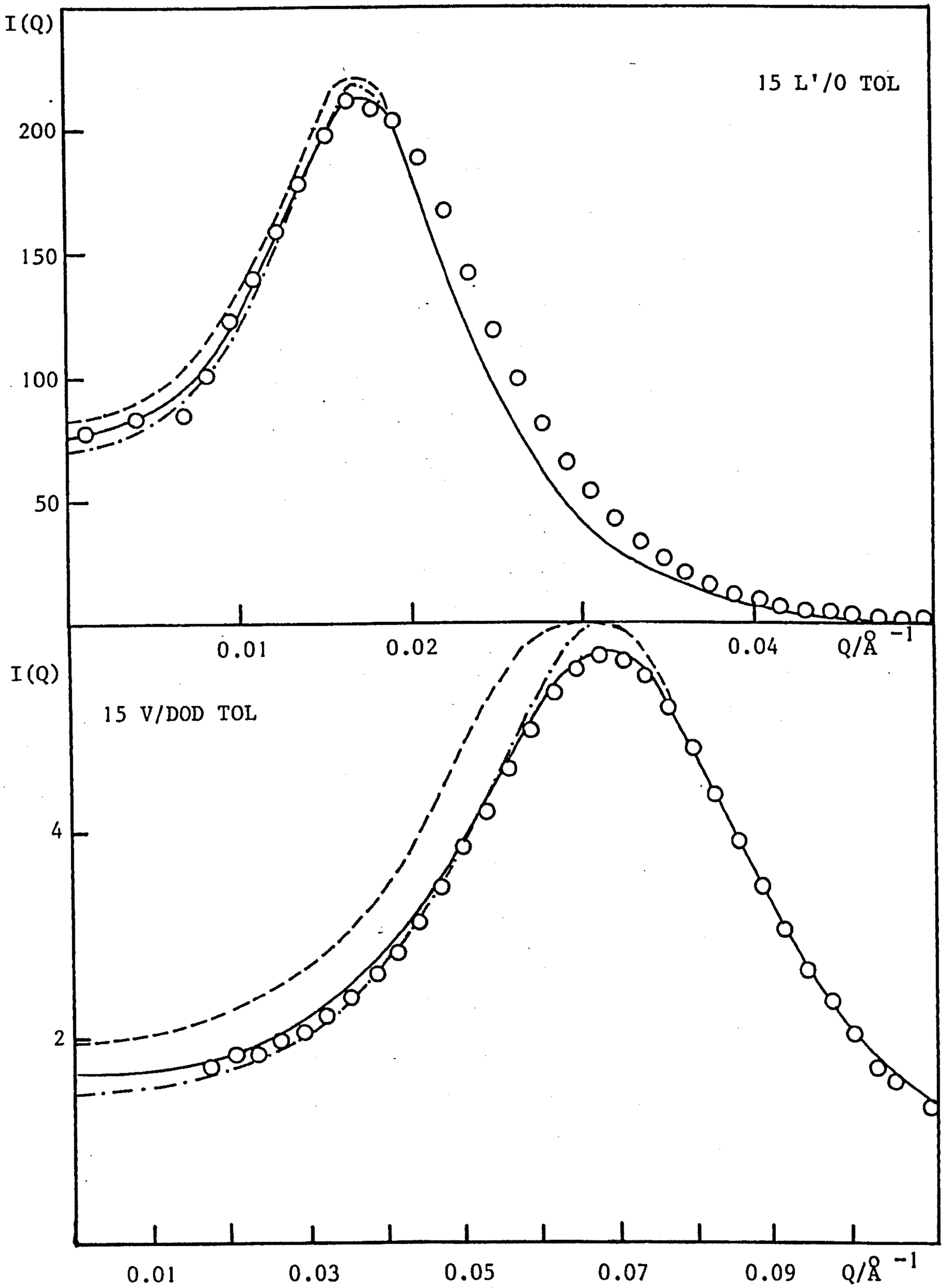

FIGURE 6.13 Sensitivity of curve fitting procedure

O, experimental data; ——— , best theoretical fit;

---, R_1 + 1 Å; —·—·—, (R_2-R_1) - 1 Å and t_{HS} + 1 Å.

on the interparticle structure factor, S(Q), if the standard deviation of the size distribution is less than ≃0.1.

The V-series

It is clear from Figures 6.1 to 6.12 in the preceding section that a very good match was obtained between the experimental and the theoretically calculated absolute intensity curves for most of the samples in this study. The only exception to this was the V/O TOL series which could not be fitted to a calculated curve. However, it was shown in Section 5.2.2 of Chapter 5 that the intraparticle form factor for a concentric sphere displays a pronounced peak when the scattering length density of the medium is just below that of the contrast match point of the particles - the situation for the V-particles dispersed in h_8 - toluene (see Figure 5.24 showing $[\bar{P}(Q)]_{c.s.}$ for 2V/O TOL). Moreover, the height of the $[\bar{P}(Q)]_{c.s.}$ peak is exceedingly sensitive to the actual value of ρ_m. In addition, the $[\bar{P}(Q)]_{c.s.}$ peak position occurs approximately in the same Q-range as the expected first maximum in S(Q) for the V-particles. Consequently, the pronounced peaks seen in the intensity curves for the V/O TOL series are the product of a maximum in $[\bar{P}(Q)]_{c.s.}$ and a maximum in S(Q) and ipso facto impossible to fit. Moreover, the values of the absolute intensities for this series were very low. Hence, it is advisable, from an experimental point of view, to simulate theoretically or to determine experimentally the form of $[\bar{P}(Q)]_{c.s.}$ for a sample prior to carrying out measurements on the concentrated sample.

In the case of the other three series of V-particles, the scattering length density of the medium was substantially different from the contrast match point of the particles so that the profile of $[\bar{P}(Q)]_{c.s.}$ was that of a single, isotropic sphere. In particular, for the case of the V/DOD TOL series, the dispersion medium was chosen because the curve fitting of the

dilute sample (see Figure 5.25, Chapter 5) had shown that the profile of $[\bar{P}(Q)]_{c.s.}$ was essentially flat for this value of ρ_m, which facilitates the fitting of the structure factor S(Q). Consequently, a good match was obtained for all three series between the experimental data and the calculated curves. However, it can be seen in Tables 6.1, 6.3 and 6.5 that in order to fit a series of increasing concentration of particles, the thickness of the adsorbed layer (and in some cases the particle core radius) had to be progressively decreased. Hence, the intraparticle form factor was changing throughout each series, and the method of determining S(Q) by dividing the intensity of a concentrated sample by that of a dilute sample (equation (6.23)) could not be applied. Thus, the theoretically calculated hard-sphere structure factor used to obtain a fit to the experimental data was assumed to be analogous to the experimental S(Q).

Figure 6.14 shows the Percus-Yevick structure factor used in the theoretical fitting of the V/70 TOL series. It is clear from Table 6.3 that in the fitting procedure carried out for this series a nearly constant value of 12 Å was used for the hard-sphere thickness, whereas the value of the adsorbed layer thickness decreased as the concentration of the particles increased. A possible explanation for the progressive decrease in the value of $(R_2 - R_1)$ is that as the total volume fraction of the particles increases, desorption of some of the surface active molecules occurs with concomitant compression of the remaining surface active agent. It was postulated in Section 5.1.3 of Chapter 5 that the surface active agent adsorbs in a wedged shape conformation on the surface of the calcium carbonate core; in addition, for the case of the F-series (prepared with a smaller amount of S.A.A. than the other two series) the relatively low value obtained for $(R_2 - R_1)$ was attributed to the stabilizer occupying a

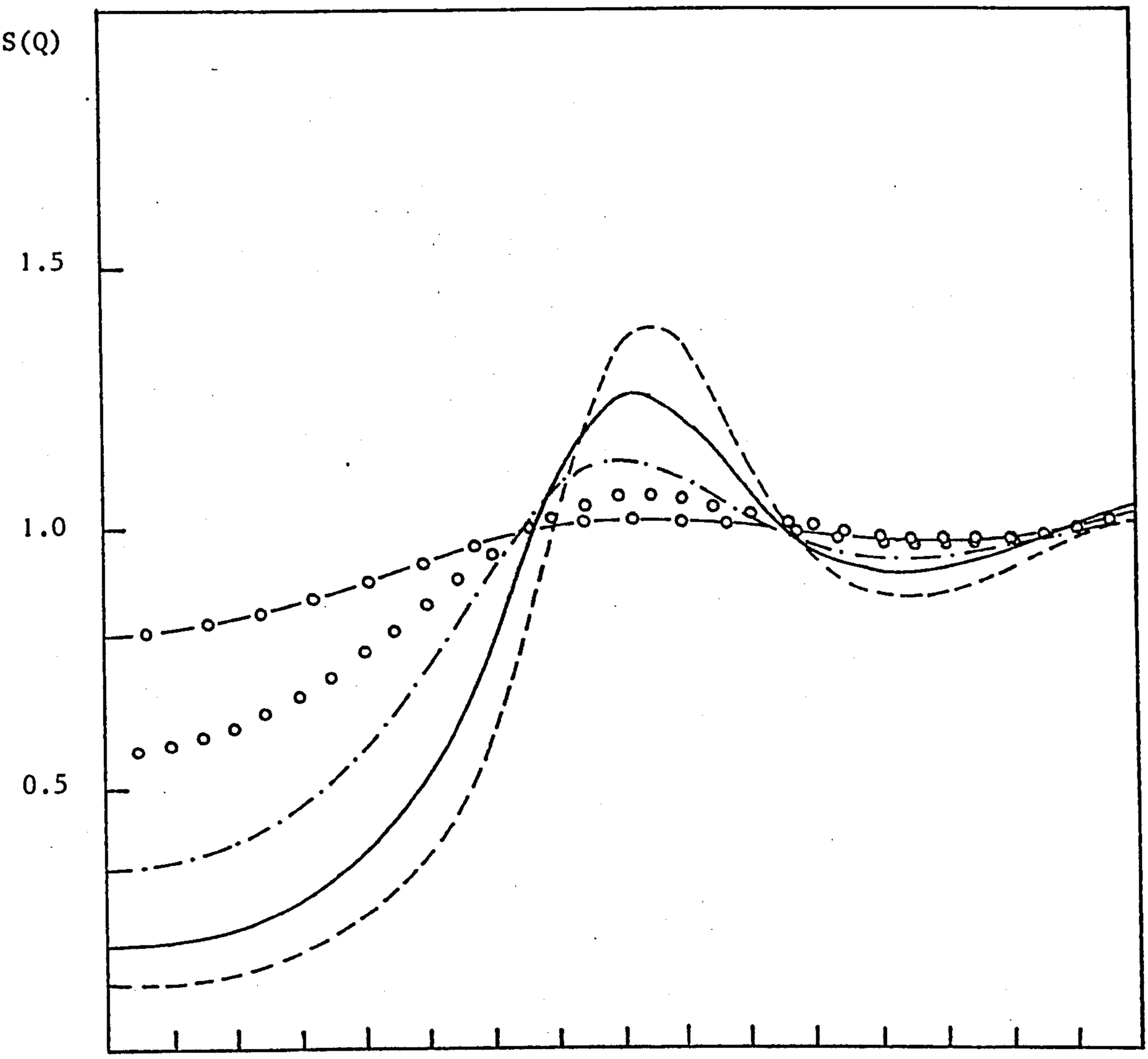

FIGURE 6.14 Theoretical S(Q) against Q for V/70 TOL series

—o—o— , 2 V/70 TOL

ooo , 5 V/70 TOL

·—·—·—, 10 V/70 TOL

———, 15 V/70 TOL

– – – –, 20 V/70 TOL

larger surface area per molecule, i.e. exhibiting a more pronounced wedge shape. In the case of the V/70 TOL series, the hard-sphere thickness was smaller than the adsorbed layer thickness so that interpenetration of the adsorbed layers could occur, resulting in desorption of some of the stabilizer which, in turn, would enable the surface active agent molecules on the particle to occupy a larger surface area. The concordance obtained in the trend of the values for both $(R_2 - R_1)$ and t_{HS} for the three V-series tends to support this hypothesis. It is interesting to note that the value for the hard-sphere thickness used to obtain a fit to the experimental data of the V/DOD TOL series was ~15 Å and that the values of $(R_2 - R_1)$ were slightly lower than those for the corresponding samples in the other series. The latter effect could be a consequence of inter alia the fact that the scattering length density of the medium ($\simeq 0.5 \times 10^{10}$ cm^{-2}) was similar to that of the adsorbed layer (0.35×10^{10} cm^{-2}) causing the fitting of this parameter to be less accurate. However, no problems were encountered in the fitting of the dilute sample, 1V/DOD TOL, in Chapter 5 and the results obtained were consistent with those of the other V-samples. The increase in the hard-sphere thickness appears to signify that the onset of steric repulsion occurs at a greater distance of separation between the two $CaCO_3$ core particles than in the case of the other V-series. The presence of the dodecane molecules in the dispersion medium will affect both of the terms which control the energy of steric interaction, namely the mixing term and the entropic term (see Chapter 2). Since the dodecane molecules are of a similar chemical nature to the surface active chains, the free energy of mixing will differ from that with only toluene as the dispersion medium, whereas the presence of these molecules in the region of interaction will influence the volume restriction term. Figure 6.15 shows the theoretical hard-sphere structure factors used to fit the V/DOD TOL series.

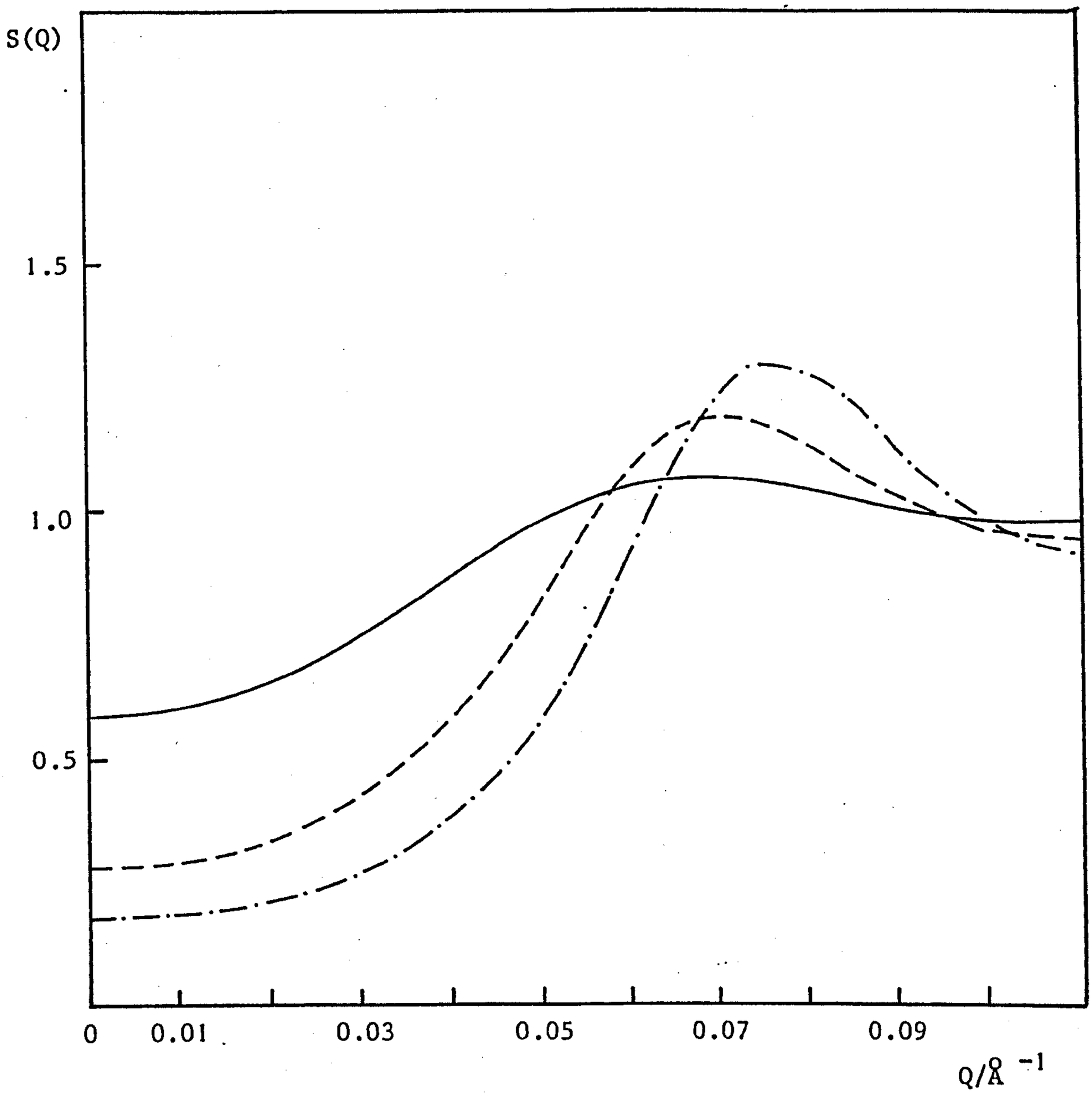

FIGURE 6.15 Theoretical S(Q) against Q for V/DOD TOL series

——— , 5 V/DOD TOL

– – – – , 10 V/DOD TOL

—·—·— , 15 V/DOD TOL

The L'-series

It can be seen from the preceding section that a good match was obtained between the theoretically calculated scattering curves and the experimental data for all seven samples of the L'-series. However, in contradistinction to the V-series, the adsorbed layer thickness remained constant throughout the series and furthermore, its value was always lower than that of the hard-sphere thickness. Indeed, in the case of the most dilute sample, the value of t_{HS} was as much as 2.3 times greater than that of $(R_2 - R_1)$. Although there was a change of 10 Å in the value used for the particle core radius, it did not alter significantly the form of $[\overline{P(Q)}]_{c.s.}$ Hence, it could be assumed that the intraparticle form factor was the same for all the samples in the series so that S(Q) could be determined by dividing the intensity for the concentrated sample by that for the dilute sample and correcting for the difference in the volume fractions. This was carried out for all the samples in the series, using the data for 1L'/0 TOL (see Section 5.2 of Chapter 5) for the dilute sample. It was then possible to compare the experimentally determined structure factor with the theoretical hard-sphere structure factor used in the fitting procedure.

Figures 6.16 to 6.20 show the match obtained between the experimental S(Q) and the theoretical hard-sphere S(Q) for the samples of the L'-series. It can be seen that a very good match was obtained for all the samples, especially in the low Q-region and in terms of the height and position of the first maximum in S(Q). In the case of the less concentrated samples (i.e. up to 25L'/0 TOL) it was difficult to match the width of the peak, whereas a good agreement was obtained up to the first minimum in S(Q) for 30L'/0 TOL and 40L'/0 TOL (see later).

It was already mentioned that the value used in the fitting procedure

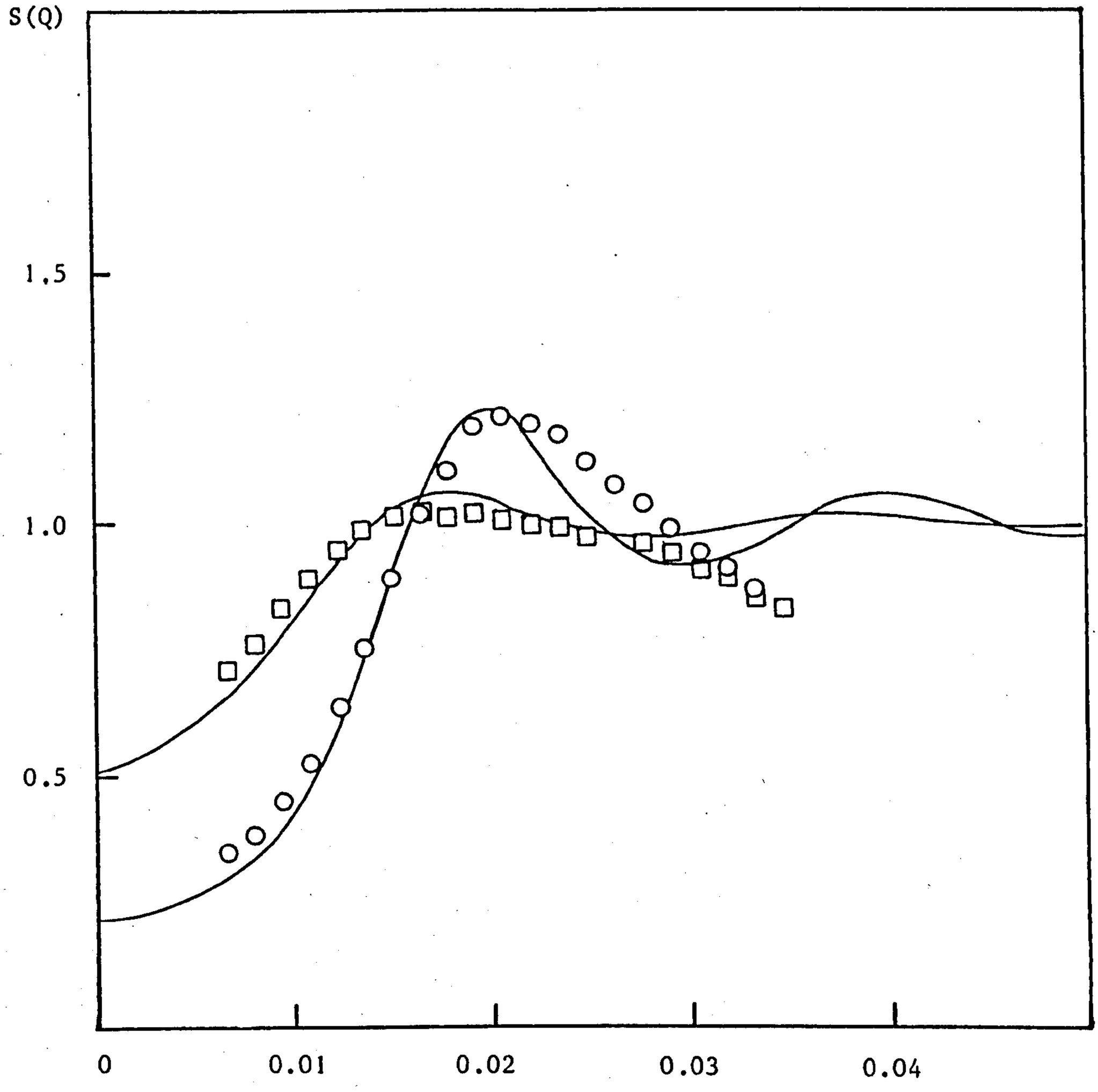

FIGURE 6.16 S(Q) against Q for two samples of the L'/0 TOL series

——— , calculated hard-sphere S(Q);

□ , experimental S(Q) for 5 L'/0 TOL;

○ , experimental S(Q) for 15 L'/0 TOL.

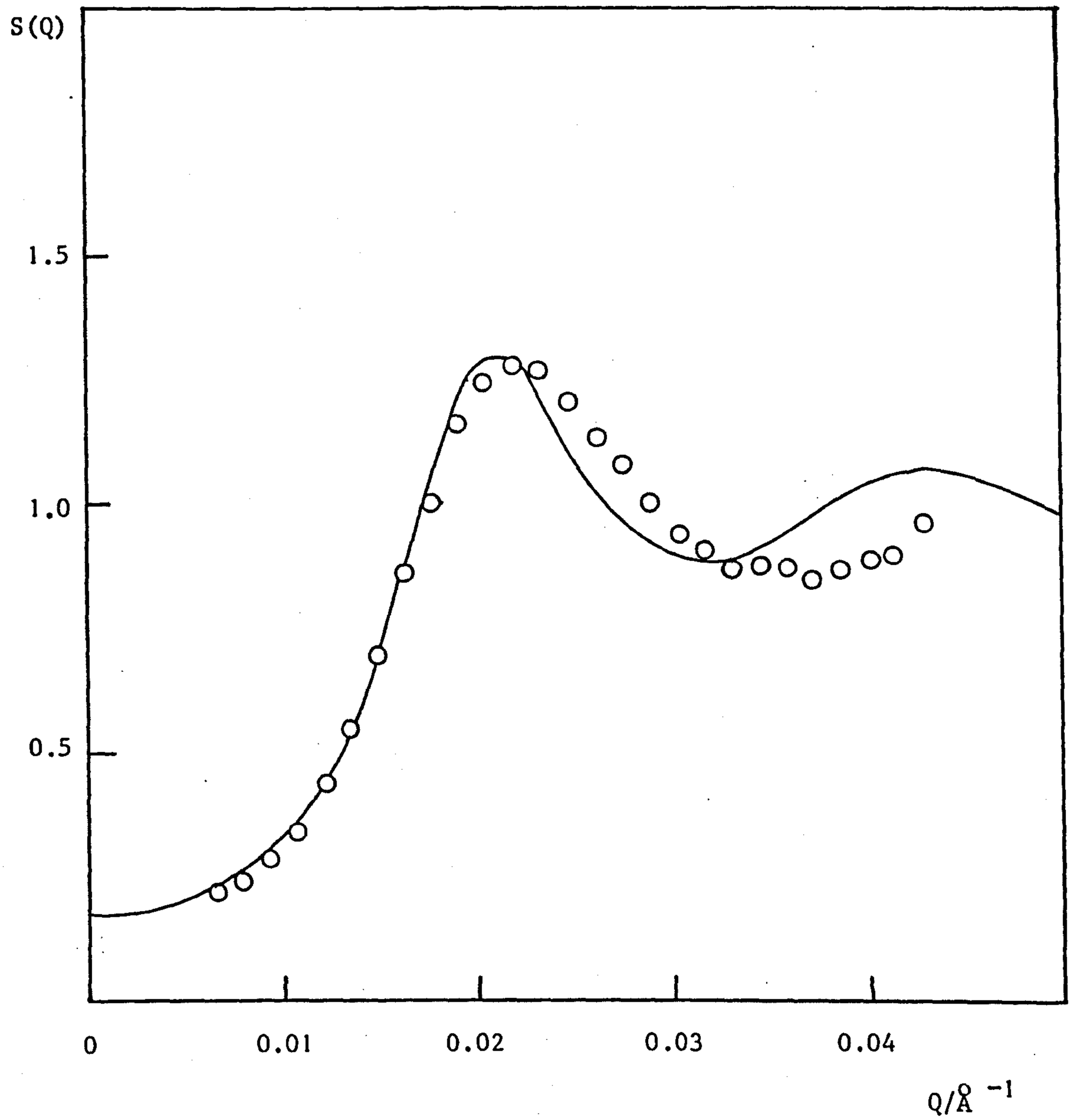

FIGURE 6.17 S(Q) against Q for 20 L'/0 TOL

——, calculated hard-sphere S(Q)

O , experimental S(Q)

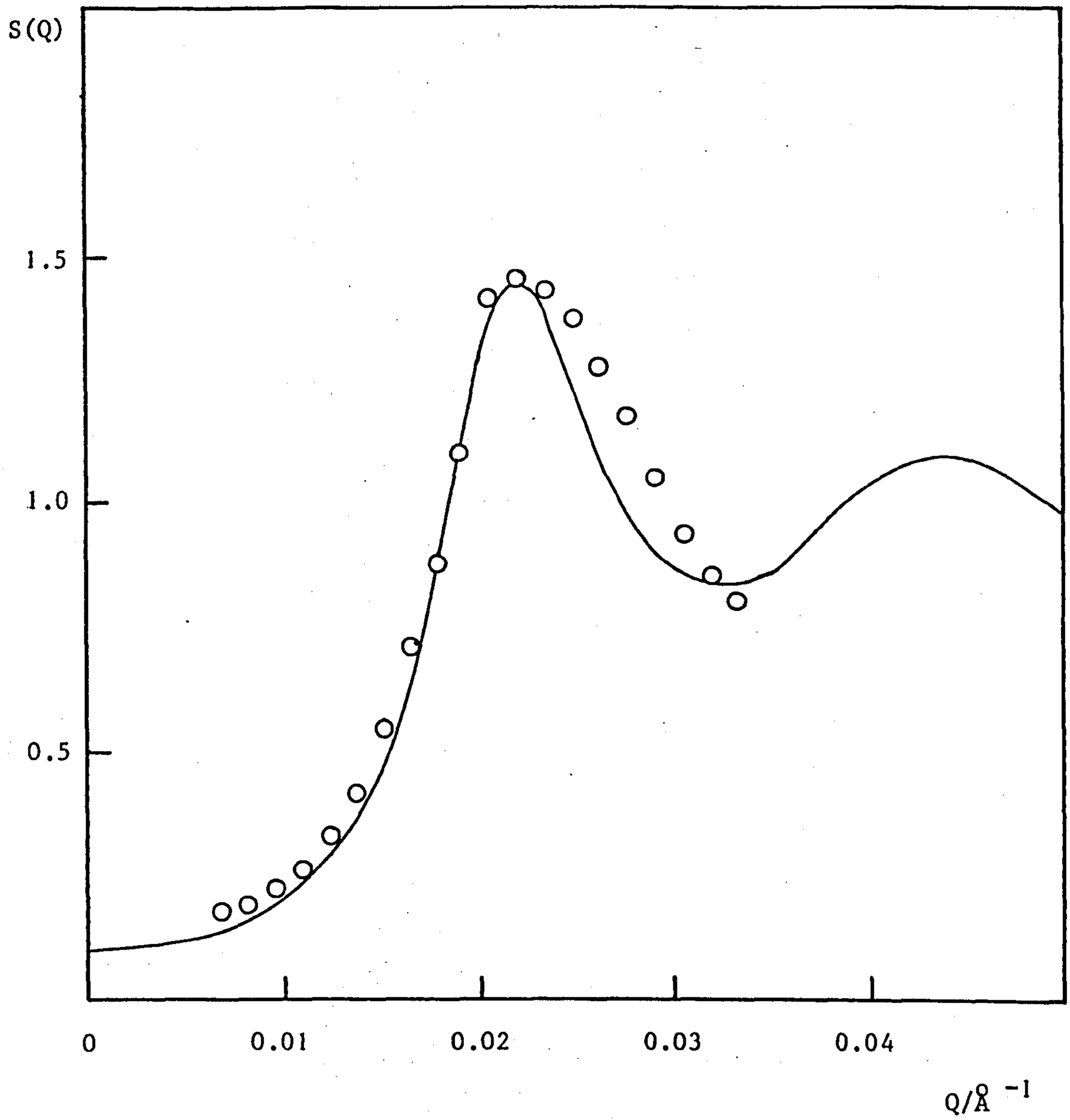

FIGURE 6.18 S(Q) against Q for 25 L'/0 TOL

——, calculated hard-sphere S(Q);

O , experimental S(Q)

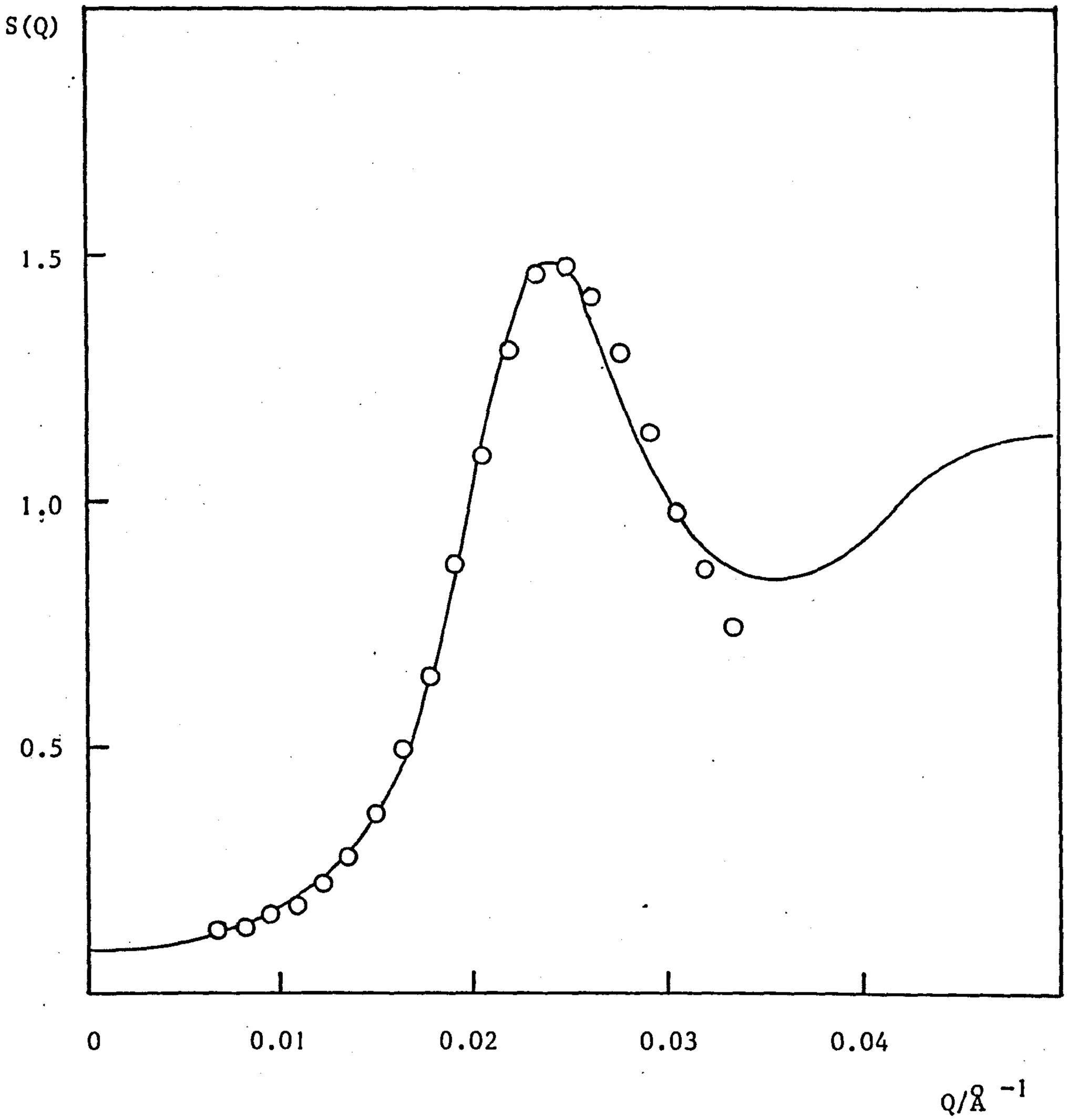

FIGURE 6.19 S(Q) against Q for 30 L'/0 TOL

——, calculated hard-sphere S(Q);

O , experimental S(Q)

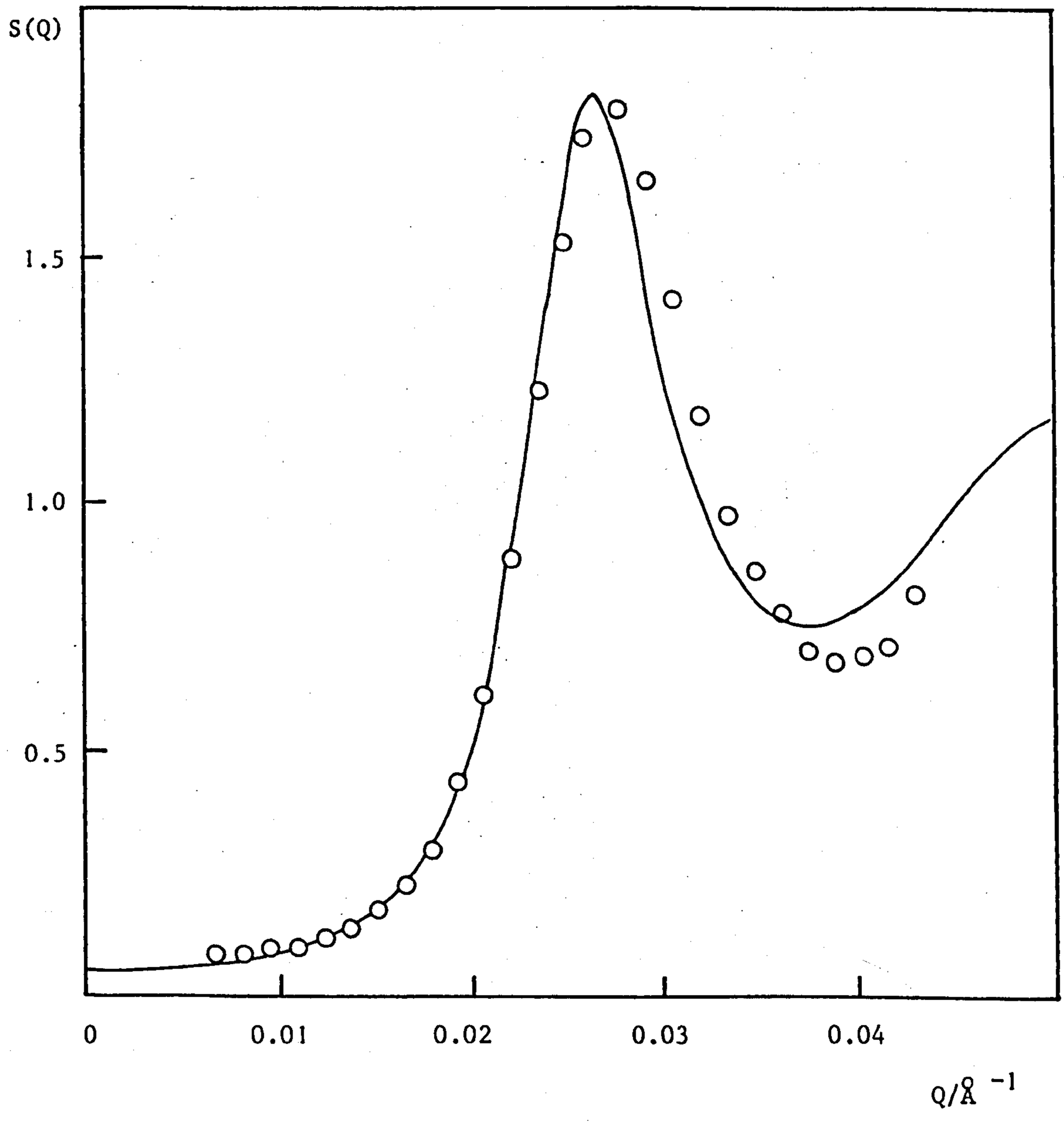

FIGURE 6.20 S(Q) against Q for 40 L'/0 TOL

——, calculated hard-sphere S(Q);

O , experimental S(Q)

for the adsorbed layer thickness was 26 Å; hence the parameters R_1 and $(R_2 - R_1)$ used to fit the less concentrated samples were equivalent to those obtained from the fitting of $[\bar{P}(Q)]_{c.s.}$ for 1L'/0 TOL in Chapter 5. However, in order to match the experimental data for samples of increasing concentration of particles, the value of R_1 had to be progressively decreased. A possible explanation for this effect is that for the cases when R_1 was ca. 105 Å, the head group of the surface active agent was included in the measurement of the radius, whereas when R_1 was ca. 95 Å the true calcium carbonate core radius was determined. This is plausible since the scattering length density of the benzene sulphonate head group ($\sim 2 \times 10^{10}$ cm^{-2}) is intermediate between those of the calcium carbonate core and the hydrocarbon chains. Consequently, a more accurate model for the particles in this study would have consisted of a core particle surrounded by two concentric shells; the inner shell representing the head groups and the outer shell representing the hydrocarbon chains of the surface active agent. However, the equations for the differential scattering cross-section for a particle of this type would have been rather complicated and this model was not adopted.

It is clear from Table 6.8 that the hard-sphere thickness is considerably greater than the adsorbed layer thickness for the more dilute samples, and that its value decreases with increasing concentration of the particles to equal approximately the value for the adsorbed layer thickness in the case of 40L'/0 TOL. It has already been mentioned that the particles of the L'-series (prepared in the same manner as the original L-series) were stabilized by a low molecular weight polymer, polyisobutene succinic anhydride (PIBSA), in addition to the alkyl benzene sulphonate. Although these comparatively long polymer chains were not present in sufficient concentration to affect the average value determined for the adsorbed layer

thickness, their presence, however, would influence the interaction (i.e. distance of closest approach) between two particles. It therefore seems highly probable that a hard-sphere thickness of 60 Å corresponds to the average length of a PIBSA molecule (a very rough calculation, assuming from the molecular weight that there are 17 repeat units, each 4.4 Å, gives the fully extended length of the chain as 75 Å). As the concentration of the particles increases and the distance of separation between them decreases, the PIBSA chains appear to become compressed, i.e. they coil around the particle. The progressive compression of the PIBSA chains is ultimately obstructed by the presence of the adsorbed layer and consequently, in the case of 40L'/O TOL, the hard-sphere thickness is nearly equivalent to the adsorbed layer thickness.

The above-mentioned hypothesis is consistent with the match obtained between the hard-sphere S(Q) and the experimental S(Q), as depicted in Figures 6.16 to 6.20. In the case of the more dilute samples, where compression of the PIBSA chains is likely to be occurring, it was found difficult to match the width of the first maximum in the experimental S(Q) curve. This suggests that under these conditions the simple hard-sphere potential is not representative of the interactions between the particles and that a more accurate model for the interaction would be a hard repulsion with a "soft tail". However, in the case of 30L'/TOL and 40L'/TOL where no compression of the stabilizer can take place, the particles behave like hard-spheres and a very good agreement between the two structure factors is obtained. Consequently, it was considered justifiable to Fourier transform the theoretical hard-sphere S(Q) in order to determine the radial distribution function g(r). This was done by truncating the Ashcroft and Lekner S(Q) data at a value of S(Q) which was very close to 1.0.

Figure 6.21 shows g(r) obtained for 40L'/0 TOL and 30L'/0 TOL, from which a number of points can be noted. Firstly, with decreasing volume fraction the primary peak in g(r) moves outwards to higher values of r; secondly, the peak decreases in magnitude with decreasing volume fraction; and thirdly, the value of r at which $g(r) \rightarrow 0$ increases with decreasing volume fraction. Moreover, in the case of 40L'/0 TOL the secondary peak in g(r) is clearly defined, signifying a higher degree of ordering than in the case of 30L'/0 TOL. The value of r for which g(r) = 0 gives the distance of closest approach (in terms of the hard-sphere diameter, σ_{HS}) for two particles in the system. For the case of 40L'/0 TOL σ_{HS} = 200 Å giving R_{HS} = 100 Å, whereas for the sample 30L'/0 TOL σ_{HS} = 230 Å and R_{HS} = 115 Å. Finally, it is interesting to note that both values of R_{HS} were approximately 20 Å smaller than the values $(R_1 + t_{HS})$ derived from the fitting procedure.

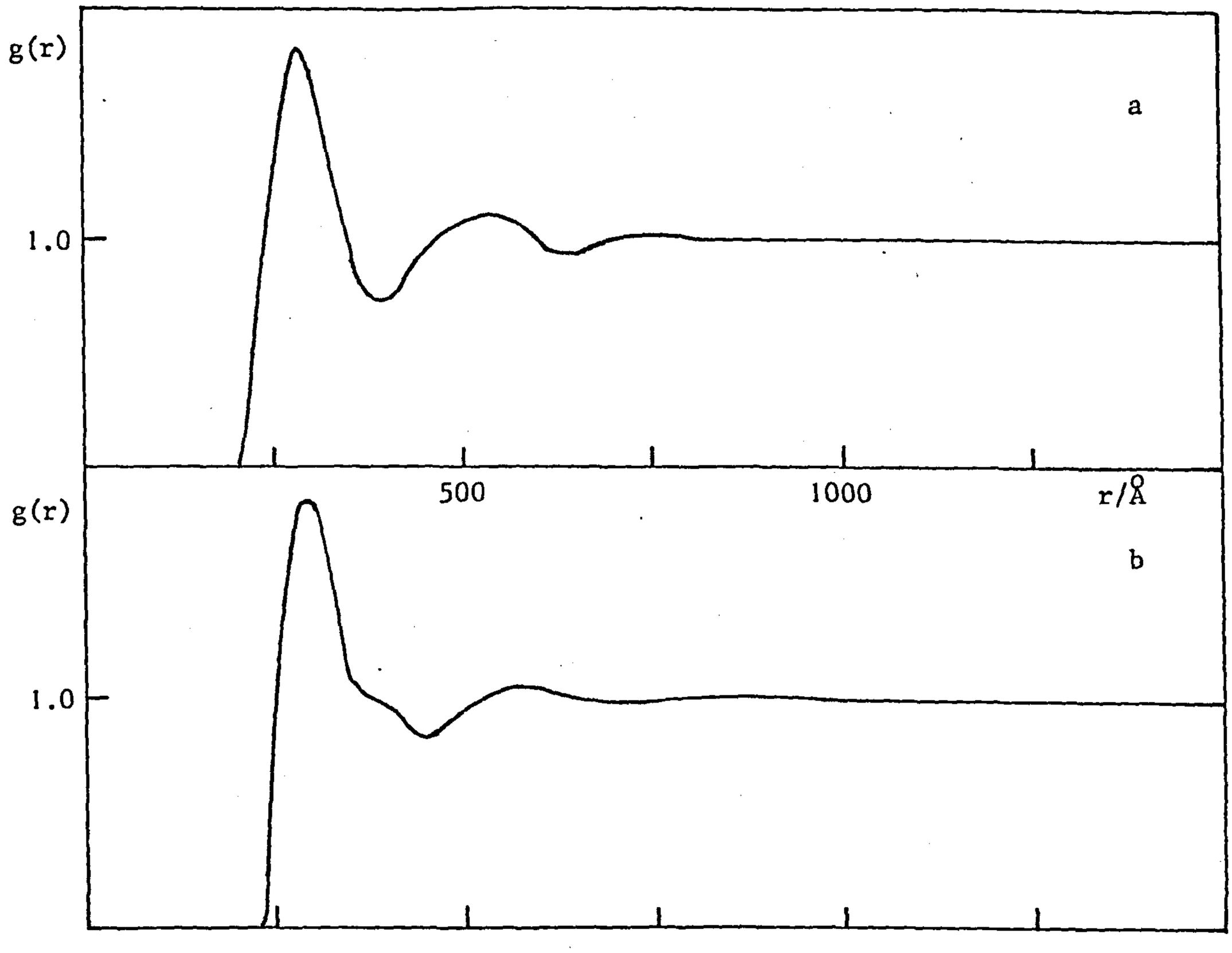

FIGURE 6.21 g(r) against r for

a) 40 L'/0 TOL and

b) 30 L'/0 TOL

CHAPTER SEVEN

CHAPTER 7

ULTRACENTRIFUGATION

Introduction

In a gravitational field of force, a particle suspended in a less dense medium tends to migrate through the fluid in a downward direction. For a given medium and fixed external conditions, the rate at which the particle sediments will depend on its size, mass and shape, suggesting that these characteristic parameters of the particle may be determined if one can measure the rate of sedimentation. However, in certain cases sedimentation either does not take place or is too slow to measure. This is because the transport of the particles due to sedimentation is counter-balanced by the transport due to backward diffusion; the latter resulting from the concentration gradient created by the partial sedimentation of the particles. In such cases ultracentrifugation, which creates a much stronger field of force (about 10^5 times gravity), provides the best means of obtaining measurable sedimentation rates. Svedberg and his collaborators[45] were the first to exploit centrifugal fields for the study of macromolecules and colloidal particles.

The analytical ultracentrifuge is generally used to carry out two types of experiments. It can be operated either for a short period of time at high speed to obtain a rapid separation of particles from medium, or for a longer period of time at a relatively low speed. In the latter case, an equilibrium state is eventually established between the rates of sedimentation and diffusion of the particles so that the concentration gradient in the cell remains constant. The former method, known as the sedimentation velocity method, was the one adopted in this study.

N.B.

In this chapter the Greek symbol - ρ - is used to represent the density.

7.1 Theory

The principle of the sedimentation velocity technique is to apply a centrifugal field of sufficient magnitude to overcome the opposing diffusional forces and thus cause the particles to sediment at a measurable rate.

7.1.1. Derivation of the Stokes equation

A particle sedimenting under gravity in a medium will experience a frictional resistance from that medium.

Balancing the forces on the particle:

$$f \frac{dx}{dt} = m(1 - \upsilon\rho_o)\, g \qquad \ldots \quad (7.1)$$

where f = the frictional coefficient

dx/dt = the rate of sedimentation

m = the mass of the particle

υ = the partial specific volume of the particle

ρ_o = the density of the medium

g = the gravitational acceleration

The buoyancy correction term, $(1 - \upsilon\rho_o)$, arises as a result of the upthrust produced by the displacement of the medium.

For a bare, spherical particle of radius a, this becomes:

$$6\pi\eta_o\, a \frac{dx}{dt} = \frac{4}{3}\pi a^3 \rho_1 (1 - \upsilon\rho_o)\, g \qquad \ldots \quad (7.2)$$

where η_o = the viscosity of the medium

ρ_1 = the density of the particle

The rate of sedimentation is therefore given by,

$$\frac{dx}{dt} = \frac{2a^2\rho_1}{9\eta_o} (1 - \upsilon\rho_o)\, g \qquad \ldots \quad (7.3)$$

This is known as the Stokes[46] equation and it can be expressed as,

$$\frac{dx}{dt} = \frac{2a^2}{9\eta_o} (\rho_1 - \rho_o)\, g \qquad \ldots \quad (7.4)$$

In a centrifugal field equation (7.1) becomes,

$$f \frac{dx}{dt} = m(1 - v\rho_o)\, \omega^2 x \qquad \ldots \quad (7.5)$$

where $\omega^2 x$ is the acceleration due to the applied field.

The sedimentation coefficient, s, is defined as the velocity of the particles divided by the centrifugal field, hence

$$s = \frac{dx/dt}{\omega^2 x} \qquad \ldots \quad (7.6)$$

Substituting for s in equation (7.5) and rearranging gives,

$$s = \frac{m}{f} (1 - v\rho_o) \qquad \ldots \quad (7.7)$$

Since $D = \frac{kT}{f}$

$$s = \frac{Dm}{kT} (1 - v\rho_o) \qquad \ldots \quad (7.8)$$

where D = the diffusion coefficient

k = the Boltzmann constant

T = the absolute temperature

$$s = \frac{Dm}{kT} \frac{N_A}{N_A} (1 - v\rho_o) \qquad \ldots \quad (7.9)$$

i.e. $$s = \frac{DM}{RT} (1 - v\rho_o) \qquad \ldots \quad (7.10)$$

or $$M = \frac{RTs}{D(1 - v\rho_o)} \qquad \ldots \quad (7.11)$$

where N_A = the Avogadro number

M = the molecular weight

R = the universal gas constant

Equation (7.11) is the well known Svedberg equation[47], expressed in terms of the molecular weight of the sedimenting species. The value of the diffusion coefficient necessary for the calculation of the molecular weight is usually obtained from a free-boundary diffusion measurement or from an altogether different technique such as photon correlation spectroscopy. It is also necessary to know the partial specific volume of the sedimenting entity and this can be calculated from measurements of the specific density as a function of concentration. This will be discussed in the experimental section 7.3.

The Stokes equation (equation (7.4)) can also be derived for the case of centrifugation in the following manner. The centrifugal force on the particle is opposed by the resultant of two other forces. In addition to the frictional force created by the motion of the particle through the medium, there will also be, according to Archimedes principle, an upthrust caused by the displacement of the liquid medium. Thus,

centrifugal force = upthrust + frictional force

i.e. $$m\omega^2 x = \frac{4}{3}\pi a^3 \rho_o (\omega^2 x) + 6\pi\eta_o a v_o \qquad \ldots \quad (7.12)$$

where v_o = the velocity of the particle

$$m = \frac{4}{3}\pi a^3 \rho_1$$

Rearranging equation (7.12),

$$\frac{4}{3}\pi a^3 (\rho_1 - \rho_o)\ \omega^2 x = 6\pi\eta_o a v_o \qquad \ldots \quad (7.13)$$

and substituting $s = v_o/\omega^2 x$, one obtains,

$$s = \frac{2a^2}{9\eta_o} (\rho_1 - \rho_o) \qquad \ldots \quad (7.14)$$

7.1.2 <u>The Stokes equation for a particle with an adsorbed layer</u>

The classical Stokes equation is applicable to electrically neutral, spherical particles of radius a. However, the system in this study consisted of particles stabilised by an adsorbed layer of surface active agent so that an extended form of the equation had to be used.

Consider a particle of core radius a, surrounded by an adsorbed layer of thickness δ and density ρ_2, whose volume is given by $\frac{4}{3}\pi (a + \delta)^3$. The same three forces are operating on the sedimenting particle and therefore, once again,

centrifugal force = upthrust + frictional force

where centrifugal force = $\left\{\frac{4\pi a^3}{3} \rho_1 + \frac{4\pi}{3} \rho_2 (3a^2\delta + 3\delta^2 a + \delta^3)\right\} \omega^2 x$

$\ldots \quad (7.15)$

$$\text{upthrust} = \left\{\frac{4\pi a^3}{3} \rho_o + \frac{4\pi}{3} \rho_o (3a^2\delta + 3\delta^2 a + \delta^3)\right\} \omega^2 x \qquad \ldots \quad (7.16)$$

$$\text{frictional force} = 6\pi\eta_o (a + \delta) v_o \qquad \ldots \quad (7.17)$$

Combining equations (7.15), (7.16) and (7.17) in the manner of equation (7.13),

$$\omega^2 x \left\{\frac{4\pi a^3}{3} (\rho_1 - \rho_o) + \frac{4\pi}{3} (3a^2\delta + 3\delta^2 a + \delta^3)(\rho_2 - \rho_o)\right\}$$

$$= 6\pi\eta_o (a + \delta) v_o \qquad \ldots \quad (7.18)$$

Substituting the sedimentation coefficient, s,

$$s = \frac{2a^3(\rho_1 - \rho_o) + 2(3a^2\delta + 3\delta^2 a + \delta^3)(\rho_2 - \rho_o)}{9\eta_o(a + \delta)} \qquad \ldots \quad (7.19)$$

This is the modified Stokes equation for a single spherical particle surrounded by a uniform adsorbed layer[48]. Thus, using an experimentally determined sedimentation coefficient and extrapolating to infinite dilution, it is possible to calculate one unknown parameter if values are assigned to all the other parameters. If, however, there are two unknown parameters (for example, a and δ), then a fitting procedure has to be used. In this case, the variation of the sedimentation coefficient is calculated as a function of one of the unknown parameters for various values of the other parameter. The value of the experimentally determined sedimentation coefficient is then fitted to a theoretically calculated value. However, since this procedure is based on fitting a single point it is clearly not very accurate. This will be discussed again in Section 7.4.

7.1.3 Sedimentation coefficients

The sedimentation coefficient is the parameter most frequently determined in the ultracentrifuge. It can be defined as the rate of sedimentation per unit centrifugal field or, as already shown, by the equation

$$s = \frac{dx/dt}{\omega^2 x} = \frac{d \ln x}{\omega^2 dt} \qquad \ldots \quad (7.6)$$

Thus, a plot of the logarithm of the distance of the peak in the concentration gradient curve from the centre of rotation against time should give a straight line, from the slope of which s is obtained. The unit of the sedimentation coefficient is the Svedberg (S), defined as 10^{-13} seconds. It is customary to express the sedimentation coefficient in a corrected form as s^{o}_{20}, which is the value of the coefficient at zero concentration of particles and at $20^{o}C$. For aqueous systems it can be further corrected to a value when pure water is used as the solvent.

During sedimentation, a boundary is set up between pure solvent and solvent containing particles (see Figure 7.1). This boundary travels down the cell at a rate dependent upon the sedimentation rate of the particles. If sedimentation starts at the distance x_o from the centre of rotation at the time t = o, assuming no diffusion, the boundary will have moved to x_1 after time t_1. The new position, x_1, can be calculated from equation (7.6), which can also be written as,

$$x_1 = x_o e^{t_1\omega^2 s} \quad \ldots \quad (7.20)$$

If diffusion were negligible and the particles uniform in size, shape and density, the transition zone between the supernatant solvent and the dispersion would be infinitely sharp. In most sedimentation velocity experiments, however, this boundary, represented by a peak in the concentration gradient curve, becomes progressively more diffuse and/or blurred due to diffusion and polydispersity. The maximum ordinate of the peak may, therefore, no longer represent the true sedimentation rate of the particles. Goldberg[49] has shown that, in a sector shaped cell, the true position of the boundary corresponds to the position of the second moment of the concentration gradient curve. The systems in this study were found to exhibit reasonably sharp and symmetrical peaks, and it therefore seemed justifiable to use the apex of the peak as the position of the boundary for the determination of s.

Concentration dependence of sedimentation coefficients

The sedimentation coefficients for most systems are found to vary with the concentration of the sedimenting material, and therefore have to be corrected to the value at infinite dilution, s^o. For most colloidal and macromolecular systems, the sedimentation coefficient decreases with concentration[50]. In the few cases where it is found to increase with

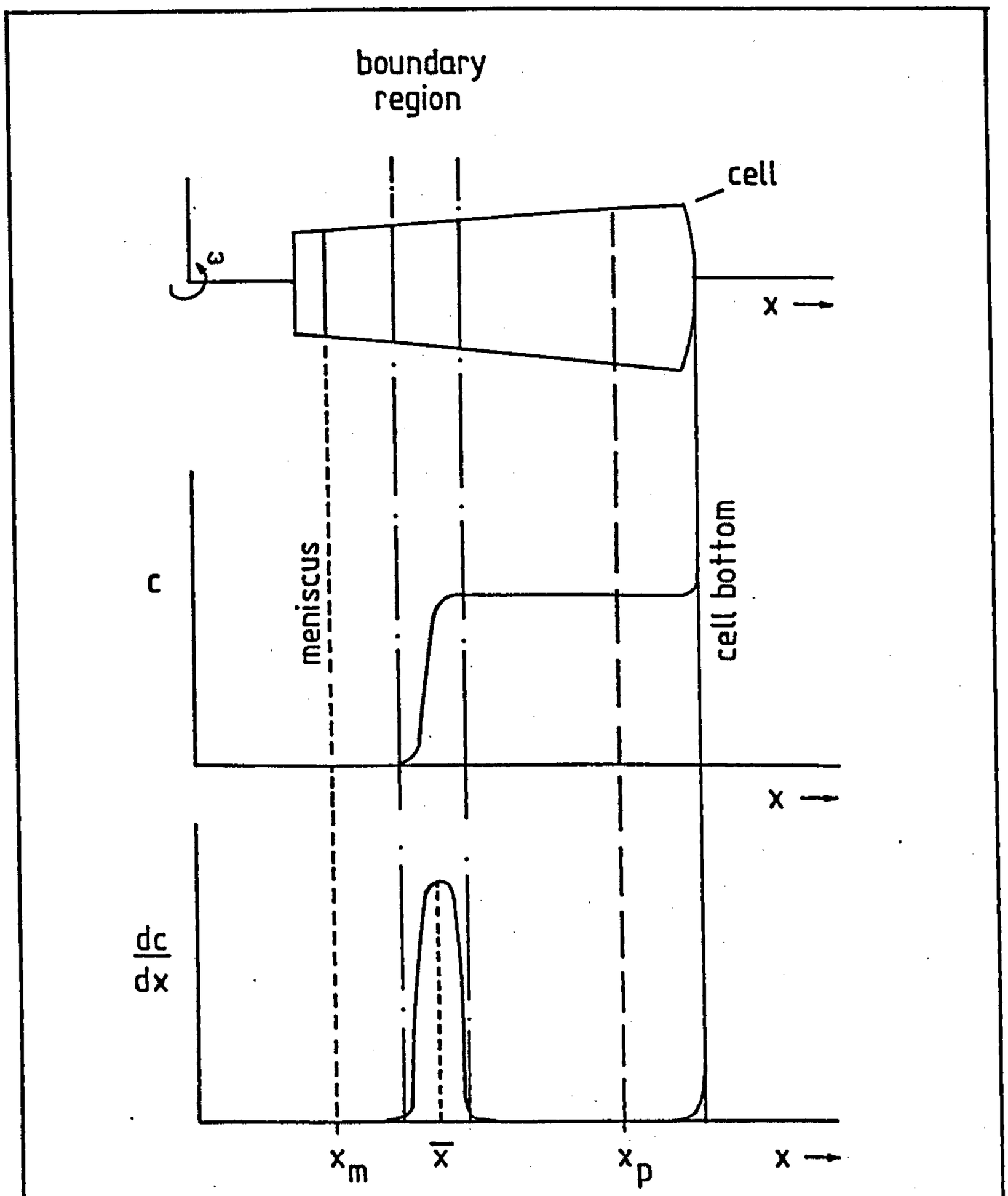

FIGURE 7.1

Variation of concentration and concentration gradient along the cell path during sedimentation

concentration, there is a dynamic equilibrium operating between the various components of a mixture.

A general understanding of the dependence of sedimentation velocity on concentration, in quantitative terms, is lacking, especially for the case of colloidal non-aqueous dispersions, as most of the work reported in the literature has been carried out on macromolecular systems in aqueous media. Though admittedly of an empirical nature, the most complete treatment is that of Burgers[51] and Schachman et al.[52], who derived relations of the type,

$$s = s^o / (1 + k\phi) \qquad \ldots \quad (7.12)$$

which, over a small concentration range (i.e. $k\phi << 1$), can be expressed as

$$s = s^o (1 - k\phi) \qquad \ldots \quad (7.22)$$

where k is a constant characteristic of the system and ϕ the volume fraction of the particles in solution.

The concentration dependence of the sedimentation velocity is often ascribed to the change in the viscosity of the dispersion with concentration since one can write

$$\eta = \eta_o (1 + k_v\phi) \qquad \ldots \quad (7.23)$$

where η_o is the viscosity of the pure solvent and k_v, according to Einstein, has the value 2.5 for spheres. Thus, this value could be assigned to the constant k in equations (7.21) and (7.22). However, it has been pointed out that in many cases the correction of the sedimentation coefficient for the macroscopic dispersion viscosity is insufficient to account for the experimentally observed decrease in sedimentation rate with ϕ. Schachman and Kauzmann[53] have postulated that an additional factor should be considered, namely the backward flow of the solvent. As the particles sediment in a closed vessel, there must be a flow of solvent in the

opposite direction to fill the space formerly occupied by the particles in the region above the sedimentation boundary. They point out that there is also a backward flow of solvent to compensate for the solvent which is carried by the sedimenting particles. (In the derivation of Stokes law it is assumed that the fluid at the surface of the particle sticks to it so firmly that it moves with the same velocity as the particle. This layer in turn, through the viscous forces in the liquid, drags along an adjoining layer of solvent at slightly lower velocity, and so on, out into the liquid). If the effective fractional volume of liquid moving in this way with the particles is denoted by $k_s\phi$, then the corrected sedimentation constant is given by

$$s = s^o / (1 + (1 + k_s)\ \phi) \qquad \ldots \quad (7.24)$$

Hence, the concentration dependence of the sedimentation coefficient can be ascribed to a combination of two effects: the viscosity of the dispersion and the total backward flow of solvent. Burgers, however, assumed that there is a layer of solvent immediately adjacent to each particle which has a lower viscosity than that of the bulk dispersion. This layer apparently arises for purely geometrical reasons; i.e., the centres of two spherical particles cannot come closer than the sum of their radii, so that no particles are ever found within one radius of the surface of a given particle. This region is therefore more dilute than the bulk of the dispersion. Burgers predicted that the mean effective viscosity in the neighbourhood of a particle is then given by,

$$\eta_{eff} = \eta_o\ (1 + \alpha k_v \phi) \qquad \ldots \quad (7.25)$$

where α is a number less than unity. Burgers calculated that $\alpha = 0.75$ for spheres.

Thus, the sedimentation coefficient corrected for both effects can be written as,

$$s = s_o / (1 + (1 + k_s + \alpha k_v)\ \phi) \qquad \ldots \quad (7.26)$$

The applicability of these equations for the case of colloidal non-aqueous dispersions is uncertain. Moreover, the obvious problem is in assigning a value to the constant, k_s. This will be further discussed in Section 7.4.

Radial dilution and pressure effects

The combined effects of the sector shape of the cell and the inhomogeneity of the centrifugal field (it increases linearly with the distance from the centre of rotation) produce a phenomenon called radial dilution. It results in a decrease in the concentration of sedimenting material in the cell during the experiment. This was first discussed by Svedberg and Rinde[54] who derived the so-called radial dilution equation which relates the concentration of the dispersion at some time t, c_t, to the initial concentration, c_o, in terms of the boundary positions at the respective times, i.e.

$$\frac{c_t}{c_o} = \left(\frac{x_m}{x_t} \right)^2 \qquad \ldots \quad (7.27)$$

where x_m = the position at the meniscus

x_t = the position of the boundary at time, t.

Trautman and Schumaker[55] have shown the validity of the radial dilution equation for systems exhibiting concentration-dependent sedimentation coefficients. Since the contents of an ultracentrifuge cell may be diluted to about 70% of their initial value, it is important to allow for this effect in the treatment of the data. Thus, the concentrations used in establishing a relationship between s and c should be the average concentration between

the first and last pictures within each experiment.

At high speeds of rotation, often employed in sedimentation velocity experiments, a large pressure difference, which can amount to a few hundred atmospheres, is produced between the air-liquid meniscus and the bottom of the cell. Svedberg and Pedersen[56] were the first to point out that the high pressures can alter the density and viscosity of the solvent as well as the partial specific volume of the particles. The former effects cause the particles to sediment more slowly, whereas the latter, which is usually of a smaller magnitude, acts in the opposite sense.

Mosimann and Signer[57] formulated the following correction for the influence of pressure on the sedimentation coefficient:

$$s_1 = s_p \frac{\eta_p}{\eta_1} \left(\frac{1 - v_1\rho_1}{1 - v_p\rho_p} \right) \quad \ldots \quad (7.28)$$

where the subscripts 1 and p refer to a pressure of 1 and p atmospheres respectively, and the various symbols refer to terms defined earlier.

The pressure gradient in the sector-shaped centrifuge cell may be determined from

$$\frac{dP}{dx} = \rho\omega^2 x \quad \ldots \quad (7.29)$$

Assuming the compressibility of the solvent to be negligible and the density of the solution to be constant, the pressure can then be expressed as[48]:

$$P = \frac{\rho}{2} \omega^2 (x^2 - x_m^2) \quad \ldots \quad (7.30)$$

Pressure effects can account for as much as a 30% error in the sedimentation coefficient in non-aqueous systems[48], and were thought to depress the gradient of the ln x against time plot by Thompson[48]. It is interesting to note that the radial dilution equation does not apply if pressure effects are not negligible.

7.2 Experimental

7.2.1 The ultracentrifuge

The instrument used in this study was a Spinco Model E (Beckman Instruments Inc.) analytical ultracentrifuge. The dispersion to be studied was placed in a 4^{o} sector-shaped cell, (the shape of the cell eliminating collision reflection from the cell walls) which was in turn inserted into an Analytical-D rotor, together with a counterpoise. The rotor was placed in a chamber and attached to the drive shaft. The drive unit, a $1\frac{1}{2}$ hp water-cooled electric motor, drove step-up gears which could turn the drive shaft at up to 59780 rpm. The speed-control gearbox automatically controlled the rotor at any of 57 selected speeds. To prevent frictional drag and heating of the rotor, the rotor chamber was evacuated to 1 micron of mercury by a water-cooled diffusion pump.

The rotor temperature was controlled by a rotor temperature indication and control system (RTIC).

Schlieren optics

The schlieren optical system was employed to monitor the concentration changes in the cell. This method is most widely used with the ultracentrifuge and utilizes the deviation of light due to the difference between the refractive index of the particles and that of the medium. In fact, the amount of deviation of the light passing through any level of the cell is proportional to the rate of change of the refractive index. Since the refractive index is in turn proportional to the particle concentration, the boundary of sedimenting particles (i.e. the maximum rate of change of concentration) will produce the maximum deviation. The schlieren pattern obtained is thus analogous to the concentration gradient curve. The refractive index method in conjunction with the Philpot-Svensson[58] cylindrical lens modification makes it possible to record

photographically the movement of the schlieren peak as a function of the distance from the axis of rotation.

The Beckman Model E ultracentrifuge was equipped with an automatically controlled camera which recorded five pictures onto each photographic plate. Various exposure times as well as exposure intervals could be selected, depending upon the type of system under investigation.

The light source was a 1000 watt water-cooled mercury-arc lamp.

7.2.2 Experimental procedure

The sample under investigation was prepared prior to the experiment and was placed in a 4^{o} sector cell of path length 12 mm. Each run was carried out at $25^{o}C$ since it was found that at $20^{o}C$ the peak moved very slowly away from the meniscus. The most frequently used rotor speed was 15220 rpm, although in some cases (samples of higher concentration dispersed in dodecane) speeds up to 31410 rpm had to be reached before any sedimentation took place.

The schlieren patterns were monitored automatically and recorded at intervals of 2 or 4 minutes onto Ilford photographic film. The mercury lamp slit width was adjusted so that the exposure time for each picture was 5 seconds. The photographic films were developed and fixed in the usual manner using Kodak Universal developer and Kodafix.

The timing of each sedimentation run was started when the rotor had reached its preset speed. Although this ignores the sedimentation that occurs during the acceleration of the rotor[59] it does not alter the slope of $\ln x$ against time, i.e. the value of the sedimentation coefficient. Furthermore, since very low centrifugal speeds were used in this study, a negligible amount of sedimentation would have occurred in the first few minutes of a run.

Determination of sedimentation coefficients

A schematic representation of a schlieren pattern is shown in Figure 7.2. The distances between the various reference marks illustrated in Figure 7.2 were interpolated for each frame of a photographic plate using a projectorscope. The three distances required were:

i) the distance between the upper counterpoise mark and the meniscus $(x_r' - x_m)$

ii) the distance between the upper counterpoise and the apex of the peak, $(x_r' - \bar{x}) = \Delta x$

iii) the distance between the upper and lower counterpoise marks $(x_r' - x_r'')$

The distances mentioned in i) and iii) should remain nearly constant during the run. The position of the meniscus was monitored as a check that no leakage of the cell had occurred whilst the distance between the two counterpoise marks was needed to calculate the magnification factor of the projectorscope. In the Model E ultracentrifuge, the centre of rotation was 5.70 cm (± 0.02 cm at maximum centrifugal field) away from the upper counterpoise mark and the cell length was 1.60 cm. The magnification factor, X, was thus given by,

$$X = \frac{(\overline{x_r' - x_r''})}{1.60} \qquad \ldots \quad (7.31)$$

The value of X was calculated to be 2.13.

The position of the schlieren peak could then be calculated from the following equation:

$$x = \left(\frac{x_r' - \bar{x}}{2.13} \right) + 5.70 \text{ cm.} \qquad \ldots \quad (7.32)$$

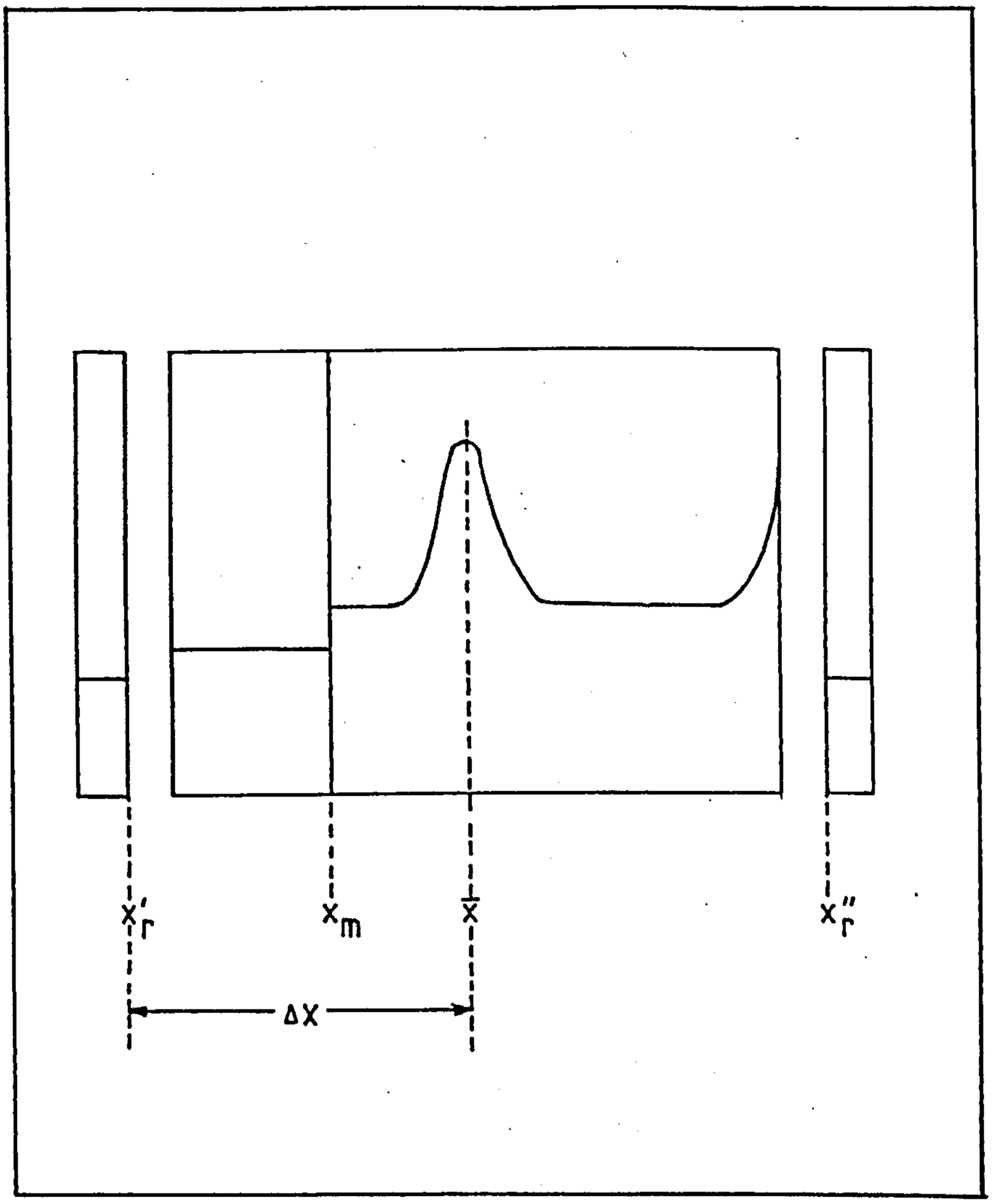

FIGURE 7.2

Photographic plate reference marks (x'_r, x''_r)

The sedimentation coefficient was then calculated using equation (7.6), taking into account that the centrifugal speed, ω, had to be converted to radians per second. A number of runs at various concentrations were carried out for each system in order to extrapolate the sedimentation coefficient to infinite dilution.

7.3 Partial Specific Volume of the Particles

The buoyancy correction term, $(1 - \upsilon\rho_o)$ has already been discussed briefly in the derivation of the Svedberg equation (equation (7.11)), and was said to arise as a consequence of the principle of Archimedes. Although the calculation of the molecular weight of the particles was not of primary importance in this study, the determination of the partial specific volume of the particles, υ, would yield interesting information about the solvation of the adsorbed layer of the particles.

The partial specific volume (expressed in units of $cm^3\ g^{-1}$) can be defined as the volume increase when 1 gram of solute (in this case, particles) is added to an infinite volume of the solution (i.e. dispersion). It is equivalent to the reciprocal of the effective density of the particle, in its state of solvation, in the solvent, i.e.,

$$\upsilon = 1/\rho_{eff} \qquad \ldots \quad (7.33)$$

The partial specific volume was determined by densitometry using an Anton Paar Density Meter. Since the instrument was rather complicated, the description of the operation of the instrument will be omitted. It is sufficient to note that all the measurements were carried out at 25^oC and that the instrument was calibrated with dry air and water. The densities of a number of low concentration dispersions, as well as the density of the solvent, were measured, and the partial specific volume of the particles was calculated from the equation derived below.

Consider 100 ml of dispersion containing wg of particles and w_o g of solvent.

If the density of the dispersion is ρ_s and that of pure solvent is ρ_o then,

$$\rho_s = \frac{w + w_o}{100} \quad g\ cm^{-3} \qquad \ldots \quad (7.34)$$

Volume of solvent present = $100 - w\upsilon$ cm^3 ... (7.35)

Mass of solvent = $(100 - w\upsilon)\ \rho_o$ g ... (7.36)

Thus $\rho_s = \frac{w + (100 - w\upsilon)}{100}\ \rho_o$ g cm^{-3} ... (7.37)

and $w\upsilon\rho_o = w + 100\rho_o - 100\rho_s$

$$\upsilon = \frac{1}{\rho_o} - \frac{100}{w}\left(\frac{\rho_s - \rho_o}{\rho_o}\right) \quad \ldots \quad (7.38)$$

When υ is independent of the concentration of particles, i.e. w, it can be measured from a plot of ρ_s against w/100

i.e. $\upsilon\rho_o = 1 - \frac{100}{w}(\rho_s - \rho_o)$

and $(\rho_s - \rho_o) = (1 - \upsilon\rho_o)\ \frac{w}{100}$

The partial specific volume of the particles was thus calculated from the slope of the plot of ρ_s against w/100. The intercept of the plot was ρ_o, while the linearity of the plot was an indication of the constancy of υ. This was to be expected at the low concentration range used, but at higher concentrations of particles υ may vary with w due to hydrodynamic effects and a possible change in the degree of solvation. The results obtained for the V-particles and the L-particles dispersed in toluene and dodecane are given in Table 7.1, and the results for two of the series are shown in Figure 7.3.

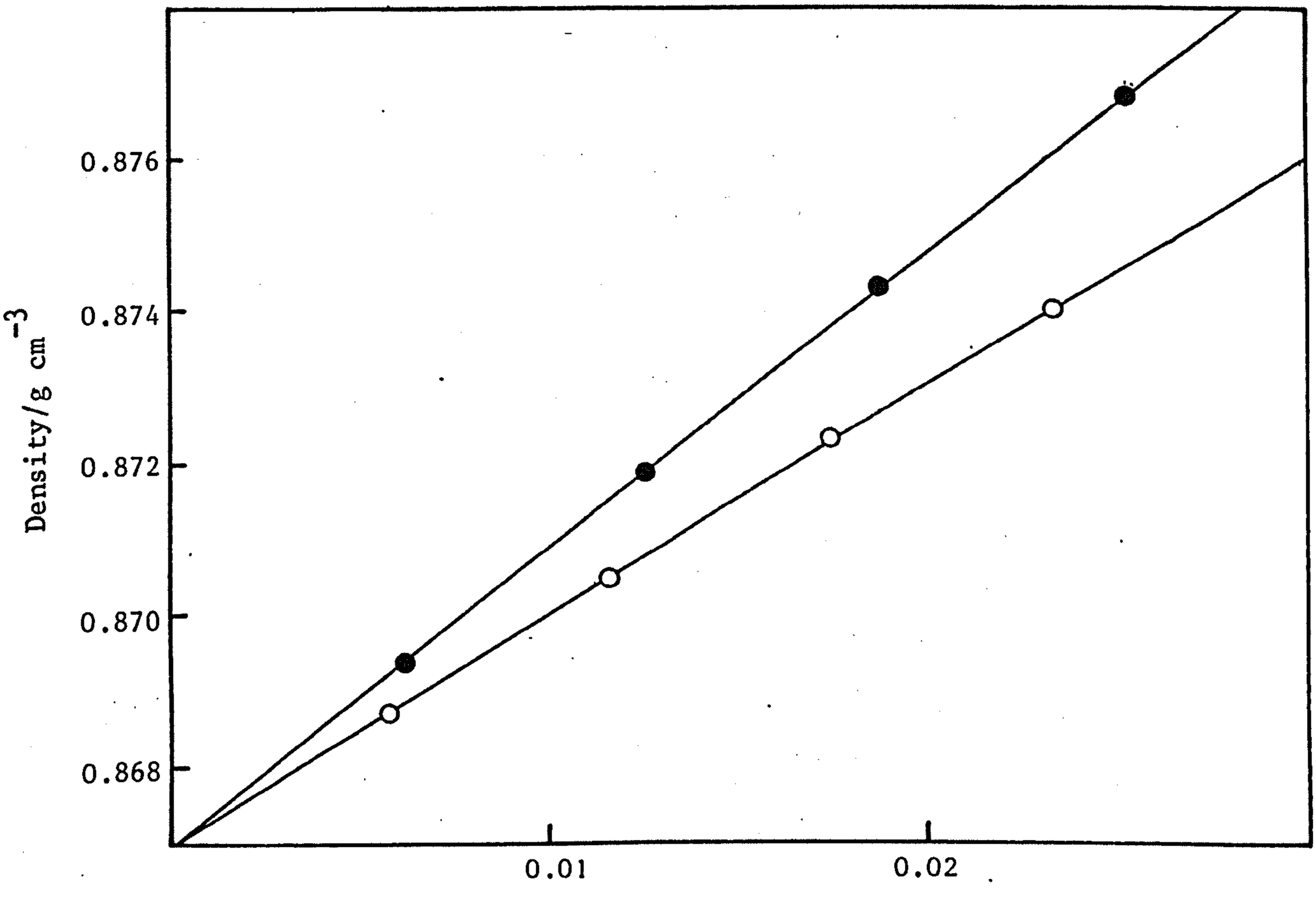

FIGURE 7.3 Partial specific volume results for the V-particles and the L-particles in toluene

●——● , L-series in toluene

○——○ , V-series in toluene

TABLE 7.1 Partial specific volume and effective density of various systems

SAMPLE	$v/cm^3\ g^{-1}$	$\rho_{eff}/g\ cm^{-3}$
V-particles in toluene	0.800 ± 0.005	1.25 ± 0.008
V-particles in dodecane	0.845 ± 0.005	1.18 ± 0.005
L-particles in toluene	0.688 ± 0.005	1.45 ± 0.007
L-particles in dodecane	0.754 ± 0.005	1.33 ± 0.075

7.4 Results and Discussion

Sedimentation velocity experiments were carried out as a function of the concentration of particles for all three systems in this study, namely the V-series, the L-series and the F-series. The samples, which were dispersed in either toluene or dodecane, were examined at concentrations of 0.25% up to 3.0% w/w of calcium carbonate. The labelling of the samples was identical to that used for the SANS data.

The experimental procedure has been described in detail in the preceding section but it is interesting to note here that in the case of the V-particles dispersed in dodecane, a rotor speed of 31410 rpm was necessary, whereas for all the other samples a speed of 15220 rpm was adequate to produce sedimentation. Good, straight line plots of ln x against time were obtained for all the samples from which the sedimentation coefficient was calculated using equation (7.6). The sedimentation coefficient at infinite dilution, s^o, was obtained by extrapolation of the plot of s against concentration. However, it was found that the effect of radial dilution was not negligible and hence the value of c used was the average concentration between the first and last pictures within each experiment, calculated using equation (7.27).

The V-series

The sedimentation coefficients obtained for dispersions of varying concentration of the V-particles in toluene are given in Table 7.2, and those obtained when dodecane was the dispersion medium are given in Table 7.3. c_{cor} corresponds to the concentration of the sample corrected for the effect of radial dilution. A comparison of the values of c_{cor} in the two tables indicates that the effect of radial dilution was greater when the dispersion medium was dodecane.

TABLE 7.2 V-particles in toluene

SAMPLE	c_{cor}/% w/w	Sedimentation coefficient/S
0.50 V/TOL	0.48	35.50
0.75 V/TOL	0.73	34.60
1.0 V/TOL	0.97	33.55
1.25 V/TOL	1.22	32.75
2.0 V/TOL	1,92	29.55
3.0 V/TOL	2.91	27.10

TABLE 7.3 V-particles in dodecane

SAMPLE	c_{cor}/% w/w	Sedimentation coefficient/S
0.50 V/DOD	0.48	15.65
0.75 V/DOD	0.71	14.80
1.0 V/DOD	0.94	14.25
1.25 V/DOD	1.18	13.65
2.0 V/DOD	1.84	11.50
3.0 V/DOD	2.71	10.25

Figures 7.4 and 7.5 show the plots of s against c for the V-particles dispersed in toluene and in dodecane respectively. It is clear that in both cases the plots are linear up to a w/w concentration of $CaCO_3$ of ~1.25% and that the concentration dependence of the sedimentation coefficient appears to

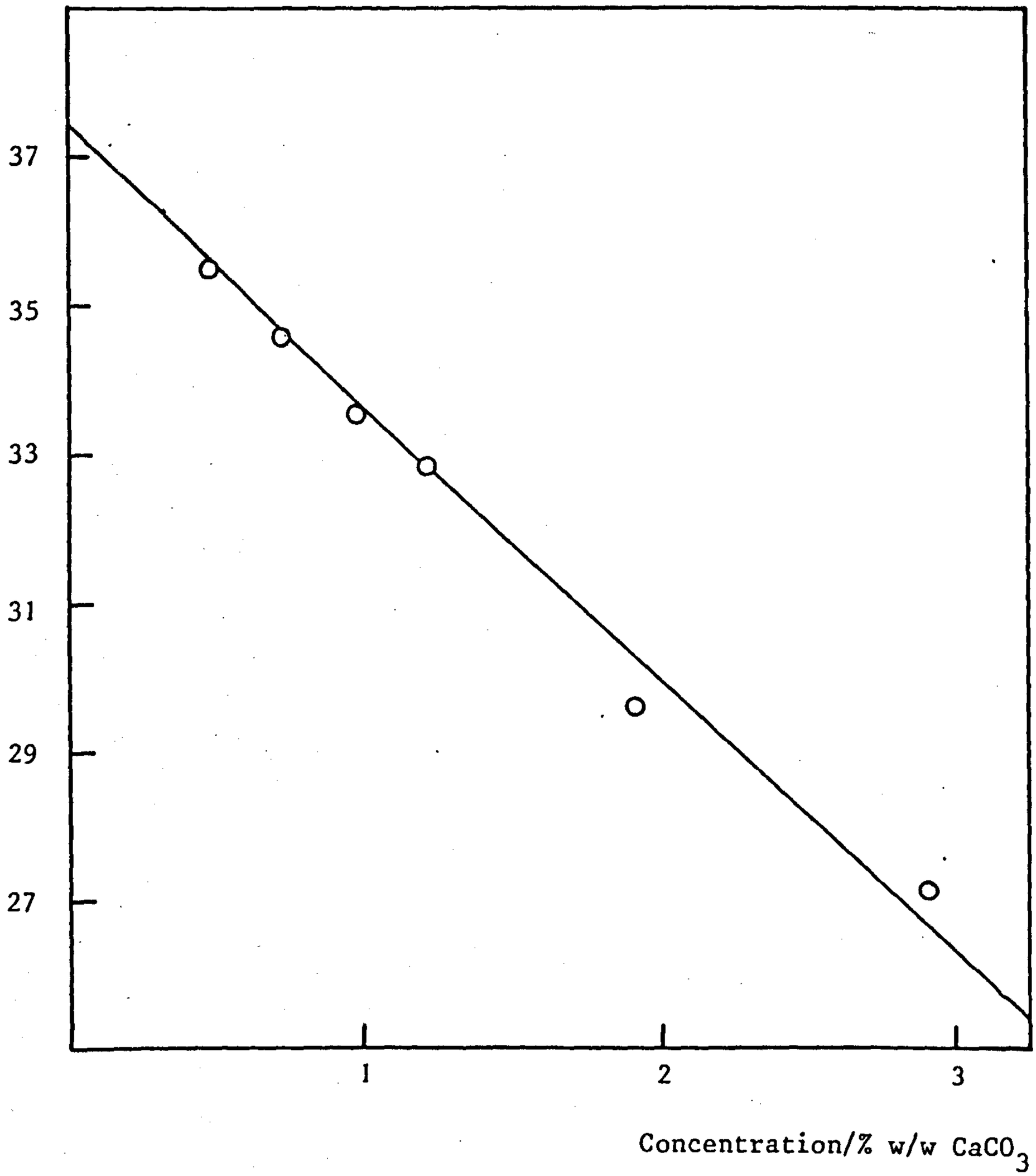

FIGURE 7.4 Sedimentation coefficient against concentration for V-particles dispersed in toluene

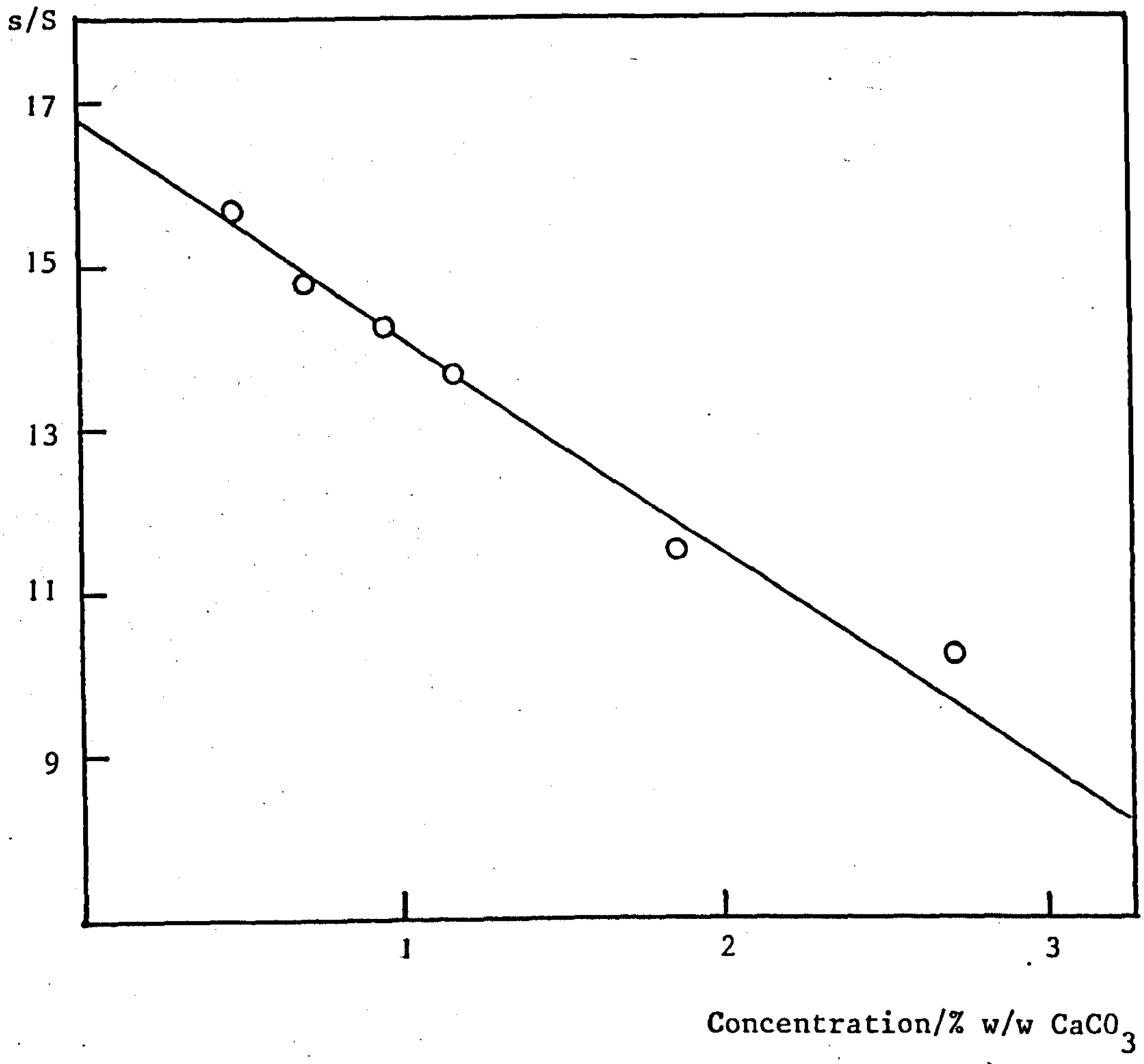

FIGURE 7.5 Sedimentation coefficient against concentration for V-particles dispersed in dodecane.

decrease above this value. The low concentration data was extrapolated to zero concentration in order to obtain $\bar{s}^o$. In the case of the V-particles in toluene s^o = 37.4 S, whereas for the V-particles in dodecane s^o = 16.8 S.

The experimentally determined value of s^o could then be used in conjunction with equation (7,19) for the characertization of the particles. However, in the case of the particles in this study, there are at least two unknown parameters in equation (7.19) and consequently a fitting procedure has to be used. Although it would be justifiable to use the value of the particle core radius determined by SANS, both the hydrodynamic thickness of the adsorbed layer and its density are not known. Hence, theoretical curves of the variation of s^o as a function of the adsorbed layer thickness were constructed for various values of the adsorbed layer density (Figure 7.6) and the particle core radius (Figure 7.7). Similar plots were constructed for the case of the V-particles in dodecane and these are shown in Figures 7.8 and 7.9. It is immediately clear that, owing to the curvature of the plots, there are two possible values of the adsorbed layer thickness, δ, which correspond to the experimental value of s^o. However, since it is extremely unlikely that the hydrodynamic layer thickness is smaller than the adsorbed layer thickness determined by SANS, the lower value of δ can be discounted in each case.

It can be seen from Figures 7.6 and 7.7 that the s^o value of 37.4 S corrsponds to a layer thickness of ca. 26 Å, a layer density, ρ_2, of 1.03 g cm^{-3} and a core particle radius of 25 Å. In the case of the V-particles in dodecane, s^o = 16.8 S corresponds to δ = 28 Å, ρ_2 = 0.925 g cm^{-3} and a = 25 Å. However, values of a = 24 Å, ρ_2 = 0.95 g cm^{-3} and δ = 29 Å also fit. It is interesting to note that in both cases the value of the particle core radius is 3 Å greater than that determined by SANS. The values obtained for δ are not surprising since the particles are likely to

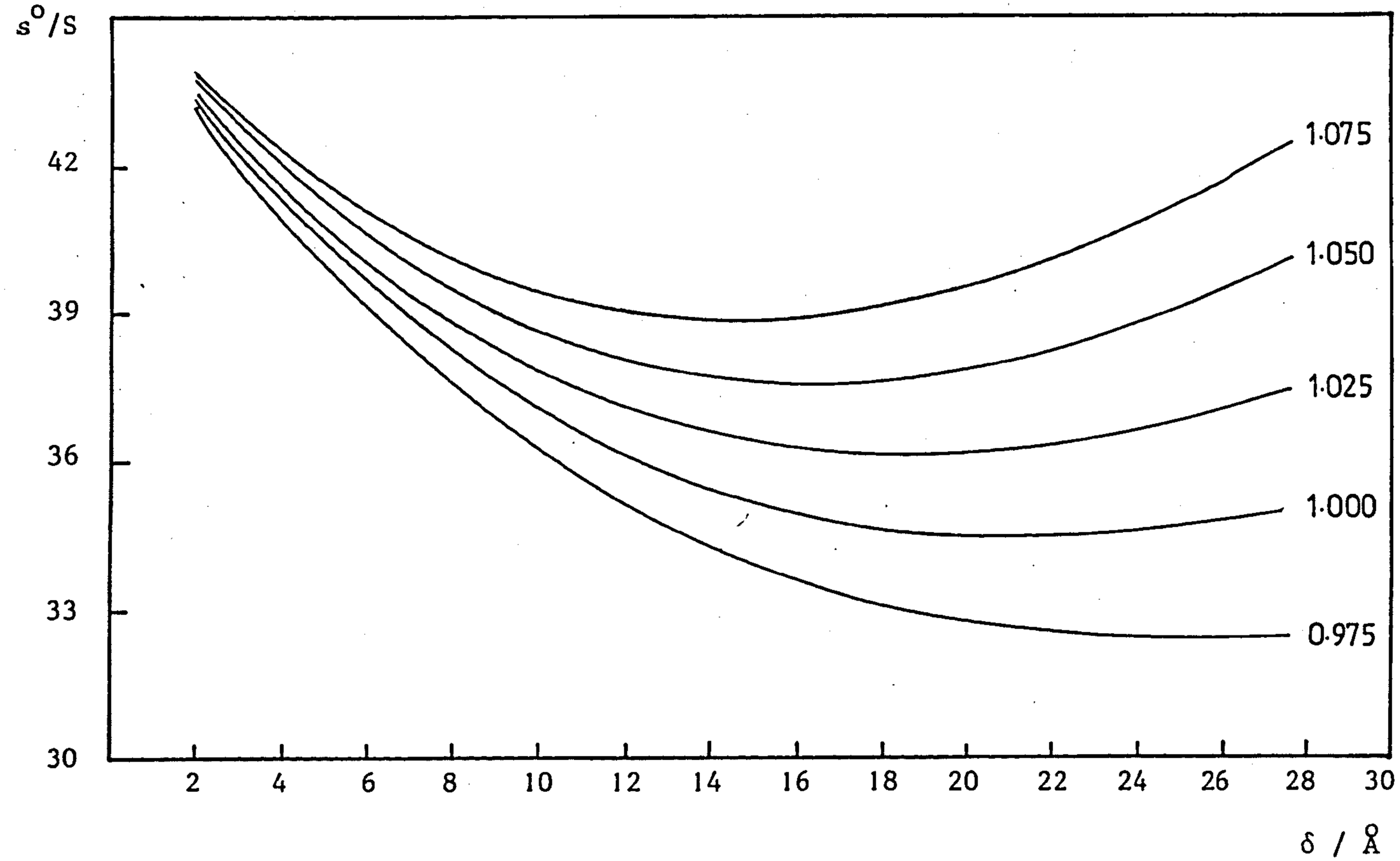

FIGURE 7.6 Calculated curves of sedimentation coefficient against adsorbed layer thickness for various values of the adsorbed layer density for V-particles in toluene ($a = 25$ Å; $\rho_o = 0.867$ g cm^{-3})

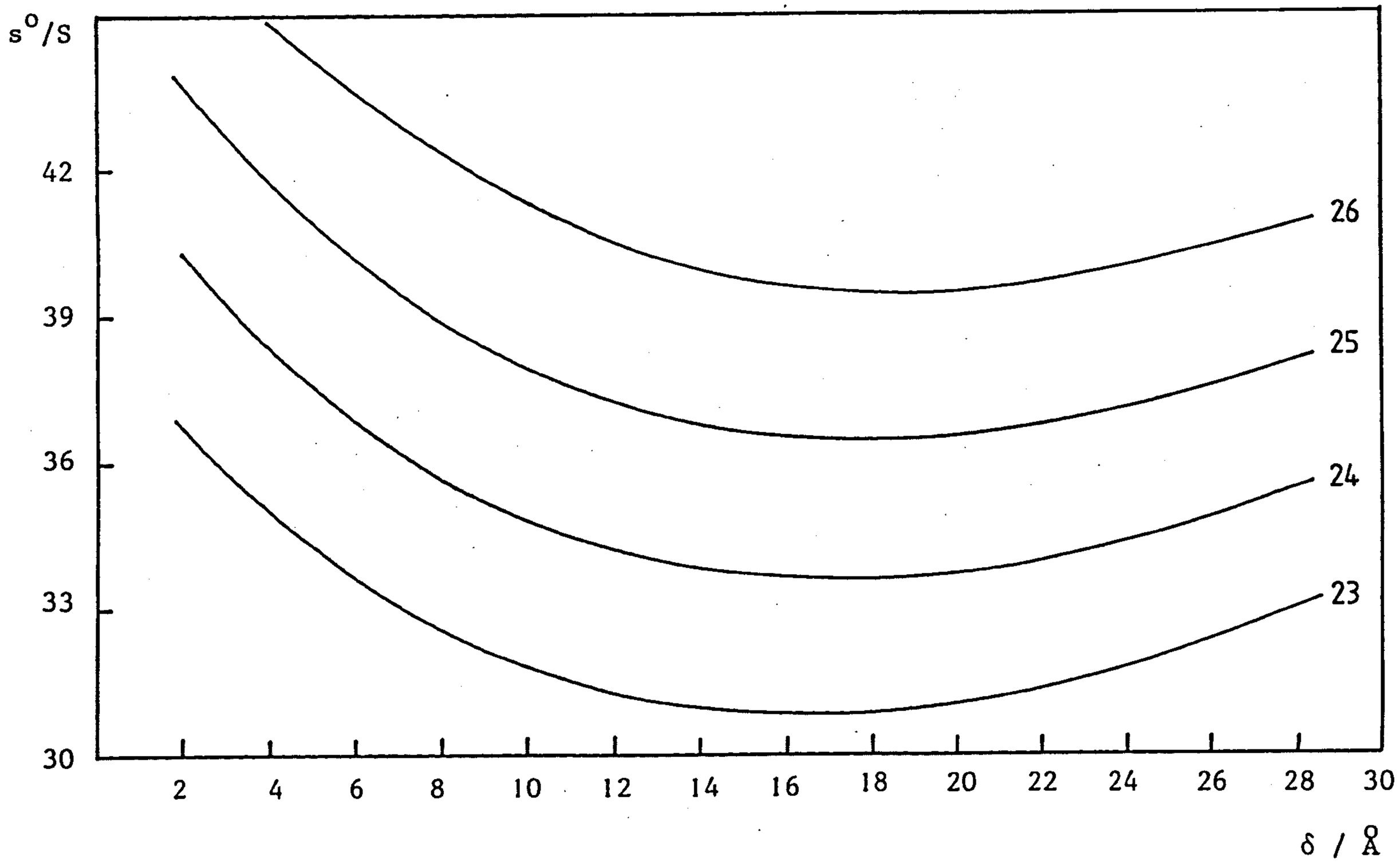

FIGURE 7.7 Calculated curves of sedimentation coefficient against adsorbed layer thickness for various values of the particles core radius for V-particles in toluene (ρ_2 = 1.03 g cm^{-3}; ρ_o = 0.867 g cm^{-3})

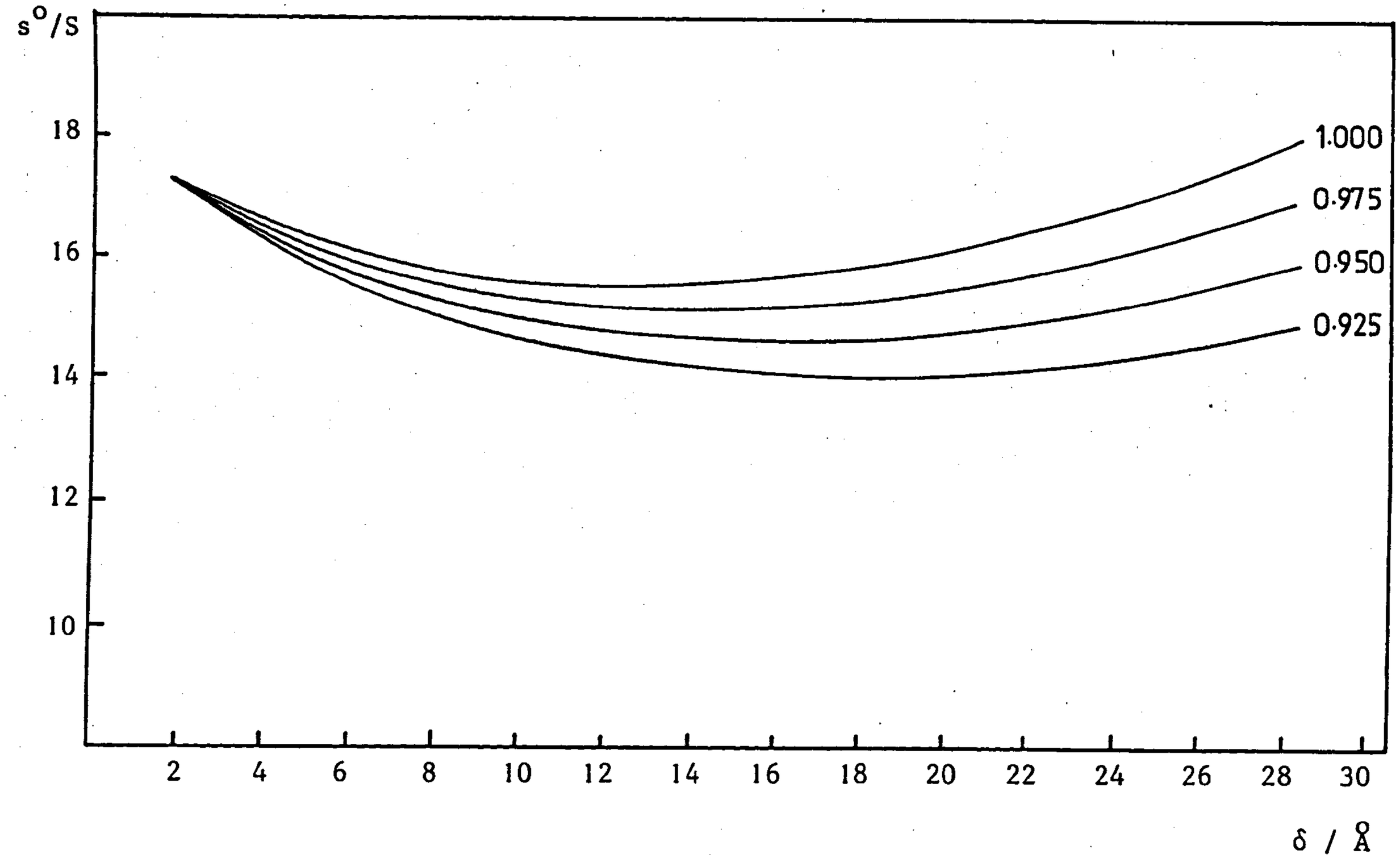

FIGURE 7.8 Calculated curves of sedimentation coefficient against adsorbed layer thickness for various values of adsorbed layer density for V-particles in dodecane (a = 25 Å; ρ_o = 0.747 g cm^{-3})

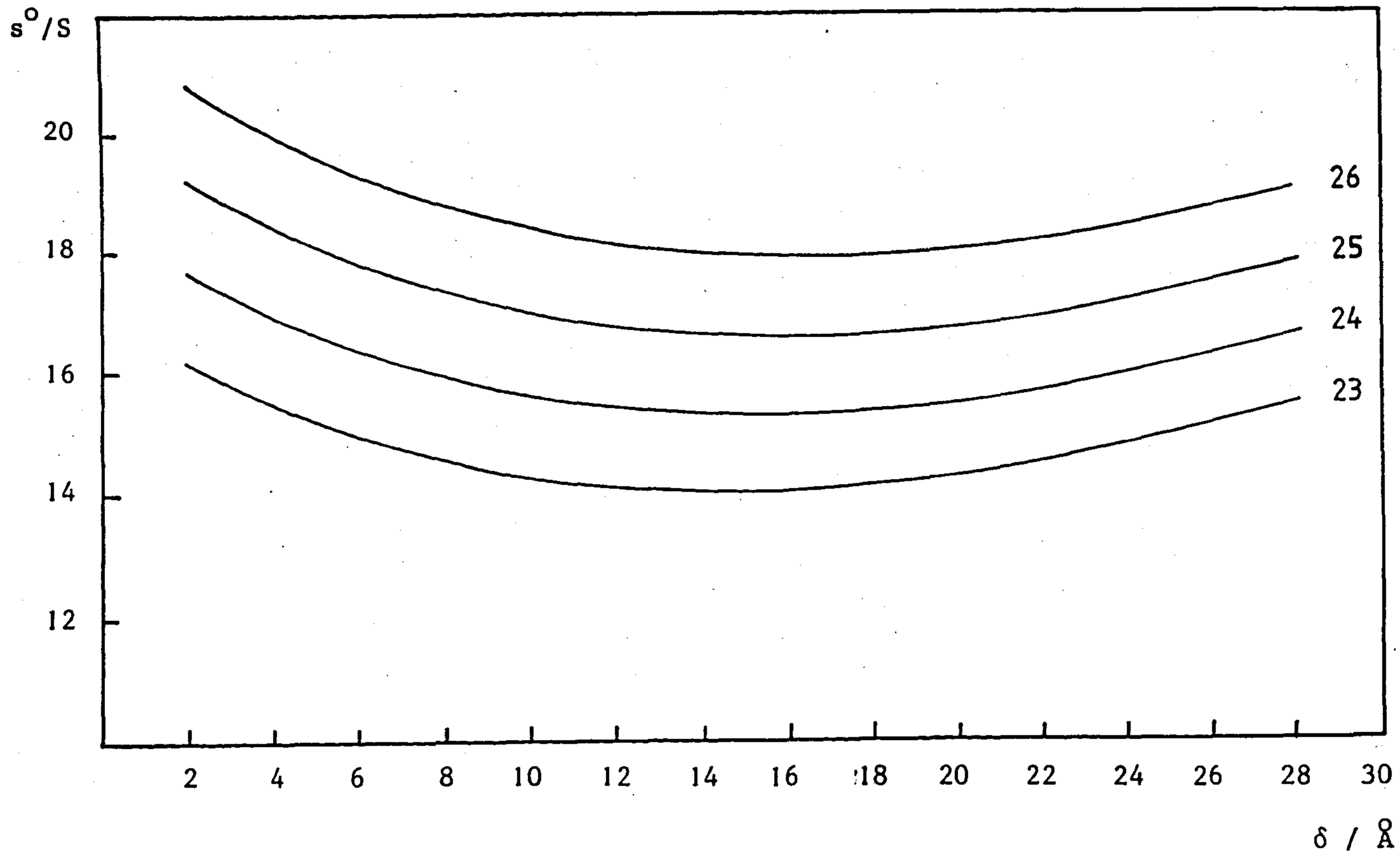

FIGURE 7.9 Calculated curves of sedimentation coefficient against adsorbed layer thickness for various values of the core particle radius for V-particles in dodecane (ρ_2 = 0.950 g cm^{-3}; ρ_o = 0.767 g cm^{-3})

be carrying a layer of solvent around them which would increase the adsorbed layer thickness. The discrepancy in the values of ρ_2 appears to indicate a different degree of solvation of the adsorbed layer in the two systems.

A speculative calculation to determine the amount of solvent present in the adsorbed layer was carried out. For the V-series in toluene, assuming that the density of the unsolvated layer is 1.05 g cm^{-3} and that of toluene 0.867 g cm^{-3} at 25°C, then ρ_2 = 1.03 g cm^{-3} corresponds to ca. 11% of the volume of the adsorbed layer being toluene. A similar calculation for the V-particles in dodecane, assuming that the density of the solvent is 0.748 g cm^{-3} predicts that 41.4% of the volume of the adsorbed layer is solvent when ρ_2 = 0.925 g cm^{-3} and 33.1% when ρ_2 = 0.95 g cm^{-3}. Despite the inaccuracy of these values, they do, however, appear to indicate a greater degree of solvation of the adsorbed layer when dodecane is the dispersion medium. Moreover, using the values of the various parameters determined by this method, it is possible to calculate the effective density of the whole particle and compare it to the value determined by densitometry.

$$(a + \delta)^3 \rho_{eff} = a^3 \rho_1 + \left[(a + \delta)^3 - a^3 \right] \rho_2 \qquad \ldots \quad (7.39)$$

Using ρ_1 = 2.71 g cm^{-3}, the calculated value of ρ_{eff} for the V-particles in toluene is 1.23 g cm^{-3} and in dodecane is 1.11 g cm^{-3}. A comparison with the experimental ρ_{eff} values given in Section 7.3 shows that whereas in toluene the values are in good agreement, in dodecane the calculated value of ρ_{eff} is somewhat lower. This appears to signify that the value used for ρ_2 is too low.

It was pointed out in Section 7.1.3 that the concentration dependence of the sedimentation coefficients can be represented by the equation

$$s = s^o / (1 + k\phi) \qquad \ldots \quad (7.21)$$

where ϕ is the effective, total volume fraction of the particles in the dispersion. Using the value of c_{cor}, one can obtain ϕ_p, the volume fraction of the core particles and hence N_p, the number of particles per cm^3, since $N_p = \phi_p/V_p$ (V_p is the volume of the core particle). ϕ can then be calculated from $\phi = N_p V_T$ where $V_T = 4\pi(a + \delta)^3/3$. Thus, for example, 1.0% w/w of $CaCO_3$ (c_{cor} = 0.94%) corresponds to ϕ = 0.033.

Using equation (7.21) k was calculated to be equal to 3.48 for the V-series in toluene and 5.17 for the V-series in dodecane. Since both these values are greater than 2.5, then clearly correcting the sedimentation coefficient for the change in the viscosity with concentration is inadequate to explain the results. Consequently, the additional effect of the backward flow of solvent must be included as given by equation (7.26). Assuming, according to Burgers that α = 0.75, then k_s is calculated to be 0.6 in toluene and 2.29 in dodecane. Although both these values are lower than Burgers estimated value of 4, they indicate that both backward flow and viscosity effects are operative in causing a decrease in sedimentation rate.

The L-series

The results obtained for the L-particles in toluene and in dodecane are listed in Tables 7.4 and 7.5 respectively.

TABLE 7.4 L-particles in toluene

SAMPLE	c_{cor}/% w/w	Sedimentation coefficient/S
0.50 L/TOL	0.44	201.5
0.75 L/TOL	0.68	191.0
1.0 L/TOL	0.91	180.5
1.25 L/TOL	1.15	172.5

TABLE 7.5 L-particles in dodecane

SAMPLE	c_{cor}/% w/w	Sedimentation coefficient/S
0.50 L/DOD	0.44	99.4
0.75 L/DOD	0.66	95.0
1.0 L/DOD	0.90	90.0
1.25 L/DOD	1.10	89.0

Figures 7.10 and 7.11 show the plots of the sedimentation coefficient against the concentration of the L-particles. In the case of the L-series in toluene s^o = 220 S, whereas for the L-series in dodecane s^o = 107.9 S. Once again, it was necessary to calculate theoretical sedimentation coefficients as a function of the adsorbed layer thickness and density according to equation (7.19). It was found that the experimental values of s^o for the L-particles dispersed in toluene and dodecane corresponded to identical values of the core particle radius, adsorbed layer thickness and density, namely a = 62 Å, δ = 32 Å and ρ_2 = 1.0 g cm^{-3}. This is in contradistinction to the V-series for which different results were obtained for the two dispersion media.

Whereas the value of the particle core radius is in excellent agreement with that determined by SANS, the value of the thickness of the adsorbed layer is considerably bigger. This is possibly a consequence of the presence of PIBSA chains in addition to the surface active agent in the adsorbed layer of the L-particles. It was found in Chapter 6 that for the case of the most dilute dispersion of the L-series the hard-sphere thickness was 60 Å and this was attributed to the length of the fully extended PIBSA chains.

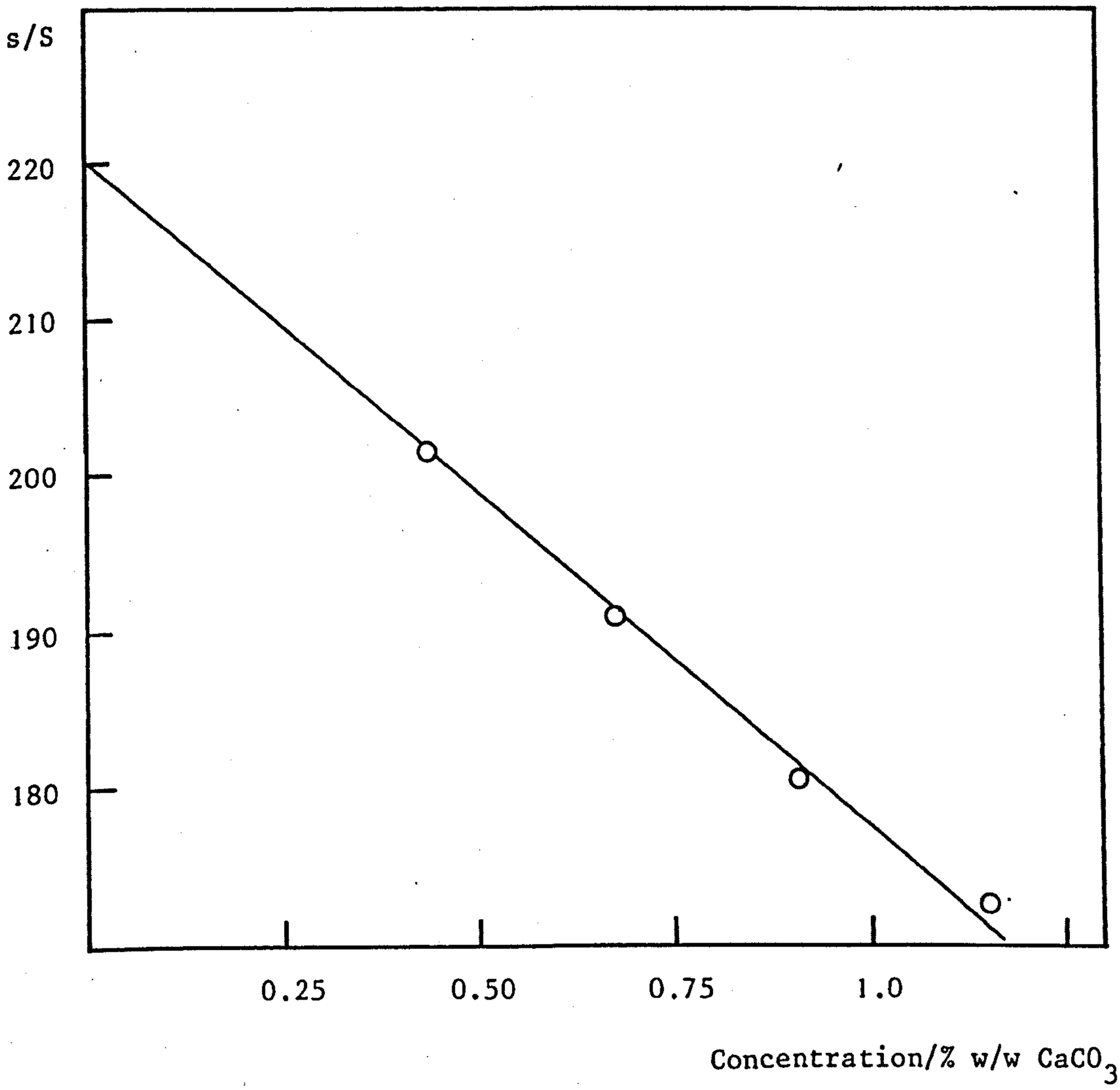

FIGURE 7.10 Sedimentation coefficient against concentration for L-particles dispersed in toluene

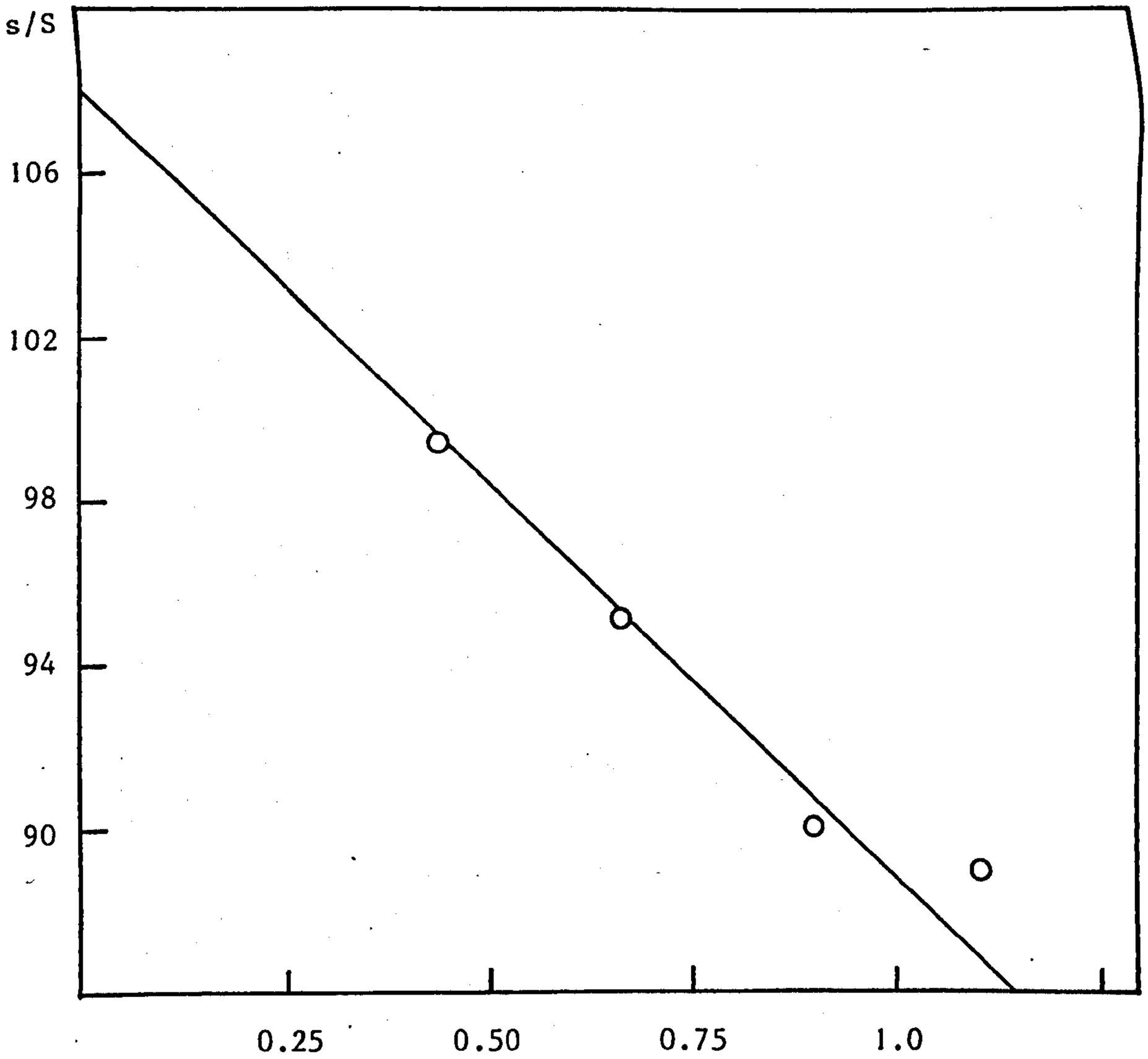

FIGURE 7.11 Sedimentation coefficient against concentration for L-particles dispersed in dodecane

Using this assumption it appears that, under the influence of a centrifugal field, the PIBSA chains coil round the adsorbed layer possibly trapping a layer of solvent within. Similarly to the V-series, it is possible to calculate the effective density of the whole particle using equation (7.39). The calculated value of ρ_{eff} is 1.49 g cm^{-3} whereas different values were experimentally determined for the two dispersion media. This suggests that whereas different degrees of solvation may exist when the PIBSA chains are extended, this difference disappears under a centrifugal field.

The concentration dependence of the sedimentation coefficient was much more pronounced in the case of the L-series than for the V-series. Using equation (7.21) k was calculated to be ~20 for the L-particles in toluene and ~18 for the L-particles in dodecane. Using Burgers values in equation (7.26) k should be ~7 and hence the experimental values of k_s are both much greater than Burgers estimated value of 4.

The F-series

The results obtained for the F-particles in toluene and in dodecane are listed in Tables 7.6 and 7.7 respectively.

TABLE 7.6 F-particles in toluene

SAMPLE		c_{cor}/% w/w	Sedimentation coefficient/S
1	F/TOL	0.96	68.3
1.5	F/TOL	1.45	65.8
2	F/TOL	1.93	63.6
3	F/TOL	2.90	58.9

TABLE 7.7 F-particles in dodecane

SAMPLE	c_{cor}/% w/w	Sedimentation Coefficient/S
0.5 F/DOD	0.44	29.8
1.5 F/DOD	1.42	27.8
2 F/DOD	1.90	26.7
3 F/DOD	2.87	24.7

The results for the two F-series are shown in Figures 7.12 and 7.13. It can be seen that very good straight line plots were obtained for both series from which the sedimentation coefficients at zero concentration were extrapolated. The accuracy of these plots is surprising since it was determined by SANS that the F-series was a polydisperse system. Hence, it appears that polydispersity straightens out the plot of the sedimentation coefficient against concentration. In the case of the F/TOL series s^o = 72.8 S and for the F/DOD series s^o = 30.8 S. Using equation (7.19) theoretical values of the sedimentation coefficient as a function of the adsorbed layer thickness were calculated. The experimental value of s^o for the F/TOL series corresponds to the following values:

$$a = 36\ \text{Å}, \qquad \delta = 22\ \text{Å} \qquad \text{and} \qquad \rho_2 = 1.0\ \text{g cm}^{-3}.$$

In the case of the F/DOD series the following values were obtained:

$$a = 33\ \text{Å}, \qquad \delta = 20\ \text{Å} \qquad \text{and} \qquad \rho_2 = 1.0\ \text{g cm}^{-3}.$$

The values of both the particle core radius and the adsorbed layer thickness agree with those obtained by SANS. Hence, in contradistinction to the previous two series, the hydrodynamic thickness of the F-particles appears not to differ from the adsorbed layer thickness. This suggests that little solvation of the adsorbed layer occurs.

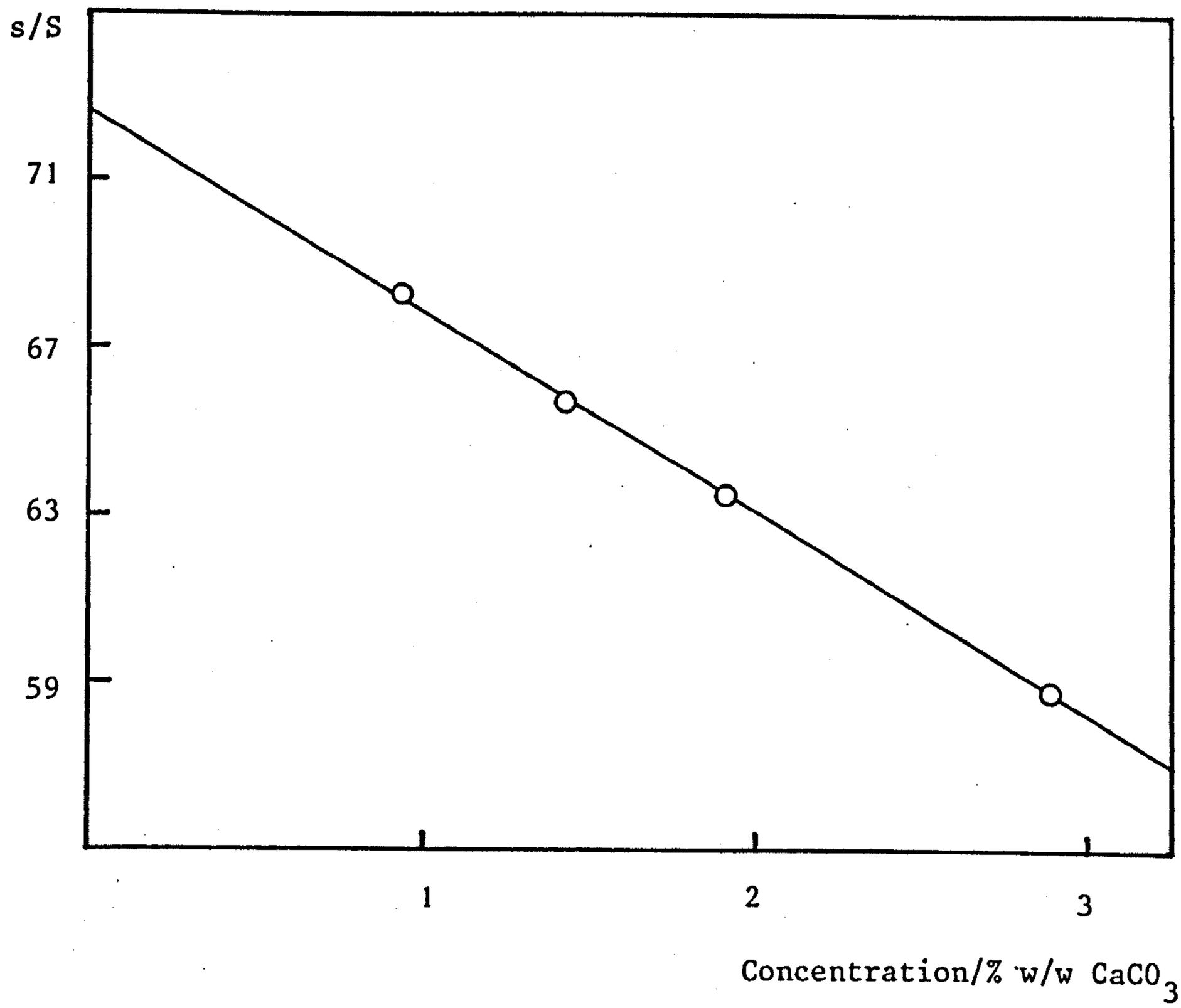

FIGURE 7.12 Sedimentation coefficient against concentration for F-particles dispersed in toluene

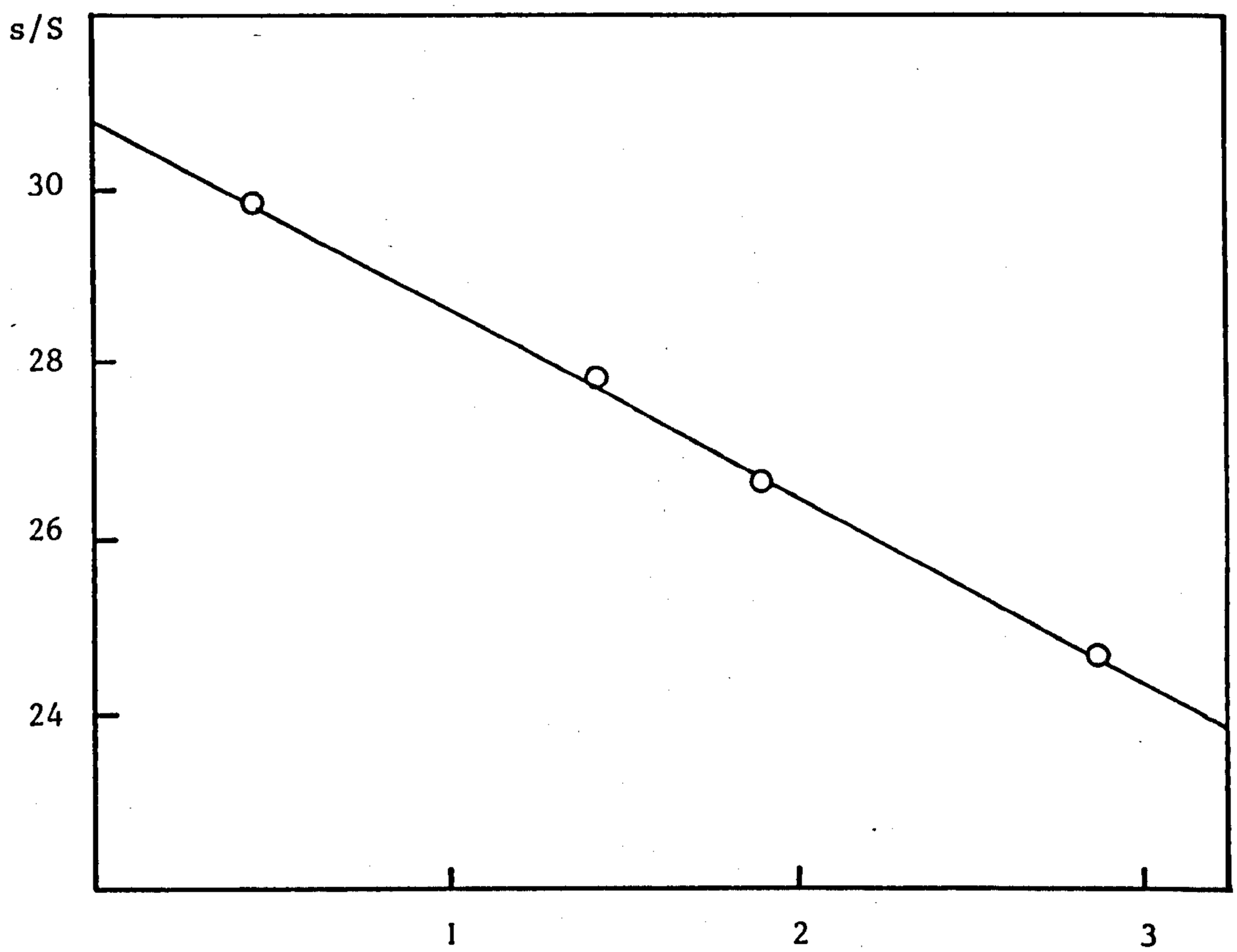

FIGURE 7.13 Sedimentation coefficient against concentration for F-particles dispersed in dodecane

Using equation (7.21) the value of k was calculated from the plots of the sedimentation coefficient against concentration. The concentration dependence of the sedimentation coefficient was identical for the F-particles in both dispersion media, viz. k = 4.7. Assuming Burgers value of 0.75 for α in equation (7.26) k_s was calculated to be ~1.8, which is considerably lower than his predicted value of 4. However, the value of k = 4.7 suggests that the sole consideration of viscosity effects is insufficient to account for the decrease in sedimentation rate.

From the ultracentrifugation results values of the particle core radius, adsorbed layer thickness and adsorbed layer density were determined, using a fitting procedure. The values of the particle core radius were in good agreement with those determined by SANS for all three series. In the case of the V-series and the L-series the hydrodynamic thickness of the adsorbed layer was, as expected, greater than the thickness determined by SANS. Moreover, from the different values obtained for the adsorbed layer density in dodecane and in toluene for the V-series, it appeared that greater solvation of the adsorbed layer occurred when dodecane was the dispersion medium. In the case of the F-series, good straight line plots of the sedimentation coefficient against concentration were obtained up to a concentration of 3% w/w of $CaCO_3$; this suggested that polydispersity increased the concentration range over which a linear relationship between s and c is valid. Finally, it was found that for all three systems the concentration dependence of the sedimentation coefficient was a result of both viscosity effects and the backward flow of solvent.

CHAPTER EIGHT

CHAPTER 8

CONCLUSION

The work described in this thesis involved the characterization of an industrial system, namely a lubricating oil additive. This system consisted of calcium carbonate particles stabilized by an adsorbed layer of alkyl aryl sulphonate and dispersed in a non-aqueous medium. Since the particles were prepared using industrial chemicals, a number of experimental problems were encountered. Firstly, the system consisted of brown dispersions which were very viscous at higher concentrations of particles; secondly, the exact chemical composition of the constituents was not known.

In order to determine the nature of the system a model was adopted which represented the particles as a spherical calcium carbonate core particle surrounded by a concentric shell of adsorbed material. This model was used for the interpretation of the experimental data obtained on both dilute and concentrated dispersions of the three systems under investigation, namely the V-series, the L-series and the F-series.

For the case of small-angle neutron scattering of dilute dispersions, a theory was developed for concentric spheres which lead to the determination of the radius of the core particle and the thickness of the adsorbed layer. This was accomplished for the particles in situ, i.e. it was possible to determine the extent of adsorption keeping the whole particle intact. Two methods of approach were used:

1) The Guinier approach involved the determination of the mean radius of gyration of the particle from which the particle core radius and the thickness of the adsorbed layer could be calculated.

2) The curve fitting approach consisted of obtaining a match between the

experimental and the theoretically calculated absolute scattering intensities over a range of scattering vectors.

The analysis and the development of this theory highlighted the dependence of the scattering intensity on the scattering length density of the medium. In particular, a range of scattering effects were shown to occur in the region of the contrast match between the average coherent scattering length of the particle and the scattering length of the dispersion medium. The experimental results obtained for the V-series and the L-series were in very good agreement with the theory. The F-series was a polydisperse system and consequently much more difficult to treat; despite this, reasonable intensity results were obtained from which an estimate of the degree of polydispersity could be determined.

Many industrial dispersions are used at high concentrations and, as such, constitute concentrated colloidal dispersions. Until recently, very few methods have existed for the examination of such systems, especially when the dispersion medium is non-aqueous. The technique of small-angle neutron scattering is particularly useful for these studies, and it was applied to dispersions of the V-series and the L-series containing up to 40% w/w of calcium carbonate. Methods were developed for the treatment and the analysis of the data which allowed the interparticle structure factor to be extracted. This provided information on the nature of the interactions between the particles and the factors controlling the stability of the systems.

In the case of the V-series, it was found that the colloidal particles were essentially interacting as hard spheres. This short range interaction is concordant with the idea that the adsorbed layer of surface active agent acts as a sterically stabilizing layer. Moreover, it was found that the hard-sphere thickness was less than the thickness of the adsorbed layer

suggesting that,

a) interpenetration of the adsorbed layers occurs which signifies that a solvation layer may also exist around the particle;

b) some desorption of surface active agent occurs from the stabilizing layer as the concentration of particles increases.

The L-series, which consisted of bigger core particles than those of the V-series, stabilized by an adsorbed layer of surface active agent and polyisobutene succinic anhydride, exhibited a somewhat different behaviour. The results obtained indicated that at low concentrations the hard-sphere thickness was much greater than the adsorbed layer thickness. However, as the concentration of particles increased the value of the hard-sphere thickness decreased towards the value for the adsorbed layer thickness. This suggested a gradual compression of the longer PIBSA chains with increasing concentration of the particles. Consequently, it is only at very high concentrations of the L-particles that the hard-sphere potential is operative, whereas the interaction between the particles at lower concentrations would be better explained with a softer interaction potential.

In order to investigate the hydrodynamic properties of the systems the totally different technique of ultracentrifugation was used. Once again, the model of a spherical core particle with a concentric adsorbed layer was used to develop the equations for sedimentation. These equations were applied to estimate values of the core radius and the hydrodynamic thickness, δ. All three systems were investigated by this technique and the results obtained for the particle core radii were within 12% of the values determined by SANS. However, the values of the hydrodynamic thickness were, as expected, slightly larger than the adsorbed layer thickness obtained by SANS since the hydrodynamic volume of the particle is not equivalent to the scattering volume.

The results obtained for the V-series and the L-series suggested that a greater degree of solvation of the adsorbed layer occurred when dodecane rather than toluene was the dispersion medium. In addition, all three systems exhibited a marked concentration dependence of the sedimentation coefficient. This dependence decreased above a concentration of ca. 1% w/w of $CaCO_3$ for the case of the V-series and the L-series and was more pronounced when dodecane was the dispersion medium. It is interesting to note that the polydisperse F-series exhibited a constant concentration dependence of the sedimentation coefficient up to ca. 3% w/w of $CaCO_3$, which was lower when dodecane was used as the dispersion medium. All the results indicated that it is the combined effects of backward flow and viscosity which are responsible for the decrease in sedimentation rate.

In addition to the above-mentioned techniques, some preliminary results were also obtained using photon correlation spectroscopy which have not been reported in the thesis. These experiments were carried out on very dilute dispersions of the V-series and the L-series in toluene and dodecane. The value of the hydrodynamic radius of the V-particles was ca. 50 Å and that of the L-particles was ca. 90 Å; both these results agree with those obtained by ultracentrifugation.

Finally, taking into account the complexity of these systems, considerable progress has been made in their characterization. Moreover, the monodispersity and stability of the particles has enabled advances to be made in the theory of small-angle neutron scattering of concentric spheres. Some progress has also been made in the determination of the type of potential operating between the particles and consequently the factors controlling the stability of these systems.

REFERENCES

REFERENCES

1. Wood, G.P., J. Inst. Petrol., 55, 194 (1969).

2. Esso Magazine, No. 117, 1981.

3. Napper, D.H., "Polymeric Stabilization of Colloidal Dispersions", Academic Press, London, 1983.

4. Mackor, E.L., J. Colloid Sci., 6, 492 (1951).

5. Jäckel, K., Kolloid - Z., 197, 143 (1964).

6. Fischer, E.W., Kolloid - Z., 160, 120 (1958).

7. Ottewill, R.H., in "Non-ionic Surfactants", Ed. Schick, M.J., Marcel Dekker, 1, 627 (1967).

8. Ottewill, R.H., and Walker, T.W., Colloid & Polymer Sci., 227, 108 (1968).

9. Doroszkowski, A., and Lambourne, R., J. Polymer Sci., C34, 253 (1971).

10. London, F., Trans. Faraday Soc., 33, 8 (1937).

11. Hamaker, H.C., Physica, 4, 1058 (1937).

12. Vold, M.J., J. Colloid Sci., 16, 1 (1961).

13. Osmond, D.W.J., Vincent, B., and Waite, F.A., J. Colloid and Interface Sci., 42, 262 (1973).

14. Lifshitz, E.M., Soviet Phys., 2, 273 (1956).

15. Evans, R., and Napper, D.H., J. Colloid and Interface Sci., 45, 138 (1973).

16. Smith, E.R., Mitchell, D.J., and Ninham, B.W., J. Colloid and Interface Sci., 45, 55 (1973).

17. Ottewill, R.H., and Walker, T.W., J. Chem. Soc. Faraday Trans. I, 70, 917 (1974).

18. Weeks, J.D., Chandler, D., and Andersen, H.C., J. Chem. Phys., 54, 5237 (1971).

19. Ottewill, R.H., in "Science and Technology of Polymer Colloids", Ed. Poehlein, G.W., Ottewill, R.H., and Goodwin, J.W., NATO ASI Series, The Hague, 503 (1983).

20. Croxton, C.A., "Introduction to Liquid State Physics", John Wiley and Son, London, 1975.

21. Barker, J.A., and Henderson, D., Rev. Mod. Phys., 48, 587 (1976).

22. Percus, J.K., and Yevick, G.J., Phys. Rev., 110, 1 (1958).

23. Carnahan, N.F., and Starling, K.E., J. Chem. Phys., 51, 635 (1969).

24. White, W.B., in "The Infrared Spectra of Minerals", Ed. Farmer, V.C., Mineralogical Society (1974).

25. Partington, J.R., "General and Inorganic Chemistry", MacMillan & Co., 1946.

26. "Selected Values of the Physical and Thermodynamic Properties of Hydrocarbons", American Petroleum Institute Research Project 44, Texas A & M University.

27. Guinier, A., and Fournet, G., "Small-Angle Scattering of X-rays", Wiley, 1955.

28. Bacon, G.E., "Neutron Scattering in Chemistry", Butterworths, London, 1977.

29. Marshall, W., and Lovesey, S.W., "Theory of Thermal Neutron Scattering", Clarendon Press, Oxford, 1971.

30. Jacrot, B., Rep. Prog. Phys., 39, 911 (1976).

31. Windsor, G.G., "Pulsed Neutron Scattering", Taylor and Francis, London, 1981.

32. Kerker, M., "The Scattering of Light and other Electromagnetic Radiation", Academic Press, New York, 1969.

33. "Neutron Research Facilities at the High Flux Reactor of the ILL", Institut Max von Laue-Paul Langevin, Grenoble, France, 1975.

34. Schmatz, W., and Schelten, J., J. Appl. Cryst., 13, 385 (1980).

35. Harris, N., D - Phil., Oxford, 1980.

36. Ghosh, R.E., "A Computing Guide for Small-Angle Scattering Experiments", 78 GH 247 T Institut Laue-Langevin, Grenoble, 1978.

37. Harris, N., Ottewill, R.H., and White, J.W., in "Adsorption from Solution", Eds. Ottewill, R.H., Rochester, C.H., and Smith, A.L., Academic Press, London, 139 (1976).

38. Ottewill, R.H., in "Colloidal Dispersions", Ed. Goodwin, J.W., Royal Society of Chemistry, London, 143 (1982).

39. Cebula, D.J., Goodwin, J.W., Ottewill, R.H., Jenkin, G., and Tabony, J., Colloid and Polymer Sci., 261, 555 (1983).

40. Davies, E.K., Chemgraf program suite Chemical Crystallography Laboratory, University of Oxford, 1982.

41. Ottewill, R.H., in "Colloidal Dispersions", Ed. Goodwin, J.W., Royal Society of Chemistry, London, 197 (1982).

42. Cairns, R.J.R., Ottewill, R.H., Osmond, D.W.J., and Wagstaff, I., J. Colloid and Interface Sci., 54, 45 (1976).

43. Ashcroft, N.W., and Lekner, J., Phys. Rev., 45, 33 (1966).

44. van Beurten, P., and Vrij, A., J. Chem. Phys., 74, 2744 (1981).

45. Svedberg, T., and Nichols, J.B., J. Am. Chem. Soc., 45, 2910 (1923).

46. Stokes, G.G., Mathematical & Physical Papers, University Press, Cambridge, Vol.III, 59-60 (1901).

47. Svedberg, T., Kolloid Z. Zsigmondy-Festschrift, Eng. Bd. Zu. 36, 53 (1925).

48. Thompson, W.I., Ph.D. Thesis, University of Bristol, 1973.

49. Goldberg, R.J., J. Phys. Chem., 57, 194 (1953).

50. Fujita, H., "Mathematical Theory of Sedimentation Analysis", Academic Press, 1959.

51. Burgers, J.M., Proc. Acad. Sci. Amsterdam, 45, 9, 126 (1942).

52. Cheng, P.Y., and Schachman, H.K., J. Polymer Sci., 16, 19 (1955).

53. Schachman, H.K., and Kauzmann, W.J., J. Phys. & Colloid Chem., 53, 150 (1949).

54. Svedberg, T., and Rinde, H., J. Am. Chem. Soc., 45, 943 (1923); 46, 2677 (1924).

55. Trautman, R., and Schumaker, V.N., J. Chem. Phys., 22, 551 (1954).

56. Svedberg, T., and Pedersen, K.O., "The Ultracentrifuge", Oxford University Press, London/New York (1940).

57. Mosimann, H., and Signer, R., Helv. Chim. Acta, 27, 1123 (1944).

58. Bowen, T.J., "An Introduction to Ultracentrifugation", University Press, 1970.

59. Schachman, H.K., "Ultracentrifugation in Biochemistry", Academic Press, 1959.

A P P E N D I X

```
10 REM TAPE NO 10 ; FILE NO 19
20 REM ZEROTH LOG NORMAL DISTRIBUTION
30 REM INPUT MODAL MEAN RADIUS
40 REM ENTER SIGMA ZERO AS NUMBER NOT AS PERCENT
50 DIM R[20],Z[20],P[20],T[20],U[20],O[20]
60 REM S1=SIGMA 0  R1= MODAL MEAN
70 SCALE 0,0.1,0,2
80 XAXIS 0,0.01
90 YAXIS 0,0.2
100 DISP "  ENTER SIGMA ZERO ";
110 INPUT S1
120 DISP "  ENTER MODAL RADIUS";
130 INPUT R1
140 DISP " ENTER INITIAL VALUE OF Q";
150 INPUT Q1
160 DISP " ENTER INCREMENT IN Q";
170 INPUT Q2
180 DISP " ENTER FINAL VALUE OF Q";
190 INPUT Q3
200 DISP " ENTER THICKNESS OF LAYER D";
210 INPUT D
220 DISP "  ENTER SCAT LEN DENS SHELL L1";
230 INPUT L1
240 DISP "ENTER SCAT LEN DENS MEDIUM L2";
250 INPUT L2
260 DISP " ENTER SCAT LEN DENS PARTICLE L3";
270 INPUT L3
280 V=S1↑2
290 V1=EXP(4*V)-EXP(3*V)
300 V2=SQR(V1)
310 S2=R1*V2
320 S3=1.5*S1*S1
330 R2=LOG(R1)
340 R3=R2+S3
350 REM R4= MEAN VALUE OF RADIUS
360 R4=EXP(R3)
370 PRINT "MODAL RADIUS TAKEN IS ";R1
380 PRINT "   MEAN  RADIUS = ";R4
390 PRINT " SIGMA ZERO IS = ";S1
395 PRINT " STANDARD DEVIATION IS = ";S2
400 PRINT " THICKNESS OF LAYER=";D
410 PRINT " SCATTERING LENGTH DENSITY SHELL =";L1
420 PRINT " SCATTERING LENGTH DENSITY OF MEDIUM =";L2
430 PRINT " SCATTERING LENGTH DENSITY OF PARTICLE =";L3
440 C=SQR(2*PI)
450 C1=S1*S1/2
460 C2=EXP(C1)
470 C3=C*S1*R1*C2
480 FOR I=1 TO 13 STEP 1
490 M=I-7
500 R[I]=R4+M*(S2/2)
510 R5=LOG(R[I])
520 R6=R5-R2
530 R7=(R6↑2)/(2*S1*S1)
540 R8=EXP(-R7)
550 P1=R8/C3
560 Z[I]=P1*(S2/2)*100
570 P[I]=P1*(S2/2)
580 NEXT I
590 WRITE (15,600)
600 FORMAT 5X,"I",8X,"R",8X,"P.CENT"
```

```
600 FORMAT 5X,"I",8X,"R",8X,"P.CENT"
610 FOR I=1 TO 13 STEP 1
620 WRITE (15,630)I,R[I],Z[I]
630 FORMAT 4X,F4.0,5X,F6.1,5X,F6.1
640 NEXT I
650 PRINT
660 PRINT
670 PRINT
672 F5=((L1-L2)↑2)*(R4+D)↑6
674 F6=((L3-L1)↑2)*(R4↑6)
676 F7=2*(L3-L1)*(L1-L2)*(R4↑3)*((R4+D)↑3)
678 F8=F5+F6+F7
680 WRITE (15,690)
690 FORMAT 12X,"Q",13X," F1 ",8X,"F2",8X,"F3",8X,"F",8X,"P(Q)"
700 FOR Q=Q1 TO Q3 STEP Q2
710 S=0
720 U=0
730 O=0
740 FOR I=1 TO 13 STEP 1
750 T1=Q*R[I]
760 T2=SIN(T1)
770 T3=T1*COS(T1)
780 P9=3*(T2-T3)/(T1↑3)
790 P8=P9↑2
800 R9=R[I]+D
810 T9=Q*R9
820 T8=SIN(T9)
830 T7=T9*COS(T9)
840 B9=3*(T8-T7)/(T9↑3)
850 B8=B9↑2
860 T[I]=P[I]*P8
870 U[I]=P[I]*B8
880 O[I]=P[I]*P9*B9
890 S=S+T[I]
900 U=U+U[I]
910 O=O+O[I]
920 NEXT I
930 F1=F5*U
940 F2=F6*S
950 F3=F7*O
960 F=F1+F2+F3
965 F9=F/F8
970 WRITE (15,980)Q,F1,F2,F3,F,F9
980 FORMAT 2X,E10.3,3X,E10.3,3X,E10.3,3X,E10.3,3X,E10.3,3X,E10.3,3X,E10.3
982 PLOT Q,F9
984 PEN
990 NEXT Q
1000 GOTO 140
1010 END
```

```
10 REM TAPE NO 14 ; FILE NO 3
20 REM P(Q)*S(Q)
30 REM ZEROTH LOG NORMAL DISTRIBUTION
40 REM INPUT MODAL MEAN RADIUS
50 REM ENTER SIGMA ZERO AS NUMBER NOT AS PERCENT
60 DIM R[20],Z[20],P[20],T[20],U[20],O[20]
70 REM S1=SIGMA 0  R1= MODAL MEAN
80 SCALE 0,0.05,0,500
90 XAXIS 0,0.01
100 YAXIS 0,50
110 DISP "  ENTER SIGMA ZERO ";
120 INPUT S1
130 DISP "  ENTER MODAL RADIUS";
140 INPUT R1
150 DISP " ENTER INITIAL VALUE OF Q";
160 INPUT Q1
170 DISP " ENTER INCREMENT IN Q";
180 INPUT Q2
190 DISP " ENTER FINAL VALUE OF Q";
200 INPUT Q3
210 DISP " ENTER THICKNESS OF LAYER D";
220 INPUT D
225 DISP "ENTER H.S.THICKNESS D1";
227 INPUT D1
230 DISP "  ENTER SCAT LEN DENS SHELL L1";
240 INPUT L1
250 DISP "ENTER SCAT LEN DENS MEDIUM L2";
260 INPUT L2
270 DISP " ENTER SCAT LEN DENS PARTICLE L3";
280 INPUT L3
290 DISP " ENTER ACTUAL VOLUME FRACTION";
300 INPUT V9
301 DISP "  ENTER WAVELENGTH IN ANGSTROMS";
302 INPUT D9
303 DISP "  ENTER TRANSMISSION OF SAMPLE";
304 INPUT K9
305 DISP " ENTER TRANSMISSION OF WATER";
306 INPUT K8
310 V=S1↑2
320 V1=EXP(4*V)-EXP(3*V)
330 V2=SQR(V1)
340 S2=R1*V2
350 S3=1.5*S1*S1
360 R2=LOG(R1)
370 R3=R2+S3
380 REM R4= MEAN VALUE OF RADIUS
390 R4=EXP(R3)
400 N1=3*V9*1E+24/(4*PI*(R4↑3))
410 V8=4*PI*((R4+D1)↑3)*N1*1E-24/3
411 D8=4.45+0.46*LOG(D9)
412 D7=EXP(D8)
413 D6=D7*1E-24
414 D5=D6*3.341E+22/(4*PI)
415 K7=K9/K8
420 PRINT "MODAL RADIUS TAKEN IS ";R1
430 PRINT "   MEAN  RADIUS = ";R4
440 PRINT " SIGMA ZERO IS= ";S1
445 PRINT " STANDARD DEVIATION IS =";S2
450 PRINT " THICKNESS OF LAYER=";D
```

```
455 PRINT " THICKNESS OF H.S.LAYER=";D1
460 PRINT " SCATTERING LENGTH DENSITY SHELL =";L1
470 PRINT " SCATTERING LENGTH DENSITY OF MEDIUM =";L2
480 PRINT " SCATTERING LENGTH DENSITY OF PARTICLE =";L3
490 PRINT " ACTUAL VOLUME FRACTION";V9
500 PRINT " EFFECTIVE VOLUME FRACTION";V8
501 PRINT " SCATTERING CROSS-SECTION OF WATER=";D6
502 PRINT " TRANSMISSION FACTOR TP/TW=";K7
505 PRINT " D5=";D5
510 G=((1+2*V8)↑2)/((1-V8)↑4)
520 H=(-6*V8*((1+0.5*V8)↑2))/((1-V8)↑4)
530 K=(0.5*V8*((1+2*V8)↑2))/((1-V8)↑4)
540 C=SQR(2*PI)
550 C1=S1*S1/2
560 C2=EXP(C1)
570 C3=C*S1*R1*C2
580 FOR I=1 TO 13 STEP 1
590 M=I-7
600 R[I]=R4+M*(S2/2)
610 R5=LOG(R[I])
620 R6=R5-R2
630 R7=(R6↑2)/(2*S1*S1)
640 R8=EXP(-R7)
650 P1=R8/C3
660 Z[I]=P1*(S2/2)*100
670 P[I]=P1*(S2/2)
680 NEXT I
690 WRITE (15,700)
700 FORMAT 5X,"I",8X,"R",8X,"P.CENT"
710 FOR I=1 TO 13 STEP 1
720 WRITE (15,730)I,R[I],Z[I]
730 FORMAT 4X,F4.0,5X,F6.1,5X,F6.1
740 NEXT I
750 PRINT
760 PRINT
770 PRINT
780 F5=((L1-L2)↑2)*(R4+D)↑6
790 F6=((L3-L1)↑2)*(R4↑6)
800 F7=2*(L3-L1)*(L1-L2)*(R4↑3)*((R4+D)↑3)
810 F8=F5+F6+F7
820 WRITE (15,830)
830 FORMAT 6X,"Q",12X,"P(Q)",8X,"S(Q)",9X,"PQ*SQ",8X,"Q*D",8X,"IP/IW
840 FOR Q=Q1 TO Q3 STEP Q2
850 S=0
860 U=0
870 O=0
880 FOR I=1 TO 13 STEP 1
890 T1=Q*R[I]
900 T2=SIN(T1)
910 T3=T1*COS(T1)
920 P9=3*(T2-T3)/(T1↑3)
930 P8=P9↑2
940 R9=R[I]+D
950 T9=Q*R9
960 T8=SIN(T9)
970 T7=T9*COS(T9)
980 B9=3*(T8-T7)/(T9↑3)
990 B8=B9↑2
```

```
1000 T[I]=P[I]*P8
1010 U[I]=P[I]*B8
1020 O[I]=P[I]*P9*B9
1030 S=S+T[I]
1040 U=U+U[I]
1050 O=O+O[I]
1060 NEXT I
1070 F1=F5*U
1080 F2=F6*S
1090 F3=F7*O
1100 F=F1+F2+F3
1110 F9=F/F8
1120 Y=Q*2*(R4+D1)
1130 Z1=-COS(Y)+SIN(Y)/Y
1140 Z2=-(Y↑2)*COS(Y)+2*Y*SIN(Y)+2*COS(Y)-2
1150 Z4=-(Y↑4)*COS(Y)+4*(Y↑3)*SIN(Y)+12*(Y↑2)*COS(Y)
1160 Z5=-24*Y*SIN(Y)-24*COS(Y)+24
1170 Z3=Z4+Z5
1180 S9=G*Z1/(Y↑2)+H*Z2/(Y↑4)+K*Z3/(Y↑6)
1190 S8=1/(1+24*V8*S9)
1200 S7=F9*S8
1201 K6=N1*F8*F9*S8*K7*5.8585E-28/D5
1202 REM K6 IS ABSOLUTE INTENSITY
1210 REM S8=S(Q)  AND F9 = P(Q)
1220 WRITE (15,1230)Q,F9,S8,S7,Y,K6
1230 FORMAT 2X,E10.3,3X,E10.3,3X,E10.3,3X,E10.3,3X,E10.3,3X,E10.3
1240 PLOT Q,K6
1250 PEN
1260 NEXT Q
1270 GOTO 150
1280 END
```